Phase-field modeling of equilibrium shapes of precipitate and growth instabilities in the presence of coherency stresses

A Thesis

Submitted for the Degree of

Doctor of philosophy

in the **Faculty of Engineering**

by

Bhalchandra Bhadak

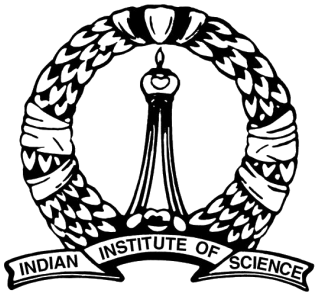

Department of Materials Engineering
Indian Institute of Science
Bangalore – 560 012 (INDIA)

MARCH 2020

DEDICATED TO

My Parents and Teachers

Acknowledgements

I would like to thank my thesis advisor Prof. Abhik Choudhury, who has consistently motivated me and persuade me to always think out of the box, he has always been immensely supportive. I learnt a lot of things from him while working on the thesis, and still a many more things like the fundamental understanding towards the subject and the approach to resolve the problems are somethings that I would like to work towards in the future. Also, I would like to thank our Chairman, Prof. Abinandanan, R.Sankarasubramanian from DMRL, Prof. S. Bhattacharya and Tushar Jogi from IIT Hyderabad, with whom we really had stimulating discussion on the subject, which helped me a lot while working on my thesis.

All my current and past labmates Arka Da, Sumeet, Fiyanshu, Kiran, Ravi, Bikram, Sai, Swapnil, Supriyo, Pramod and Apaar who helped me a lot while my stay at the campus and indeed, I feel great to be the part their group. Also, I would like to mention that, Kedar, Vijay, Prajakta, Meera, Mihir, Dhairya, Dipali, Swapnil and Kiran these are the people, who made my journey really pleasant, without them life would have been very monotonous. A big thanks to all of you.

Synopsis

Precipitation is a first-order solid-state phase transformation that typically occurs during heat treatments which leads to the improvement of strength in the material. One of the most common strengthening mechanisms is due to the presence of coherency between the precipitate and matrix that leads to the formation of strain fields in the matrix, whose interaction with the dislocation networks leads to an improvement in the strength. Therefore, the spatial distribution of precipitates as well as their individual shapes influence the strengthening mechanism occurring due to coherent precipitation. This therefore forms the basic motivation of our thesis wherein, we investigate equilibrium shapes of precipitates and configurations as a function of the elastic and interfacial properties using a numerical approach based on the phase-field method.

We firstly propose a diffuse interface model which allows us to minimize grid-anisotropy related issues applicable to sharp-interface methods. In this context, we introduce a novel phase-field method for computing equilibrium shapes where we minimize a functional consisting of the elastic and surface energy contributions while preserving the precipitate volume. Using this technique we reproduce the shape-bifurcation diagrams for the cases of pure dilatational misfit in 2D that have been studied previously using sharp interface methods and then extend them to include interfacial energy anisotropy with different anisotropy strengths which has not been a part of previous sharp-interface models. Thereafter, we extend these calculations to three dimensions. Here, we find some important differences between the features of the shape-bifurcation diagrams that are derived in 2D and 3D. In this work, our focus is theoretical in extent, however, we make possible connections with microstructures in experiments. We also compare our diffuse-interface model against the previous/available models for the calculation of equilibrium morphologies of precipitates.

In the second part, we extend the diffuse interface model for the calculation of multi-variant configurations of the precipitates that arise out of a solid-state precipitate reaction. Here, the volume of each variant of the precipitate in the configuration is conserved while the total energy i.e. the sum of the elastic and the interfacial energies is minimized using an extension of the

volume-preserved Allen-Cahn algorithm [1, 2], thus delivering the equilibrium configuration. Using this technique, we investigate precipitate self-organization for three solid-state reactions. The first is the classical two-phase precipitate reaction that leads to the formation of core-shell microstructures, where we clarify the influence of elasticity on the formation of such clusters. Following this, we investigate two symmetry-breaking transitions (cubic to tetragonal) and (hexagonal to orthorhombic), that lead to the formation of multi-variant clusters where we study the organization of the precipitates as a function of the elastic properties of the precipitate and the matrix.

While the previous two parts of the thesis are involved in the computation of equilibrium shapes and configurations, in the final chapter we focus on precipitate growth and in particular the morphologies that arise out of diffusive instabilities because of growth in a supersaturated matrix. We formulate a phase-field model based on a grand-potential functional for modeling growth of a precipitate in a binary alloy in the presence of coherency stresses. Using the formulation, we show that the presence of anisotropy in the elastic energy leads to the formation of dendrite-like shapes similar to microstructures arising out of a Mullins-Sekerka like instability during solidification. Here, we characterize the instability as a function of the different material properties and supersaturations. The principal finding is that while the basis of the instability is similar to what is typically observed during solidification, the presence of coherency stresses brings in an important change with respect to the selection of the dendrite tip radius and velocity, where we find an absence of steady-state in contrast to dendrites occurring during solidification.

In the following sections, we briefly outline the specific details in each of the above mentioned studies and the novel results obtained in each of them.

Equilibrium precipitate shapes under the influence of coherency stresses

In this study, using a novel phase-field model described in [1], we calculate the equilibrium shapes of the precipitate as well as derive the corresponding shape bifurcation diagrams as a function of different elastic as well as interfacial properties. Firstly, we predict the equilibrium shapes of the precipitate (in 2D) in the presence of isotropic elastic energy (Zener anisotropy parameter ($A_z = 2C_{44}/(C_{11} - C_{12})$ where C_{ij} are the elastic constants) which is essentially a dimensionless number that is used to quantify the anisotropy in the elastic energy, $A_z = 1.0$) and dilatational misfit i.e. $\epsilon^*_{xx} = \epsilon^*_{yy}$, for the case of softer precipitates,(inhomogeneity ratio

$\delta = \mu_{\text{ppt}}/\mu_{\text{mat}} < 1$, where μ is the shear moduli), where precipitates of smaller sizes acquire a circular shape in two dimensions, whereas beyond a particular precipitate size (R) or in terms of the characteristic length (a ratio of the characteristic elastic energy to the parameter controlling the interfacial energy of the precipitate-matrix interface ($L = R\mu_{mat}\epsilon^{*2}/\gamma$), where μ_{mat} is shear modulus of the matrix phase, ϵ^* is the magnitude of the misfit strain and γ is the magnitude of the parameter that controls the interfacial energy) the symmetry in shape is broken giving rise to an elliptical shape of the precipitate. The plot depicting the change in the shape of the precipitate as a function of increasing characteristic length is essentially a shape bifurcation diagram. We compare our phase-field results against the results obtained from the classical analytical solution provided by Johnson and Cahn [3] and the results from the sharp interface numerical technique from [4]. The results are in excellent agreement with previous work, as shown in Fig. 1. Similarly, we have performed phase-field simulations when there is anisotropy in the elastic energy i.e. $A_z = 3.0$ and dilatational misfit, where the precipitate with the smaller size yields a square-like shape with four-fold anisotropy. In contrast, the larger precipitate acquires a rectangular shape with its faces parallel to $\{10\}$ planes. As shown in Fig. 1, the bifurcation diagram extracted from phase-field simulation results at $A_z = 3.0$ also agrees quite well with the results obtained from the sharp interface numerical method. There is one more possibility where the misfit is different along different principal directions i.e. tetragonal misfit. We find that the shape bifurcation also occurs for this case for the combination of $A_z = 0.3$ and tetragonal misfit ($t = \epsilon^*_{xx}/\epsilon^*_{yy}$=2.0) as shown in Fig. 1. In our model, we can introduce anisotropy in the interfacial energy as well, using which we have studied the competition between anisotropy in the elastic and interfacial energies. We find that the modifications in the shape of the precipitate both above and below the bifurcation point do not change remarkably. However, for certain combinations of strengths of the anisotropies in the interfacial and elastic energies a completely isotropic shape may be retrieved below the bifurcation point. The phase-field formulation which is utilized for the calculations of equilibrium shapes of the precipitate is so generic that it allows an easy extension for the prediction of equilibrium precipitate shapes and their corresponding shape bifurcation diagrams in 3D as well. We have performed the simulations for isotropic as well as anisotropic elastic energy. Fig. 2 and 3 shows such exemplary results from 3D simulations, where for $A_z = 3.0$, precipitates with smaller size acquire a cubic shape with rounded corners that is typically observed in precipitation-hardened alloys e.g. $\gamma - \gamma'$ microstructure in superalloys. For larger sizes (see Fig. 3), the precipitate breaks its four-fold anisotropy giving rise to two variants which are a flat plate-like shape (oblate-like) and a rod-like shape (prolate-like). Here we find that the shape bifurcation diagrams obtained in 3D are different in character from that obtained in 2D. In short, the phase-field model

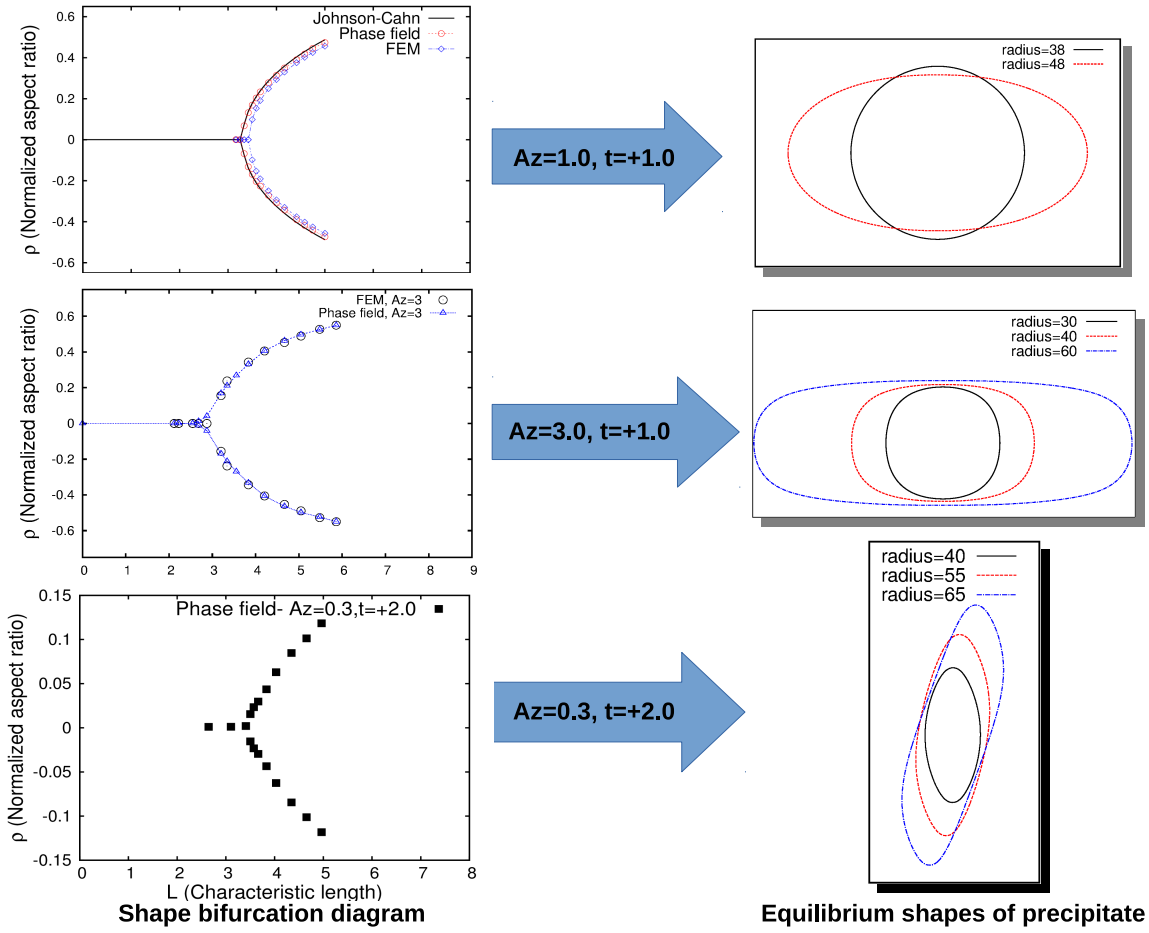

Figure 1: Shape bifurcation plot (on left) for different conditions and corresponding equilibrium shapes of the precipitate (on right), (a) $A_z = 1.0, t = +1.0$ (top) (b) $A_z = 3.0, t = +1.0$ (center) and (c) $A_z = 0.3, t = +2.0$ (bottom).

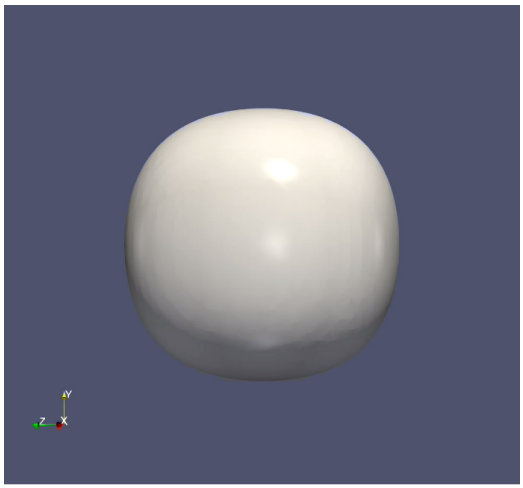

Figure 2: Equilibrium shapes of the precipitate as cube at $A_z = 3.0, \quad \delta = 0.5$, $L = 2.5$, with dilatational misfit-strain of 0.01.

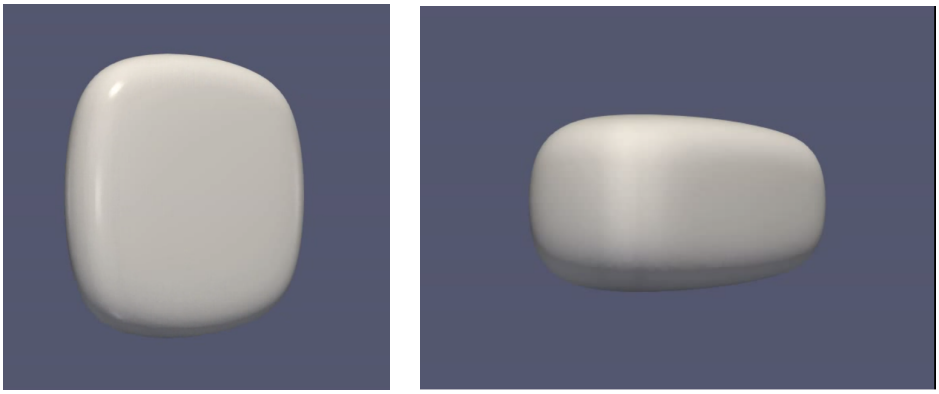

(a) (b)

Figure 3: Equilibrium shapes of the precipitate (a) oblate and (b) prolate at $A_z = 3.0, \quad \delta = 0.5$, $L = 5.0$, with dilatational misfit-strain of 0.01.

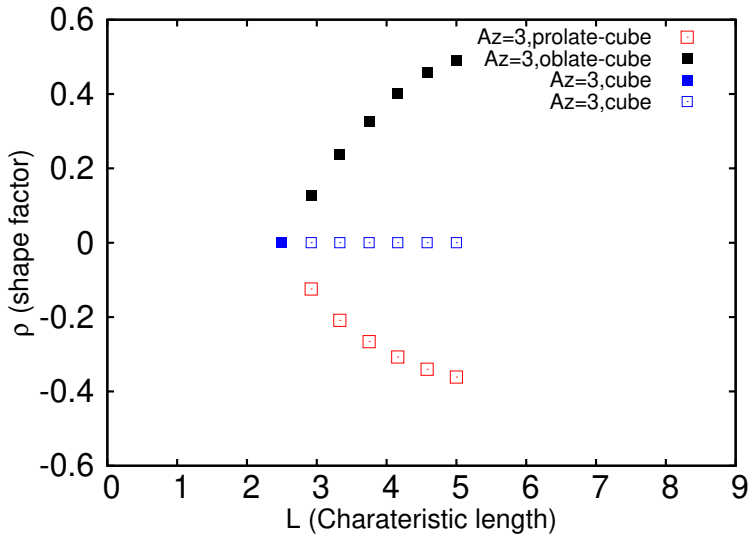

Figure 4: Plot depicts the shape bifurcation diagram for $A_z = 3.0, \quad \delta = 0.5$, with dilatational misfit-strain of 0.01 and $\rho = \dfrac{(I_{001} - I_{010})}{(I_{001} + I_{010})}$, where I_{001} is the sum of the projected length in magnitude (along 001) for any vector that is contained in the equilibrium shape of the precipitate, where every possible vector originating at the center of the precipitate is considered..

developed here predicts the equilibrium shapes of the precipitate in two dimensions as well as in three dimensions. The phase-field results are benchmarked with the results obtained from an analytical solution and an existing sharp interface numerical technique. A range of equilibrium shapes of the precipitate is derived as a function of precipitate size (characteristic length (L)), the magnitude of misfit strain, nature of misfit strain i.e. dilatational or tetragonal misfit, and anisotropy in the elastic as well as the interfacial energy.

Equilibrium multi-precipitate configurations

In this chapter, we extend the phase-field model for the calculation of multi-variant configurations of the precipitate that yield from a solid-state precipitate reaction. We have computed the equilibrium configurations of the precipitates for a given volume by varying the anisotropy in the elastic energy, the magnitude of the shear moduli and the interfacial energies, sign and the magnitude of the misfit-strain and the anisotropy in the misfit-strain. In one such study, we have determined the necessary and sufficient conditions for the formation of the core-shell microstructures for a two-precipitation reaction. We have observed that the core-shell structure forms (see Fig. 5) if and only if the criteria of solid-state wetting is satisfied i.e. the magnitude of the interfacial energy of one of the interfaces has to be larger than the sum of the magnitudes

of the interfacial energies of the remaining interfaces, so the system minimizes the interface possessing the larger interfacial energy, upon formation of the core-shell structure. This result is notwithstanding the elastic interaction between the precipitates. The influence of elasticity manifests itself through modification of the inter-precipitate interactions. Here we note that the precipitates with opposite sign of the misfit strain and softer than the matrix phase (inhomogeneity ratio, $\delta < 1.0$), have the most attractive interaction. Thus we postulate that, in this case where there exists an attractive interaction, one would expect to find a statistically larger number of events of core-shell formation of the precipitates in the experiments, if the wetting condition is satisfied, as here the precipitates would approach each other until they come in contact, where the wetting reaction can occur. For the configuration with harder precipitates ($\delta > 1.0$), since there exists a repulsive interaction between the precipitate, the probability of precipitates coming in contact will be lower and therefore also the number of core-shell forming events. Secondly, we have determined the equilibrium configurations of the variants of the

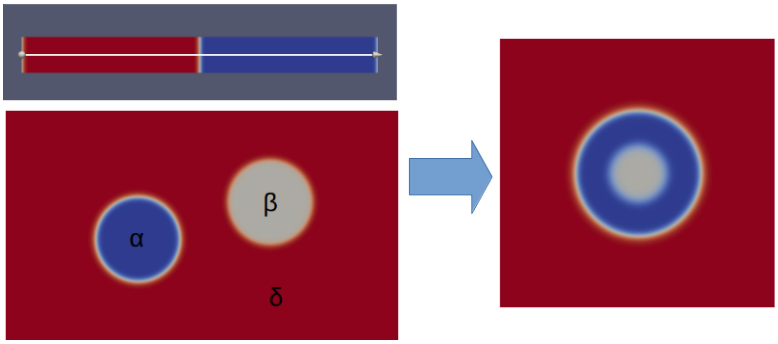

Figure 5: Schematic showing one dimensional profile of phase interface and core-shell microstructure.

precipitates that form during two symmetry-breaking transitions, namely cubic to tetragonal and hexagonal to orthorhombic transitions. In the cubic to tetragonal transformation, we have derived the equilibrium configurations as a function of precipitate size. Here, using energetic calculations, we have determined that, beyond a critical precipitate size, co-nucleation of two variants is energetically favorable in comparison to the nucleation of a single precipitate of the same volume, as the increase in the interfacial energy due to the formation of the cluster is well compensated by the reduction in the elastic energy. We have also calculated the equilibrium configuration of the precipitates that form out of the combination of tetragonal variants and a third precipitate with dilatational misfit-strain, that are observed in the experiments [5]. In this situation, when the signs of the tetragonal misfit strains are opposite to the dilatational misfit of the third precipitate, there exists a force of attraction between the precipitates that

gives rise to the formation of a sandwich-type structure. However, in contrast to this, if both the misfit-strains i.e. tetragonal and the dilatational have the same signs there exists a repulsive interaction between the precipitates without the formation of compact structures.

The equilibrium configurations of the precipitate that form during hexagonal to orthorhombic transformations are shown in Fig. 6(a), where different orthorhombic variants arrange themselves with respect to each other in a hexagonal matrix as an effect of anisotropy in the misfit strain matrix. The energetic calculations, in this case, shows that the co-nucleation of a multivariant configuration of the precipitates is energetically favored to the nucleation of a single precipitate beyond a certain precipitate size (see Fig. 6(b)).

In summary, using this novel multiphase-field model formulation a range of equilibrium configurations can be investigated providing useful insights about the possible microstructures that form in experiments.

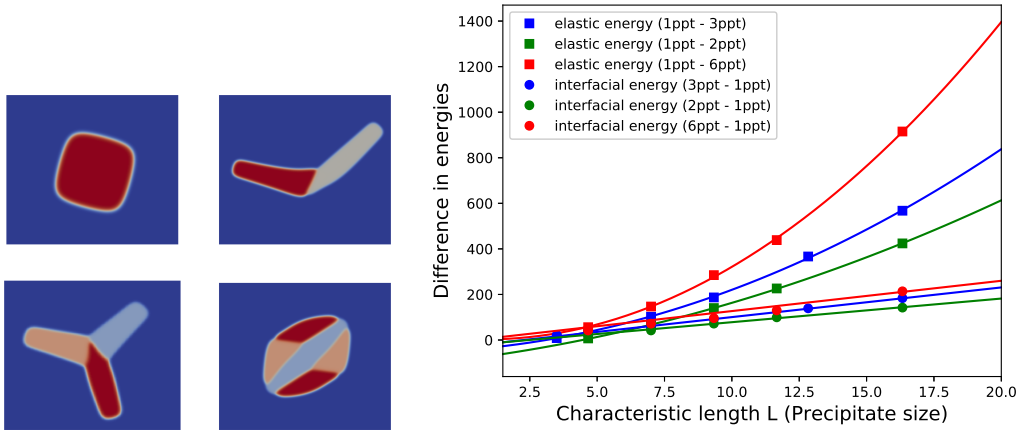

(a) (b)

Figure 6: (a) Equilibrium configurations of the precipitates with increasing number of variants at a given volume and (b) the plot showing the difference in the energies of equilibrium configurations as a function of increasing characteristic length of the precipitate L, the characteristic length (L) of the precipitate which is essentially a ratio of the characteristic elastic energy to the parameter controlling the interfacial energy of the precipitate-matrix interface ($L = R\mu_{mat}\epsilon^{*2}_{xx}/\gamma_\alpha$), at $A_z = 1.0, t = -1$ with $\mu = 1400$.

Precipitate growth under the influence of coherency stresses

In the previous studies of the thesis, the energy minimization is carried out under the constraint where the volume of the precipitate or the precipitates in the configuration is conserved. Here,

we relax this condition of volume preservation, and simulate precipitate growth in a supersaturated matrix, with anisotropy in the elastic and interfacial energies. Fig. 7 shows results from such an exemplary simulation, where a small coherent circular precipitate embedded in the matrix phase supersaturated at 53% grows into a dendrite-like structure due to anisotropy in the elastic energy ($A_z = 3.0$). In this chapter, we have characterized the evolution of dendrite-like shapes as a function of elastic parameters such as the misfit-strains, Zener anisotropy strength A_z, supersaturation and anisotropy in the interfacial energy. We have observed that in the presence of coherency stresses, the shapes of the tip characterized by the tip-radius (R_{tip}) and the velocity (V_{tip}) of the tip do not achieve a steady state. Also, the selection constant $\sigma^* = 2d_0D/R_{tip}^2V_{tip}$ (where d_0 is capillary length and D is the diffusivity) increases linearly with simulation time once the primary arms appear, for all the simulation conditions. Thus, there is no selection of a unique tip shape as is observed in the case the solidification. Therefore, structures derived in solid-state in the presence of elastic anisotropy may only be referred to as dendrite-like.

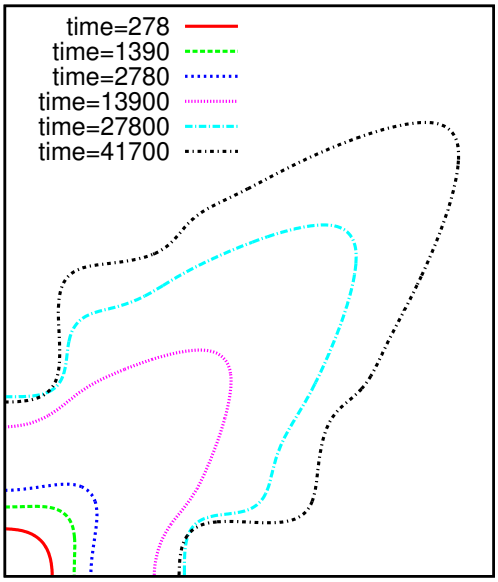

Figure 7: Evolution of the precipitate in 53% supersaturated matrix at $A_z = 3.0$, $\epsilon^* = 1\%$ at normalized time.

Contents

List of Figures

List of Tables

List of Symbols

Symbol	Description	Units
ϕ	Phase-field variable	-
F	Free energy functional	J
f_{el}	Elastic energy	J/m^3
$\boldsymbol{u}$	displacement vector	m
γ_α	Parameter controling the interfacial energy	J/m^2
W	Parameter relating the interface width	-
τ	Relaxation constant	Js/m^4
λ	Lagrange multiplier	J/m^3
α, β, γ	Phase indices	-
h	Interpolation polynomial	-
ϵ_{ij}	Strain	-
ϵ^*_{ij}	Eigenstrain or misfit-strain	-
C_{ijkl}	Elastic constant	J/m^3
σ_{ij}	Stress	N/m^2
A_z	Zener anisotropy parameter	-
L, L_c	Characteristic length	m
ν	Poisson's ratio	-
$\delta = \mu_{ppt}/\mu_{mat}$	Inhomogeneity ratio of shear moduli of precipitate to matrix	-
μ_{ppt}, μ_{mat}	Shear moduli of precipitate and matrix respectively	J/m^3
ρ	Normalized shape factor	-
R	Equivalent size of the precipitate	m
$t = \epsilon^*_{xx}/\epsilon^*_{yy}$	misfit-strain ratio	-
I	Sum of projected length for any vector contained in shape	m
Ψ	Grand potential density	J/m^3
μ	Chemical potential	J/m^3
ε	Strength of anisotropy in the interfaical energy	-
c^α, c^β	components	-
D	Diffusivity	m^2/s
M	Mobility	m^5/Js
ω	Percentage of supersaturation	-
σ^*	Selection constant	-
R_{tip}	Radius of the dendritic tip	m
V_{tip}	Velocity of the dendritic tip	m/s
d_0	Capillary length	m

Chapter 1

Literature review and motivation

This chapter contains the comprehensive review of the existing literature on the particular thematic focal points in the thesis, followed by the corresponding motivation for the work in the thesis. We first review the topic of analytical and numerical estimation of equilibrium shapes of a single precipitate as a function of the elastic and interfacial properties. Thereafter, we review the experimental and numerical studies on multi-phase precipitation and motivate the investigation of computation of equilibrium configurations in this thesis. Finally, we describe the studies existing in literature relating to the formation of solid-state dendritic structures from the supersaturated matrix, where we motivate the requirement for studying the selection of the tip radius and the tip velocity as a function of the elastic and interfacial properties.

1.1 Equilibrium precipitate shapes under the influence of coherency stresses

Precipitate strengthened alloys are one of the most commonly used materials for high temperature applications, whereby, the strengthening is achieved through precipitate-dislocation interactions. The mechanical properties of these alloys predominantly depend on precipitate size, morphologies and their distribution. Thus, there are several experimental studies carried out which focus on the precipitate morphology [6, 7], their growth and coarsening [8, 9, 10, 11], strengthening [12, 13]. In this regard, there are two mechanisms, one in which the precipitates are large enough such that there is no coherency between the precipitate and the matrix from which it formed, and the second in which the precipitates are small such that there is still substantial coherency between the matrix and the precipitate. While in the former, the interaction of the dislocation with the precipitate is purely physical; in the latter, the coherency stresses

around the precipitate also influence the interaction with the precipitate. In both cases, the shape of the precipitate plays an essential role in the interaction with the dislocation. Our investigation in this study will be related to the investigation of shapes of coherent precipitates, more particularly the understanding of the equilibrium morphology of precipitates as a function of the misfit-strain, elastic and interfacial energy anisotropies.

The first theoretical efforts are from Johnson and Cahn [3] who predict an equilibrium shape transition of an elastically isotropic misfitting precipitate in a stiffer matrix. The equilibrium shape of a precipitate is determined by minimization under the constraint of a constant volume of the precipitate, of the total energy, constituting of the sum of elastic and interfacial energies. The theory proposes the shape transition with size, akin to a second-order phase transformation with the shape of the precipitate as an order parameter. The theory analytically predicts the order parameters characterizing the equilibrium shape as a function of the precipitate size whereby for certain conditions, below a critical size there is an unique order parameter describing the shape of the particle and a bifurcation into two or more variants beyond it. In their work, one of the transitions the authors discuss is the case where, beyond a particular size of a precipitate, a purely circular cross-section of a cylindrical precipitate elongates along either of two orthogonal directions, thereby retaining only a two-fold symmetry. This is therefore, an example of a symmetry-breaking transition.

Voorhees and coworkers [14, 15] give numerical predictions for the equilibrium morphologies of a precipitate in a system with dilatational and tetragonal misfit in an elastically anisotropic medium (cubic anisotropy). In this work, the authors discretize the interface co-ordinates in terms of the arc-length and use this to write the total energy of the system, that is a sum of the elastic and the interfacial energies. Thereafter, the minimizer of the total integrated energy of the system is described by the one which satisfies the jump condition at the interface. The condition equates the difference of the chemical potential between the phases (which is a function of the uniform diffusion potential in the system) at the interface to the total of the elastic configuration and capillarity forces. This balance condition for each of the discretized interface points leads to a set of integro-differential equations, which along with the constraint of constant area, leads to the determination of the uniform diffusion potential that satisfies the interface balance conditions at all the co-ordinates. The solution set for the co-ordinates, thereby constitutes the equilibrium shape of the precipitate. The method has also been extended into three dimensions in work by Voorhees and coworkers [16, 17].

Schmidt and Gross [18] use a boundary integral technique for performing the energy minimization in order to determine the equilibrium precipitate shapes in an elastically inhomogeneous and anisotropic medium, which is also used for studying multi-particle interactions

in [19]. As an extension, Schmidt et al. [20] have determined the 3D equilibrium precipitate morphologies using a boundary integral method. They have observed that there is a strong influence of elastic inhomogeneity, elastic anisotropy and characteristic length on the morphological stability of precipitates. Similarly, Jog et al. [4, 21] use a finite element method coupled with a congruent-gradient based optimization technique to minimize the sum of elastic and interfacial energies for determining equilibrium precipitate shapes of isolated, coherent particles with cubic anisotropy in elastic energy. They have also estimated symmetry breaking as a function of particle size for different combinations of elastic anisotropies and misfits. Jou et al. [22] use a boundary integral method to study single precipitate growth as well as two-precipitate interactions. Kolling et al. [23] use a finite element and optimization-based method to predict the equilibrium precipitate shape for misfitting particles with dilatational misfit-strain. The authors show that the value of the elastic constants, particle size and inhomogeneity affect the stability of the equilibrium shape of the precipitate. Akaiwa et al. [24] utilize the boundary integral method with a fast multipole method for integration, in order to simulate growth and coarsening of large number of precipitates.

An interesting extension of the finite element based method for the prediction of the equilibrium shape is the utilization of the level-set method where a prescribed value of the level-set surface is used to describe the interface morphology [25]. The model is used for modeling solid-state dendrite growth as well as coarsening, by coupling with an evolution equation for the composition field. The modification of the modeling scheme for the study of equilibrium shapes of precipitates is done by using a Lagrange parameter which maintains the same volume of the precipitate while the normal velocities of the interfacial nodes are calculated [26]. The equilibrium shape is determined when the velocity of all the interfacial nodes becomes zero. As an extension of the model, the authors also study chemo-mechanical equilibrium where the misfit strains are a function of the composition in [27], and the authors solve for diffusional equilibrium along with the equations for mechanical equilibrium.

In terms of the determination of the equilibrium morphologies of precipitates the preceding models are all sharp-interface based methods and also prescribe optimization solutions for the shape of the equilibrium precipitate under the constraint of constant volume. A corresponding approach using a microstructural evolution based method is proposed by Khachaturyan et al. [28], wherein, precipitate evolution is simulated using a modified version of the Cahn-Hilliard equation [29] until there is a complete loss of saturation or the situation where the diffusion potential everywhere becomes the same. In this situation, the shape of the precipitate corresponds to equilibrium. However, there is no explicit volume constraint during evolution and the variation of the equilibrated shapes as a function of the sizes/volume of the precipi-

tate may only be tracked through a corresponding change in the alloy composition, yielding different volume fractions of the precipitate in a box of a given size. Using this model the authors have studied the effect of elastic stresses on precipitate shape instability during growth of single precipitates embedded in an elastically anisotropic system. Similar models have also been formulated by Leo et al. [30], where the authors solve for diffusional equilibrium along with the constraint of mechanical equilibrium in order to determine the equilibrium particle shape. The authors also compare with the results from their corresponding boundary-integral based modeling methods [22]. The authors highlight the advantage of using the diffuse-interface schemes where merging and splitting of particles can be handled easily in contrast to the sharp-interface methods which require re-meshing. A similar dynamic evolution model has also been used to predict equilibrium shapes in three dimensions in [31]. Apart from the determination of equilibrium shapes, the diffuse-interface methods have also been used for the study of growth and coarsening of multi-particle systems [30, 32, 33, 34, 35, 36, 37], instabilities [38] and rafting [39, 40, 41, 42, 43, 44].

In all the above studies, the central focus of the investigation has been the study of equilibrium shapes of precipitates where the anisotropy exists only in the elastic energy. The coupled influence of both the interfacial energy and elastic anisotropies on the equilibrium morphologies is performed using the boundary integral method by Leo et al. [45]. In a study by Greenwood et al. [46], the authors have developed a phase-field model of microstructural evolution, where they study the morphological evolution of solid-state dendrites as a function of anisotropies in both surface as well as elastic energy. While the study is not particularly aimed at the computation of equilibrium shapes, the authors illustrate transitions in the growth directions of solid-state dendrites from those dominated by the surface energy anisotropy to those along elastically harder directions, stimulated by a change in the relative strengths of the anisotropies.

This brings us to the motivation of our work in the thesis, wherein, we formulate a diffuse-interface model for the determination of equilibrium shapes of precipitates under the combined influence of anisotropies in both elastic as well as interfacial energies, with any combination of misfits. Here, the shape of the precipitate will be defined by a smooth function, which varies from a fixed value in the bulk of the precipitate to another in the matrix. The shape of the precipitate will be described by a fixed contour line of this function. Our work can be seen as a diffuse-interface counterpart of previous work by Voorhees et al. [14] and other sharp-interface models by Schmidt and Gross [18] and Jog et al. [4] as well as the level-set based FEM method proposed by Duddu et al. [25] and Zhao et al. [26, 27]. Herein, we use a modification of the volume-preserved Allen-Cahn evolution equation that was proposed previously by Nestler et al. [2], wherein the Allen-Cahn equation prescribing the evolution of a given order parameter is

modified such that the integrated change in the volume that is computed over the entire domain of integration returns zero. The motivation for proposing a diffuse-interface model is three-fold: firstly given that the Allen-Cahn dynamics for the order parameter ensures energy minimization, there is no requirement for an additional optimization routine that is used in corresponding works by Schmidt and Gross [18] and Jog et al. [4]. Secondly, complicated discretization and solution routines adopted in [14] can be avoided allowing for an easy extension from two dimensions (2D) to three dimensions (3D). Thirdly, a diffuse-interface approach allows for an easy coupling of elastic and surface energy anisotropies. Further, a corollary to the ease of discretization is that quite complicated shapes with rapid change in curvatures can be treated with a great deal of accuracy, which we will demonstrate by comparing our results with those from a sharp-interface model. Additionally, our diffuse-interface presentation will be different from the previous phase-field models where we do not solve for the composition field while deriving the equilibrium shape of the precipitate which allows us to reduce the computational effort. Chapter 3 describes the computation of equilibrium shapes as a function of the different elastic and interfacial properties using the novel phase-field formulation.

1.2 Equilibrium multi-precipitate configurations

The mechanical properties of precipitation-hardened alloys depend on the precipitate size, shape and their arrangement in the matrix [7, 8, 9, 13, 47, 5, 48]. Of particular interest are precipitate reactions where multiple solid-phases precipitate from the matrix as here we find interesting examples of self-organized patterns/configurations. For coherent interfaces, there exist elastic interactions between the precipitates which influence the eventual configuration of the precipitate cluster as well as the individual shapes of the precipitates that arise out of a precipitation reaction. Hence, it is important to determine these attributes of the precipitates or the cluster of the precipitates that evolve as a function of different parameters such as the anisotropy in the elastic energy and the misfit-strain, the characteristic size of the precipitates, inhomogeneity of the elastic stiffness matrices etc. There are several possibilities for equilibrium precipitate configurations that could arise out of a precipitate reaction. For example, in certain multi-component alloy systems, such as Al-based alloys [49, 50, 51, 52, 53, 54, 55, 56, 57, 58], given a certain heat treatment, the matrix yields a microstructure where the precipitate morphologies are characterized by the formation of a core-shell type structure. The precipitates that form the core-shell microstructures are not homogeneous in composition, where the central precipitate is surrounded by another precipitate phase with a different composition. As the interface between the phases is coherent in nature, eventually due to anisotropy in the elastic

energy the core-shell type structure gives rise to cubic shapes which is described by Tolley and coworkers [49]. Research is also focused on the evolution of such core-shell type microstructure, their coarsening behavior and subsequent mechanical properties obtained at the room as well as elevated temperatures [50, 51, 52, 53, 57, 58]. With regards to the criteria for the formation of such structures, there is however some lack of clarity. Wolverton and coworkers [59] have performed first-principles calculations for evaluating the bulk thermodynamics, elastic misfit and stiffness and interfacial energies for two precipitate phases in the Al-Li-Sc alloy system. Using the calculations, the authors have determined the conditions for nucleation and the stability of formation of such core-shell microstructures between the Al_3Li and Al_3Sc phases in the Al- matrix. Based on the calculations of the interfacial energies and their dependence on the compositions, the authors have concluded that it is only possible for the Al_3Li phase to wet/engulf the Al_3Sc precipitates as the interfacial energies of the corresponding interfaces satisfy the wetting condition, which is supported by experimental observations in this alloy. These conditions are also in agreement with the theory of Cahn [60] describing the conditions of wetting in liquid-liquid phase separating systems. However, Lee[61, 62] utilizes a model based on the discrete atom method which incorporates the influence of coherency stresses for determining conditions for the formation of core-shell microstructures. The major conclusion of the papers is that core-shell structures can result just because of strain-energy interactions even when the interfacial energies do not satisfy the wetting condition. Therefore, there exists still lack of clarity on the role of elastic interactions on the formation of core-shell microstructures in solid-solid phase transformations in the presence of coherency stresses.

There is another class of solid-state reactions, where the matrix phase co-exists with clusters of different variants of the precipitates. One such example is observed in Ni-based alloys [63, 64, 65], where the γ'' precipitate phase clusters are embedded in the γ matrix. Here a cubic $(L1_2)(\gamma)$ matrix yields tetragonal variants of the precipitates (body-centered tetragonal)(γ''). Several other examples include sandwich and compact structures involving the γ' and $\gamma^{''}$ precipitates which have been observed in the IN718 superalloy and its variants[66, 67, 68, 69, 70, 71], that have also been modeled using phase-field simulations [69, 71]. The existence of such multivariant clusters in different alloy systems is attributed to the elastic interaction between the precipitates which leads to a reduced energy of the system [70]. Similarly, in certain Co-Pt system [72, 73] and Mg-partially stabilized ZrO_2 [74], the cubic phase produces tetragonal precipitates. Here, different tetragonal variants of the precipitates arrange themselves in a particular structure which is an influence of different magnitudes of the anisotropy in the misfit strain, the elastic energy and the shear moduli of the phases. Wang et al. [75] have modeled the cubic to tetragonal phase transformation in Mg-partially stabilized ZrO_2 system

using a phase-field technique, where they have shown the evolution of the multiple lens-shaped variants of the precipitates from the cubic matrix. Similarly, an interesting case is observed in Al-based alloys by Mekineni et al. [5], where the tetragonal variants of the precipitates co-exits with a precipitate having dilatational misfit-strain. The authors have shown that the coarsening kinetics becomes very sluggish in the presence of such configurations of the precipitates. Similarly, certain Ti-based alloys [76, 77, 78, 79] yield multivariant configurations of the precipitates from the hexagonal matrix. The variants of the precipitates align themselves to form star-shaped or triangular structures in the matrix. This has been studied by several researchers using the phase-field method [80, 81, 82, 83], where they have also observed the formation of clusters of the multivariant precipitates giving rise to the shapes described, as an influence of the anisotropy in the misfit-strain and the applied stress.

Therefore, in this thesis, we focus our investigation to the calculation of equilibrium configurations of the precipitates that form from the matrix phase for the different possibilities of elastic interactions that are typically observed in experiments. We formulate a multi-phase field model that allows the calculation of such equilibrium phase clusters, where we modify the volume preserved algorithm for single-phase equilibrium shape calculation. The algorithm essentially involves the solution to multiple Allen-Cahn equations composed of the different phase fields corresponding to the precipitates, under the constraint of constant volume and mechanical equilibrium. In this part of the work that is elaborated in Chapter 4, we determine the necessary and sufficient conditions for the formation of a core-shell microstructure. Additionally we investigate the formation of equilibrium configurations of the variants of the precipitates due to two symmetry-breaking transitions, namely cubic to tetragonal and hexagonal (isotropic in 2D) to orthorhombic structures.

1.3 Precipitate growth under the influence of coherency stresses

In the preceding sections, we have discussed studies that are related to the calculation of the equilibrium shape of a single precipitate as well as the equilibrium configurations of the precipitates, which investigate the influence of different properties such as the nature of the sign of misfit-strain and its magnitudes, the magnitude of the shear moduli, the strength of anisotropy in the elastic as well as the interfacial energies and the characteristic length of the precipitate, on the precipitate shapes. In the following we review studies in precipitate growth and in particular the formation of instabilities that lead to the formation of solid-state dendritic

structures. Formation of dendritic structures during solidification processes is a well-known phenomenon. Thermal supercooling in the case of pure metals and constitutional supercooling in the case of alloys have traditionally been used to explain the instability that gives rise to such structures and a detailed review of the theory of dendritic growth during solidification may be found in the reviews [84, 85, 86, 87, 88, 89, 90, 91]. Hence, while the study of dendritic growth during solidification has been studied quite extensively leading to an almost complete understanding of the parameters that lead to the selection of a unique dendritic tip radius and velocity, the same is not true for the case of solid-state dendritic growth, wherein the number of experimental observations of such growth is itself limited. Henry et al. [92] have observed that during the precipitation of γ'-phase in Ni-base superalloys, after giving a specific heat treatment to the alloy, i.e. when it is cooled to the ageing temperatures very close to the solvus temperature, the coherent precipitates grow into dendritic structures, where the arms of the dendrite grow along the $< 111 >$ directions. Doherty [93] had discussed various factors that appear to explain the shape instabilities in some solid-state reactions, such as the solid-state dendrites of γ-brass precipitates in β-brass matrix in the Cu-Zn alloy. Husain et al. [94] report that the precipitation of γ_2-phase in Cu-Al β-phase alloys yield dendritic morphologies. It is also observed that the rapid bulk diffusion and fast interfacial reaction kinetics would promote the formation of such morphologies. They have predicted the occurrence of dendritic morphologies during solid-state precipitation in many binary systems such as Cu-Zn, Cu-Al, Ag-Al, Ag-Zn, Cu-Ga, Au-Zn, Ni-Zn, Cu-An, Ag-Cd and Cu-Sn. The authors comment that the crystallographic similarities between the parent phase and the precipitates is the dominating factor that gives rise to the formation of the dendritic structures. Yoo el at. [95] have observed that the spherical precipitates changed into a flower-like structure as the supersaturation in the matrix is increased. They have shown that the results were concurrent with the Mullins-Sekerka theory, where they comment that the morphological instabilities should be evident if the point effect of the diffusion is significant in the vicinity of the precipitate-matrix interface regardless of the nature of the matrix phase and the ageing stage. Khan et al. [96] have also noticed the formation of solid-state dendritic structures during the elevated temperature treatment of maraging steel. There, the oxy-nitride phase acquires dendritic morphologies in the martensitic matrix.

At a fundamental level, the presence of a supersaturation in the matrix makes the interface unstable to diffusive instabilities of the Mullins-Sekeraka type and therefore the observation of such dendritic structures during solid-state reactions is not surprising. However, there is an important difference from the case of solidification, wherein, the solid-solid interface in precipitation reactions is typically coherent in the initial stages of precipitation and thereby

the precipitate and the matrix are also elastically stressed. Since, the elastic effects scale with the size of the precipitate, the presence of coherency will therefore naturally influence the selection of length scales during dendritic evolution. Leo and Sekerka [97] have extended the linear stability analysis performed by Mullins and Sekerka [98] by including the influence of elastic coherency stresses and have investigated the morphological stability of the precipitate grown from the solid solution. The analysis reveals that the elastic effects manifest through the boundary conditions, based on local equilibrium that determines the compositions at a coherent solid-solid interface. The elastic effects increase in importance relative to capillarity as the scale of the system increases, and so will become very important at small initial supersaturations, as the supersaturation is inversely proportional to the critical nucleus radius. Elastic fields can also influence the selection of the fastest-growing harmonic, with stabilizing elastic fields favoring long-wavelength harmonics while destabilizing elastic fields favoring short-wavelength harmonics. The stability analysis reveals the dependence of the different elastic parameters in either amplifying or decaying of the perturbations at the solid-solid interface.

While such a linear stability analysis give an idea about the characteristics of the diffusive instability they cannot explain the selection of a unique dendritic tip radius and velocity as is known from solidification experiments. The selection requires the presence of anisotropy in either the interfacial energy or the attachment kinetics and the selected growth shape of the dendrite may be predicted using the well established microsolvability theory [99, 100, 101, 102]. Formulation of such a theory is presently lacking for solid-state dendritic growth and a possible strategy here is the use of dynamical phase-field simulations that naturally lead to the selection of a unique tip radius and velocity. Here, Greenwood and coworkers [46] have proposed a phase-field model for microstructural evolution which includes the effects of the elastic strain energy. The authors show that the solid-state dendritic structures undergoes a transition from a surface energy anisotropy dominated $< 10 >$ growth direction to an elastically driven $< 11 >$ growth direction induced by changes in the elastic anisotropy, the surface anisotropy and the supersaturation in the matrix. Our work in this paper will be an extension of this investigation where we will study dendritic tip selection using a phase-field model as a function of the different elastic and interfacial parameters as well as the supersaturation. Similar to dendrites formed during the solidification experiments our studies will aim at identifying the variation of the classical selection constant(σ^*) as a function of the material and process parameters and in particular the strength of anisotropy in the stiffness matrix and the interfacial energies.

Thus, our motivation in this thesis (Chapter 5), is to determine the effect of several physical properties on the formation of the solid-state dendritic structures, and characterize the influence on the selection constant (σ^*). Here, we will utilize a diffuse interface formulation, where we

solve the Allen-Cahn equation along with the evolution of the diffusion potential of the relevant species that ensures mass conservation. While solving for the evolution equations for the order parameter and the diffusion potential, we ensure that the mechanical equilibrium is satisfied at every grid point of the system. The simulations gives rise to the evolution of a precipitate morphology in the supersaturated matrix with imposed anisotropies in the elastic energy as well as the interfacial energy. We will systematically study the effect of change in different properties of the phases on the selection of radius of the dendrite tip and velocity.

1.4 Setting up the problem

In the forthcoming chapters, we therefore study different aspects about the equilibrium shapes of single precipitates and multi-precipitate configurations as well as diffusional instabilities during precipitate growth in a supersaturated matrix. In order to set up the model formulation, it is useful to list the parameters and the setting in which the different topics will be studied.

1.4.1 Equilibrium precipitate shapes and configurations

The problem of determining equilibrium shapes of precipitates is similar to the problem of investigating nucleation. Therefore, the natural setting of the problem involves the solution to the shape of the nucleus that is in equilibrium with a supersaturated matrix. We set up this problem in a diffuse-interface framework where the solution to the shape of the nucleus involves the spatially varying order parameter field(phase-field). The equilibrium phase-field profile implicitly describing the nucleus requires the solution to a Euler-Lagrange equation. In this thesis, we adopt the volume-preservation technique as described previously [2] that enables the solution to this problem of nucleation using the same Allen-Cahn[103] relaxation dynamics, that is typically utilized in phase-field models for ensuring energy minimization. This is in contrast to the time-independent solution corresponding to the Euler-Lagrange equation which is classically utilized for the solution to the shape of the critical nucleus. This particular method is chosen as it allows us to complicate the physics in an unrestricted fashion, without the need for a corresponding increase in the complexity of the numerical schemes that are required for the solution of the critical nucleus.

The essential idea behind this technique [2] involves the usage of a Lagrange parameter/s (referred to as λ_β or λ_β^v in the thesis), which ensures that the cumulative update of the phase-field parameter/s returns zero in every iteration of the relaxation scheme. This construction therefore ensures that the functional is minimized following the Allen-Cahn dynamics while the

volume of the concerned phase-field(precipitate) remains conserved. When the stationary point is reached the update of the phase-field returns zero that essentially implies that the solution to the corresponding Euler-Lagrange equation is derived. At this state, one can associate the Lagrange parameter with the departure of the chemical potential from the equilibrium value at a planar interface, or the driving force that is required, such that a particular size of the precipitate is stationary. Therefore, while the classical time-independent method of solution to the Euler-Lagrange equation involves the determination of the critical shape of the nucleus for a given supersaturation that controls the size of the equilibrium cluster, in this method based on the Allen-Cahn relaxation scheme, we implicitly solve for the driving force or the chemical potential difference that will lead to a particular chosen size of the cluster to be critical as well as the equilibrium shape. Both methods are therefore equivalent. We note that the relaxation method described here has similarities to the sharp interface approaches[15] that have been utilized for the determination of the equilibrium shapes of precipitates in the presence of coherency stresses, in that the position of the interfacial nodes are solved such that the corresponding Gibbs-Thomson conditions at all the points can be satisfied by the same unknown chemical potential, that is solved along with the equilibrium precipitate shape.

Setting up of the Allen-Cahn dynamics requires the definition of the functional which encapsulates all the energetic ingredients that are under consideration. The surface energy γ is considered using the standard sum of the square gradient and obstacle/double-well potentials. In order to incorporate linear elasticity along with coherency stresses, we require to include the elastic energy of the system as part of the functional. Additionally, since the stresses in the system arise due to coherency it requires the association of strains in each phase with respect to their natural states. This is essentially the eigen-strain ϵ^*_{ij}(also known as transformation strain) corresponding to each phase. For the definition of ϵ^*_{ij} we choose the matrix as a reference and the strains in the precipitate phases are described with this as the reference. Due to this, the eigen-strains in the matrix are always zero while they are non-zero only in the precipitates. Going by this definition, a phase will be stressed only if it is strained differently from its eigen-strain. Along with this, one requires the definition of the stiffness matrices corresponding to each of the phases. In the entire forthcoming thesis, we have focused on cubic systems. This implies that the entire set of elastic properties of each phase may be defined by just three independent parameters. Thus, the stiffness tensor can be simplified and generically defined in the following manner, where we utilize the commonly used short-hand notation for the non-zero stiffness components, which are, $C_{11} = C_{1111}$, $C_{22} = C_{2222}$, $C_{12} = C_{1122}$ and $C_{44} = C_{1212}$, where additionally $C_{11} = C_{22}$ because of symmetry considerations. Thereafter, these terms can be derived in the form of the known material parameters, that are the Zener anisotropy (i.e.

$A_z = 2C_{44}/(C_{11} - C_{12}))$ which is essentially a dimensionless number that is used to quantify the anisotropy in the elastic energy, Poisson ratio (ν) and shear modulus (μ) and can be written as,

$$C_{44} = \mu, \quad C_{12} = 2\nu \left(\frac{C_{44}}{1 - 2\nu} \right), \quad C_{11} = C_{12} + \frac{2C_{44}}{A_z}. \tag{1.1}$$

From these definitions, we can classify that for $A_z = 1$ the elastic properties correspond to isotropic systems while for $A_z < 1$ and $A_z > 1$ we have anisotropy forms that correspond to diamond and cubic shapes respectively in 2D, while in 3D, the former leads to octahedron shapes while the latter leads to a cube. In addition, we will explore additional anisotropy resulting from the particular choice of the misfit-strain matrices. In the entire study, we will deal with diagonal misfit-strain matrices where choosing different values of the principal misfit-strain components correspond to different forms of anisotropy. This ratio will be termed as $t = \epsilon_{yy}/\epsilon_{xx}$. For values of $t = 1$ imparts isotropic equilibruim shapes, while the choice of values $t > 1$ and $t < 1$ leads to precipitate shapes that are elongated horizontally and vertically respectively. In 3D, the number of such possibilities increase and may be appropriately be defined using one of the principal strain values as reference. A particularly interesting choice is $t = -1$, which corresponds to pure shear resulting in the formation of diamond shapes in 2D.

In addition, anisotropy in the interfacial energy is described by choosing the gradient energy coefficient in the functional as a function of the interface normal using the classical approach of [104], with the strength of the anisotropy has been defined by the variable ϵ. Here, we will restrict ourselves to four-fold symmetries that result in diamond in 2D as well as octahedron in 3D.

1.4.2 Precipitate growth

Finally, studying growth requires the coupled solution of evolution equations describing the phase transformation(Allen-Cahn) with the mass conservation equation. While most of the ingredients of the functional have already been described, what remains for the precipitate growth is the description of the alloy thermodynamics. Here, we have utilized the weighted average of the grand-potential(ψ) densities of the respective phases in the functional, whose minimization provides the thermodynamic driving force for the phase transformation. Since, the grand-potential densities have the diffusion potential (μ) as the natural state variable, we will also utilize the mass conservation equation that is transformed into an evolution equation for the diffusion potential(μ). As is relevant for solid-state phase transformations we will utilize

a two-sided diffusion model with equal diffusivities(D) in both precipitate and the matrix that avoids thin-interface defects like solute trapping.

With this we are ready for the consideration of the formulations in the following chapter that will be utilized for the different problems that have been described and motivated.

Chapter 2

Phase-field model: Formulation

In this thesis, we formulate phase-field models for the calculation of equilibrium shapes of single precipitates as well as multi-precipitate configurations. Additionally, we formulate a phase-field model for simulating growth of solid-state dendritic structures arising from diffusive instabilities. We will elaborate the corresponding formulations in the forthcoming subsections.

2.1 Equilibrium shapes of the precipitate

During solid-state phase transformations, a difference of the lattice parameter between the precipitate and the matrix gives rise to misfit strains/stresses for a coherent interface. This in turn, contributes to the system energy in terms of an elastic contribution which scales with the volume of the precipitate. Similarly, the interfacial energy which is the other component of the energy in the system, varies with the interfacial area. In this context, the equilibrium shape of the precipitate is the one which minimizes the sum total of the contributions from both the elastic energy and interfacial components, which given the scaling of the two energy components is a function of the size of the precipitate.

In this section, we formulate a phase-field model, where the functional consists of both the elastic and the interfacial energy contributions. Since, the equilibrium precipitate shape depends on the size of the precipitate, we formulate a model which minimizes the system energy while preserving the volume of the precipitate, and thereby allows the computation of the equilibrium shape of precipitates. This allows the determination of the precipitate shapes as a function of the different precipitate sizes as has been done previously using sharp-interface methods. This constrained minimization is achieved through the technique of volume preservation which is also described elsewhere [2], that is essentially the coupling of the Allen-Cahn type evolution

equation with a correction term using a Lagrange parameter that ensures the conservation of the precipitate volume during evolution.

In the following we discuss the details of the phase-field model. We begin with the free energy functional that reads,

$$\begin{aligned}\mathcal{F}(\phi) = \int_V \left[\gamma W a^2(\boldsymbol{n}) |\nabla\phi|^2 + \frac{1}{W} w(\phi)\right] dV \\ + \int_V f_{el}(\boldsymbol{u}, \phi)\, dV + \lambda_\beta \int_V h(\phi)\, dV,\end{aligned} \tag{2.1}$$

where V is the total volume of system. ϕ is the phase field order parameter that describes the presence and absence of precipitate (α phase) $\phi = 1$ and matrix (β phase) $\phi = 0$ phases. The first integral constitutes the interfacial energy contribution, which in a phase-field formulation is done using a combination of the gradient-energy and potential contributions. Here, the term γ controls the interfacial energy in the system, while W influences the diffuse interface width separating the precipitate and the matrix phases. The function $a(\boldsymbol{n})$ which is a function of the interface normal $\boldsymbol{n} = -\dfrac{\nabla\phi}{|\nabla\phi|}$, describes the interfacial energy anisotropy of the precipitate/-matrix interface. The second term in the first integral describes the double obstacle potential, which writes as,

$$\begin{aligned} w(\phi) &= \frac{16}{\pi^2}\gamma\phi(1-\phi) \qquad \phi \in [0,1], \\ &= \infty \qquad\qquad\qquad \text{otherwise.}\end{aligned} \tag{2.2}$$

The second integral enumerates the elastic energy contribution to the free-energy density of the system which is a function of the order parameter ϕ that is also used to interpolate between the phase properties and the misfit. λ_β is the Lagrange parameter that is added in order that the volume of the precipitate represented by the integral $\int_V h(\phi)\, dV$, where $h(\phi) = \phi^2(3-2\phi)$ is an interpolation polynomial that smoothly varies from 0 to 1, is conserved. The evolution of the order parameter ϕ is derived using the classical Allen-Cahn dynamics that writes as,

$$\tau W \frac{\partial\phi}{\partial t} = -\frac{\delta F}{\delta\phi}, \tag{2.3}$$

and elaborates as,

$$\tau W \frac{\partial\phi}{\partial t} = 2\gamma W \nabla \cdot \left[a(\boldsymbol{n}) \left[\frac{\partial a(\boldsymbol{n})}{\partial\nabla\phi}|\nabla\phi|^2 + a(\boldsymbol{n})\nabla\phi\right]\right]$$

$$-\frac{16}{\pi^2}\frac{\gamma}{W}(1-2\phi)-\frac{\partial f_{el}(\boldsymbol{u},\phi)}{\partial\phi}-\lambda_\beta h'(\phi), \tag{2.4}$$

where τ is the interface relaxation constant, which in the present modeling context is chosen as the smallest value that allows for a stable explicit temporal evolution using a simple finite difference implementation of the forward Euler-scheme. Note, $'$ denotes differentiation of the function with respect to its argument. In order to complete the energetic description, it is important to elaborate the elastic energy density $f_{el}(\boldsymbol{u},\phi)$ in terms of the physical properties of the matrix and the precipitate phases, that are the stiffness matrices, as well as the misfit. Here, we adopt two ways of interpolating the phase properties, one of them bearing similarity to the Khachaturyan scheme [105] of interpolation and the other which is a tensorial formulation which is elaborately described in [106].

2.1.1 Khachaturyan interpolation

In this interpolation method, the elastic energy density writes as,

$$f_{el}(\boldsymbol{u},\phi)=\frac{1}{2}C_{ijkl}(\phi)(\epsilon_{ij}-\epsilon^*_{ij}(\phi))(\epsilon_{kl}-\epsilon^*_{kl}(\phi)), \tag{2.5}$$

where the total strain can be computed from the displacement $\boldsymbol{u}$ as,

$$\epsilon_{ij}=\frac{1}{2}\left(\frac{\partial u_i}{\partial x_j}+\frac{\partial u_j}{\partial x_i}\right), \tag{2.6}$$

while the elastic constants C_{ijkl} and eigenstrain ϵ^*_{ij} can be expressed as:

$$\begin{aligned} C_{ijkl}(\phi)&=C^{\alpha}_{ijkl}\phi+C^{\beta}_{ijkl}(1-\phi),\\ \epsilon^*_{ij}(\phi)&=\epsilon^{*\alpha}_{ij}\phi+\epsilon^{*\beta}_{ij}(1-\phi). \end{aligned} \tag{2.7}$$

To simplify the equations, without any loss of generality we additionally impose that the eigenstrain exists only in the precipitate phase (α phase), which makes $\epsilon^{*\beta}_{ij}=0$. Thereafter, the elastic energy density can be recast as,

$$f_{el}(\phi)=Z_3(\phi)^3+Z_2(\phi)^2+Z_1\phi+Z_0, \tag{2.8}$$

where, in Eqn. 2.8, we segregate the terms in powers of ϕ, i.e. Z3, Z2, Z1, Z0. Each pre-factor is a polynomial of ϕ, elastic constants and the misfit strains. The expansion of these pre-factors is illustrated in Appendix .A.1. Therefore, the term corresponding to the elastic energy in the

evolution equation of the order parameter can be computed as,

$$\frac{\partial f_{el}\left(\boldsymbol{u},\phi\right)}{\partial\phi} = 3Z_3(\phi)^2 + 2Z_2(\phi) + Z_1. \tag{2.9}$$

2.1.2 Tensorial interpolation

In this subsection, we utilize an interpolation scheme which allows the stress/strain terms normal and tangential to the phase-interface to be interpolated differently. An elaborate description for the motivation behind this can be found in [106, 107]. Concisely, this allows for an efficient control on the excess energy at the interface that in principle should enable an easier comparison with analytical models. We elaborate the scheme for two dimensions, but can also be generalized for more than two dimensions.

In this interpolation scheme, we rotate the stiffness tensors which are prescribed in the Cartesian co-ordinate system into the system that is described by the local unit normal vector and the tangent to the α/β interface. This is done using the unit normal vector of the interface,

$$\boldsymbol{n} = -\frac{\nabla\phi}{|\nabla\phi|}. \tag{2.10}$$

Describing a transformation from the Cartesian system $\boldsymbol{x}$, $\boldsymbol{y}$ to $\boldsymbol{n}$, $\boldsymbol{t}$ where after rotation, $\boldsymbol{x}$ matches $\boldsymbol{n}$ and $\boldsymbol{t}$ matches $\boldsymbol{y}$, the transformation of the stiffness tensor can be written as:

$$C_{nrts} = a_{ni}a_{tj}a_{rk}a_{sl}C_{ijkl}. \tag{2.11}$$

Similarly, the transformation of stress and strain tensor(including the eigenstrain tensor) can be written as:

$$\begin{aligned} \sigma_{nn} &= a_{nx}a_{nx}\sigma_{xx}, \quad \sigma_{nt} = a_{nx}a_{ty}\sigma_{xy}, \\ \epsilon_{nn} &= a_{nx}a_{nx}\epsilon_{xx}, \quad \epsilon_{nt} = a_{nx}a_{ty}\epsilon_{xy}. \end{aligned} \tag{2.12}$$

where, the transformation matrix can expressed using a rotation matrix, where we elaborate each element of the rotation matrix as follows:

$$\begin{aligned} a_{xn} &= cos\left(tan^{-1}\frac{n_x}{n_y}\right) = a_{nx}, \\ a_{xt} &= -sin\left(tan^{-1}\frac{n_x}{n_y}\right) = a_{tx}, \end{aligned}$$

$$a_{yn} = sin\left(tan^{-1}\frac{n_x}{n_y}\right) = a_{ny},$$
$$a_{yt} = -cos\left(tan^{-1}\frac{n_x}{n_y}\right) = a_{ty}.$$

The elastic energy of each of the phases writes as,

$$f_{el} = \frac{1}{2}\sigma_{ij}\left(\epsilon_{ij} - \epsilon^*_{ij}\right), \tag{2.13}$$

which can be further elaborated in the transformed co-ordinate system, where we express the elastic energy in terms of normal and tangential components of stresses and strains as,

$$f_{el} = \frac{1}{2}\left(\sigma_{nn}\left(\epsilon_{nn} - \epsilon^*_{nn}\right) + 2\sigma_{nt}\left(\epsilon_{nt} - \epsilon^*_{nt}\right) + \sigma_{tt}\left(\epsilon_{tt} - \epsilon^*_{tt}\right)\right). \tag{2.14}$$

The interpolated elastic energy can then be described as,

$$\begin{aligned} f_{el}\left(\boldsymbol{u},\phi\right) = {} & f^{\alpha}_{el}(\epsilon^{\alpha}_{nn}\left(\boldsymbol{u},\phi\right), \epsilon^{\alpha}_{nt}\left(\boldsymbol{u},\phi\right), \epsilon_{tt})h(\phi) \\ & + f^{\beta}_{el}(\epsilon^{\beta}_{nn}\left(\boldsymbol{u},\phi\right), \epsilon^{\beta}_{nt}\left(\boldsymbol{u},\phi\right), \epsilon_{tt})(1 - h(\phi)). \end{aligned} \tag{2.15}$$

Note, the usage of the superscripts on some of the terms, with the terms $\epsilon_{nn}, \epsilon_{nt}, \sigma_{tt}$, while the others $\epsilon_{tt}, \sigma_{nn}, \sigma_{nt}$ are left free, which is related to the jump conditions at the interface. In this interpolation scheme, the normal stress components σ_{nn}, σ_{nt} and ϵ_{tt} are continuous variables across the interface, which are derived from the condition of continuity of normal tractions at the interface (in the absence of interfacial stresses as well as situations where the interfacial energies are isotropic. The jump in the normal strains equals the surface divergence of the interfacial stresses which become non-zero when the interfacial energies become anisotropic.) and the Hadamard boundary conditions [108] respectively, while the others $\epsilon_{nn}, \epsilon_{nt}, \sigma_{tt}$ have a discontinuity in the sharp interface free-boundary problem, which would translate to a smooth variation across the interface in the diffuse interface description. In order to affect this idea, the following scheme for the determination of the stress and strain components is adopted.

Firstly the individual normal stress components of each of the phases are written down explicitly as a function of the stiffness and the strains as,

$$\begin{aligned} \sigma_{nn} = {} & C^{\alpha,\beta}_{nntt}(\epsilon_{tt} - \epsilon^{*\alpha,\beta}_{tt}) + C^{\alpha,\beta}_{nnnn}(\epsilon^{\alpha,\beta}_{nn} - \epsilon^{*\alpha,\beta}_{nn}) \\ & + 2C^{\alpha,\beta}_{nnnt}\left(\epsilon^{\alpha,\beta}_{nt} - \epsilon^{*\alpha,\beta}_{nt}\right) \end{aligned}$$

$$\sigma_{nt} = C^{\alpha,\beta}_{ntnt}(\epsilon_{tt} - \epsilon^{*\alpha,\beta}_{tt}) + C^{\alpha,\beta}_{ntnn}(\epsilon^{\alpha,\beta}_{nn} - \epsilon^{*\alpha,\beta}_{nn}) + 2C^{\alpha,\beta}_{ntnt}\left(\epsilon^{\alpha,\beta}_{nt} - \epsilon^{*\alpha,\beta}_{nt}\right),$$

where, ϵ^* is the eigenstrain at the interface produced due to a lattice mismatch between the precipitate and matrix. As mentioned before, we will be assuming that the eigenstrain is accommodated in the α phase, such that the eigenstrain in the β phase is zero. After some re-arrangement, the individual non-homogeneous normal strain-fields in either phase can be written as functions of the continuous variables which are the normal stresses and the tangential strain as,

$$\begin{bmatrix}(\epsilon^{\alpha}_{nn} - \epsilon^{*\alpha}_{nn})\\ (\epsilon^{\alpha}_{nt} - \epsilon^{*\alpha}_{nt})\end{bmatrix} = \begin{bmatrix}C^{\alpha}_{nnnn} & 2C^{\alpha}_{nnnt}\\ C^{\alpha}_{ntnn} & 2C^{\alpha}_{ntnt}\end{bmatrix}^{-1}\begin{bmatrix}\sigma_{nn} - C^{\alpha}_{nntt}\left(\epsilon_{tt} - \epsilon^{*\alpha}_{tt}\right)\\ \sigma_{nt} - C^{\alpha}_{nttt}\left(\epsilon_{tt} - \epsilon^{*\alpha}_{tt}\right)\end{bmatrix}. \tag{2.16}$$

Similarly, for matrix phase, where there is no eigenstrain, the phase normal strains read,

$$\begin{bmatrix}\epsilon^{\beta}_{nn}\\ \epsilon^{\beta}_{nt}\end{bmatrix} = \begin{bmatrix}C^{\beta}_{nnnn} & 2C^{\beta}_{nnnt}\\ C^{\beta}_{ntnn} & 2C^{\beta}_{ntnt}\end{bmatrix}^{-1}\begin{bmatrix}\sigma_{nn} - C^{\beta}_{nntt}\epsilon_{tt}\\ \sigma_{nt} - C^{\beta}_{nttt}\epsilon_{tt}\end{bmatrix}. \tag{2.17}$$

In order to have a smooth variation of non-homogeneous variables, we impose the following interpolation upon the individual strain components as,

$$\begin{bmatrix}\epsilon_{nn}\\ \epsilon_{nt}\end{bmatrix} = \begin{bmatrix}\epsilon^{\alpha}_{nn}\\ \epsilon^{\alpha}_{nt}\end{bmatrix}h(\phi) + \begin{bmatrix}\epsilon^{\beta}_{nn}\\ \epsilon^{\beta}_{nt}\end{bmatrix}(1 - h(\phi)). \tag{2.18}$$

Expressing the inverse matrices in the previous relations as S^{α}_{nt} and S^{β}_{nt} for the respective phases and further simplifying for the stress tensor σ_{nn} and σ_{nt} we can derive,

$$\begin{bmatrix}\sigma_{nn}\\ \sigma_{nt}\end{bmatrix} = \left(S^{\alpha}_{nt}h(\phi) + S^{\beta}_{nt}(1 - h(\phi))\right)^{-1} \left\{\begin{bmatrix}\epsilon_{nn} - \epsilon^{*\alpha}_{nn}h\left(\phi\right)\\ \epsilon_{nt} - \epsilon^{*\alpha}_{nt}h\left(\phi\right)\end{bmatrix} + S^{\alpha}_{nt}\begin{bmatrix}C^{\alpha}_{nntt}(\epsilon_{tt} - \epsilon^{*\alpha}_{tt})\\ C^{\alpha}_{nttt}(\epsilon_{tt} - \epsilon^{*\alpha}_{tt})\end{bmatrix}h(\phi) + S^{\beta}_{nt}\begin{bmatrix}C^{\beta}_{nntt}\epsilon_{tt}\\ C^{\beta}_{nttt}\epsilon_{tt}\end{bmatrix}(1 - h(\phi))\right\}, \tag{2.19}$$

where, the local strains $\epsilon_{nn}, \epsilon_{tt}, \epsilon_{nt}$ can be derived from the displacement using Eqn.2.6 followed by a co-ordinate transformation to the $\boldsymbol{n}, \boldsymbol{t}$ space. Thus, we can derive the values of $\epsilon_{nn}^{\alpha,\beta}$ and $\epsilon_{nt}^{\alpha,\beta}$ by inserting the preceding relation in previous strain calculations, i.e Eqns.2.16,2.17.

The remaining stress component σ_{tt} i.e. the tangential component of stress is also non-homogeneous and can be derived by firstly imposing a smooth interpolation across the diffuse interface, i.e.

$$\sigma_{tt} = \sigma_{tt}^{\alpha} h(\phi) + \sigma_{tt}^{\beta}(1 - h(\phi)), \tag{2.20}$$

where each of the phase stress components $\sigma_{tt}^{\alpha,\beta}$ can be written as a function of the normal strain components that have already been derived and the continuous tangential strain component that is just a function of the local displacement.

Therefore, relations for σ_{tt}^{α} and σ_{tt}^{β} write as,

$$\begin{aligned}\sigma_{tt}^{\alpha} &= C_{ttnn}^{\alpha}(\epsilon_{nn}^{\alpha} - \epsilon_{nn}^{*\alpha}) + 2C_{ttnt}^{\alpha}(\epsilon_{nt}^{\alpha} - \epsilon_{nt}^{*\alpha}) \\ &\quad + C_{tttt}^{\alpha}(\epsilon_{tt} - \epsilon_{tt}^{*\alpha}), \qquad (2.21)\\ \sigma_{tt}^{\beta} &= C_{ttnn}^{\beta}\epsilon_{nn}^{\beta} + 2C_{ttnt}^{\beta}\epsilon_{nt}^{\beta} + C_{tttt}^{\beta}\epsilon_{tt}. \qquad (2.22)\end{aligned}$$

Since, the values of $\epsilon_{nn}^{\alpha,\beta}$, $\epsilon_{nt}^{\alpha,\beta}$ are already determined in terms of ϵ_{nn}, ϵ_{nt} and ϵ_{tt}, the value of $\sigma_{tt}^{\alpha,\beta}$ can be solved using the preceding relations. Inserting them into the equation for σ_{tt}, helps to determine the final stress component as a function of strains.

In this event, the variational derivative of elastic energy of the system at constant stress, strain and displacement can be derived from Eqn.2.15 as,

$$\begin{aligned}\left(\frac{\partial f_{el}}{\partial \phi}\right)_{\sigma,\epsilon,u} &= \left(f_{el}^{\alpha} - f_{el}^{\beta}\right)\frac{\partial h(\phi)}{\partial \phi} + \sum_{\alpha}\frac{\partial f_{el}^{\alpha}}{\partial \epsilon_{nn}^{\alpha}}\frac{\partial \epsilon_{nn}^{\alpha}}{\partial \phi}h_{\alpha}(\phi) \\ &\quad + 2\sum_{\alpha}\frac{\partial f_{el}^{\alpha}}{\partial \epsilon_{nt}^{\alpha}}\frac{\partial \epsilon_{nt}^{\alpha}}{\partial \phi}h_{\alpha}(\phi), \qquad (2.23)\end{aligned}$$

where for conciseness we introduce the notation $h_{\alpha}(\phi) = h(\phi)$ and $h_{\beta}(\phi) = 1 - h(\phi)$, and summations on the R.H.S, run over the phases, α, β. The derivative with respect to the variable ϵ_{tt} returns zero, as it is a homogeneous quantity. In order to determine the derivative of non-homogeneous variables we utilize Eqn. 2.18. Differentiating Eqn. 2.18 at constant displacement

and strain, gives us following relations,

$$-\begin{bmatrix}\epsilon_{nn}^{\alpha}-\epsilon_{nn}^{\beta}\\ \epsilon_{nt}^{\alpha}-\epsilon_{nt}^{\beta}\end{bmatrix}\frac{\partial h_{\alpha}(\phi)}{\partial\phi}=\sum_{\alpha}\begin{bmatrix}\frac{\partial\epsilon_{nn}^{\alpha}}{\partial\phi}\\ \frac{\partial\epsilon_{nt}^{\alpha}}{\partial\phi}\end{bmatrix}h_{\alpha}(\phi). \tag{2.24}$$

Also recall that,

$$\frac{\partial f_{el}^{\alpha,\beta}}{\partial\epsilon_{nn}^{\alpha,\beta}}=\sigma_{nn},\quad \frac{\partial f_{el}^{\alpha,\beta}}{\partial\epsilon_{nt}^{\alpha,\beta}}=\sigma_{nt}, \tag{2.25}$$

which follow from the definition of the elastic energy.

Substituting these values and rewriting the variational derivative, we derive,

$$\begin{aligned}\left(\frac{\partial f_{el}}{\partial\phi}\right)&=\left(f_{el}^{\alpha}-f_{el}^{\beta}-\sigma_{nn}(\epsilon_{nn}^{\alpha}-\epsilon_{nn}^{\beta})\right)\frac{\partial h\left(\phi\right)}{\partial\phi}\\&\quad-2\sigma_{nt}(\epsilon_{nt}^{\alpha}-\epsilon_{nt}^{\beta})\frac{\partial h\left(\phi\right)}{\partial\phi}.\end{aligned} \tag{2.26}$$

This relation can be simplified further by substituting the values for f_{el}^{α} and f_{el}^{β} explicitly in terms of the stresses and the strains as,

$$\begin{aligned}\left(\frac{\partial f_{el}\left(\boldsymbol{u},\phi\right)}{\partial\phi}\right)&=\Big[-\frac{1}{2}\sigma_{nn}\left(\epsilon_{nn}^{\alpha}-\epsilon_{nn}^{\beta}\right)-\sigma_{nt}\left(\epsilon_{nt}^{\alpha}-\epsilon_{nt}^{\beta}\right)\\&\quad-\frac{1}{2}\sigma_{tt}^{\alpha}\epsilon_{tt}^{*\alpha}-\frac{1}{2}\sigma_{nn}\epsilon_{nn}^{*\alpha}-\sigma_{nt}\epsilon_{nt}^{*\alpha}\\&\quad+\frac{1}{2}\left(\sigma_{tt}^{\alpha}-\sigma_{tt}^{\beta}\right)\epsilon_{tt}\Big]\frac{\partial h\left(\phi\right)}{\partial\phi}.\end{aligned} \tag{2.27}$$

2.1.3 Conservation of volume

The remaining part of the evolution equation in Eqn.2.4 that is yet to be determined is the Lagrange parameter λ_{β} which would conserve the volume during interface evolution. Volume conservation is affected through the constraint,

$$\int h\left(\phi\right)\cdot dx=const\quad or \tag{2.28}$$

$$\int\delta h\left(\phi\right)dx=0, \tag{2.29}$$

where $\delta h(\phi)$ is the change in the value of $h(\phi)$ at a given spatial location. Reformulation, of this condition in discrete terms is performed in the following manner. From the Eqn.2.4, we have the rate of change of the order parameter at a given location, i.e

$$\tau W \frac{\partial \phi}{\partial t} = \text{rhs}_\alpha - \lambda_\beta h'(\phi), \tag{2.30}$$

where the term rhs_α constitute all the terms in the evolution equation of the order parameter in Eqn.2.4 leaving out the Lagrange parameter. In order to affect the volume constraint as given by Eqn.2.29, the Lagrange parameter λ_β is computed as,

$$\lambda_\beta = \frac{\sum_V rhs_\alpha}{\sum_V h'(\phi)}, \tag{2.31}$$

where, the summation $\sum_V$ is over the entire volume. This essentially ensures that the summation of all the changes in the order parameter over the entire volume returns zero, thus affecting the volume constraint in the discrete framework.

2.1.4 Mechanical equilibrium

As a final aspect, what remains is the computation of the displacement fields as a function of the spatial distribution of the order parameter. This is done iteratively by solving the damped wave equation written as,

$$\rho \frac{d^2 \boldsymbol{u}}{dt^2} + b \frac{d\boldsymbol{u}}{dt} = \nabla \cdot \boldsymbol{\sigma}, \tag{2.32}$$

that is solved until the equilibrium is reached, i.e $\nabla \cdot \boldsymbol{\sigma} = \mathbf{0}$. The terms $\rho = 100$ and $b = 0.4$ are chosen such that the convergence is achieved in the fastest possible time. The computation of the stresses differs depending upon the interpolation schemes used for estimating the elastic energies. For the case of the Khachaturyan interpolation, the stresses at every point can be readily computed as a partial derivative of the elastic energy as $\sigma_{ij} = \frac{\partial f_{el}(\boldsymbol{u}, \phi)}{\partial \epsilon_{ij}}$, while for the tensorial interpolation, the estimation of the stresses is done differently as laid out in the preceding subsection (see 2.1.2).

The optimization procedure for finding the equilibrium shape is performed by solving the evolution of the order parameter ϕ in Eqn.2.4 along with the equation of mechanical equilibrium at each time step, until a converged shape is reached. We utilize this formulation to simulate equilibrium shapes of the precipitate in 2D as well as in 3D, which are described in Chapter 3.

2.1.5 Discretization scheme

The calculations of the equilibrium shapes of the precipitate in two dimensions is performed by using the MPI exchange parallelization scheme, where the corresponding discretization of different terms is elaborated here. We start with the discretization of the terms in the evolution of phase-field given in Eqn. 2.4, which involves the variational derivative of the gradient energy functional incorporating anisotropy in the interfacial energy. As described, the variational derivative of the gradient energy function gives rise to a functional that is dependent on both gradients $\nabla\phi_x$ and $\nabla\phi_y$. This implies that in order to have the divergence of the variational derivative computed at the grid-point where the ϕ update occurs, requires that depending on the direction in which the derivatives related to the divergence are computed, one must compute the components $\nabla\phi_x$ and $\nabla\phi_y$ accordingly. Here, we calculate the magnitude of $\nabla\phi_x$ and $\nabla\phi_y$ at the mid-position (open circles: see Fig. 2.1) of the grid points along x-direction, where the magnitude of $\nabla\phi_y$ is taken as an average of its values at consecutive grid points along x-direction i.e. (i,j) and $(i+1,j)$ as shown in Fig. 2.1. Similarly, we calculate the $\nabla\phi_x$ and $\nabla\phi_y$ at the mid-position i.e. $(i,j+1/2)$ along y-direction as shown in Fig. 2.2, where the magnitude of $\nabla\phi_x$ is computed as an average of its values at positions (i,j) and $(i,j+1)$ along y-direction. This is then utilized to compute the magnitude of divergence of $\left(a\left(\boldsymbol{n}\right)\left(\frac{\partial a\left(\boldsymbol{n}\right)}{\partial\nabla\phi}|\nabla\phi|^2+a\left(\boldsymbol{n}\right)\nabla\phi\right)\right)$, where we apply backward difference scheme, so that the magnitude of the divergence can be computed at the grid point (i,j), which writes as,

$$\begin{aligned}
&\nabla\cdot\left[a\left(\boldsymbol{n}\right)\left(\frac{\partial a\left(\boldsymbol{n}\right)}{\partial\nabla\phi}|\nabla\phi|^2+a\left(\boldsymbol{n}\right)\nabla\phi\right)\right]\\
&=\frac{\left(a\left(\boldsymbol{n}\right)\left(\frac{\partial a\left(\boldsymbol{n}\right)}{\partial\nabla\phi_x}|\nabla\phi|^2+a\left(\boldsymbol{n}\right)\nabla\phi\right)\right)^{i,j}-\left(a\left(\boldsymbol{n}\right)\left(\frac{\partial a\left(\boldsymbol{n}\right)}{\partial\nabla\phi_x}|\nabla\phi|^2+a\left(\boldsymbol{n}\right)\nabla\phi\right)\right)^{i-1,j}}{dx}\\
&+\frac{\left(a\left(\boldsymbol{n}\right)\left(\frac{\partial a\left(\boldsymbol{n}\right)}{\partial\nabla\phi_y}|\nabla\phi|^2+a\left(\boldsymbol{n}\right)\nabla\phi\right)\right)^{i,j}-\left(a\left(\boldsymbol{n}\right)\left(\frac{\partial a\left(\boldsymbol{n}\right)}{\partial\nabla\phi_y}|\nabla\phi|^2+a\left(\boldsymbol{n}\right)\nabla\phi\right)\right)^{i,j-1}}{dy}.
\end{aligned}\tag{2.33}$$

Further, to calculate the mechanical equilibrium (see Eqn. 2.32), we compute components of the displacement field iteratively, where we use the L^2 norm for measuring the approach towards convergence, with a tolerance value of (10^{-6}). The relative change(RC) is given by,

$$RC=\left(\sum_{i=1}^{M}\sum_{j=1}^{N}(u_{n+1}^{i,j}-u_n^{i,j})\cdot(u_{n+1}^{i,j}-u_n^{i,j})\right)^{1/2},\tag{2.34}$$

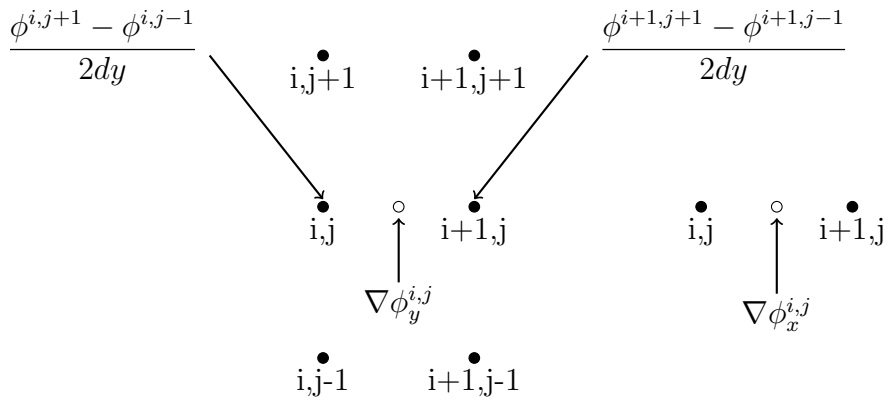

Figure 2.1: Schematic of discretization of $\nabla\phi_x$ and $\nabla\phi_y$ along x-direction.

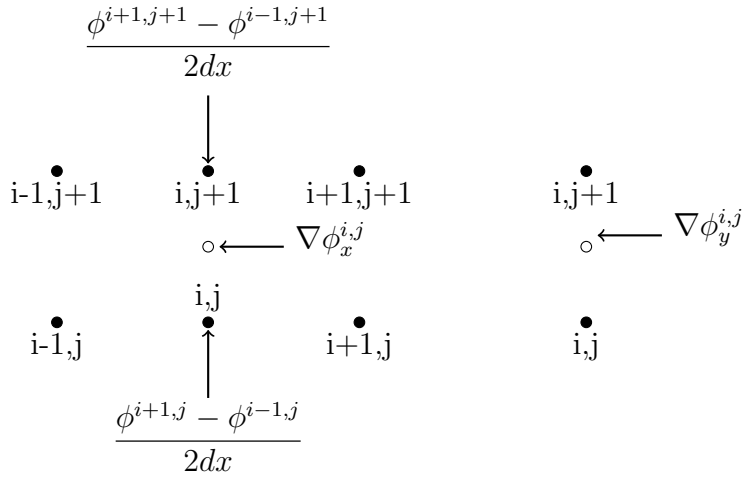

Figure 2.2: Schematic of discretization of $\nabla\phi_x$ and $\nabla\phi_y$ along y-direction.

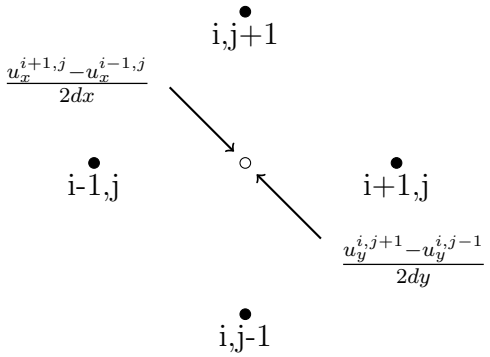

Figure 2.3: Schematic of discretization of displacement field for the calculation of normal components of the total strain.

where, $u_{n+1}^{i,j}$ and $u_n^{i,j}$ are displacements at two successive times at the grid point (i, j). The total number of grid points in x and y directions are M and N respectively. For the discretization of total strain, we use the central difference method, where the normal components of total strain are written as,

$$\epsilon_{xx}^{i,j} = \frac{u_x^{i+1,j} - u_x^{i-1,j}}{2dx}, \quad \epsilon_{yy}^{i,j} = \frac{u_y^{i,j+1} - u_y^{i,j-1}}{2dy}, \tag{2.35}$$

which are shown in Fig. 2.3, where we calculate the normal strains at the grid point (i, j) (i.e. an open circle). Similarly, other strain components can be computed as,

$$\begin{aligned} \epsilon_{xy}^{i,j} &= \frac{1}{2}\left(\frac{u_x^{i,j+1} - u_x^{i,j-1}}{2dy} + \frac{u_y^{i+1,j} - u_y^{i-1,j}}{2dx}\right), \\ \epsilon_{yx}^{i,j} &= \frac{1}{2}\left(\frac{u_y^{i+1,j} - u_y^{i-1,j}}{2dx} + \frac{u_x^{i,j+1} - u_x^{i,j-1}}{2dy}\right), \end{aligned} \tag{2.36}$$

which are shown in Fig. 2.4. The relevant stress values at the grid-point may be obtained following the interpolation schemes as described in the previous sections. Finally, the components of the force along x and y directions, i.e. $F_x^{i,j} = \frac{\sigma_{xx}^{i+1,j}-\sigma_{xx}^{i-1,j}}{2dx} + \frac{\sigma_{yx}^{i,j+1}-\sigma_{yx}^{i,j-1}}{2dy}$ and $F_y^{i,j} = \frac{\sigma_{xy}^{i+1,j}-\sigma_{xy}^{i-1,j}}{2dx} + \frac{\sigma_{yy}^{i,j+1}-\sigma_{yy}^{i,j-1}}{2dy}$, are discretized as shown in Fig. 2.5.

For the calculation of equilibrium shapes in three dimensions, we utilize an open source software OpenFoam, where we solve the phase-field and the mechanical equilibrium equations using the finite volume method. This software is a formula manipulation library which allows for a quick implementation of partial differential equations arising in multi-physics problems. Here, the first derivatives are calculated at cell faces and the second derivatives are calculated at

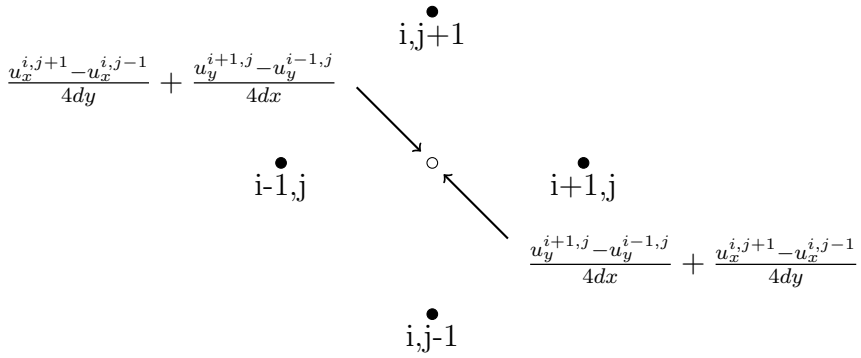

Figure 2.4: Schematic of discretization of displacement field for the calculation of shear components of the total strain.

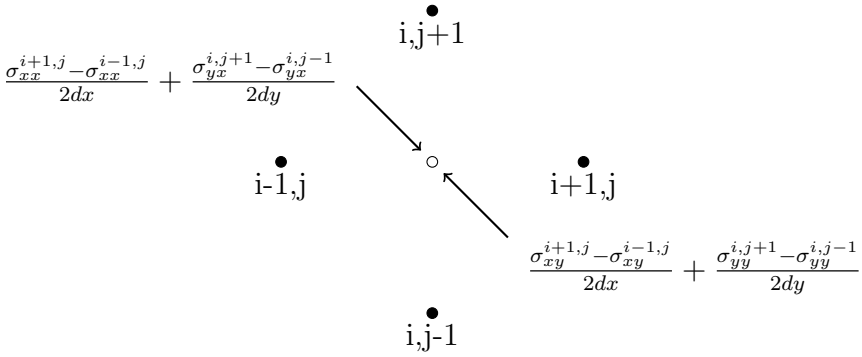

Figure 2.5: Schematic of discretization of stress field for the calculation of $F_x^{i,j}$ and $F_y^{i,j}$ at i, j (open circle).

cell centers. Further, we employ the in-built GAMG solver (Geometric-Algebraic Multi-grid), where it generates a quick solution on a mesh with small number of cells while mapping this solution onto a finer mesh and uses it as an initial guess to obtain an accurate solution on finer mesh. GAMG is a faster solver compared to other standard methods, as the increase in speed by solving first on coarser meshes outweighs the additional cost of mesh refinement and mapping of the field data. We utilize the same scheme for the calculation of equilibrium configurations of the precipitate which is elaborated in the following section 2.2.

2.2 Equilibrium multi-precipitate configurations

In the preceding subsection, we have described the phase-field formulation for the calculation of the equilibrium shapes of a single precipitate embedded in the matrix phase. Here, in this section, we will elucidate the diffuse interface formulation which is utilized to calculate the equilibrium configurations of multiple precipitates with coherent interfaces. In the preceding section, we have formulated a phase-field model for the computation of equilibrium shapes of precipitates, where we minimize the sum of the elastic and interfacial energy contributions while preserving the volume of the precipitate. In this study, since we are interested in computing equilibrium configurations of two or more precipitates, we need to extend the formulation in order to incorporate multiple phases. In this section, we formulate a multiphase-field model, where the functional consists of both the elastic and the interfacial energy contributions. Here, we solve for multiple Allen-Cahn equations along with the condition of mechanical equilibrium, while conserving the volume of each of the precipitates during the minimization. This constrained minimization is achieved through the technique of volume preservation which is also described elsewhere [2] and also in [1], that is essentially the coupling of the Allen-Cahn type equations with correction terms using Lagrange parameters that ensure the conservation of the volume of the precipitates during evolution.

We introduce a vector $\boldsymbol{\phi} = \{\phi_1, \phi_2, \phi_3 \dots \phi_N\}$, where the elements of the vector are order parameter fields that denote the distribution of the volume fraction of a given phase in the system. Consequently, the elements of the vector are constrained by the condition $\sum_{\alpha}^{N} \phi_\alpha = 1$ at every point in the domain. In our system, the first $\alpha = 1 \dots (N-1)$ phases represent the precipitate, while the last phase will always correspond to the matrix. Along with this, the state variables include the displacement vector $\boldsymbol{u} = \{u_x, u_y\}$, using which we construct the elastic energy contribution. The free-energy functional which is the sum of the interfacial and

elastic energy contributions reads,

$$\mathcal{F}(\boldsymbol{\phi}) = \int_V \sum_{\alpha=1}^{N} \left[\gamma_\alpha W |\nabla \phi_\alpha|^2 + \frac{1}{W} w\left(\phi_\alpha\right) \right] dV + \int_V f_{el}\left(\boldsymbol{u}, \boldsymbol{\phi}\right) dV + \int_V \sum_{\alpha=1}^{N-1} \lambda_\alpha^v h\left(\phi_\alpha\right) dV + \lambda_p \int_V \left(\sum_{\alpha=1}^{N} \phi_\alpha - 1 \right) dV, \tag{2.37}$$

where V is the total volume of system. The first integral constitutes the interfacial energy contribution, which in a phase-field formulation is done using a combination of the gradient-energy and potential contributions. Here, the term γ_α influences the interfacial energy in the system, while W influences the diffuse interface width separating the phases. The second term in the first integral describes a multi-well type potential, which writes as,

$$w\left(\boldsymbol{\phi}\right) = \sum_{\alpha=1}^{N} 9\gamma_\alpha \phi_\alpha^2 \left(1 - \phi_\alpha\right)^2. \tag{2.38}$$

The second integral enumerates the elastic energy contribution to the free-energy density of the system which is a function of the order parameters ϕ_α that is also used to interpolate between the phase properties and the misfit. The elastic energy density $f_{el}\left(\boldsymbol{u}, \boldsymbol{\phi}\right)$ from Eqn.2.37 is elaborated in terms of the physical properties of the precipitate and matrix phases. These are the stiffness and misfit strain matrices providing the information of the respective phases. The anisotropy in the system enters through these physical properties. Thus, the elastic energy density writes as (written in Einstein notation),

$$f_{el}(\boldsymbol{u}, \boldsymbol{\phi}) = \frac{1}{2} C_{ijkl}(\boldsymbol{\phi})(\epsilon_{ij} - \epsilon_{ij}^*(\boldsymbol{\phi}))(\epsilon_{kl} - \epsilon_{kl}^*(\boldsymbol{\phi})), \tag{2.39}$$

where the effective stiffness is written as an interpolation of the bulk stiffness matrices as $C_{ijkl}(\boldsymbol{\phi}) = \sum_{\alpha=1}^{N} h(\phi_\alpha) C_{ijkl}^\alpha$ and similarly the misfit-strain matrix is interpolated as $\epsilon_{ij}^*(\boldsymbol{\phi}) = \sum_{\alpha=1}^{N} h(\phi_\alpha)\epsilon_{ij}^{*\alpha}$, $h\left(\phi_\alpha\right) = \phi_\alpha^2\left(3 - 2\phi_\alpha\right)$ being an interpolation polynomial that smoothly varies from 0 to 1 and $\epsilon_{ij}^{*\alpha}$ represents the eigen-strain matrix of the phase α with respect to the matrix which is taken as the reference and thereby is assigned a null matrix.

The third and final term in the functional is added for the conservation of volume. λ_α^v is the Lagrange parameter that is incorporated such that the volume of the precipitate represented by the integral $\int_V h\left(\phi_\alpha\right) dV$, is conserved. Note that we have a Lagrange parameter each, for the conservation of the volume of each of the precipitates. λ_p is a Lagrange parameter that is utilized for ensuring that the sum of the order parameters remains unity at every point in space.

The evolution of the order parameters ϕ_α is derived using the classical Allen-Cahn dynamics that writes as,

$$\tau W \frac{\partial \phi_\alpha}{\partial t} = -\frac{\delta \mathcal{F}}{\delta \phi_\alpha}, \tag{2.40}$$

where $\alpha = 1, 2, 3, ..N$. The evolution equations elaborate as,

$$\tau W \frac{\partial \phi_\alpha}{\partial t} = -\frac{\delta \mathcal{F}}{\delta \phi_\alpha} - \lambda_p - \lambda_\alpha^v h'\left(\phi_\alpha\right), \tag{2.41}$$

for the precipitate phases $\alpha = 1, 2, 3, ..N-1$, while for the matrix phase the evolution equation reads,

$$\tau W \frac{\partial \phi_\alpha}{\partial t} = -\frac{\delta \mathcal{F}}{\delta \phi_\alpha} - \lambda_p. \tag{2.42}$$

The update of the order parameters requires the computation of the driving forces in terms of the variational derivatives with respect to the phase-field variables. While, the gradient and the potential energy contributions are straightforward, we elaborate upon the contribution of the elastic energy to the driving force. Taking the derivative of terms relating to elastic energy with respect to the corresponding order parameters, we obtain the elastic energy term for the corresponding evolution Eqns.2.41 and 2.42 which is given by (written in Einstein notation),

$$\begin{aligned}\frac{\partial f_{el}\left(\boldsymbol{u}, \boldsymbol{\phi}\right)}{\partial \phi_\alpha} &= \frac{1}{2}\frac{\partial C_{ijkl}(\boldsymbol{\phi})}{\partial \phi_\alpha}(\epsilon_{ij} - \epsilon^*_{ij}(\boldsymbol{\phi}))(\epsilon_{kl} - \epsilon^*_{kl}(\boldsymbol{\phi})) \\ &+ \frac{1}{2}C_{ijkl}(\boldsymbol{\phi})\left(-\frac{\partial \epsilon^*_{ij}(\boldsymbol{\phi})}{\partial \phi_\alpha}\right)(\epsilon_{kl} - \epsilon^*_{kl}(\boldsymbol{\phi})) \\ &+ \frac{1}{2}C_{ijkl}(\boldsymbol{\phi})\left(-\frac{\partial \epsilon^*_{kl}(\boldsymbol{\phi})}{\partial \phi_\alpha}\right)(\epsilon_{ij} - \epsilon^*_{ij}(\boldsymbol{\phi})),\end{aligned} \tag{2.43}$$

where, $\frac{\partial C_{ijkl}(\boldsymbol{\phi})}{\partial \phi_\alpha} = C^\alpha_{ijkl}\frac{\partial h(\phi_\alpha)}{\partial \phi_\alpha}$ and $\frac{\partial \epsilon^*_{ij}(\boldsymbol{\phi})}{\partial \phi_\alpha} = \epsilon^{*\alpha}_{ij}\frac{\partial h(\phi_\alpha)}{\partial \phi_\alpha}$. Also, the stress can be calculated as $\sigma_{ij} = C_{ijkl}(\boldsymbol{\phi})(\epsilon_{kl} - \epsilon^*_{kl}(\boldsymbol{\phi}))$ and we introduce $\delta\sigma_{ij} = C^\alpha_{ijkl}(\epsilon_{kl} - \epsilon^*_{kl}(\boldsymbol{\phi}))$. Therefore, substituting all the quantities to the preceding equation we obtain,

$$\frac{\partial f_{el}\left(\boldsymbol{u}, \boldsymbol{\phi}\right)}{\partial \phi_\alpha} = h'(\phi_\alpha)\left(\frac{1}{2}\delta\sigma_{ij} : (\epsilon_{ij} - \epsilon^*_{ij}(\boldsymbol{\phi})) - \sigma_{ij} : \epsilon^{*\alpha}_{ij}\right), \tag{2.44}$$

where $h'(\phi_\alpha)$ is the derivative of the interpolation function with respect to the corresponding ϕ_α. Thus, we derive the magnitude of elastic driving force for the corresponding evolution of

the order parameters.

In order to complete the time update of the order parameters, the values of the Lagrange parameters are required. We do the time update of the equations in two steps. In the first the change in the values of the order parameters are computed by incorporating only the interfacial and the elastic energy contributions i.e. essentially considering the response to the first three terms in the functional in Eqn.2.37, without the contribution from the volume-preservation term (second last integral). For this, the value of λ_p, can be simply evaluated as the negative of the average of the rest of the terms in the evolution equations in Eqn.2.41 and Eqn.2.42. Therefore, the update of these equations leads to an intermediate stage in the evolution of each of the order parameters which will be denoted as ϕ'_α, that are then corrected such that the volume of each of the precipitates is conserved. The correction step for each of the order parameters can be written as,

$$\tau W \frac{\partial \phi_\alpha}{\partial t} = \tau W \frac{\partial \phi'_\alpha}{\partial t} - \lambda^v_\alpha h'\left(\phi'_\alpha\right) + \lambda'_p, \tag{2.45}$$

for the precipitates, while for the matrix the order parameter will be corrected as,

$$\tau W \frac{\partial \phi_\alpha}{\partial t} = \tau W \frac{\partial \phi'_\alpha}{\partial t} - \lambda'_p, \tag{2.46}$$

where $\lambda'_p = \dfrac{\sum_\alpha^N \lambda^v_\alpha}{N}$ is the correction to the original Lagrange parameter λ_p, such that the volume fractions of each of the phases still follow the sum constraint. In order to derive the Lagrange parameters λ^v_α, we now utilize the required conservation constraint that $\int_V \dfrac{\partial \phi_\alpha}{\partial t} dV$ which discretely is $\dfrac{1}{\Delta t}\sum_V \Delta\phi_\alpha$(sum over the entire domain) returns zero for each of the precipitate phases, where Δt is the time-step for temporal integration. This gives us $N-1$ conditions for the solutions to the Lagrange parameters for the conservation of the volumes of each of the precipitates. Once these are obtained, these are substituted in Eqns. 2.45 and 2.46, in order to derive the corrected time updates $\dfrac{\partial \phi_\alpha}{\partial t}$ that conserve the volume of each of the precipitates and the matrix. The optimization procedure for finding the equilibrium structures of the precipitates is performed by solving the evolution of the order parameters ϕ_α in Eqn.2.41 and 2.42 along with the equation of mechanical equilibrium i.e. Eqn. 2.32 at each time step, until converged shapes for the precipitates are obtained. The corresponding results on the formation of the equilibrium configurations of the precipitates are described in Chapter 4.

2.3 Precipitate growth under the influence of coherency stresses

In the previous subsections, the formulations that are elaborated, are dealing with the calculation of equilibrium shape of a single precipitate or a cluster of precipitates embedded in the matrix. The energy minimization is carried out under the constraint of constant volume. For simulating precipitate growth in a supersaturated matrix, we relax the contraint of volume preservation.

We formulate a phase-field model based on a grand-potential functional, which includes the interfacial properties as well as the thermodynamics of the bulk phases in the system,

$$\begin{aligned}\Psi(\mu, \mathbf{u}, \phi) = \int_V \left[\gamma W a^2(\mathbf{n}) |\nabla\phi|^2 + \frac{1}{W} w(\phi) + \psi(\mu, \phi)\right] dV \\ + \int_V f_{el}(\mathbf{u}, \phi)\, dV,\end{aligned} \tag{2.47}$$

where V is the total volume of the system undergoing solid state phase transformation. The phase-field order parameter ϕ, that describes the presence and absence of precipitate (α phase) and matrix (β phase), acquires value $\phi = 1$ in the precipitate phase whereas $\phi = 0$ in the matrix phase. The double obstacle potential, i.e. $w(\phi)$ (see Eqn. 2.2) provides a potential barrier between two phases. Here, the term γ controls the interfacial energy density, while W influences the diffuse interface width separating the precipitate and the matrix phases. Anisotropy in the interfacial energy is incorporated using the function $a(\mathbf{n})$, which further writes as [109]:

$$\begin{aligned}\gamma &= \gamma_0 a(\mathbf{n}), \\ \gamma &= \gamma_0 \left(1 - \varepsilon \left(3 - 4\frac{\phi_x'^4 + \phi_y'^4}{(\phi_x'^2 + \phi_y'^2)^2}\right)\right),\end{aligned} \tag{2.48}$$

where, ε is the strength of anisotropy in interfacial energy, $a(\mathbf{n})$ is the anisotropy function of the interface normal $\mathbf{n} = -\dfrac{\nabla\phi}{|\nabla\phi|}$. $\psi(\mu, \mathbf{u}, \phi)$ is the grand potential density that is a function of the diffusion potential μ. Finally, $f_{el}(\mathbf{u}, \phi)$ is a function of the displacement $\mathbf{u}$.

By taking the variational derivative of the functional with respect to the phase-field order parameter, using Allen-Cahn dynamics, we derive the evolution of order parameter ϕ, which

writes as,

$$\tau W \frac{\partial \phi}{\partial t} = -\frac{\delta F}{\delta \phi}, \tag{2.49}$$

$$\begin{aligned} \tau W \frac{\partial \phi}{\partial t} = 2\gamma W \nabla \cdot \left[a\left(\mathbf{n}\right) \left[\frac{\partial a\left(\mathbf{n}\right)}{\partial \nabla \phi} |\nabla \phi|^2 + a\left(\mathbf{n}\right) \nabla \phi \right] \right] \\ - \frac{16}{\pi^2} \frac{\gamma}{W} \left(1 - 2\phi\right) - \Delta\psi \frac{\partial h(\phi)}{\partial \phi} + \frac{\partial f_{el}\left(\mathbf{u}, \phi\right)}{\partial \phi}, \end{aligned} \tag{2.50}$$

where τ is relaxation constant for the evolution of ϕ. The last two terms in Eqn. 2.50 contributes to the driving force necessary for the evolution of the precipitate phase. Here the term $\Delta\psi$ is the difference of the grand-potential densities between the α and the β phases and the corresponding term in the update of the order parameter derives from $\psi\left(\mu, \phi\right) = \psi_\alpha\left(\mu\right) h\left(\phi\right) + \psi_\beta\left(\mu\right)\left(1 - h\left(\phi\right)\right)$, where $h(\phi) = \phi^2(3 - 2\phi)$ is an interpolation polynomial. Further, the difference of the grand-potential densities between the phases may be written as a function of the departure of the diffusion potential from its equilibrium valus as, $\psi_\alpha - \psi_\beta = \left(c_{eq}^{\alpha} - c_{eq}^{\beta}\right)\left(\mu - \mu_{eq}\right)$, where c_{eq}^{α} and c_{eq}^{β} are the equilibrium compositions of the bulk precipitate and matrix phases respectively. We note that this is the driving force at leading order for an arbitrary description of the free-energies while it is the exact driving force for a situation where the free-energy composition relations of the matrix and precipitates are parabolic with equal curvatures. The second term in the driving force for phase transitions comes from the derivative of the elastic free-energy density given in Eqn. 2.8 (Subsection 2.1.1). Eqn. 2.50 is solved along with the update of the diffusion potential that follows the equation,

$$\frac{\partial \mu}{\partial t} = \left(\sum_{\alpha} h(\phi) \frac{\partial c_\alpha}{\partial \mu} \right)^{-1} \left[\nabla \cdot M \nabla \mu - \sum_{\alpha} c_\alpha(\mu) \frac{\partial h}{\partial \phi} \frac{\partial \phi}{\partial t} \right], \tag{2.51}$$

where M is the atomic mobility that is explicity related to the diffusivity D as $D\frac{dc}{d\mu}$. For, our calculations we assume a parabolic description $f\left(c\right)$ of the matrix and precipitate phases with equal leading order terms $A = (1/2)\frac{\partial^2 f}{\partial c^2}$, thereby the mobility becomes $\frac{D}{2A}$. Finally, we compute the displacement field as a function of the spatial distribution of the order parameters, which is utilized to calculate the magnitude of the strain field across the domain as explained earlier (see subsection 2.1.4). The corresponding results obtained using this formulation are depicted in Chapter 5.

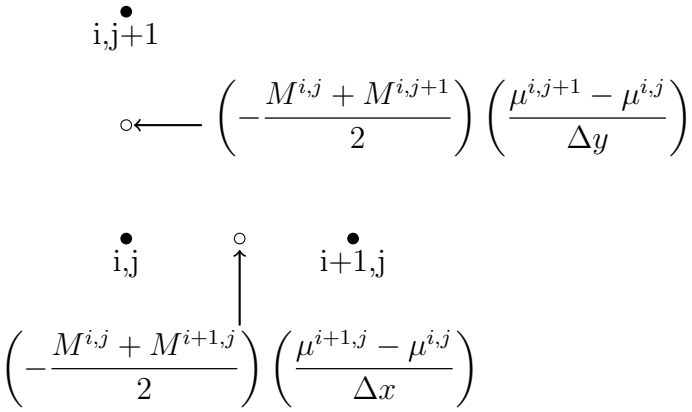

Figure 2.6: Schematic of discretization of $J = -M\nabla\mu$ along x and y directions at mid-positions (open circles) of the grid points i.e. at locations $i + 1/2, j$ and $i, j + 1/2$ respectively.

2.3.1 Discretization scheme

Here, we use the same discretization scheme for the calculation of the terms in the anisotropy in the interfacial energy, the components of the total strain and the force as that has been utilized in subsection 2.1.5. Along with this, for the discretization of the term $\nabla \cdot M\nabla\mu = -\nabla \cdot J$ (from Eqn. 2.51), we compute the gradients of the chemical potential using one-sided differences, that ensures second-order accuracy for the spatial discretization midway between two consecutive grid-points along a given direction. Similarly, we calculate the value of the mobility (M) at mid-positions by taking the average of two neighboring grid points (see Fig. 2.6). Combining the two, we derive the flux at the mid-points between two grid locations in each direction. Using these values, we compute divergence of flux ($\nabla \cdot J$) at the grid point (i, j) as shown in Fig. 2.7.

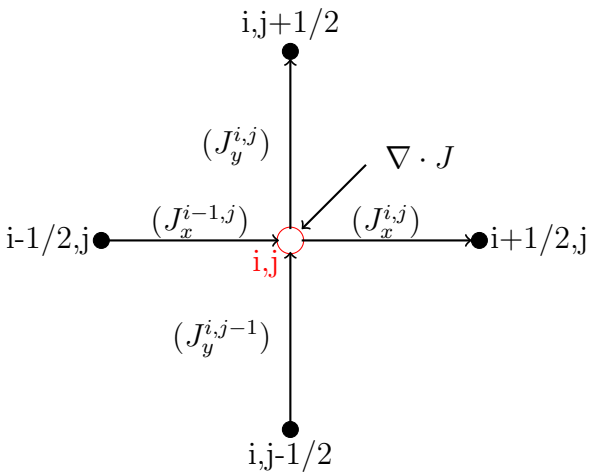

Figure 2.7: Schematic of discretization of $\nabla \cdot J = \dfrac{J_x^{i,j} - J_x^{i-1,j}}{\Delta x} + \dfrac{J_y^{i,j} - J_y^{i,j-1}}{\Delta y}$.

Chapter 3

Phase-field modeling of equilibrium precipitate shapes under the influence of coherency stresses

This chapter deals with the simulation of equilibrium precipitate shapes under the constraints of constant volume for different elastic and interfacial properties. Here, we utilize the formulation detailed in Chapter 2.1 and derive shape bifurcation diagrams as a function of size. The phase-field simulation results are compared against both classical analytical calculations as well as other sharp-interface based solution methodologies for benchmarking in 2D and thereafter is utilized for predicting equilibrium morphologies and bifurcations in 3D. In the end, we also highlight the theoretical equivalence of our approach with previous sharp-interface based methods thereby making our model equivalent to a diffuse-interface mapping of the sharp-interface problem.

3.1 Equilibrium shapes in 2D

3.1.1 Model parameters

In this section, we list out the material parameters and the non-dimensionalization scheme that will be used in the subsequent sections. Firstly, we will limit ourselves to isotropic and cubic systems in two dimensions, such that the stiffness tensor can be simplified. These systems can be generically defined in the following manner, where we use the commonly used short-hand notation for the non-zero stiffness components, $C_{11} = C_{1111}$, $C_{22} = C_{2222}$, $C_{12} = C_{1122}$ and $C_{44} = C_{1212}$, where additionally $C_{11} = C_{22}$ because of symmetry considerations. Thereafter,

these terms can be derived in terms of the known material parameters, those are the Zener anisotropy (A_z), Poison ratio (ν) and shear modulus (μ) and can be written as,

$$C_{44} = \mu, \quad C_{12} = 2\nu \left(\frac{C_{44}}{1 - 2\nu} \right), \quad C_{11} = C_{12} + \frac{2C_{44}}{A_z}. \tag{3.1}$$

The eigenstrain matrix will be considered diagonal in the Cartesian co-ordinate system and reads,

$$\epsilon^* = \begin{bmatrix} \epsilon^*_{xx} & 0 \\ 0 & \epsilon^*_{yy} \end{bmatrix}. \tag{3.2}$$

We use a non-dimensionalization scheme where the energy scale is set by the interfacial energy scale $1.0 J/m^2$, and division by the scale of the shear modulus $1 \times 10^9 J/m^3$ yields a length scale $l^* = 1$nm. In the results, hence all the parameters will be reported in non-dimensional units. Unless otherwise specified, all results are produced with $\mu_{mat} = 125$, $\nu_{ppt} = \nu_{mat} = 0.3$ and A_z varies from 0.3 to 3.0. When $A_z = 1.0$, elastic constants become isotropic. When A_z is greater than unity, elastically soft directions are $< 10 >$, whereas elastically hard directions are $< 11 >$. Similarly, in the case where A_z is less than unity, elastically soft (hard) directions are $< 11 >$ ($< 10 >$). For all the cases, the precipitate and matrix have the same magnitude of A_z.

The diagonal components of misfit strain tensor are assumed to be aligned along $< 10 >$ directions in (10) plane of the cubic system, whereas, the off-diagonal terms are zero. The misfit strain or eigenstrain (ϵ^*) can be dilatational i.e. the same along principle directions ($\epsilon^*_{xx} = \epsilon^*_{yy}$) or tetragonal i.e. different along principle directions ($\epsilon^*_{xx} \neq \epsilon^*_{yy}$). For different cases, the magnitude of eigenstrain varies from 0.5 to 2%.

For all our simulations, we have utilized a two dimensional system of a precipitate embedded in a matrix, with a lattice mismatch at the interface that is coherent. Domain boundaries follow periodic conditions. The ratio of the initialized precipitate size (equivalent radius) to the matrix size is maintained as 0.08, such that there is a negligible interaction of the displacement field at the boundaries. This resembles the condition of an infinitely large matrix containing an isolated precipitate without any influence of external stress. The interfacial energy between the matrix and precipitate is assumed to be isotropic until specified. The magnitude of interfacial energy is considered to be 0.15.

The model is generic enough for incorporating any combination of anisotropies in elastic energy which are possible in two dimensional space. In addition, different stiffness values in the

phases can also be modeled. In our model formulation, we will use the ratio of the shear moduli δ in order to characterize the degree of inhomogeneity, wherein, a softer precipitate is derived by a value of δ that is less than unity, and vice-versa for the case of a harder precipitate.

3.1.2 Isotropic elastic energy

As the first case, we consider isotropic elastic moduli ($A_z = 1.0$) with dilatational misfit at the interface between precipitate and matrix ($\epsilon^*_{xx} = \epsilon^*_{yy} = 0.01$). For this case, we consider the precipitate to be softer than the matrix i.e. the inhomogeneity ratio, $\delta = 0.5$.

We begin the simulation with an arbitrary shape as an initial state of precipitate e.g. an ellipse with an arbitrary aspect ratio, that is the ratio of the lengths of the major and the minor axes. We formulate a shape factor in terms of the major axis(c) and minor axis(a), which is expressed as $\rho = \frac{c-a}{c+a}$, that parameterizes the possible equilibrium shapes. An exemplary simulation showing the influence of the size is shown in Fig. 3.1, where a precipitate with equivalent radius $R = 38$ (the radius of an equivalent circle of equivalent area) has a circular shape. With increase in the size of precipitate, the precipitate transforms to an elliptical shape, which is captured in Fig. 3.1, where a precipitate with larger size i.e. equivalent radius, $R = 48$, acquires an ellipse-like configuration as the equilibrium shape.

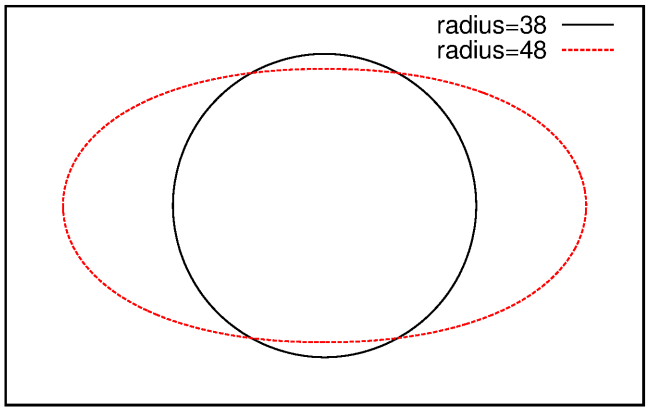

Figure 3.1: Equilibrium shapes of precipitate with R=38 (L=3.16, thick line) and R=48 (L=4.0, dotted line), with $\delta = 0.5$, $\mu_{matrix} = 125$, $\epsilon^* = 0.01$.

This phenomenon has been theoretically studied by Johnson and Cahn [3], which they term as a symmetry breaking transition of a misfitting precipitate in an elastically stretched matrix. The shape transition from a circular to an ellipse-like shape can be presented distinctly by plotting the shape factor(that is essentially a ratio of the difference of length of the precipitate along the two principal axes, divided by the sum of two lengths) as a function of the character-

istic length. The characteristic length is defined as the ratio of the characteristic elastic energy to the interfacial energy which can be written as follows,

$$L = \frac{R\mu_{mat}\epsilon^{*2}}{\gamma}, \tag{3.3}$$

where, R is the radius of a circular precipitate of equivalent area and γ is the magnitude of surface energy. Here, we briefly describe the Johnson-Cahn theory for shape bifurcation of a cylindrical precipitate. A solution different from a circle for an elastically induced shape bifurcation of an inclusion can be derived, only when the precipitate is softer than a matrix. To do so, we express the surface energy (f_s) and the elastic energy (f_{el}) in terms of the area of the precipitate (A) and shape factor (ρ).

Thus, the total surface energy can be expressed as a Taylor series expansion in terms of ρ,

$$f_s = 2\sigma\sqrt{\pi A}\left(1 + \frac{3}{4}\rho^2 + \frac{33}{64}\rho^4 + ...\right). \tag{3.4}$$

In the same way, we express total elastic energy as,

$$\begin{aligned} f_{el} = \frac{2A\epsilon^{*2}\mu_{ppt}}{1+\delta-2\nu_{ppt}}\Bigg\{1 - \frac{\delta(1-\delta)(1+\kappa)}{(1+\kappa\delta)(1+\delta-2\nu_{ppt})}\rho^2 \\ + \frac{\delta(1-\delta)^2(1+\kappa)}{(1+\kappa\delta)^2(1+\delta-2\nu_{ppt})^2}\rho^4 + ...\Bigg\}, \end{aligned} \tag{3.5}$$

where, ϵ^* is misfit at interface, $\delta = \mu_{ppt}/\mu_{mat}$ and $\kappa = 3 - 4\nu$.

The total energy (F^T) is the sum of f_s and f_{el}. Shape bifurcation takes place when the precipitate acquires a critical area A_c at which the energy landscape that is plotted as a function of the shape factor has distinct minima corresponding to the bifurcated shapes. This is akin to the example of classical spinodal decomposition where the compositions of the phases bifurcate below a critical temperature. Therefore, the critical size and the bifurcated shapes beyond it, can be derived using the same common tangent construction as in spinodal decomposition, with the shape-factor being used similarly as the composition. Given the symmetry of the isotropic system, this equilibrium condition simplifies to,

$$\frac{dF^T}{d\rho} = 0. \tag{3.6}$$

In this way, we take derivatives of the coefficients of the Taylor series from Eqn. 3.4 and Eqn. 3.5

w.r.t. shape factor (ρ), and add the respective terms to solve for Eqn. 3.6 as,

$$\rho\Bigg\{\overbrace{3\sigma\sqrt{\pi A_c}}^{df_s^1} - \overbrace{\frac{4A\epsilon^{*2}\mu^*\delta(1-\delta)(1+\kappa)}{(1+\kappa\delta)(1+\delta-2\nu^*)^2}}^{df_{el}^1}\Bigg\} + \rho^3\Bigg\{\underbrace{\frac{33}{8}\sigma\sqrt{\pi A_c}}_{df_s^2} + \underbrace{\frac{8\delta(1-\delta)^2(1+\kappa)A_c\epsilon^{*2}\mu^*}{(1+\kappa\delta)^2(1+\delta-2\nu^*)^4}}_{df_{el}^2}\Bigg\} = 0. \tag{3.7}$$

By rearranging the terms, we get a stable solution for ρ that reads,

$$\rho = \pm\sqrt{\frac{df_{el}^1 - df_s^1}{df_s^2 + df_{el}^2}}. \tag{3.8}$$

By substituting for the variables in Eqn. 3.8, we plot the shape factors corresponding to the equilibrium solution as a function of the characteristic length. This is shown in Fig. 3.2, where the thick dark line represents the analytical solution obtained from Eqn. 3.8. Maxima or unstable solutions occur for $\rho = 0$ for all the characteristic lengths beyond the critical value.

Before venturing into a critical comparison between analytical and the phase-field results it is important to ensure the numerical accuracy with respect to the choice of the parameters, particularly the choice of the interface width in the phase-field simulations. In the phase-field model that is described, the parameter that defines the diffuse-interface width W is a degree of freedom which may be increased or decreased depending on the morphological and macroscopic length scales that are being modeled. This choice of the diffuse-interface width W is typically chosen in a range such that the quantities being derived from the simulation results remain invariant. So for example in the present scenario it would be the shape-factor of the precipitate and its variation with the change in the interface widths allows us to determine the range of W in which the shape-factor is relatively constant. We have performed this convergence test for both the interpolation methods (recall from the model formulation 2.1.1, 2.1.2: Khachaturyan and the Tensorial) and the comparison is described in Fig. 3.3.

We find that for both interpolation methods relative invariance with change in the value of the interface width is achieved for values of $W <= 2, (W/R = 0.08)$, while for values greater, the variation is non-linear and changes rapidly. Therefore, we have chosen values of $W = 2$ for performing the comparison between the different numerical methods (FEM [4] and phase-field) and analytical calculations. It is noteworthy, that in general phase-field methods show this variation with the change in the interface widths because of variation in the equilibrium phase-

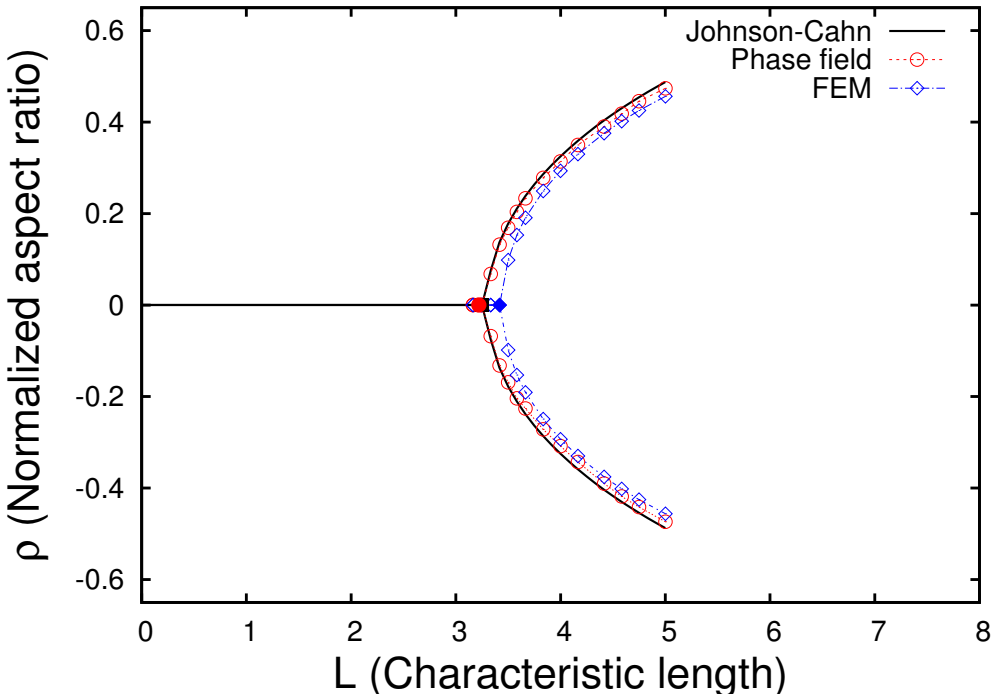

Figure 3.2: Plot depicts the shape bifurcation diagram- comparison of analytical solution ($L_c = 3.25$ with dark square) with phase field ($L_c = 3.21$ with red circle) and FEM [4] ($L_c = 3.42$ with blue diamond) results, $A_z = 1.0$, $\epsilon^* = 0.01$, $\delta = 0.5$.

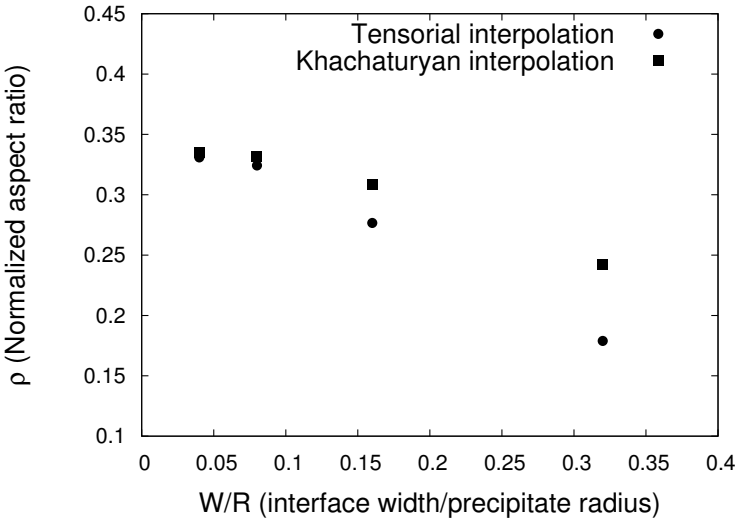

Figure 3.3: Plot shows the variation of normalized aspect ratio (shape factor) as function of W/R, for $R = 25$, $A_z = 1.0$, $\epsilon^* = 0.01$, $\delta = 0.5$.

field profile arising out of a contribution to the total effective interfacial excesses from the bulk energetic terms that scales with the interface width. The other reason for variation with W arises because of higher order corrections in the stress/strain profiles as a result of the imposition of an interface between the two bulk phases. Here, it is interesting that although the tensorial formulation is seemingly more correct with regards to the removal of the interfacial excess contribution [106] to the interfacial energy, however, this leads to no advantage with respect to the choice of larger interfacial widths, in comparison to the Khachaturyan interpolation method. A possible reason for this is the nature of the macroscopic length scale which in this case is the length over which the stress/strain profiles decay from the precipitate to the matrix, that typically are proportional to the local radius of curvature of the precipitate. This implies that for smaller precipitates the decay is faster and occurs over a shorter length and vice-versa for a larger precipitate. The accuracy of the phase-field method then, will naturally depend on the ratio W/R, which is applicable for both interpolation methods.

Given, that the results of the variation of the shape-factor for different interface widths for both interpolation methods, a seemingly qualitative conclusion that can be made is that it is the ratio of the interface width w.r.t to the macroscopic decay length of the stress/strain profiles and the error caused due to the use of larger values that leads to a more stringent condition for the choice of the interface widths than the errors arising from the contribution to the interfacial excesses due to incorrect interpolations of the stresses/strains at the interface. Therefore, given that the Khachaturyan method is numerically more efficient we have chosen this as the method in all our future simulation studies. The convergence test w.r.t the variations with the interface widths is repeated for the different bifurcation shapes both to verify and confirm the validity of the results as well as to perform the simulations in the most efficient manner by choosing the largest possible W with an admissible deviation in shape-factor.

We now comment on the comparison between the different numerical and the analytical Johnson-Cahn theories with our phase-field results. We have obtained the normalized aspect ratio (ρ) and plotted it as a function of normalized precipitate size (characteristic length), from phase field simulations. From Fig. 3.2, it is evident that the precipitate has a circular shape ($\rho = 0$) below the critical point, and turns elliptical ($\rho \neq 0$) beyond it. Also, the transition from a circle to an ellipse-like shape is continuous, i.e. ρ approaches zero, as L approaches a critical value L_c. It is evident from Fig. 3.2 that, phase-field results are in very good agreement with the analytical solution derived from the work of Johnson and Cahn [3], with a maximum error of 2.9% in the studied range of characteristic lengths. It is expected that deviations occur for larger characteristic lengths where the truncation errors in the analytical expressions to approximate the surface and the elastic energies start to become larger. Therefore, the

phase-field results should be more accurate here.

Additionally, we compare our phase-field results with existing numerical methods, such as the model adopted by Jog et.al. [4], where they used a sharp-interface, finite element method coupled with an optimization technique to determine the equilibrium shape of a coherent, misfitting precipitate. Using this method, we have reproduced the equilibrium shapes of precipitates, for the same set of conditions. It is clear that the results obtained from the sharp interface FEM model, follows similar trends as that of the phase-field results (Fig. 3.2). Note, that the errors are larger near the critical point, which is expected to be better retrieved in the phase-field method, given its greater resolution of the shape and lesser grid-anisotropy. Similarly for larger precipitate shapes where the curvatures of the precipitates become larger at certain locations, again the phase-field method should yield a better estimate. Nevertheless, all three methods agree pretty well.

The critical size of the precipitate at shape transition can be determined from the analytical solution as well as phase field simulations and FEM methods. The parameter L_c characterizing this critical radius is determined by first fitting a curve to the data points and thereafter computing the intersection point of the curve with the line ($\rho = 0$). Analytical equation gives $R_c = 39.57(L_c = 3.25)$, whereas the phase-field method yields $R_c = 38.53(L_c = 3.21)$ while the FEM yields $R_c = 41.785(L_c = 3.42)$. Thus, with these critical comparisons, we have benchmarked our phase field model quantitatively with both the analytical solution and the sharp interface model.

Moreover, the number of variants for the bifurcated shape are infinite since all the directions in xy-plane are equivalent due to infinite fold rotation symmetry about the z-axis. We have confirmed this fact by starting the simulation with different orientations to the initial configurations, which equilibrate along different orientations but with the same bulk energy. Also, for precipitates possessing greater elastic moduli than that of the matrix i.e. $\delta > 1.0$, no bifurcation is observed. This fact is also in agreement with the analytical solution, as there exits no real solution for cases where $\delta > 1.0$.

3.1.3 Cubic anisotropy in elastic energy with dilatational misfit

Anisotropy in the elastic energy arises from the variation of elastic constants in different directions. This deviation from the elastic isotropy is reflected in the increase in the number of independent elastic constants. Here, we mainly consider cubic anisotropy in the elastic energy, as it is observed in several alloys during precipitation and growth.

As explained in the previous section, eventually it is important to determine the range of

W, where the shape factor remains constant for the different magnitudes of interfacial width. Anisotropy in the elastic elastic energy modifies the magnitude of elastic constants, that brings about changes in the stress/strain variation across the interface moving from the precipitate to the matrix. As we have mentioned in the earlier section, we perform the W-convergence test, where the variations of shape-factor with the interface width are plotted in Fig. 3.4. The shape factor is calculated as the ratio of precipitate size measured along the horizontal axis to the vertical axis i.e. the size of precipitate along the elastically softer directions. There is not a significant variation in measured shape factor as a function of interfacial width i.e. in the given range of W, the variation is weakly linear. But, as described in the earlier section, we choose an optimum value of $W = 4$ ($W/R = 0.08$) with which we can efficiently run the simulations with an acceptable deviation in the calculated shape factor (i.e, an error of about 4% from the value obtained by extrapolating to the y-axes or the case of $W = 0$, that would effectively correspond to the sharp-interface limit).

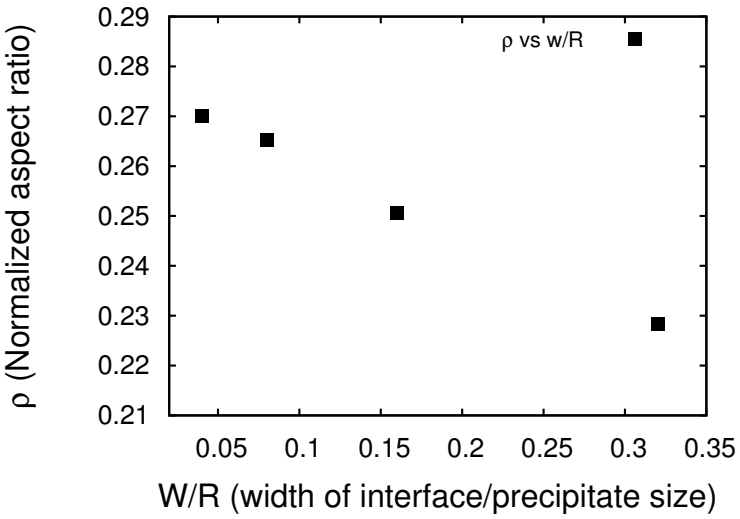

Figure 3.4: The variation of normalized aspect ratio as a function of W/R, for $R = 50$, $A_z = 3.0$, $\epsilon^* = 0.01$, $\delta = 0.5$.

Here, the elastic moduli possess cubic anisotropy while the misfit is dilatational. Thus, we have used $A_z = 3.0$, $\epsilon^* = 0.01$, $\delta = 0.5$, $\mu_{mat} = 125$. With these initial conditions, the phase field simulations yield equilibrium precipitate morphologies as a function of the characteristic length, which are illustrated in Fig. 3.5. Here, a precipitate with $R = 30$, acquires a cubic (square-like) shape with rounded corners as an effect of cubic anisotropy in the elastic energy. The precipitate faces are normal to $< 10 >$ directions, which are the elastically soft directions. In contrast to this, the precipitates with radii equal to 40 and 60 possess rectangular morphologies

with rounded corners and elongated faces normal to the [01] direction. Depending upon the orientation of the initial configuration of the precipitate i.e. the elliptical shape for a given equivalent radius, it converges to two variants that are rectangular shapes, that are either aligned vertically (along [01] direction) or along the horizontal axis (along [10] direction).

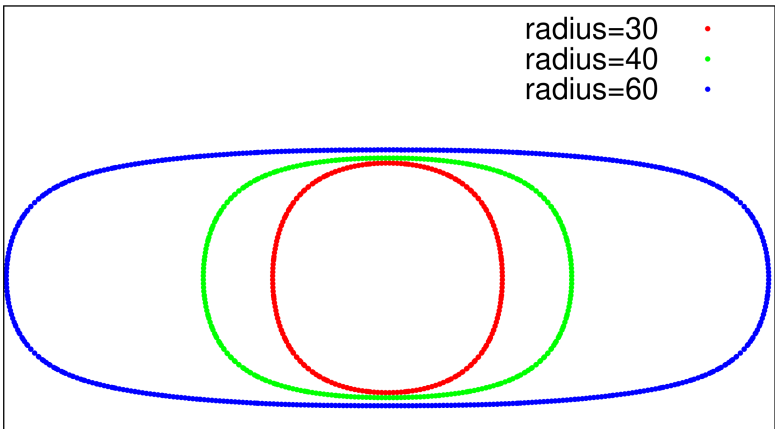

Figure 3.5: Equilibrium shapes of precipitate with cubic anisotropy in elastic energy and with different sizes, R=30 (L=2.5), R=40 (L=3.33) and R=60 (L=5) for $A_z = 3.0$, $\epsilon^* = 0.01$, $\delta = 0.5$.

Upon a change in the anisotropy to a value lesser than unity, i.e. $A_z = 0.5$, the equilibrium precipitate acquires a diamond like shape for R=15, which is shown in Fig. 3.6. With $A_z < 1$, the elastically softer directions now switch to $< 11 >$ directions. This is evident from Fig. 3.6, as the precipitate faces are oriented normal to the $< 11 >$ directions. Further, with increasing equivalent radius of precipitate, the equilibrium shape loses its four fold symmetry. The precipitate with increasing size tends to elongate along one of the elastically softer directions i.e. $< 11 >$ directions. This is captured by giving a slight angular rotation to the starting configuration, where the precipitate eventually takes up a rectangle like morphology (oriented along the $< 11 >$ direction), as shown in Fig. 3.6.

The influence of precipitate size on the equilibrium morphologies of the precipitate can be quantified by plotting the normalized aspect ratio (shape factor, ρ) as a function of characteristic length (L) of the precipitate, as a bifurcation diagram. We evaluate such a bifurcation diagram for the case of $A_z = 3$. Fig. 3.7 shows such a variation of the shape factor with respect to the precipitate size which reveals that the critical size for the bifurcation from cubic ($\rho = 0$) to the rectangle ($\rho \neq 0$), occurs for a value of $L = 2.71$.

As illustrated in the previous section, we have obtained the results for the equilibrium morphologies of the precipitate with cubic anisotropy in the elastic energy using a sharp interface model (FEM[4]), where the shape factor is calculated as a function of the characteristic length

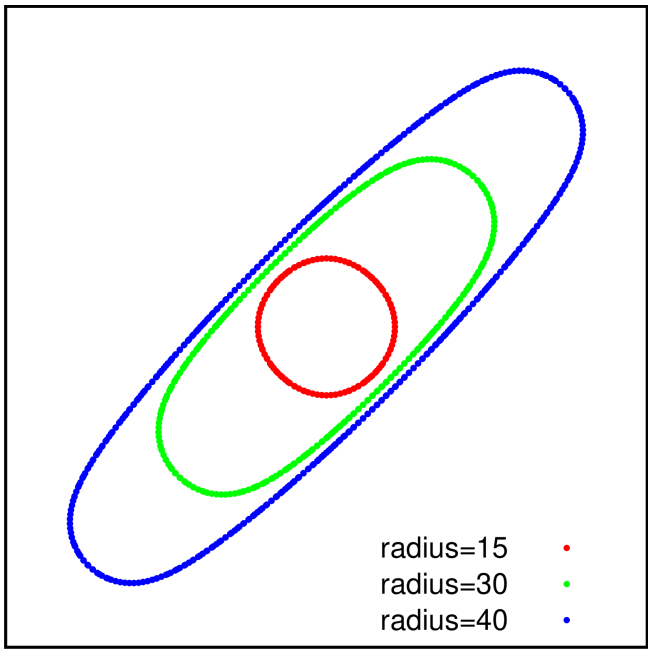

Figure 3.6: Equilibrium shapes of precipitate with cubic anisotropy in elastic energy R=15 (L=1.25), R=30 (L=2.5) and R=40 (L=3.33) for $A_z = 0.5$, $\epsilon^* = 0.01$, $\delta = 0.5$.

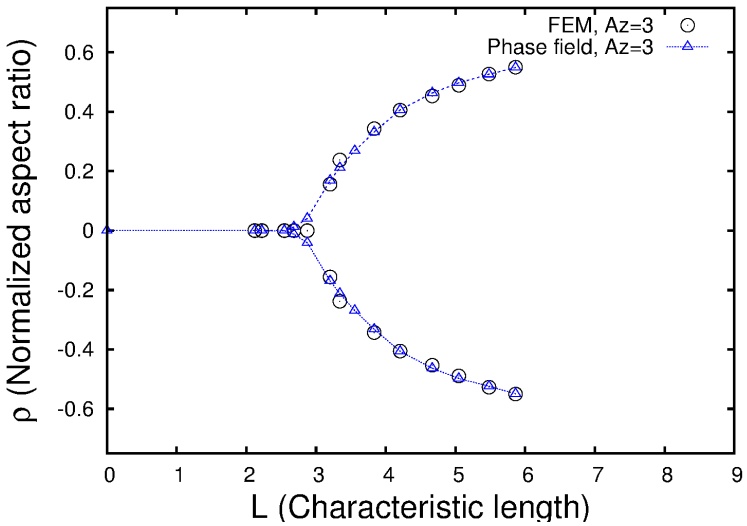

Figure 3.7: The shape bifurcation diagram with cubic anisotropy in elastic energy ($A_z = 3.0$, $\epsilon^* = 0.01$, $\delta = 0.5$), where the variation of aspect ratio is plotted as function of characteristic length, a comparison of phase field with FEM results[4].

of the precipitate. This is shown in Fig. 3.7, where the bifurcation diagram obtained from both the techniques i.e. phase-field as well as FEM are plotted against each other. It is evident that the bifurcation curves obtained from both simulation techniques agree well with each other. Both techniques predict the critical characteristic length (L_c), that are close to each other i.e. L_c retrieved from the phase field simulation equals to 2.71, whereas the one obtained from FEM equals to 2.87. Far away from the bifurcation point, the normalized aspect ratios obtained from phase field and FEM simulations predict nearly the same value, while near the bifurcation point (L_c) there is small variation, which is again expected as close to the critical point the resolution of the phase-field method should be better. In addition, the agreement between the two methods is also a critical additional benchmark of the phase-field model in the absence of an analytical solution predicting the shape factors for the case of cubic anisotropy.

3.1.4 Cubic anisotropy in elastic energy with tetragonal misfit

3.1.4.1 Misfit components with same sign

In this subsection, we study the case of tetragonal misfit where the magnitude of eigenstrain is different along the principle directions but of the same sign i.e.

$$\epsilon^* = \begin{bmatrix} 0.01 & 0 \\ 0 & 0.005 \end{bmatrix}, \tag{3.9}$$

where, we denote the misfit ratio with the parameter, $t = \epsilon^*_{xx}/\epsilon^*_{yy} = 2$. We consider three different cases, where the magnitude of A_z varies from 0.3 to 3.0 i.e. $A_z < 1$, $A_z = 1$ and $A_z > 1$. Similar to the previous cases, here the initial configuration of the precipitate is considered as an ellipse with an arbitrary aspect ratio and orientation.

Fig. 3.8, shows the equilibrium shapes of precipitate obtained with $A_z = 3.0$, for two different equivalent radii of precipitate ($R = 25, R = 50$). Here, the precipitate and matrix both possess the same elastic moduli i.e. $\delta = 1.0$. It is clear that, the precipitate assumes an ellipse like shape for the given sizes. The precipitate elongates along y-direction, i.e. the direction along which the eigenstrain is lower. This implies that, with increase in the precipitate size, it will produce an equilibrium shape which aligns itself along the direction of smaller misfit while elongating along the same direction. Thus, for this situation, no shape bifurcation is observed. Even for situations, where the magnitude of elastic anisotropy is $A_z \geq 1$ and $\delta \leq 1$, the precipitate morphologies remain ellipse like for the larger equivalent radii of precipitates.

In the succeeding condition, we consider $A_z = 0.3$ and $\delta = 1.0$ with the same tetragonality.

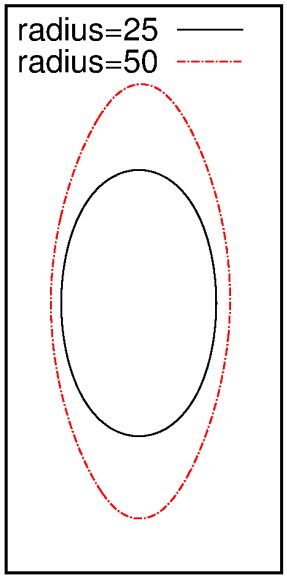

Figure 3.8: Equilibrium shapes of precipitate with tetragonal misfit and different sizes R=25(L=2.08) and R=50(L=4.16), $A_z = 3.0, t = +2.0, \delta = 1.0$.

The equilibrium morphologies for the smaller sizes are only moderately different than those observed in the previous case. Fig. 3.9 illustrates the results with $A_z = 0.3$, where the precipitate size ranges from $R = 40$ to $R = 65$. The precipitate with comparatively smaller size takes up an ellipse like morphology, which is elongated along the direction of least misfit. However, with increase in the size of precipitate, its morphology changes from an ellipse like shape to a twisted diamond like shape as shown in the Fig. 3.9. Here, the precipitates with equivalent radii of $R = 55$ and $R = 65$ have lost their mirror symmetry that is observed for the smaller sizes.

This shape bifurcation can be understood as a competition between the tendency of the precipitate to align along the elastically soft direction that is $< 11 >$ corresponding to the choice of $A_z = 0.3$ and the tetragonality influencing the shape towards an elongated ellipse in the y-direction. The precipitate with smaller sizes tend to align along the lower misfit directions, while beyond the critical point the bifurcated shapes reflect the combined influence of both the elastic anisotropy and the tetragonality resulting in a twisted diamond shape with an orientation in between the lower misfit direction ($< 10 >$) and elastically soft direction ($< 11 >$).

Here, we will follow the same procedure as adopted in the previous sections. We compare the morphologies of the precipitate obtained from the phase field simulations with FEM, which is illustrated in Fig. 3.10 for a given condition where, $(R = 75)$, $A_z = 0.3$, $\delta = 1.0$ and $t = 2$. Again, we find an excellent agreement between the shapes computed from both numerical

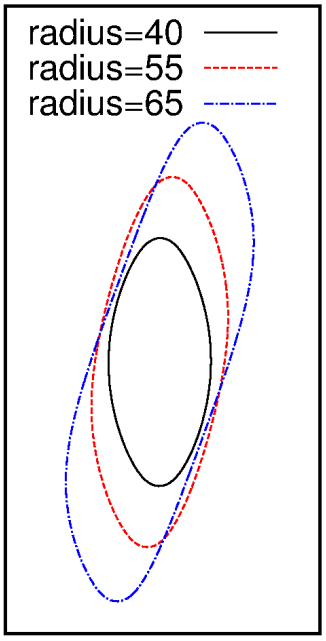

Figure 3.9: Equilibrium shapes of precipitate with tetragonal misfit and with varying precipitate sizes, below bifurcation point i.e. R=40(L=3.3) and above R=55(L=4.59) and R=65(L=5.42), $A_z = 0.3, t = +2.0, \delta = 1.0$.

methods. In both the cases, the volume occupied by the precipitates is the same as well as both the precipitates are inclined similarly. Differences occur along the extended directions, where the curvatures from the FEM simulated shapes are slightly smaller compared to the ones produced from the phase-field simulations, which again given the increased spatial resolution of the phase-field method is not surprising.

In order to derive the bifurcation diagram, we have calculated the shape factor (ρ) as a function of the precipitate size i.e. characteristic length (L). The shape factor in this situation can be defined as:

$$\rho = \sum_{i=1}^{N} \frac{X_i Y_i}{NV}, \tag{3.10}$$

where, X_i, Y_i are the co-ordinates on the precipitate-matrix interface considering the center of mass of the precipitate is at the origin, N is the total number of interfacial points and V is the volume of precipitate. This definition of the shape factor ensures that, it is equal to zero when the precipitate has mirror symmetry about the direction of least misfit i.e. the precipitate morphology is ellipse-like or elongated diamond, whereas it has non-zero values for a twisted diamond like shape.

Fig. 3.11, depicts the calculated bifurcation diagram, which contains the results obtained

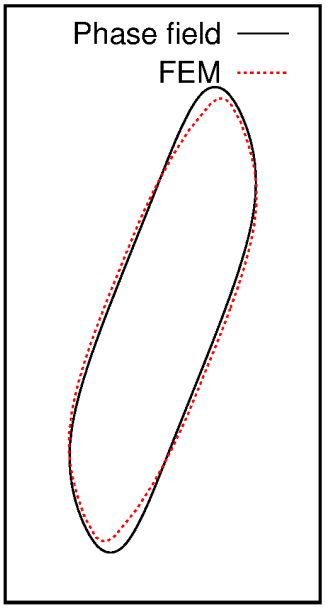

Figure 3.10: The comparison between equilibrium shapes of precipitate with equal area, obtained from the phase field and FEM results[4], R=75(L=6.25), $A_z = 0.3, t = +2.0, \delta = 1.0$.

from both the phase field as well as FEM simulations. We get a continuous transition of the shape factor beyond the bifurcation point from the phase field results, whereas the FEM results also reveal a transition with a small jump at the bifurcation point and beyond. Phase field results show that the shape bifurcation occurs at a characteristic length of 3.41, whereas FEM simulations predict 3.49. It is observed that beyond the bifurcation point the shape factors retrieved from the phase-field computations deviate from that of the FEM predictions. This difference in the calculations might be due to the increased complexity in the shape which is possibly better resolved by the phase-field method.

In order to ensure that the phase-field calculations are indeed yielding the lowest energy shapes, we have computed the equilibrium shapes beyond the bifurcation point which are ellipse-like (elongation along y-direction). This is done by starting with an initial configuration that is an ellipse with its long axis perfectly aligned with the y-axis, at x=0. Thereafter, we have calculated corresponding total energies of the precipitates, as highlighted in Fig. 3.12, with change in characteristic length. It is observed that the total energy of the twisted diamond like shapes is lower than that of the precipitates which are ellipse-like. This indicates that, the precipitates with lower energies (twisted diamond shape) are the stabler equilibrium configurations, compared to their ellipse-like counterparts, beyond the bifurcation point. Thus as shown in Fig. 3.13, if we give a slight rotation to an ellipse-like precipitate (thick dark line), it will acquire a twisted diamond like shape (dotted line) as an equilibrium state, beyond the criti-

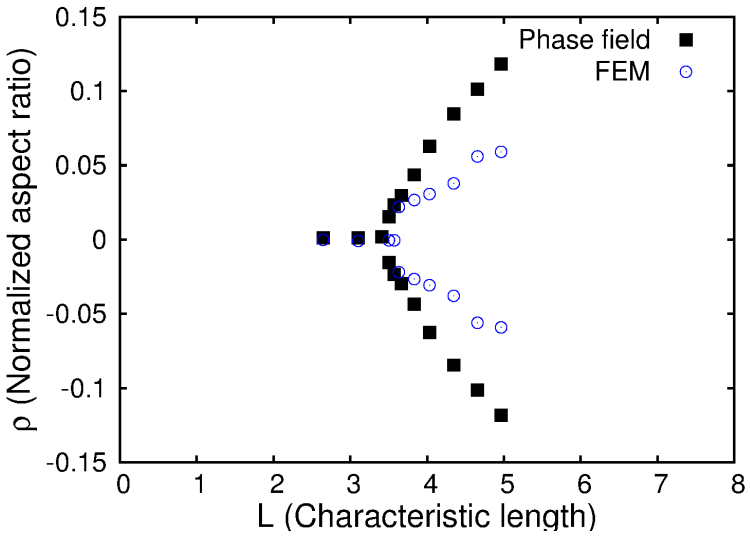

Figure 3.11: Shape bifurcation diagram for misfit ratio t=2.0, comparison between phase field and FEM results[4] ($A_z = 0.3, \delta = 1.0$), where ρ is plotted as a function of characteristic length.

cal point. With increase in the characteristic length past the bifurcation point, the difference between the total energies of the stable and metastable precipitate shapes keeps on increasing.

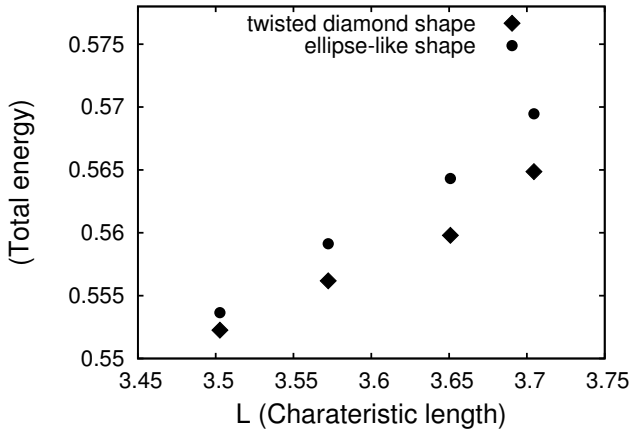

Figure 3.12: Variation of the elastic energy of precipitate as a function of characteristic length (L) for ellipse like precipitate (circle) and twisted diamond shape of precipitate (diamond).

As illustrated in the previous section, the change exhibited in the precipitate morphology is an effect of the precipitate size alone, where the misfit ratio remains constant i.e. $t = 2.0$. Further, we also characterize the effect of change in the magnitude of misfit ratio i.e. $\epsilon^*_{xx}/\epsilon^*_{yy}$ on the equilibrium morphologies of the precipitate by keeping the size constant. For this purpose,

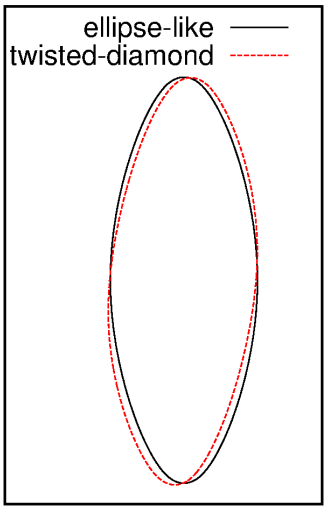

Figure 3.13: The equilibrium shapes of precipitate with same equivalent radius R=52 (L=3.5), ellipse like shape (thick-dark line) in metastable equilibrium and diamond like shape (dotted red-line) in stable equilibrium.

we keep the magnitude of ϵ^*_{xx} constant and varied ϵ^*_{yy} from 0.004 to 0.01. Accordingly, the misfit ratio takes values from 2.5 to 1.0. Fig. 3.14 shows the equilibrium shapes of the precipitate for the different values of misfit ratio with $A_z = 0.3$, $\delta = 1.0$. Here, we retain the same precipitate size for all calculations (i.e. R=65). As discussed earlier, with these conditions the precipitate acquires a bifurcated shape which is twisted diamond like. With increase in the magnitude of misfit ratio, the precipitate orientation changes towards the direction of least misfit i.e. the vertical axis. Initially, for t=1.0, the equilibrium precipitate is aligned exactly along the elastically softer directions which are $< 11 >$ with an orientation of 45^0 and a rectangular shape i.e. in this case the equilibrium shape is determined by the elastically softer directions ($A_z = 0.3$) alone. As the misfit ratio elevates from 1.0 to higher values, the precipitate acquires an orientation with a larger magnitude, which is an obvious situation, as the orientation is a compromise between the tendencies to align along the elastically softer direction ($< 11 >$) and the direction of lower misfit [01]. For t=2.5, the equilibrium morphology tends towards elongation along the lower misfit directions, where the precipitate has an elongated ellipse-like shape aligned along the vertical axis. This is again reflected in Fig. 3.15, where the magnitude of the shape factor goes to zero as the magnitude of misfit ratio becomes larger. The other way of looking at this is that with increase in the magnitude of the misfit ratio the bifurcation point for the system shifts to larger values of equivalent precipitate sizes, as the driving force for the precipitate elongating along the direction of lower misfit increases.

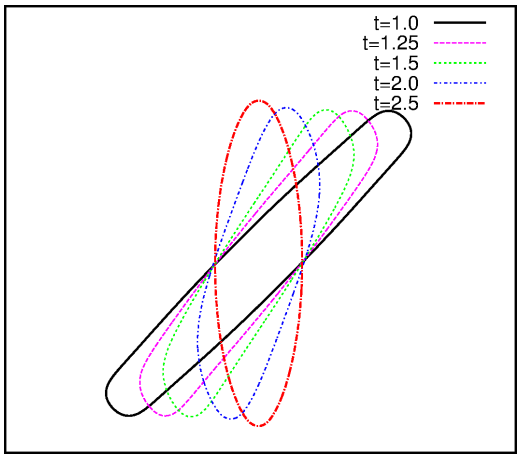

Figure 3.14: Equilibrium morphologies of precipitate with varying degree of strength of tetragonal misfit which varies from t=1.0 to t=2.5 for $A_z = 0.3, \delta = 1.0$.

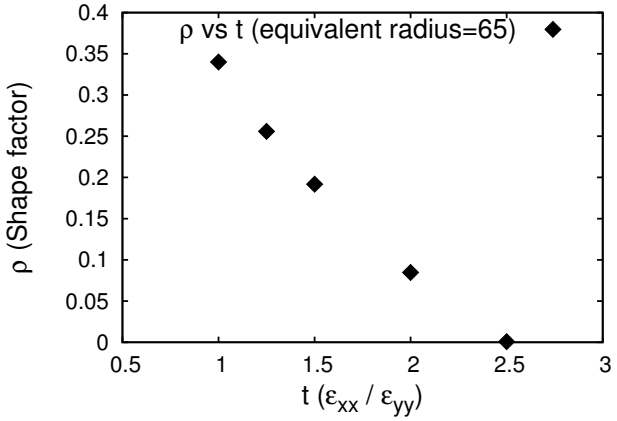

Figure 3.15: Plot depicts the change in shape factor as function of misfit ratio varying from t=1.0 to t=2.5 for $A_z = 0.3, \delta = 1.0$.

3.1.4.2 Misfit components with opposite sign

In this case, the misfit components along x and y-directions have opposite sign as well as different magnitude. Here, we have chosen $t = -2.0$ i.e. $\epsilon^*_{xx} = 0.01, \epsilon^*_{yy} = -0.005$ and $A_z = 2.0$. Although, the symmetry of misfit is the same as compared with the previous section, there is an important difference. As shown in Fig. 3.16, there is a shape transition in this case too, where a precipitate with size R=80, has an ellipse like shape, while above the critical characteristic length, precipitate (R=100), a twisted diamond like shape results as the equilibrium morphology. This shape transition is seen in all the cases where $A_z < 1.0, A_z = 1.0$ and $A_z > 1.0$. So, the shape bifurcation occurs even at $A_z = 1.0$ and $A_z > 1.0$, which is in contrast to the previous case where the principal components of misfit strains have the same sign.

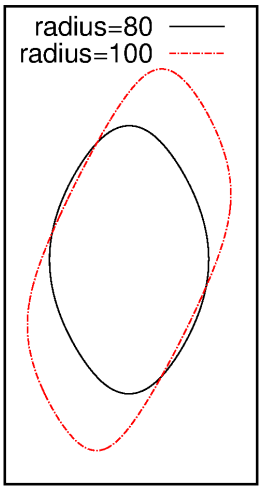

Figure 3.16: Equilibrium shapes of precipitate with tetragonal misfit and different sizes, where R=80(L=6.66) and R=100(L=8.33), $A_z = 2.0, t = -2.0$, i.e. $\epsilon^*_{xx} = 0.01, \epsilon^*_{yy} = -0.005$.

Fig. 3.17, also shows that the precipitate with a smaller radius (R=40) and A_z less than one ($A_z = 0.3$), has an equilibrium shape which has its axis elongated along the direction of lower misfit. For the larger precipitate shapes (R=90), we acquire a twisted diamond like shape. It is observed that there is an influence of the change in magnitude of inhomogeneity (δ) and the magnitude of Zener anisotropy parameter (A_z) on the critical characteristic length (L_c) of shape bifurcation. For a systematic analysis, we keep δ constant ($\delta = 1.0$), while the Zener anisotropy parameter (A_z) is varied from 0.3 to 2.0. We noticed that, the L_c is lower for $A_z = 0.3$ compared to the case of $A_z = 2.0$. For $A_z = 0.3$, the precipitates with smaller sizes acquire a twisted diamond like shape, as $< 11 >$ are elastically softer directions. This provides a driving force for the precipitates even with the smaller sizes to orient along the elastically softer directions. In contrast for $A_z > 1.0$ (in this case $A_z = 2.0$), the elastically soft directions

are $< 10 >$ which is also the same as the direction of lowest misfit. Thus, it becomes harder for the precipitates to orient along $< 11 >$ directions and acquire the twisted diamond like shape. This is evident from Fig. 3.16, where we also find that the critical characteristic length (L_c) is pushed to larger values i.e. the shape transition occurs for the larger precipitate sizes.

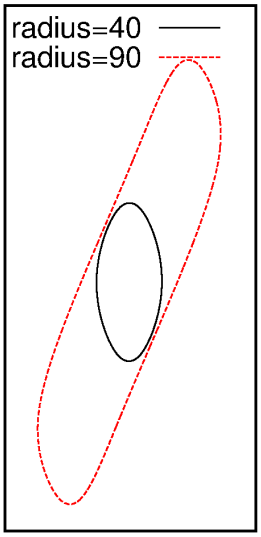

Figure 3.17: Equilibrium shapes of precipitate with tetragonal misfit and different sizes, where R=40(L=3.33) and R=90(L=7.5), $A_z = 0.3, t = -2.0$, i.e. $\epsilon^*_{xx} = 0.01, \epsilon^*_{yy} = -0.005$.

3.1.5 Competition between anisotropy in interfacial energy and elastic energy

This section illustrates two factors controlling the selection of orientation of the precipitate morphology i.e. the anisotropies in interfacial energy (ε) and elastic energy (A_z). In order to investigate the influence of this competitive nature of the energy anisotropies, we first vary the anisotropy in elastic energy by changing the magnitude of A_z (with constant tetragonality, i.e. t=+1.0), while keeping the anisotropy in interfacial energy constant and then repeat the other way around. This is achieved by incorporating anisotropy in interfacial energy as elaborated in Chapter 2.1:

$$\begin{aligned} \gamma &= \gamma_0 a(\boldsymbol{n}), \\ \gamma &= \gamma_0 \left(1 - \varepsilon \left(3 - 4\frac{\phi_x'^4 + \phi_y'^4}{(\phi_x'^2 + \phi_y'^2)^2}\right)\right), \end{aligned} \tag{3.11}$$

where, ε is the strength of anisotropy in interfacial energy, $a(\boldsymbol{n})$ is the anisotropy function of the interface normal $\boldsymbol{n}$, which has components $\boldsymbol{n_x} = -\frac{\phi_x^{'}}{|\nabla\phi|}$, $\boldsymbol{n_y} = -\frac{\phi_y^{'}}{|\nabla\phi|}$, with $\phi_x^{'}$ and $\phi_y^{'}$ being the partial derivatives of the order parameter $\phi\,(x, y)$ in the x and y-directions.

3.1.5.1 Effect of anisotropy in elastic energy (A_z)

Here, the magnitude of A_z is altered from 0.3 to 3.0 for a constant $\varepsilon = 0.02$. Fig. 3.18 - 3.20, show the equilibrium precipitate morphologies with (dotted line) and without (thick line) anisotropy in interfacial energy, with increasing A_z. In all the cases, the size of precipitate is kept the same i.e. the equivalent radius is constant ($R = 25$). In this regard, three prominent cases are investigated i.e. $A_z = 0.3, A_z = 1.0$ and $A_z = 3.0$, where the influence of the change in magnitude of A_z on the equilibrium morphology is discussed. All these simulations are performed with the precipitate sizes which are well below the bifurcation point.

In the first case, we keep $A_z = 1.0$, with $\varepsilon = 0.02$. This is to quantify the effect of anisotropy in interfacial energy alone. The results are summarized in Fig. 3.18, where the precipitate takes a circular shape (thick dark line) due to isotropic elastic energy with no anisotropy in interfacial energy. With the introduction of anisotropy in interfacial energy, the precipitate turns to a diamond like shape, with its faces normal to $< 11 >$ directions. So, the equilibrium shape of the precipitate is primarily determined by interfacial anisotropy alone.

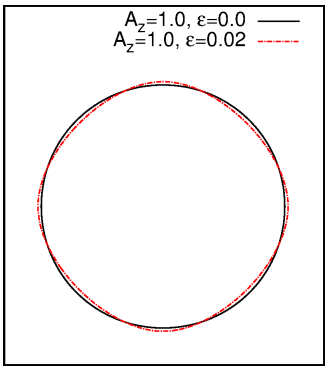

Figure 3.18: Equilibrium shapes of precipitate with (red dotted line) and without (thick dark line) anisotropy in interfacial energy, for $A_z = 1.0, t = 1$.

Fig. 3.19, shows an equilibrium precipitate morphology (thick dark line) with $A_z = 3.0$, where there is cubic anisotropy in the elastic energy which drives the precipitate to acquire a square like shape with rounded corners where the square faces are aligned normal to the elastically soft directions $< 10 >$. Again, incorporating anisotropy in interfacial energy ($\varepsilon = 0.02$), tends to align the precipitate faces normal to the $< 11 >$ directions. This minimizes the

effect of elastic anisotropy on the precipitate shape, by giving rise to a morphology between a square and a diamond, which is shown in Fig. 3.19, where the equilibrium shape of the precipitate (dotted line) has acquired a shape as explained above. There can be a possibility, where effect of both anisotropies counterbalance each other and gives rise to a morphology that is circular, though the respective energies (elastic and interfacial) possess anisotropies.

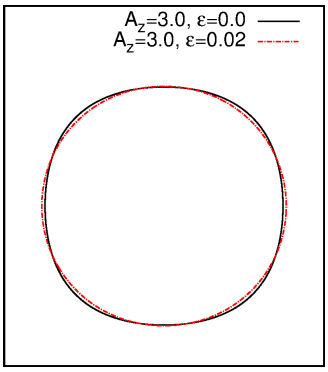

Figure 3.19: Equilibrium shapes of precipitate with (red dotted line) and without (thick dark line) anisotropy in interfacial energy, for $A_z = 3.0, t = 1$.

When $A_z < 1$, (in this case $A_z = 0.3$), the precipitate acquires a shape which prefers to align its face normal to $< 11 >$ directions that is elastically softer. This is captured in Fig. 3.20, which shows the precipitate morphologies where both the interfacial and elastic anisotropies drive the precipitate shape towards a diamond. Precipitate without anisotropy in interfacial energy, has its faces normal to $< 11 >$ directions, whereas with anisotropy in interfacial energy the precipitate faces become weakly concave towards the center of the precipitate with the corners becoming sharper. It is evident that the presence of interfacial anisotropy along with cubic anisotropy in elastic energy affects equilibrium morphologies of the precipitate distinctly.

In the preceding discussion, we characterize the effect of energy anisotropies on the precipitate shape where the precipitate size is well below the bifurcation point (L_c). Now, we shift beyond the bifurcation point (L_c) with the same argument i.e. competitive effect of both the anisotropies while accessing the larger precipitate sizes. Fig. 3.21 shows such morphologies of the precipitate with $A_z = 3.0$, where precipitates with two different sizes (R=40 and R=60) and different variants are depicted. Presence of anisotropy in interfacial energy does not affect the equilibrium morphology of precipitate significantly, whereby, though the precipitate corners become more rounded, edges of the precipitate remain strongly aligned normal to the elastically softer directions ($< 10 >$). This implies that with increase in the size of precipitate, the influence of elastic energy anisotropy dominates over interfacial energy anisotropy.

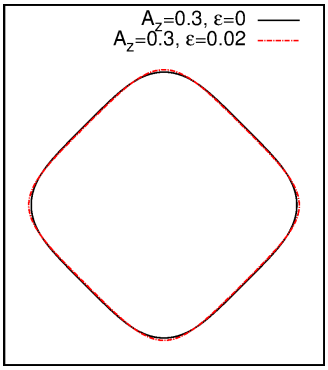

Figure 3.20: Equilibrium shapes of precipitate with (red dotted line) and without (thick dark line) anisotropy in interfacial energy, for $A_z = 0.3, t = 1$.

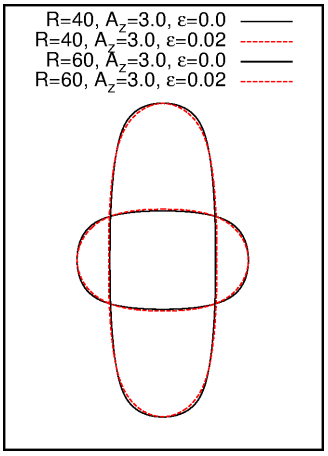

Figure 3.21: Equilibrium shapes of precipitate beyond bifurcation point with (red dotted line) and without (thick dark line) anisotropy in interfacial energy, for $A_z = 3.0, t = 1$.

3.1.5.2 Effect of anisotropy in interfacial energy (ε)

While in the previous section, the strength of anisotropy in interfacial energy (ε) is kept constant, furthering the discussion, in this section, we will consider the effect of varying ε on the precipitate morphology. Here, we vary the magnitude of ε from 0.0 to 0.04, while holding the Zener anisotropy parameter constant, at a value of $A_z = 3.0$. The equilibrium morphology of the precipitate initially acquires a cubic shape with rounded corners, while the precipitate faces are aligned normal to the elastically soft directions ($< 10 >$). Further, with increase in the strength of ε, the precipitate faces start to orient towards $< 11 >$ directions. This is due to a significant increase in the strength of anisotropy in interfacial energy, while keeping the magnitude of A_z constant. Thus, an increase in the strength of anisotropy in interfacial energy imparts a driving force for alignment of the precipitate faces normal to the $< 11 >$ directions rather than $< 10 >$ directions (elastically softer), giving rise to a diamond like shape as shown in Fig. 3.22.

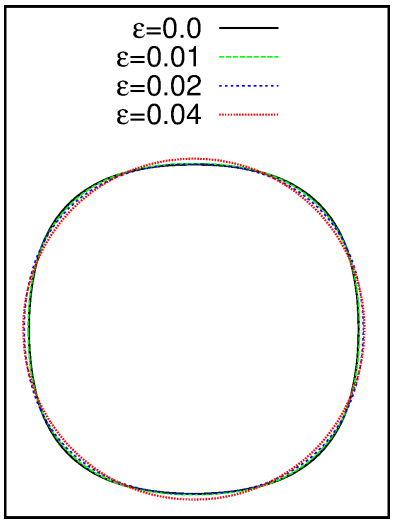

(a)

Figure 3.22: The variation of equilibrium shapes of precipitate as a function of strength of interfacial anisotropy where ε varies from 0 to 0.04 and $A_z = 3.0, t = 1$.

The characterization of change in the precipitate morphology is precisely captured by plotting the shape factor (η) as a function of the strength of elastic anisotropy for a given strength of anisotropy in interfacial energy, which is shown in Fig. 3.23. Here, the shape factor is defined as the ratio of the precipitate size along $< 10 >$ to size along $< 11 >$. The significance of calculating η in this way is that, it determines the precipitate orientation. If $\eta < 1.0$, it implies that the precipitate faces are aligned normal to the elastically soft directions i.e. $< 10 >$ directions and

the anisotropy in elastic energy is the shape determining factor provided $A_z > 1.0$. Similarly, if $\eta > 1.0$, it implies that the precipitate faces preferentially align normal to the $< 11 >$ directions which is determined by the anisotropy in interfacial energy and $\eta = 1.0$ gives a circular shape of the precipitate. Fig. 3.23 depicts a morphology map, which plots the shape factor as a function of the different anisotropy strengths in the elastic energy A_z, while considering different values of anisotropy in interfacial energy ε. While for the case where $\varepsilon \leq 0.02$, there is a critical value beyond which the shape transition occurs from a diamond to a cube, for the larger values of anisotropy in interfacial energy, the equilibrium shape remains diamond like. The map depicts that the morphology of the precipitate corresponding to $A_z = 1.5$ and $\varepsilon = 0.02$ acquires a near circular shape. However, this transition point is a function of the size of the precipitate.

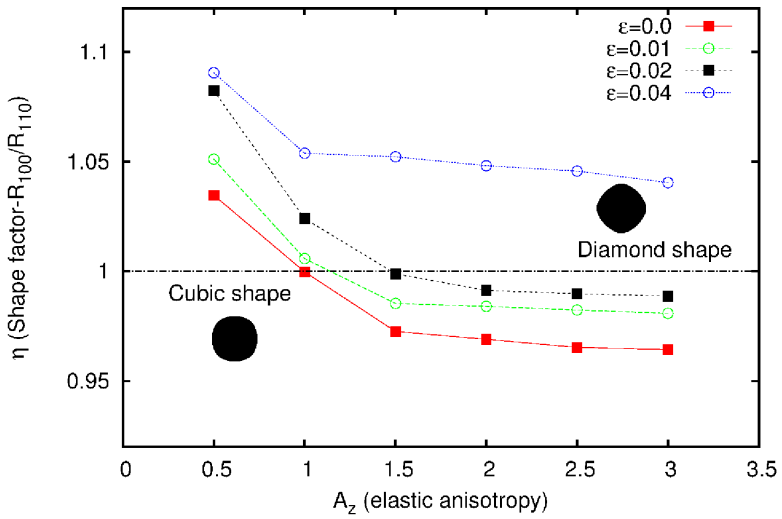

Figure 3.23: Map represents the shape factor (η) as function of A_z for different strengths of interfacial anisotropy, dark horizontal line separates the region between cube(square) like shapes of precipitate and diamond like shapes of precipitates which are characterized by η.

3.2 Equilibrium shapes in 3D

Until now, we have elaborated the calculation of the equilibrium shape of the precipitate in 2D. The phase-field formulation allows for a straightforward extension for prediction of equilibrium precipitate shapes in 3D as well. In this section we describe the results of the equilibrium shapes of the precipitate that form in 3D. Similar to studies in 2D, we derive shape bifurcation diagrams for different choices of elastic energy anisotropy determined by the value of the Zener anisotropy parameter A_z.

3.2.1 Isotropic elastic energy

As the first case, we consider isotropic elastic moduli ($A_z = 1.0$) with dilatational misfit at the interface between precipitate and the matrix ($\epsilon^*_{xx} = \epsilon^*_{yy} = \epsilon^*_{zz} = 0.01$). For this case, we consider the precipitate to be softer than the matrix phase i.e. the inhomogeneity ratio is 0.5 ($\delta = 0.5$).

We begin the simulation with an arbitrary shape as an initial state of a precipitate, e.g. an ellipsoid with an arbitrary aspect ratio, that is the ratio of the lengths of the major and the minor axes are chosen arbitrarily and the precipitate is let to evolve, until the shape factor saturates to a value which represents the equilibrium shape of the precipitate. An exemplary simulation showing the influence of the size is shown in Fig. 3.24, where a precipitate with equivalent radius $R = 30$ ($L = 2.5$) (the radius of an equivalent spherical precipitate) has a spherical shape. With an increase in the size of the precipitate, the infinite-fold symmetry breaks, which eventually gives rise to an equilibrium shape of the precipitate, which is different from the spherical shape. This is shown in Fig. 3.25, where a precipitate with a larger size, i.e. equivalent radius equals $R = 60$ ($L = 5$), acquires different structures than that of the sphere, namely an oblate-type structure which is a flat plate-like shape (Fig. 3.25(a)) or a prolate-type structure (Fig. 3.25(b)) which essentially resembles a needle-like structure. As compared to the 2D case, where there is only one geometric variant beyond the bifurcation point, here we obtain two variants of the precipitate for a given characteristic length, which differ in the total energy.

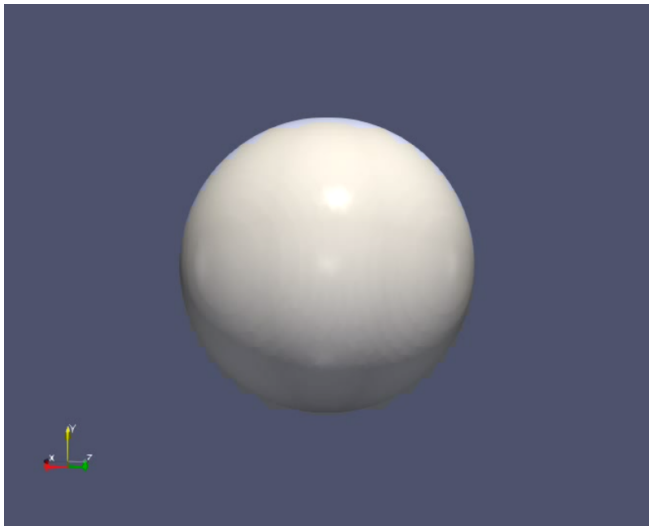

Figure 3.24: Equilibrium shapes of the precipitate as sphere at $A_z = 1.0$, $\delta = 0.5$, $L = 2.5$, with dilatational misfit-strain of 0.01.

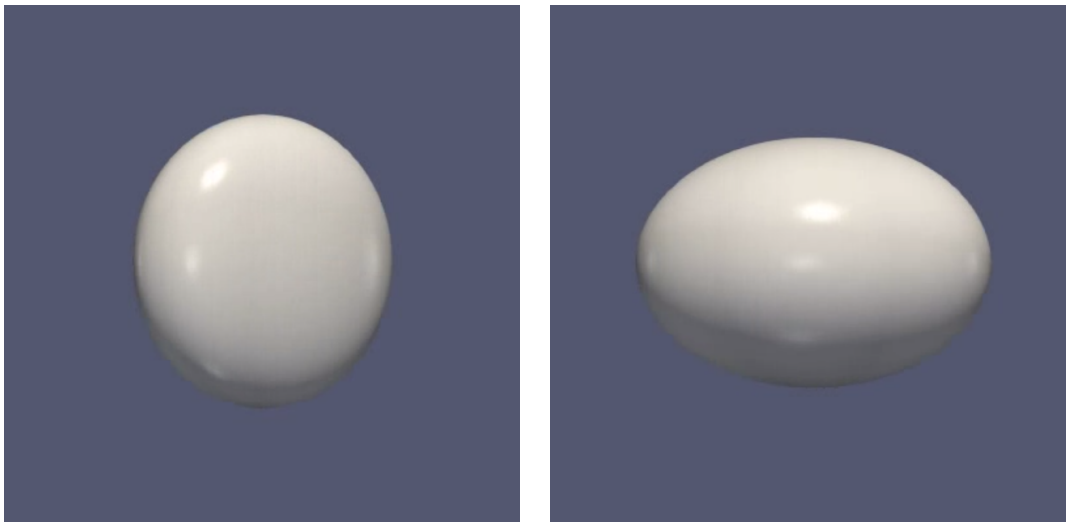

(a) (b)

Figure 3.25: Equilibrium shapes of the precipitate (a) oblate and (b) prolate at $A_z = 1.0$, $\delta = 0.5$, $L = 5.0$, with dilatational misfit-strain of 0.01.

In our simulations we initialize the shapes such that the symmetry breaking occurs along the principal $x-$, $y-$ and $z-$ axes, which is achieved by starting with an appropriate ellipsoid. In this situation, we formulate a shape factorρ in terms of the projections along the major axes (I), which is expressed as $\rho = \dfrac{(I_{001} - I_{010})}{(I_{001} + I_{010})}$, that parameterizes the possible equilibrium shapes. Here, I_{001} represents the sum of the projected length in magnitude(along 001) for any vector that is contained in the equilibrium shape of the precipitate, where every possible vector originating at the center of the precipitate is considered. Thus, for a totally symmetric shape, the measures I_{001} and I_{010} would yield identical values and therefore ρ would be zero. However, as soon as we have symmetry breaking the moments I_{001} and I_{010}, would be unequal and therefore, we would have values different from zero thereby quantifying the extent of bifurcation. Therefore, for oblate discs, where the values I_{100} and I_{010} are equal (for the starting situation that we have considered), while the I_{001} will be lower, thereby leading to a negative value for ρ. Conversely, for the case of a prolate equilibrium shape, we have I_{100} to be larger than either of I_{001} and I_{010} thereby leading to a positive value for ρ. Notice, that we have infinite number of possibitilies for the orientation of the oblate-discs or the prolate rods depending on the starting configuration of the ellipsoids.

Shape bifurcation diagrams derived for different precipitate sizes are depicted in Fig. 3.26. The filled circles on the plot are the lowest energy configurations, whereas the empty circles are the higher energy configurations at that given characteristic length. Thus, below the bi-

furcation point, the precipitates with a spherical shape are the lowest energy configurations. Similarly, beyond the bifurcation point, the precipitate acquires an oblate-like shape which is a stabler configuration than the sphere or prolate-like structures. Between the prolate and the spherical shapes the spheres have a lower energy, until a given size beyond the bifurcation point, after which the prolate shape becomes more stable compared to the sphere. Additionally we access the stability of the spherical shape to small shape perturbations. Here, we find that perturbations of the spherical shape do not lead to symmetric responses, whereby, small oblate perturbations always lead to the formation of oblate-discs as the equilibrium shapes, whereas, prolate perturbations lead to the prolate equlibrium shapes only beyond a particular size that is different from the bifurcation point beyond which the oblate-discs become the most stable morphology. This makes the bifurcation very different from that observed in 2D, wherein, firstly the possible variants are not energetically equivalent, secondly the sphere is unstable to oblate-like perturbations beyond the bifurcation point but stable towards prolate-like perturbations, which is something that is not observed in 2D. Finally, positions of the morphologies with respect to energetic hierarchy do not remain the same all through, i.e, firstly the spheres are the lowest energy configurations below the bifurcation point, after the bifurcation point the oblate-discs have the lowest energy among the three possible structures, followed by the sphere and the prolate, while beyond a particular size the prolate becomes more stable compared to the sphere, while still corresponding to a higher energy compared to the oblate-disc.

3.2.2 Cubic anisotropy in the elastic energy

Anisotropy in the elastic energy is introduced by changing the magnitude of Zener anisotropy parameter (A_z), i.e. if $A_z > 1.0$, $< 100 >$ directions are the elastically softer direction, whereas $< 111 >$ are the harder directions. Similarly, when $A_z < 1.0$, $< 111 >$ are the softer directions. This deviation from the elastic isotropy gives rise to an increase in the number of independent elastic constants. Here, we mainly consider cubic anisotropy in the elastic energy, as it is observed in the microstructures of many alloys, e.g. Ni-based superalloys. We have examined two cases with cubic anisotropy in the elastic energy, i.e. first when $A_z = 3.0$, another is at $A_z = 0.5$. The misfit at the interface is dilatational, i.e. $\epsilon^*_{xx} = \epsilon^*_{yy} = \epsilon^*_{zz} = 0.01$, where the off-diagonal terms are zero.

Firstly, when $A_z = 3.0$, the precipitate is softer than the matrix, i.e. $\delta = 0.5$ with $\mu_{mat} = 125$. With these parameters, simulations are performed as a function of the characteristic length to obtain the equilibrium shapes of the precipitate in 3D. Here, a precipitate with $R = 30$ ($L = 2.5$), acquires a cube-like shape with rounded corners as an effect of cubic anisotropy in

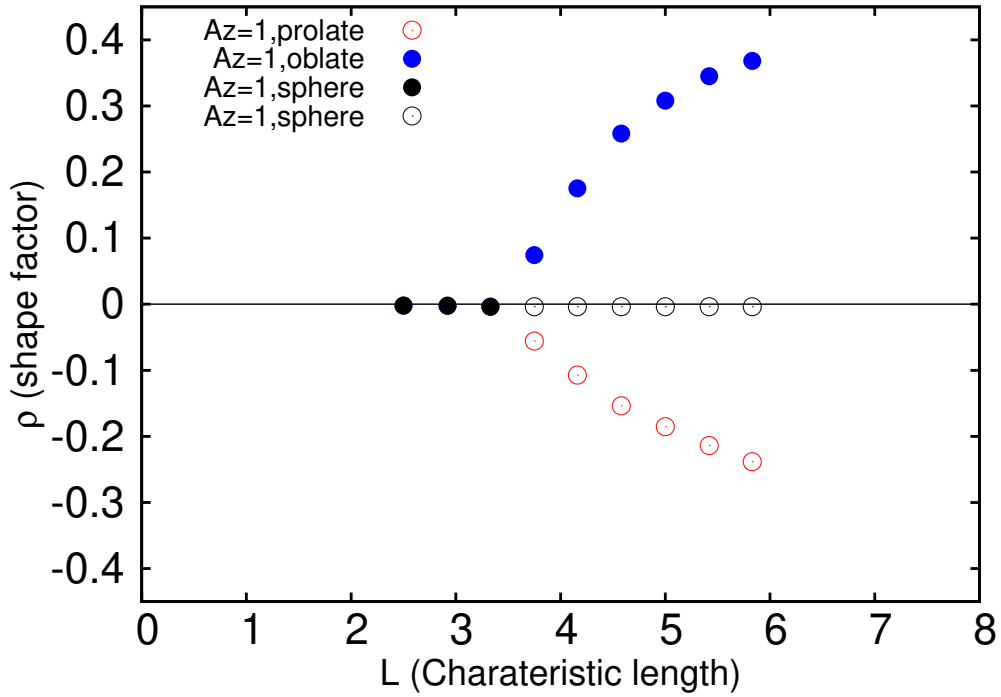

Figure 3.26: Plot depicts the shape bifurcation diagram for $A_z = 1.0, \quad \delta = 0.5$, with dilatational misfit-strain of 0.01 and $\rho = \dfrac{(I_{001} - I_{010})}{(I_{001} + I_{010})}$.

the elastic energy (see Fig. 3.27). The precipitate faces are normal to the $< 100 >$ directions, which are the elastically soft directions retaining the four-fold anisotropy, which is also observed in the microstructures possessing the cubic anisotropy in the elastic energy. In contrast to this, the precipitate with larger size, i.e. $R = 60$ ($L = 5.0$) yields two different equilibrium shapes in 3D as shown in Fig. 3.28. One of the equilibrium shapes is oblate-cuboidal that resembles a flat plate-like structure, whereas for the same characteristic length a second possiblity we find is a prolate-cuboidal shape that resembles a rod-like structure. Here again we plot the shape factor as a function of the characteristic length in order to obtain a bifurcation plot in 3D. We utilize the same definition of the shape factor as in the isotropic case, where the average projected lengths are calculated along the same given directions. As shown in Fig. 3.29, the filled squares represent the lowest energy configuration at that characteristic length, whereas the empty squares correspond to the configurations with higher energies. Thus, the bifurcation plot in 3D, depicts that below the bifurcation point, precipitates with cubic morphologies with rounded corners are the stable configurations ($\rho = 0$). Beyond the bifurcation point, the oblate plate like shape has the lowest energy among the three configurations, while the cube has the second lowest energy until a given size. Beyond this it is the prolate rod like precipitate morphology that has a lower energy compared to the cube, while still corresponding to a higher energy compared to the oblate-plate like morphology. Similar to the isotropic case, the cube has an asymmetric response to the perturbations beyond the bifurcation point, wherein it is stable to prolate perturbations until a given size(the same size where the energy of the sphere becomes higher than the prolate) while all the time being unstable to oblate perturbations.

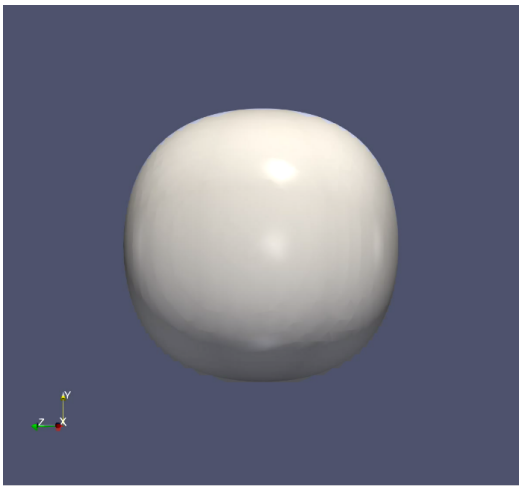

Figure 3.27: Equilibrium shapes of the precipitate as cube at $A_z = 3.0$, $\delta = 0.5$, $L = 2.5$, with dilatational misfit-strain of 0.01.

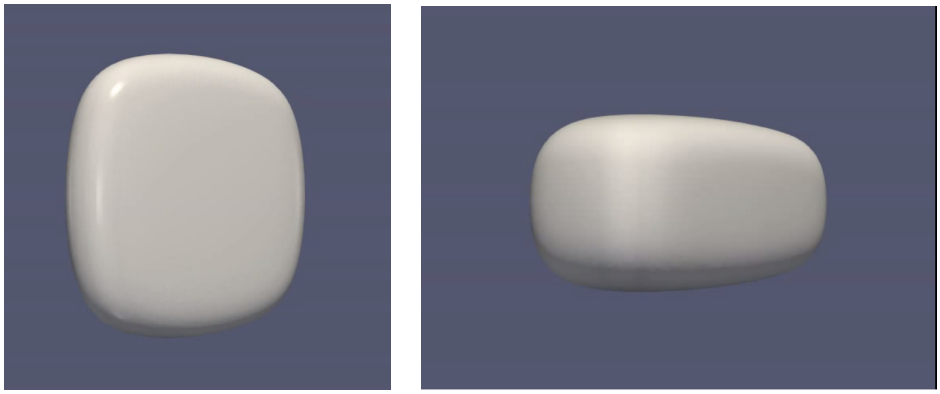

(a) (b)

Figure 3.28: Equilibrium shapes of the precipitate (a) oblate and (b) prolate at $A_z = 3.0$, $\delta = 0.5$, $L = 5.0$, with dilatational misfit-strain of 0.01.

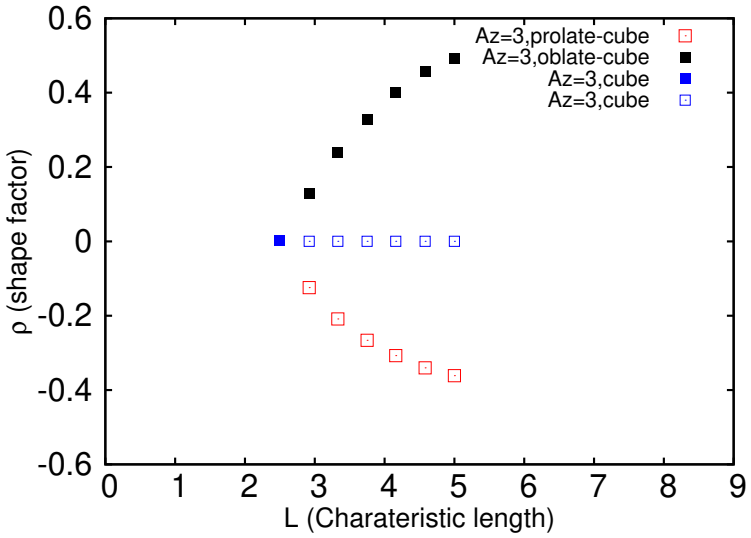

Figure 3.29: Plot depicts the shape bifurcation diagram for $A_z = 3.0$, $\delta = 0.5$, with dilatational misfit-strain of 0.01 and $\rho = \dfrac{(I_{001} - I_{010})}{(I_{001} + I_{010})}$.

Until now we have studied 3D equilibrium shapes for $A_z > 1.0$ i.e. $A_z = 3.0$, where we have seen that the faces of the precipitate align themselves normal to the $< 100 >$ directions. Further, we consider the case of $(A_z < 1.0)$ i.e. $A_z = 0.5$, where $< 111 >$ directions are the softer directions along with a dilatational misfit strain $\epsilon_{xx} = \epsilon_{yy} = \epsilon_{zz} = 0.01$. Thus, the precipitate with smaller size e.g. at $R = 30$ $(L = 2.5)$ acquires an octahedral structure with all the faces of the precipitate aligned normal to the $< 111 >$ directions as shown in Fig. 3.30. As the precipitate size increases, the precipitate loses its symmetry giving rise to multiple variants. Here we will consider two of these variants. In the first variant, the mirror symmetry about one of the {100} planes is retained (see Fig. 3.31(c)) while it is broken about the other two planes in the family i.e (010) and (001). Similarly, among the six possible {110} planes the mirror symmetry is retained about two of them (see Fig. 3.31(d)). This occurs by the stretching of the precipitate along one of the $< 110 >$ directions as shown in Fig.3.31(a) and 3.31(e). The faces of the precipitate in this particular variant are all {111} planes, however they have unequal areas, with four of the faces having smaller and conversely four larger areas than the symmetric octahedral precipitate shape. The second variant we consider is where the precipitate stretches along the $< 111 >$ direction that is depicted in Figs. 3.32(a) and 3.32(d). Here all the {100} mirror planes are lost, while the mirror symmetry is retained for three of the six possible {110} planes, each passing through two of the vertices of the precipitate at a given time as depicted in Fig. 3.32(c). Since, the precipitate variants under consideration are stretched along $< 111 >$ and $< 110 >$ directions, we have derived the normalized shape factors using the projected lengths of the precipitate in these directions in order to quantify the extent of bifurcation for each of the variants. Thus, $\rho_{110} = (I_{101} - I_{10\bar{1}})/(I_{101} + I_{10\bar{1}})$, characterizes the variants stretched along the $< 110 >$ directions. Similarly, the precipitate elongating along $< 111 >$ direction is characterized by a shape factor given by, $\rho_{111} = (I_{11\bar{1}} - I_{111})/(I_{11\bar{1}} + I_{111})$. The bifurcation diagrams for each of these variants is depicted in Fig. 3.33. We note that these are not the only possible variants and multiple possibilities exist depending on the starting configuration of the precipitate. While, we have calculated the energies for some of the possibilities, we find that the variant that is stretched along the $< 111 >$ directions to have the lowest energy and thus the points corresponding to them are marked with filled circles.

3.3 Comparison with experimental results

In this work, our focus is theoretical in extent, however, in this section we make possible connections with microstructures in experiments that may be referred to as equilibrium shapes of precipitates. It is noteworthy that such comparisons are non-trivial as the experimental

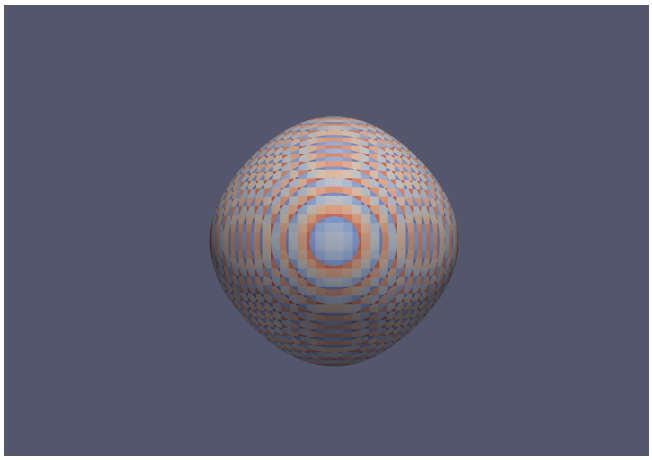

Figure 3.30: Equilibrium shape of the precipitate with characteristic length of $L = 2.5$ at $A_z = 0.5$ with dilatational misfit-strain of 0.01.

conditions giving rise to a particular shape of the precipitate may not be equivalent to the boundary conditions in the simulations. For example, even at very low volume fractions of the second phase, with increase in the precipitate size, the elastic fields around the precipitates may interact with each other that may influence the precipitate size at which symmetry breaking shape transitions are observed. On the contrary, in the simulation the precipitate is isolated in the sense that there is no interaction of elastic fields of the neighboring precipitate. With this disclaimer, we point to certain experimental reports of microstructures that bear similarity to our work.

Fahrmann et al.[110] have studied a series of low volume fraction Ni-Al-Mo alloys, with varying Mo-content. In this paper, the authors report a change in the shapes of the precipitate from a spherical to cubic morphology and a break in symmetry for larger precipitate sizes where cuboidal shapes are observed. The sizes at which the shape transition occurs are reported to be a function of the Mo-content which in turn is thought to influence the effective misfit at the interface. This finding of the authors is qualitatively in agreement with the equilibrium shape transitions obtained in our phase field simulations with changes in the values of the dilatational misfit and strength of cubic anisotropy in elastic energy (see sec 3.1.3).

An aspect of our work is to construct a general framework using which equilibrium shapes of the precipitate with tetragonal misfit at the interface have been computed as a function of different variables such as misfit ratio(t), precipitate size(R) and sign of misfit at the interface (refer Section 3.1.4). We have seen that below the bifurcation point, the shape of the precipitate is elongated diamond like, while with increase in the precipitate size the morphology turns towards a twisted diamond like shape which is also referred to as S-shape precipitates by

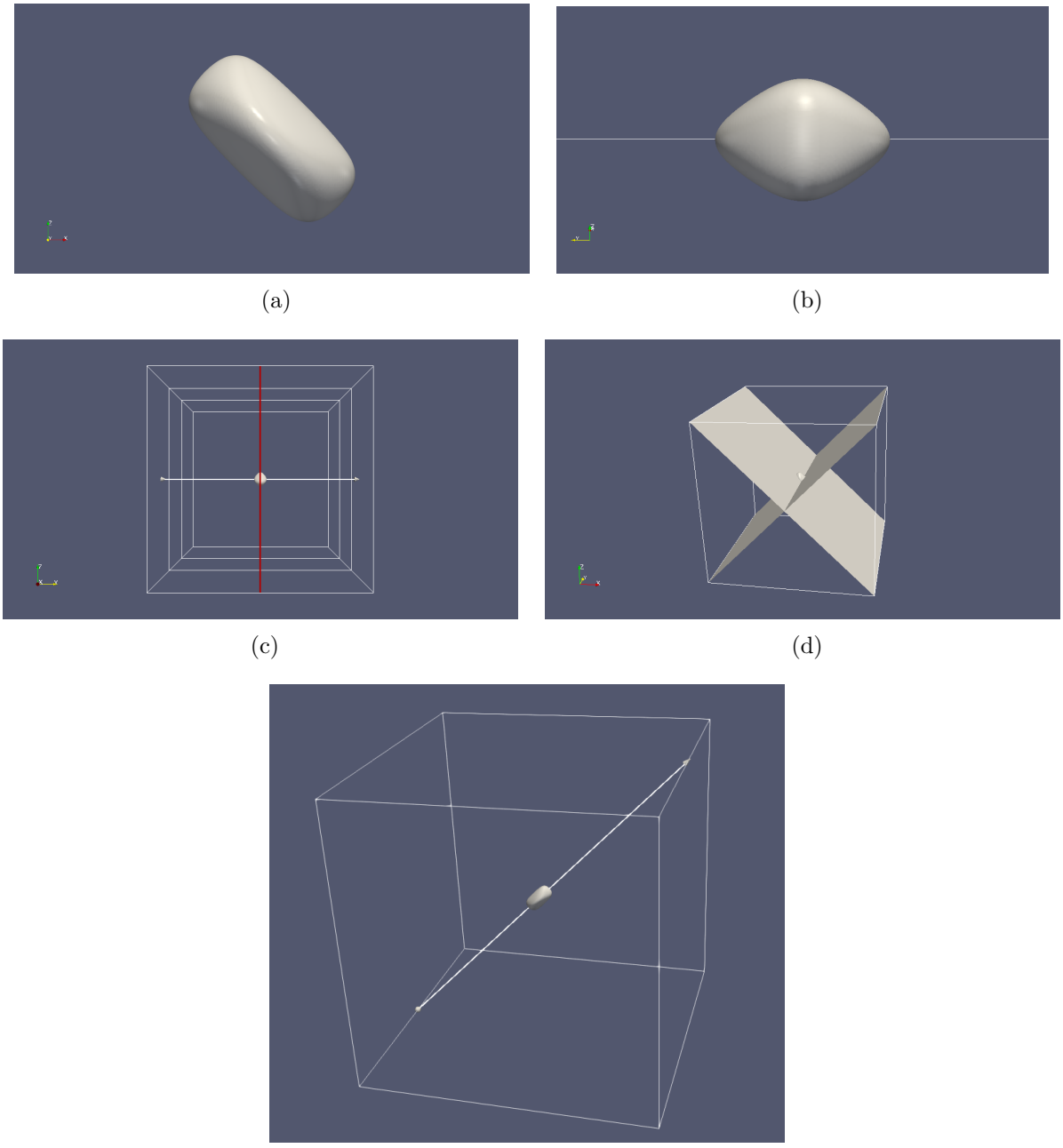

(a) (b)

(c) (d)

(e)

Figure 3.31: Equilibrium shapes of the precipitate (a) aligned along $< 110 >$ direction and (b) zoomed views along $< 110 >$ axis, (c) and (d) show the planes that determine the mirror symmetry of the precipitate across them (e) shows that the precipitate is streched along $< 110 >$ direction.

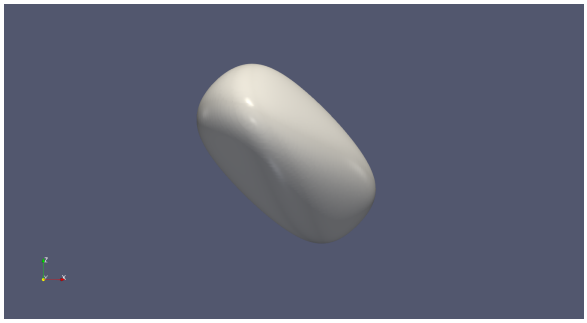

(a)

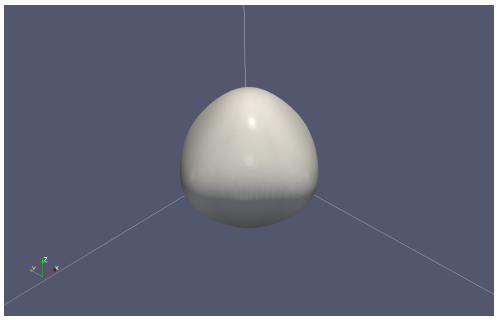

(b)

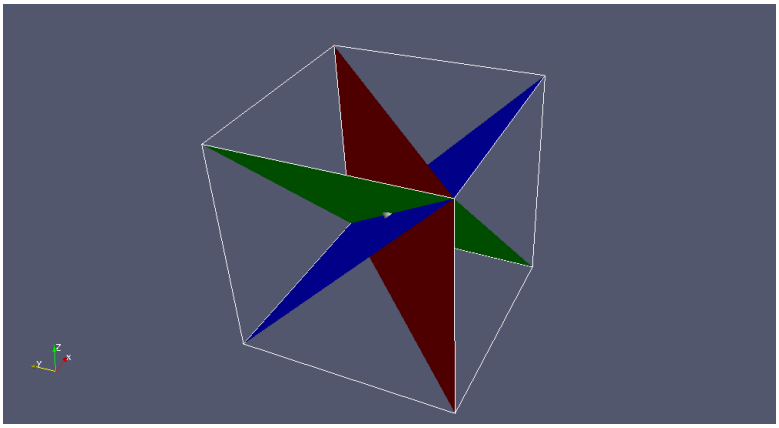

(c)

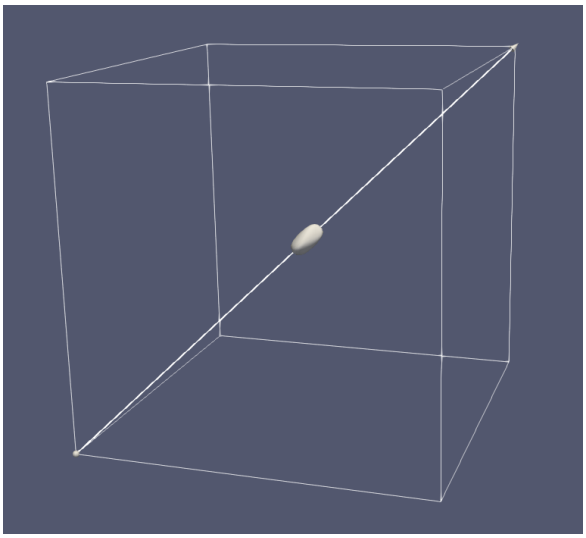

(d)

Figure 3.32: Equilibrium shapes of the precipitate (a) aligned along $< 111 >$ direction and (b) zoomed views along $< 111 >$ axis, (c) shows (110) planes that determine the mirror symmetry of the precipitate across them, (d) shows that the precipitate is streched along $< 111 >$ direction.

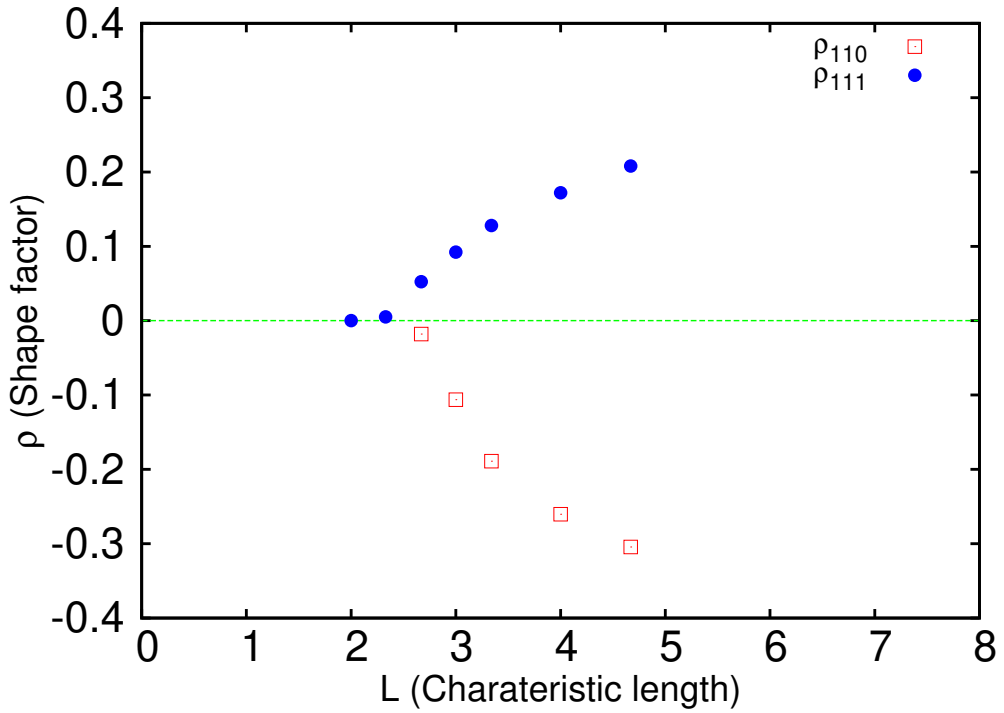

Figure 3.33: Plot depicts the shape bifurcation diagram for $A_z = 0.5$ with dilatational misfit-strain of 0.01 and ρ_{110} and ρ_{111} are the shape factors for the precipitates that aligned along $< 110 >$ and $< 111 >$ directions respectively.

Voorhees et al. [15]. In their study they mention that these S-shapes of precipitates are qualitatively consistent with shape of precipitates observed experimentally in Mg-stabilized ZrO_2 [111]. Lanteri et al.[112] have stated that the ZrO_2 precipitates acquire tetragonal morphologies and associate it with the accommodation of the coherent strains at the interface due to a lattice misfit between the precipitate ($t - ZrO_2$) and the matrix ($c - ZrO_2$).

3.4 Comparison with previous models

In this section, we compare our diffuse-interface model against the previous/available models for the calculation of equilibrium morphologies of precipitates. Here, as a starting point it is useful to analyze the sharp-interface limit of the model as this will enable comparison with other models which are either based on the level-set algorithm, FEM,boundary-integral methods or diffuse-interface methods.

For this, we recall the phase-field evolution equation, written for simplicity for the case of isotropic interfacial energy. We transform this equation into a co-ordinate system that is normal to the interface at a given location where the order parameter is being updated. Thus, the interface normal $\nabla\phi$ can be written as,

$$\nabla\phi = \mathbf{n}\frac{\partial\phi}{\partial n}, \tag{3.12}$$

which upon taking a divergence yields,

$$\nabla^2\phi = \frac{\partial^2\phi}{\partial n^2} + \frac{\partial\phi}{\partial n}\left(\nabla\cdot\mathbf{n}\right). \tag{3.13}$$

Therefore, the transformed equation reads,

$$\tau W\frac{\partial\phi}{\partial t} = 2\gamma W\left(\frac{\partial^2\phi}{\partial n^2} + \frac{\partial\phi}{\partial n}\left(\nabla\cdot\mathbf{n}\right)\right) - \frac{16}{\pi^2}\frac{\gamma}{W}\left(1-2\phi\right) - \frac{\partial f_{el}}{\partial\phi} - \lambda_\beta h'\left(\phi\right). \tag{3.14}$$

The leading order solution for the phase-field profile ϕ^0 satisfies the equation,

$$2\gamma W\frac{\partial^2\phi^0}{\partial n^2}-\frac{16}{\pi^2}\frac{\gamma}{W}\left(1-2\phi^0\right)=0, \tag{3.15}$$

which upon integration once along the interface normal along with the boundary conditions that in the bulk precipitate and the matrix $\dfrac{\partial\phi^0}{\partial n}=0$, gives,

$$\gamma W\left(\frac{\partial\phi^0}{\partial n}\right)^2=\frac{16}{\pi^2}\frac{\gamma}{W}\phi^0\left(1-\phi^0\right), \tag{3.16}$$

the solution to this is also the equilibrium phase-field profile without any driving forces. Along with this the leading order solutions to the stress-strain profiles are determined from mechanical equilibrium conditions, in the limit that the interface thickness tends to zero. Without extensive math and drawing from the results of the phase-field simulations which deliver the stress-strain profiles along the interface normal (see Appendix .A.2), we see that in the limit of vanishing interface thickness, where the values of the properties at the interface and the asymptotic extensions from the bulk on either side onto the interface become the same for the continuous variables and constitute a jump at the interface for the discontinuous variables. Thereby the following conditions will be satisfied,

$$\begin{aligned}\sigma^\alpha_{nn}&=\sigma^\beta_{nn}=\sigma^0_{nn},\\ \sigma^\alpha_{nt}&=\sigma^\beta_{nt}=\sigma^0_{nt},\end{aligned} \tag{3.17}$$

which is also the consistent with the condition for zero traction along the normal, while the strains,

$$\epsilon^\alpha_{tt}=\epsilon^\beta_{tt}=\epsilon^0_{tt}, \tag{3.18}$$

are continuous across the interface. The other components however, are going to exhibit a jump across the interface. These are the same jump conditions we utilize in the tensorial interpolation scheme and are also elaborated in [106]. Using the preceding arguments the leading order phase-field update derives as,

$$\tau W\frac{\partial\phi}{\partial t}=2\gamma W\frac{\partial\phi^0}{\partial n}\left(\nabla\cdot\mathbf{n}\right)-\frac{\partial f_{el}}{\partial\phi}-\lambda_\beta h'\left(\phi\right). \tag{3.19}$$

Additionally, using the sharp-interface limits of the stress and strain profiles, we can also derive the following,

$$\frac{\partial f_{el}}{\partial\phi}=\frac{df_{el}}{d\phi}-\frac{\partial f_{el}}{\partial\epsilon_{nn}}\frac{\partial\epsilon_{nn}}{\partial\phi}-2\frac{\partial f_{el}}{\partial\epsilon_{nt}}\frac{\partial\epsilon_{nt}}{\partial\phi}-\frac{\partial f_{el}}{\partial\epsilon_{tt}}\frac{\partial\epsilon_{tt}}{\partial\phi}. \tag{3.20}$$

Since, in the sharp-interface limit, the strain-component ϵ_{tt} is continuous across the interface the last differential in the preceding equation vanishes, in the limit that the interface thickness becomes zero, thereby, the leading order elastic driving force derives as,

$$\begin{aligned}\frac{\partial f_{el}}{\partial\phi}&=\frac{df_{el}}{d\phi}-\sigma^0_{nn}\frac{\partial\epsilon_{nn}}{\partial\phi}-2\sigma^0_{nt}\frac{\partial\epsilon_{nt}}{\partial\phi}\\&=\frac{d}{d\phi}\left(f_{el}-\sigma^0_{nn}\epsilon_{nn}-2\sigma^0_{nt}\epsilon_{nt}\right).\end{aligned} \tag{3.21}$$

Substituting in the leading-order phase-field update as in Eqn.3.19, we derive,

$$\begin{aligned}\tau W\frac{\partial\phi}{\partial t}=&\,2\gamma W\frac{\partial\phi}{\partial n}\left(\nabla\cdot\mathbf{n}\right)-\frac{d}{d\phi}\left(f_{el}-\sigma^0_{nn}\epsilon_{nn}-2\sigma^0_{nt}\epsilon_{nt}\right)\\&-\lambda_\beta h'\left(\phi\right).\end{aligned} \tag{3.22}$$

Multiplying both sides of the preceding equation with the normal derivative of the leading order phase-field profile, $\dfrac{\partial\phi^0}{\partial n}$, and integrating from inside the bulk precipitate into the matrix in the normal direction, we derive,

$$\begin{aligned}\int_{in}^{out}\tau W\frac{\partial\phi}{\partial t}\frac{\partial\phi^0}{\partial n}dn=&\,2\gamma W\int_{in}^{out}\left(\frac{\partial\phi^0}{\partial n}\right)^2\left(\nabla\cdot\mathbf{n}\right)dn\\&-\int_1^0\frac{d}{d\phi}\left(f_{el}-\sigma^0_{nn}\epsilon_{nn}-2\sigma^0_{nt}\epsilon_{nt}\right)d\phi\\&-\int_1^0\lambda_\beta h'\left(\phi\right)d\phi.\end{aligned} \tag{3.23}$$

3. PHASE-FIELD MODELING OF EQUILIBRIUM PRECIPITATE SHAPES UNDER THE INFLUENCE OF COHERENCY STRESSES

Using the property that, $\frac{\partial\phi}{\partial t}\frac{\partial\phi^0}{\partial n} = -\left(\frac{\partial n}{\partial t}\right)_\phi \left(\frac{\partial\phi^0}{\partial n}\right)^2 = -v_n\left(\frac{\partial\phi^0}{\partial n}\right)^2$, where additionally $\left(\frac{\partial n}{\partial t}\right)_\phi$ is replaced with the normal velocity v_n. Further, $\nabla\cdot\mathbf{n} = -\kappa$ (ignoring changes of curvature along the interface normal) thereby, the following equation is derived,

$$\begin{aligned}-\tau W v_n\int_{in}^{out}\left(\frac{\partial\phi^0}{\partial n}\right)^2 dn = -2\gamma W\kappa\int_{in}^{out}\left(\frac{\partial\phi^0}{\partial n}\right)^2 dn \\ -\left(f_{el}-\sigma^0_{nn}\epsilon_{nn}-2\sigma^0_{nt}\epsilon_{nt}\right)|_1^0 \\ -\lambda_\beta h\left(\phi^0\right)|_1^0.\end{aligned} \tag{3.24}$$

Using, the relation, in Eqn.3.16, we can integrate $\int_{in}^{out}\left(\frac{\partial\phi^0}{\partial n}\right)^2 dn$ as $\int_1^0\left(\frac{\partial\phi^0}{\partial n}\right)d\phi$, or, - $\int_1^0\frac{4}{\pi W}\sqrt{\phi^0\left(1-\phi^0\right)}d\phi^0$, that returns $\frac{1}{2W}$. Combining, the results into the preceding equation, we derive,

$$\frac{1}{2}\tau v_n = \gamma\kappa + (\omega_\beta-\omega_\alpha) - \lambda_\beta, \tag{3.25}$$

where we have assigned, $\omega = (f_{el}-\sigma^0_{nn}\epsilon_{nn}-2\sigma^0_{nt}\epsilon_{nt})$. The preceding sharp-interface limit is a relation between the velocity of advance of the interface front as result of the capillarity forces $\gamma\kappa$ as well as the elastic configurational forces $(\omega_\beta-\omega_\alpha)$, while the Lagrange-parameter λ_β maintains the volume constraint. This is similar to the condition that is derived by Zhao et al.[26, 27], wherein, $(\omega_\beta-\omega_\alpha)$ is nothing but the term $\mathbf{n}\cdot(\Sigma_\beta-\Sigma_\alpha)\cdot\mathbf{n}$, with Σ being the Eshelby momentum tensor $(f_{el}I-\sigma\cdot\nabla\mathbf{u})$[113] ($\mathbf{u}$ is the displacement field), that is used in the work. Similarly, for the condition of equilibrium, v_n is identically zero at all the interface points for which we have,

$$\lambda_\beta = \gamma\kappa + (\omega_\beta-\omega_\alpha). \tag{3.26}$$

Comparing this with the balance condition that is utilized in the work by Thomson and Voorhees [14], to generate the set of integro-differential equations for the solutions of the interface co-ordinates, λ_β is nothing but the difference of the chemical potential between the phases α and β for an uniform diffusion potential. This is also remarked in Schmidt and Gross [18],

although the algorithms of arriving at the interface solutions are different. Also, for the more generic case in the presence of interfacial energy anisotropy, $\gamma\kappa$ should be replaced with $\nabla \cdot \xi$, where ξ is the Cahn-Hoffmann zeta vector [114] as in [14], and which can be also shown in the present phase-field model in the sharp-interface limit. The advantage in our phase-field model is that with just a slightly additional cost of resolving the diffuse-interface model, complicated shapes may be simulated in all dimensions with quite simple discretization techniques than the ones employed in the FEM as well as level-set methods. A more subtle point but noteworthy, is that the term $(\omega_\beta - \omega_\alpha)$ is exactly the same that results from $\dfrac{\partial f_{el}}{\partial \phi}$ in the tensorial interpolation scheme that we describe in the section on the model formulation. The tensorial interpolation exactly utilizes the jump conditions of the stress and the strain profiles in the sharp-interface limit in the interpolation of the elastic energies of the individual phases.

Our present formulation of the phase-field model is in contrast to other contemporary models such as in [30, 38, 115, 31], that use the modified Cahn-Hilliard equation, incorporating for elasticity. In these models, the misfit strains are enslaved as functions of the composition field, along with the values of the stiffness tensor across the interface. The equilibrium morphology is derived by solving the modified Cahn-Hilliard evolution equation until the diffusion potential is the same everywhere. In terms of computational efficiency this is more costly than our model because our evolution equation concerns the update of the order parameter ϕ whose variation, is only over a finite length defined by the diffuse-interface region, that is much smaller in extent compared to the corresponding solution of the composition field over the entire integration domain. Apart from this, there is also a physical difference which stems from the fact that our misfits and stiffness tensors are enslaved to the value of the order parameter ϕ. This implies that the condition of diffusional and mechanical equilibrium may be decoupled as is the situation in the classical Johnson and Cahn model [3] or the numerical FEM models [14, 18, 30, 4, 26], where the composition in the matrix and precipitate satisfy just the Laplace equation with the constraint of the same diffusion potential. However, for the diffuse-interface models that use the composition to parameterize the variation of the misfits and stiffness across the interface, the diffusional and mechanical equilibrium problems become coupled. This entails that, just the diffusion potential μ arising from the chemical part of the free-energy is not constant in the domain, whereas, it is the effective chemical potential $\mu - W\nabla^2 c - \sigma : \delta\epsilon^* h'(c) + \dfrac{1}{2}\delta\sigma : (\epsilon - \epsilon^*(c))\, g'(c)$ that is same everywhere, where $\delta\epsilon^*$ is the difference of the eigenstrain between the phases, while $h(c)$ and $g(c)$ are interpolation functions of the scaled compositions, which smoothly go to fixed values in the bulk phases. $\delta\sigma = \left(C^\alpha - C^\beta\right)(\epsilon - \epsilon^*(c))$, where $\epsilon^*(c)$ is the interpolated eigenstrain. The interpolation functions $h(c)$ and $g(c)$ are typically chosen such that in the bulk their derivatives return zero, that essentially implies that the modification to

the boundary condition of the diffusion potential w.r.t the sharp-interface problem is only at the interface. In the classical Cahn-Hilliard problem without elasticity this variation of the diffusion-potential leads to a grand-potential excess at the interface, which when integrated across the interface determines the interfacial energy γ in the system. In the presence of elastic energies the variation of the diffusion potential in the interface is modified and thereby also the interfacial energy. The interfacial energy therefore scales with the interface width W while being a function of the stress and strain distribution in the interface. Additionally, the interfacial compositions as well as the effective misfits and stiffness will exhibit a change along the interface between the precipitate and the matrix, as the stresses vary with the direction of the normal to the interface. As argued by Leo et al.[30], such modifications scale with the value of the interface width W and in the limit of vanishing interface thickness the sharp-interface problem is retrieved. It is also important to mention that in our model formulation as well, the Khachaturyan type interpolation does yield an interfacial excess which modifies the interfacial energy from the model parameter γ and the deviation scales with W, although the nature of the excess is different. This interfacial excess is removed with the tensorial interpolation as described in this work and in [106] as it respects the precise jump conditions corresponding to the sharp-interface problem. However, given the subtle but important conceptual difference between our model formulation and the other diffuse-interface models, it is presently unclear to us, which amongst the modeling schemes, will yield acceptable errors with respect to the sharp-interface problem, with the larger interface width W.

With regards to the actual situation experimentally, the misfit may truly be a strong function of the composition. The problem is even quite complicated in multi-component alloys, where given the different possible equilibria, the interesting situation is that the choice of the equilibrium compositions, controls the magnitude of the misfit and thereby also the shape. The three-factors are coupled and thereby it is unlikely that the misfit parameterization can be done as a function of the order-parameter as performed in our model presentation or held as a constant value as in the classical analytical and FEM models. Consequently, the mechanical equilibrium and the equilibration of the composition field may need to be performed in a coupled fashion along with the solution to the Allen-Cahn equation for the order-parameter update under the constraint of constant volume. This is similar to the chemo-mechanical model level-set based FEM approach proposed by Zhao [27], which also incorporates interfacial stresses. Extension of our model along these lines particularly for addressing the situations of multi-component alloys is possible.

3.5 Summary

In this chapter, we have presented a phase-field model for the determination of equilibrium morphology of precipitates under coherency stresses in 2D as well as in 3D. Our phase-field model couples the Allen–Cahn dynamics of the order parameter evolution with the constraints of mechanical equilibrium as well as volume constraint. Using this model, we predict the symmetry-breaking transitions and bifurcation diagrams which occur for the shapes of the precipitates as a function of precipitate size, for various combinations of misfits as well as anisotropies in the elastic energy. These predictions are compared against an available analytical solution as well as a sharp-interface numerical method, where we find excellent agreement. In the system with non-dilatational misfits, when misfits along principal directions have the same sign, the shape transition (ellipse to twisted diamond shape) is observed only when $A_z < 1.0$; otherwise the precipitate keeps elongating along the axis of direction with a lower misfit. When misfits along principal directions have opposite signs, the precipitate shape transition occurs irrespective of the magnitude of A_z. Along, with this, we also study the combined influence of elastic and interfacial energy anisotropy both above and below bifurcation. Here, we find that in the presence of interfacial energy anisotropy, there is a continuous change in the shape of the precipitate with size before bifurcation, which is different from the case where there is just elastic anisotropy. We find that the modifications in the shape both above and below the bifurcation point do not change remarkably, although for certain combinations of strengths of the anisotropies in the interfacial and elastic energies a completely isotropic shape may be retrieved below the bifurcation point. We also calculate shape bifurcation diagrams in 3D for different forms of the elastic energy anisotropy and find that they are different in character from that in 2D. The possible variants of the precipitate that form beyond the bifurcation point are not energetically equivalent. Apart from this, we also compare and contrast our model formulation with other diffuse-interface and sharp-interface models. Here, while we discuss that the sharp-interface model descriptions are retrieved in the different diffuse-interface models in the sharp-interface limit, we also highlight the conceptual differences between our model formulation and the other diffuse-interface methods.

Chapter 4

Equilibrium multi-precipitate configurations

In this chapter, we compute and investigate equilibrium configurations that arise when multiple precipitates interact through the elastic fields. For this firstly, we have evaluated systematically the conditions that are amenable for the formation of core-shell type configurations as a function of different parameters. In particular, we investigate the influence of the elastic properties of the precipitates and the matrix on the core-shell formation and enumerate conditions that are suitable for the formation of such structures.

The second case study involves the formation of multi-variant configurations and we investigate the equilibrium structures that arise and comment upon the viability of co-nucleation of such configurations. For this, we study two symmetry-breaking transitions, the first in which tetragonal precipitates are in equilibrium with a cubic matrix, and the second in which an isotropic matrix is in equilibrium with three orthorhombic variants.

4.1 Formation of core-shell structures

4.1.1 Model parameters

For the first study on the formation of core-shell microstructures, we will limit ourselves to the case of dilatational misfit strains in two dimensions and cubic symmetry for both the precipitate and the matrix phases. While all the elastic properties of the precipitate and the matrix influence the interaction between the precipitates, in this study, we will investigate the influence of the elastic anisotropy, misfit sign and inhomogeneity in the shear moduli on their role in the formation of core-shell microstructures. Additionally, we vary the interfacial energy

of all the interfaces and examine its influence on the formation of these structures. For all our simulations, we have utilized a two-dimensional system of precipitates embedded in a matrix, with a lattice mismatch at the interface that is coherent. Domain boundaries follow periodic conditions.

The stiffness used in the system can be generically defined in the following manner, where we use the commonly used short-hand notation for the non-zero stiffness components, $C_{11} = C_{1111}$, $C_{22} = C_{2222}$, $C_{12} = C_{1122}$ and $C_{44} = C_{1212}$, where additionally $C_{11} = C_{22}$ because of symmetry considerations. Thereafter, these terms can be derived in terms of the known material parameters, that are the Zener anisotropy (A_z), Poisson ratio (ν) and shear modulus (μ) and can be written as,

$$C_{44} = \mu, \quad C_{12} = 2\nu\left(\frac{C_{44}}{1-2\nu}\right), \quad C_{11} = C_{12} + \frac{2C_{44}}{A_z}. \tag{4.1}$$

We use a non-dimensionalization scheme where the energy scale is set by the interfacial energy scale $1.0 J/m^2$, and division by the scale of the shear modulus $1 \times 10^9 J/m^3$ yields a length scale $l^* = 1$nm. In the results, hence all the parameters will be reported in terms of non-dimensional units. Unless otherwise specified, all results are produced with $\nu_{ppt} = \nu_{mat} = 0.3$ and A_z varies from 1.0 to 3.0.

4.1.2 Necessary and sufficient condition for the formation of core-shell structures

In order to form a core-shell structure (given two precipitates α, β and the matrix δ) one of the strongest conditions one can expect is the presence of a solid-state wetting condition. This implies that when the interfacial energies ($\sigma_{\alpha\beta}, \sigma_{\beta\delta}, \sigma_{\alpha\delta}$) satisfy the condition $\sigma_{\alpha\delta} + \sigma_{\alpha\beta} < \sigma_{\beta\delta}$, the formation of a $\beta-$ core and $\alpha-$ shell would be expected as this would cause the elimination of the $\beta - \delta$ interface whose magnitude is larger than the sum of the interfacial energies of the other two possible interfaces. Therefore, we set out to test the requirement of this condition for the formation of core-shell configurations. For this, we first compute the interfacial energies of the different interfaces in our phase-field model. We perform this computation by letting pairs of phases equilibrate in one-dimension (Fig. 4.1) and using the equipartitioning relation, compute the interfacial energy for the corresponding interface as twice the gradient energy contribution that is measured using a numerical integration across the equilibrated interface. This is required because there is a contribution from the bulk elastic energy density to the interfacial energy excess that needs to be accounted for and an analytical solution for the modified phase-field

profiles is not easily derived. In order to determine the conditions where the core-shell structure

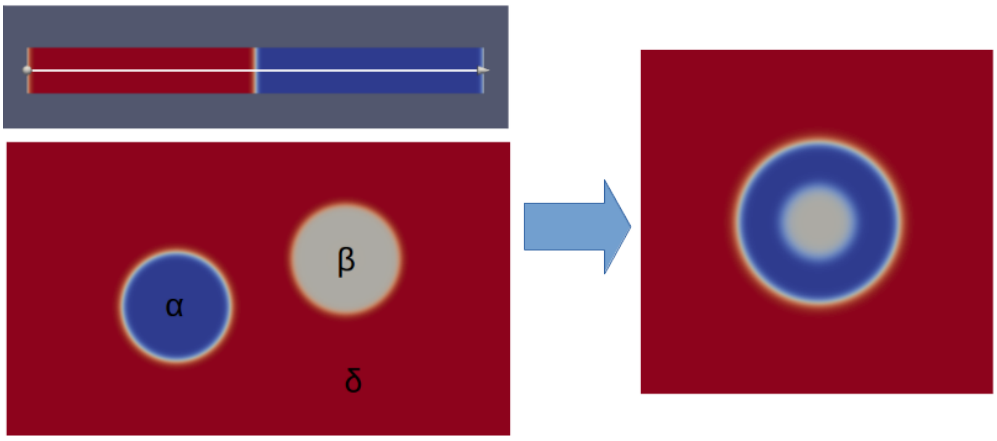

Figure 4.1: Schematic showing one dimensional profile of phase interface and core-shell microstructure.

will form, we vary the magnitude of interfacial energy of the $\beta - \delta$ and the $\alpha - \beta$ interfaces by changing the value of the parameter γ_β in the free-energy functional, all the while retaining the interfacial energy of the $\alpha - \delta$ interfaces. Further, we perform this variation for varied elasticity conditions, where we change, the anisotropy, inhomogeneity ratio and the nature of the misfit strains with the matrix. Additionally, we perform this variation starting with the initial radius of the precipitates as $R_\beta = 20$ and $R_\alpha = 40$, that ensures the availability of enough volume for the engulfment of the $\beta-$ phase by the $\alpha-$ phase. We note that this latter condition is a numerical constraint that is brought about by the necessity to resolve a finite interface thickness in the phase-field model. Therefore, for volumes where the thickness of the shell would become comparable to the interface thickness would be numerically constrained, and we would observe incomplete engulfment. However, this would not be a true reflection of the thermodynamic property of the system. In order to avoid this condition therefore, we have chosen the volume of the engulfing phase about four times that of the volume of the precipitate that forms the core.

The first set of simulations that we perform are for the case where both the precipitates have the same sign of misfit-strain matrices and are both softer than the matrix with an inhomogeneity ratio of 0.5. For the case where the elastic energy is isotropic, the results are depicted in Fig. 4.2(b), where it is observed that with increase in the magnitude of the parameter γ_β, at a certain stage when the condition $\sigma_{\alpha\delta} + \sigma_{\alpha\beta} < \sigma_{\beta\delta}$ is satisfied, it leads to the formation of a core-shell structure. Similarly, for the case where the elastic energy is anisotropic, Fig. 4.2(a), the engulfment occurs for conditions where the solid-state wetting condition is satisfied. In the

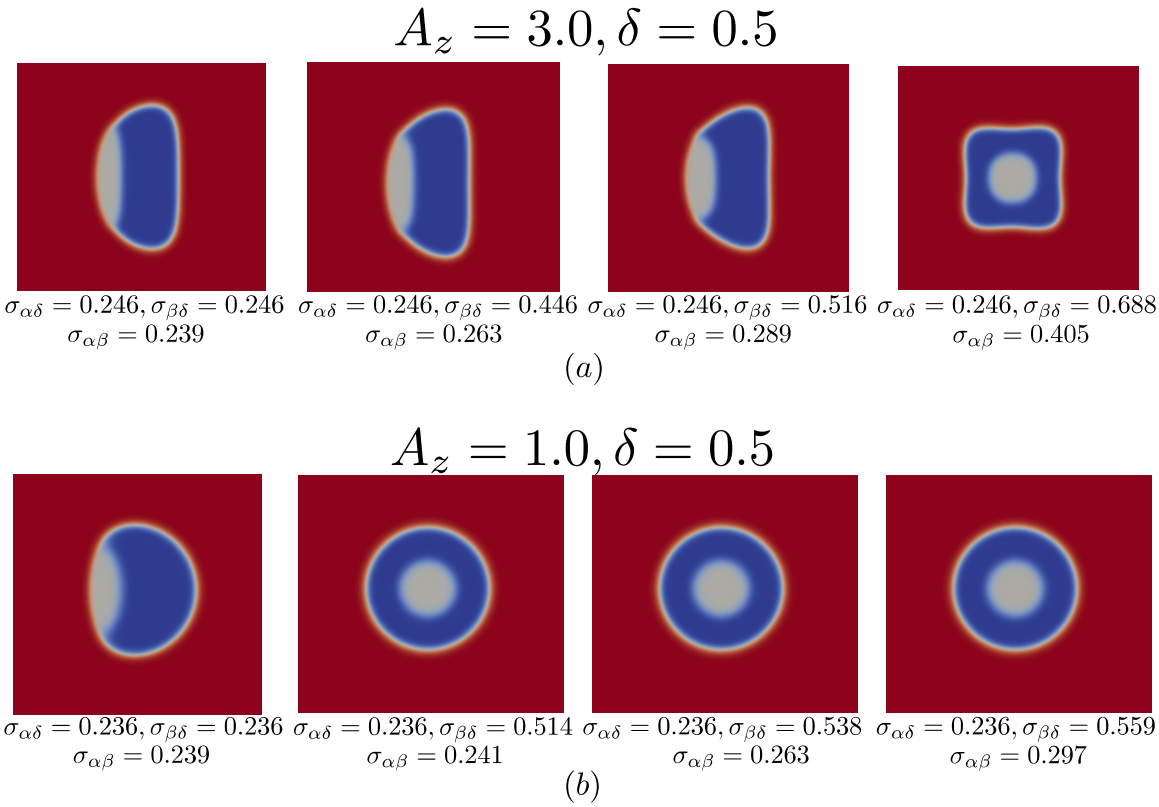

Figure 4.2: Two-precipitate configuration with (a) $A_z = 3.0$ above and (b) $A_z = 1.0$ below, $R_\alpha = 40$, $R_\beta = 20$, $\delta = 0.5$, with same sign of the misfit-strain matrices of the precipitates.

second set of simulations, we choose opposite signs for the strains in the dilatational misfit-strain matrices corresponding to the two precipitates, while we vary the interfacial energies of the $\beta-\delta$ and $\alpha-\beta$ interfaces again by changing the γ_β parameter in the free-energy functional. We perform the simulations again for the case of isotropic and anisotropic elastic energies for the condition where the precipitates are softer than the matrix with an inhomogeneity ratio of δ =0.5. The results are portrayed in Fig. 4.3(a) and Fig. 4.3(b) respectively for the anisotropic and the isotropic elastic energies, where again we find that the conditions for which the core-shell forms also correspond to the case where the solid-state wetting condition is satisfied. Lastly,

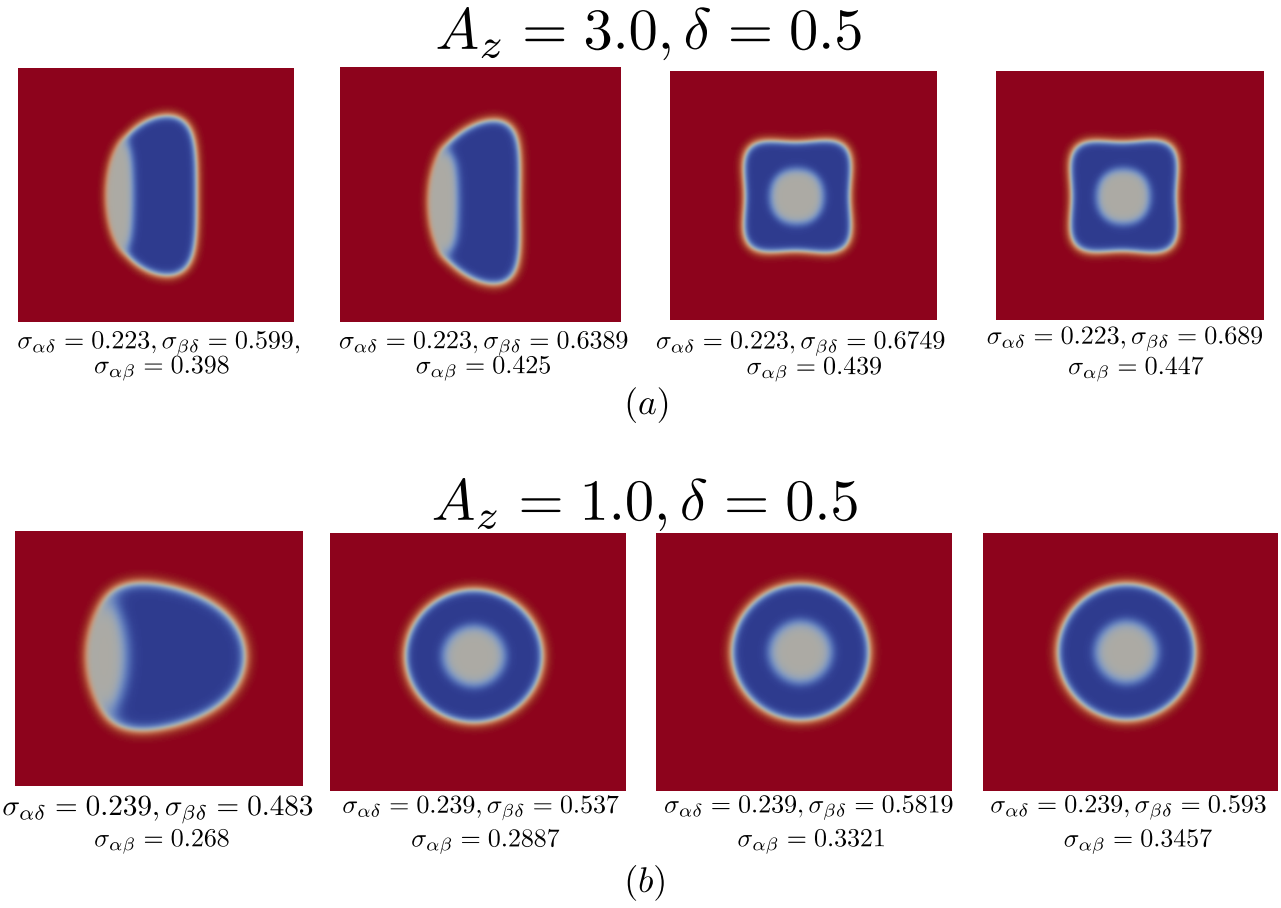

Figure 4.3: Two-precipitate configuration with (a) $A_z = 3.0$ above and (b) $A_z = 1.0$ below, $R_\alpha = 40$, $R_\beta = 20$, $\delta = 0.5$, with opposite sign in misfit-strain matrices of the precipitates.

we also perform simulations with different combinations of inhomogeneity ratios and signs of the misfit-strain matrices for the precipitates. For each such combination, we have verified that as long as the wetting condition is satisfied, the core-shell structure is formed. Conversely,

for each combination of inhomogeneity and misfit-strain matrix, one can create non-wetting conditions by appropriately choosing the parameters $\gamma_\alpha, \gamma_\beta, \gamma_\delta$ in the functional. Some of the results from the non-wetting conditions for such situations are depicted in Fig.4.4. Therefore,

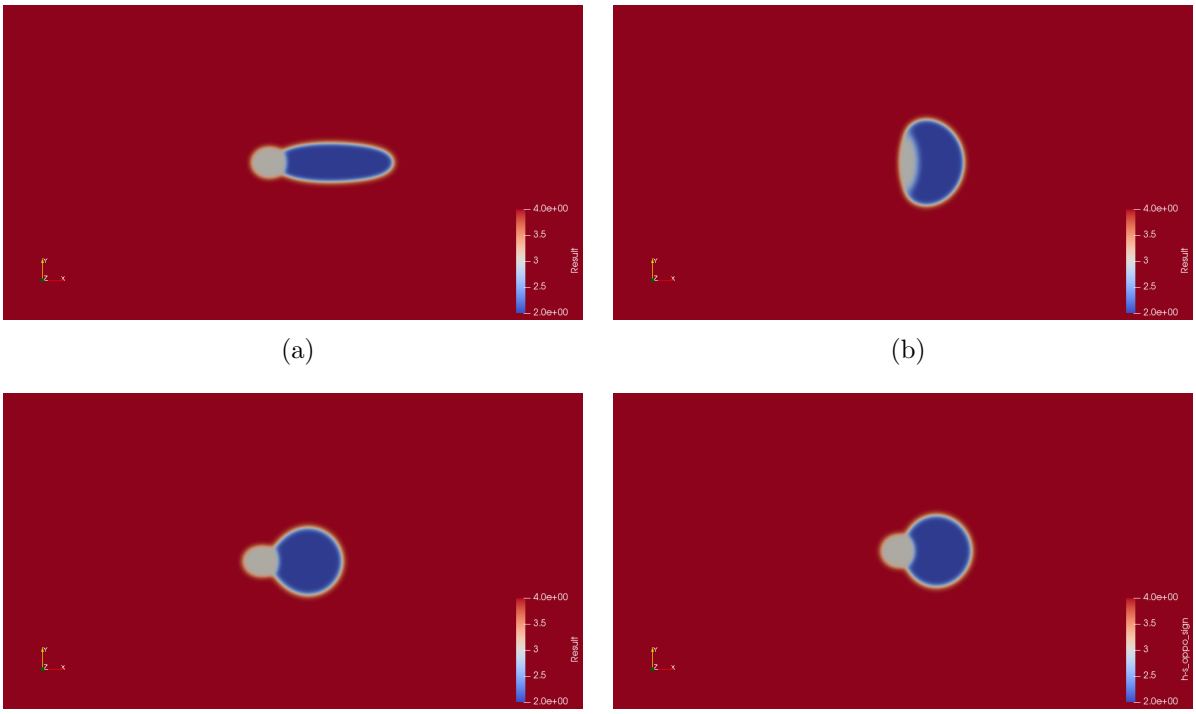

Figure 4.4: The interactions between two precipitates with non-wetting condition where there is no formation of core-shell structure (a) $\epsilon_{ij}^{*\alpha} = \epsilon_{ij}^{*\beta}, \delta_\alpha = \delta_\beta = 0.8$, (b) $\epsilon_{ij}^{*\alpha} = -\epsilon_{ij}^{*\beta}, \delta_\alpha = \delta_\beta = 0.8$, (c) $\epsilon_{ij}^{*\alpha} = \epsilon_{ij}^{*\beta}, \delta_\alpha = 0.8, \delta_\beta = 1.2$ and (d) $\epsilon_{ij}^{*\alpha} = -\epsilon_{ij}^{*\beta}, \delta_\alpha = 0.8, \delta_\beta = 1.2$.

from the simulation results, we can conclusively conclude that the core-shell morphology would form, if and only if the wetting condition is satisfied. The question, therefore remains, as to the role of the elastic properties on the formation of the core-shell morphologies. In the following, we argue that the role of elasticity manifests itself through modifying the interaction between the two disjoint precipitates, i.e. our hypothesis is that for situations where there exists an attractive interaction of the precipitates would lead to the precipitates approaching each other in a larger ensemble of precipitates, and if the wetting condition is satisfied for the given choice of interfacial energies, one would observe large scale formation of core-shell microstructures in the experiments. Here firstly we have the results as shown in Fig.4.5, that for the case of dilatational misfit-strain matrices, two precipitates interact only if there is anisotropy in the elastic energy or there is inhomogeneity in the shear moduli between the precipitate and the matrix. Therefore,

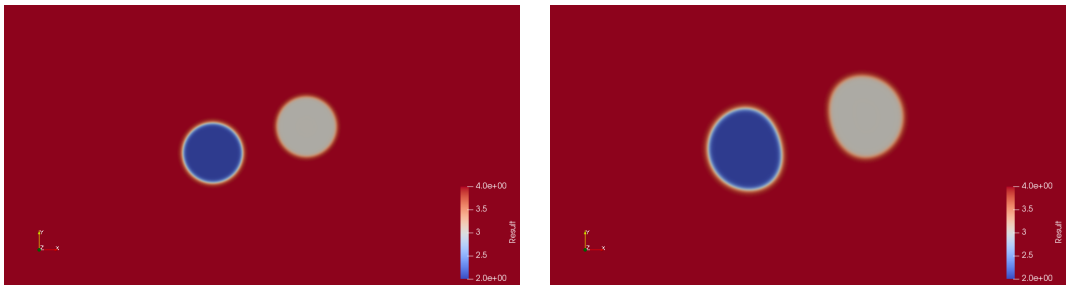

(a) (b)

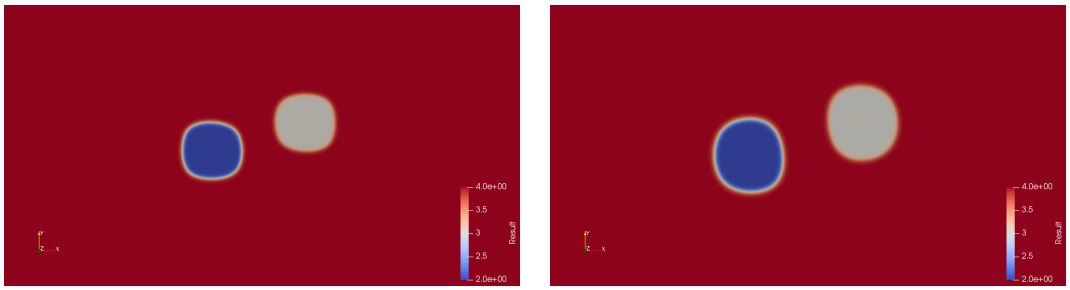

(c) (d)

Figure 4.5: The interactions between two precipitates as a function of different strength of elastic anisotropy and inhomogeneity ratio (a) $A_z = 1.0$, $\delta = 1.0$, (b) $A_z = 1.0$, $\delta = 0.5$, (c) $A_z = 3.0$, $\delta = 1.0$ and (d) $A_z = 3.0$, $\delta = 0.5$ for the dilatational misfit of 0.005.

Inhomogeneity ratio (δ)	Sign of misfit strain	Nature of interaction
$\delta_\alpha = \delta_\beta = 0.8$	$\epsilon_{ij}^{*\alpha} = -\epsilon_{ij}^{*\beta}$	attractive
$\delta_\alpha = \delta_\beta = 0.8$	$\epsilon_{ij}^{*\alpha} = \epsilon_{ij}^{*\beta}$	attractive
$\delta_\alpha = \delta_\beta = 1.2$	$\epsilon_{ij}^{*\alpha} = -\epsilon_{ij}^{*\beta}$	repulsive
$\delta_\alpha = \delta_\beta = 1.2$	$\epsilon_{ij}^{*\alpha} = \epsilon_{ij}^{*\beta}$	repulsive
$\delta_\alpha = 0.8, \delta_\beta = 1.2$	$\epsilon_{ij}^{*\alpha} = -\epsilon_{ij}^{*\beta}$	attractive
$\delta_\alpha = 0.8, \delta_\beta = 1.2$	$\epsilon_{ij}^{*\alpha} = \epsilon_{ij}^{*\beta}$	attractive

Table 4.1: List of the interactions between the precipitates for different conditions.

we have studied the elastic interactions for different choice of elastic properties corresponding to the presence of either inhomogeneity or anisotropy in the elastic energies, by performing simulations where we place the two precipitates apart by a fixed distance and plot the change in the position of the centroids as a function of time. Based on the results that are depicted in Fig.4.6 and the measurements of the centroid positions as a function of time in Fig.4.7, we can conclude the following interactions between the precipitates based on their elastic properties, that are listed in Table 4.1. Therefore, the condition where both precipitates are harder than the matrix and having the same signs of the misfit strain matrices with respect to the matrix have the most repulsive interaction whereas the case where the precipitates are soft and have opposite signs in the dilatational misfit-strains have the most attractive interaction. Based on this, we hypothesize, that in the latter situation one would expect to observe a statistically larger set of core-shell microstructures in the experiments compared to the other conditions. Additionally, we have also performed calculations for the total energy of the system, for the cases where the interactions are repulsive, comparing situations where the precipitates are disjoint, to the case where the precipitates form an interface. We find that the total energy of the system is lower in the former, that also implies that a co-nucleation of the precipitates with the latter configuration is seemingly unlikely from an energetic viewpoint. Therefore, even for situations where the solid-state wetting conditions are satisfied, core-shell microstructures in such systems would be rare, given that the precipitates would not come in contact for the manifestation of the wetting phenomenon that would give rise to the core-shell formation. Hence, the observation of core shell formation in experiments is dependent on the inhomogeneity ratios and the misfit-strain matrices of the precipitates. While, the present discussion is for isotropic situations, a similar conclusion may also be made for anisotropic elastic energies, in terms of the influence of the inhomogeneity ratios and the misfit-strain matrices on the elastic interactions.

Our results seem to be contrary to what is reported by Lee[61, 62], who perform simulations using the discrete atom method(DAM)[116] and determine conditions for which core-shell

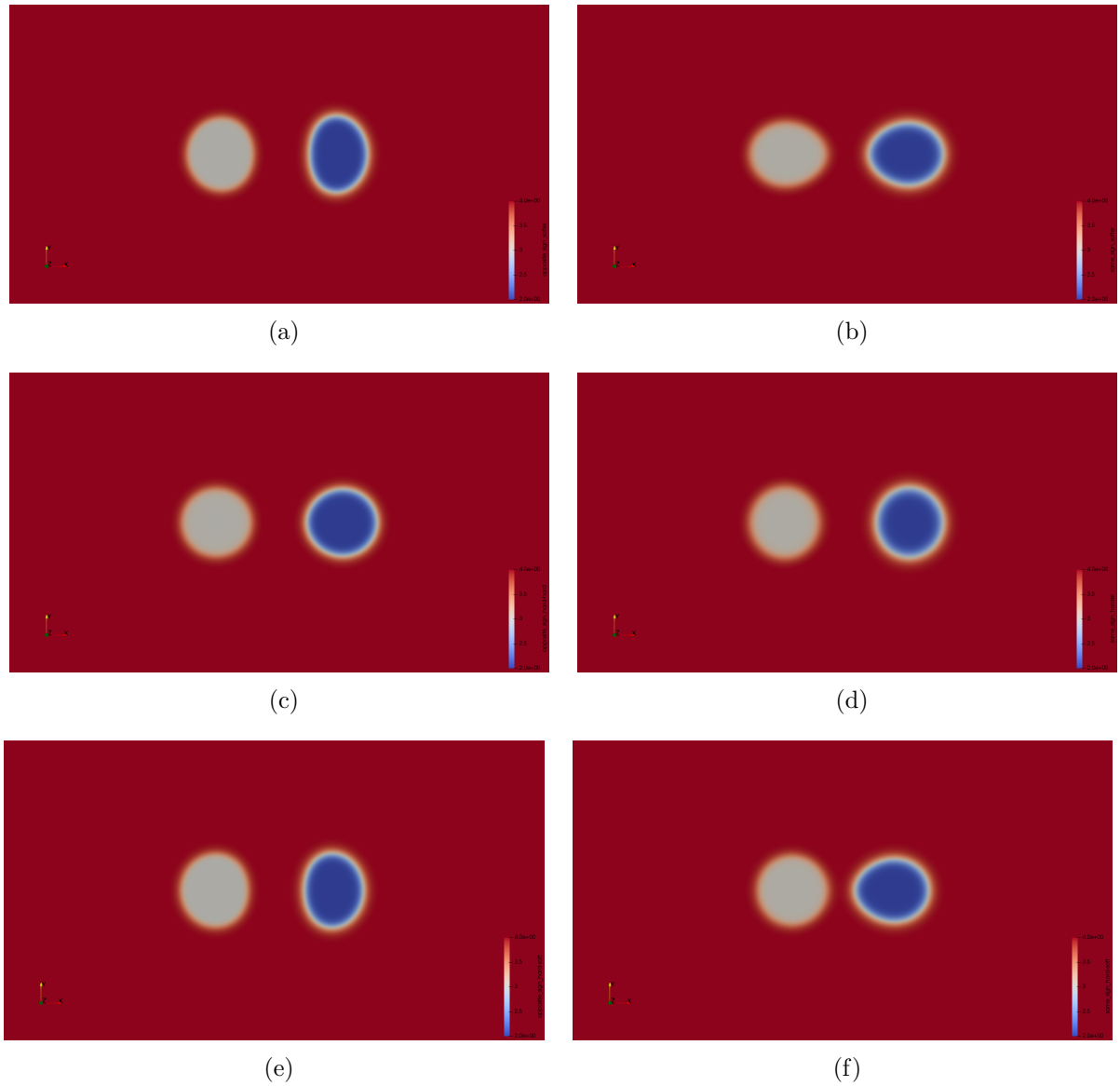

(a) (b) (c) (d) (e) (f)

Figure 4.6: The interaction between two precipitates as a function of varying inhomogeneity ratio and the nature of misfit-strain (a) $\epsilon_{ij}^{*\alpha} = -\epsilon_{ij}^{*\beta}, \delta = 0.8$, (b) $\epsilon_{ij}^{*\alpha} = \epsilon_{ij}^{*\beta}, \delta = 0.8$, (c) $\epsilon_{ij}^{*\alpha} = -\epsilon_{ij}^{*\beta}, \delta = 1.2$, (d) $\epsilon_{ij}^{*\alpha} = \epsilon_{ij}^{*\beta}, \delta = 1.2$, (e) $\epsilon_{ij}^{*\alpha} = -\epsilon_{ij}^{*\beta}, \delta_\alpha = 0.8, \delta_\beta = 1.2$, (f) $\epsilon_{ij}^{*\alpha} = \epsilon_{ij}^{*\beta}, \delta_\alpha = 0.8, \delta_\beta = 1.2$.

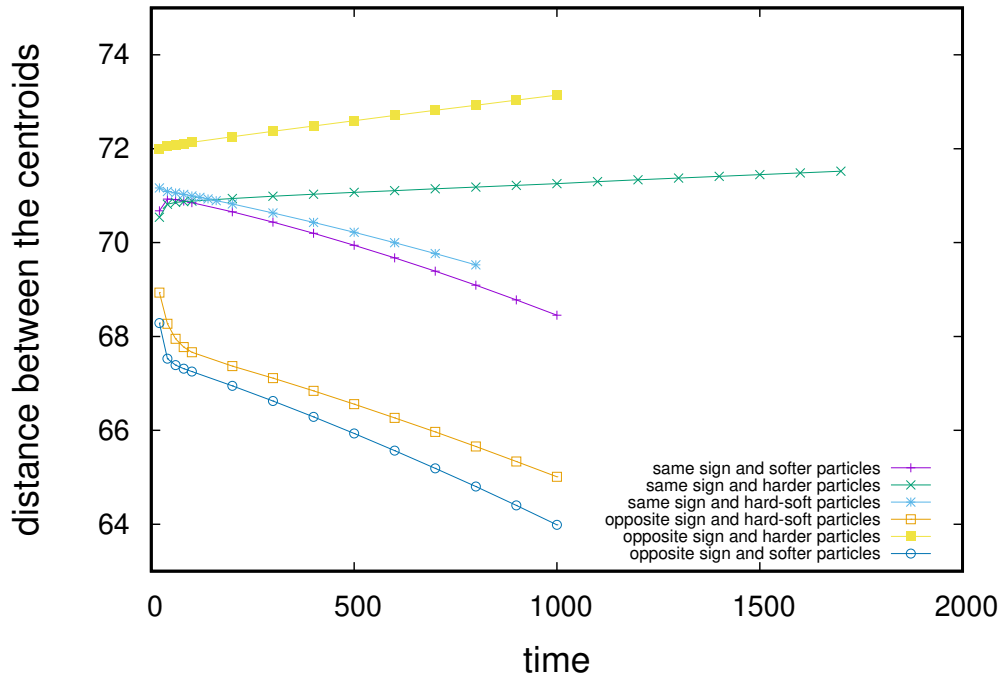

Figure 4.7: Change in the distance between centroids of the precipitate with simulation time.

structures form. Lee claims that even for the case where the interfacial energies do not satisfy the wetting conditions, there exist combinations of elastic misfit strains and inhomogeneity ratios that can lead to the formation of the core-shell structures. In the following, we argue, that this is due to a possible misrepresentation of the actual interface excess operating in the DAM model. In the DAM model as reported in [61] the interaction between the atoms is represented using a Hookean formulation. The atoms at the interface are distinguished from those in the bulk phases as those with unlike nearest neighbors and are attributed additional energies corresponding to the interfacial energy per atom as well as different elastic properties such as the spring constant k_{ij} and stress-free atomic separations a_{ij}. While the interfacial energy per atom is based on the number of unlike bonds on a given lattice, the elastic parameters are determined as an average of the value in the two phases. In our opinion, this particular assumption with regards to the elastic behavior of the interface atoms is quite arbitrary and causes the interface atoms to posess non-homogeneous stress fields as admitted by the author (Fig.4 in [61]). We believe that since the stress fields at the interface are different from a natural homogenization of the bulk stress-fields as depicted in the Eschelby solution, this should lead to a surface energy excess. This can be understood physically as well, that since the interfacial atoms behave differently in terms of their elastic response with respect to the atoms in the bulk phases, the

bulk elastic energy density in the Hamiltonian must contribute to the interfacial energy excess over and above that assumed from the parameter E_i^S that determines the interfacial energy per atom. The manifestation of this error is somewhat apparent in the presentation of the results, (see Fig.1 in [61]). While in the case where elasticity is absent, the results of the authors match with the shapes corresponding to the Wulff-construction with correct angles at the tri-junction, however, for all the cases where elasticity is present, the angles seem different from 120°which is a clear indication that the interfacial energies are modified. This is also evident in a separate article [62], where the authors study shape bifurcation in an isotopic system, of a soft precipitate embedded in a harder matrix. Fig.3 in [62] is quite noteworthy where the threshold size beyond which shape bifurcation occurs in the model is different from the value derived using the Johnson-Cahn theory [3] by approximately 29%(R_c=7a from Johnson-Cahn and R_c=9a from Lee,DAM[62]). A possible reason could again be a misrepresentation of the actual interface excess, where the contribution due to the incorrect homogenization of the elastic properties of the interface atoms leads to an increase in the effective surface energy thus increasing the critical size beyond the theoretical value from the theory of Johnson and Cahn[3]. Since, the core-shell microstructure involves three different interfaces, our opinion is that in the DAM model as reported by Lee[61, 116], the effective interface energies must have different contributions from the Hookean part of the Hamiltonian corresponding to the different elastic properties of the bulk phases. Due to this a correct interpretation or comparison with our results is seemingly unlikely without the evaluation of the effective energetic excess of each of the interfaces in the DAM model.

4.2 Multivariant configurations of the precipitates

In the previous section, we have depicted the necessary conditions for the formation of the core-shell type microstructures as a function of different parameters. Here, in this section, we will study how a multivariant configuration forms from a cluster of two or more precipitates as a function of anisotropy in misfit-strain matrices of different precipitates. For such a study we choose two different symmetry-breaking transitions, the first in which tetragonal precipitates are in equilibrium with a cubic matrix, whereas in the second case an isotropic matrix is in equilibrium with multiple orthorhombic variants.

4.2.1 Cubic–tetragonal transformation

In the first case, i.e. cubic to tetragonal transition, the cubic matrix yields two tetragonal variants of the precipitates. Each of these variants are enslaved to their own misfit-strain matrices, where one of the misfit-strain matrix ($\epsilon_{ij}^{*\beta}$) is rotated by 90^0 with respect to the base i.e. $\epsilon_{ij}^{*\alpha}$. These misfit-strain matrices are shown as follows:

$$\epsilon_{ij}^{*\alpha} = \epsilon_{xx}^{*} \begin{bmatrix} 1 & 0 \\ 0 & t \end{bmatrix}, \quad \epsilon_{ij}^{*\beta} = \epsilon_{xx}^{*} \begin{bmatrix} t & 0 \\ 0 & 1 \end{bmatrix},$$

where t is the strength of anisotropy in the misfit-strain matrix, which is given as $t = \epsilon_{yy}^{*}/\epsilon_{xx}^{*}$. In this t and ϵ_{xx}^{*} assume values of 0.5 and 0.005 respectively. The variants elongate along the lower misfit principal direction. For $A_z = 3.0$, misfit-strain ratio $t = 0.5$ and a shear modulus

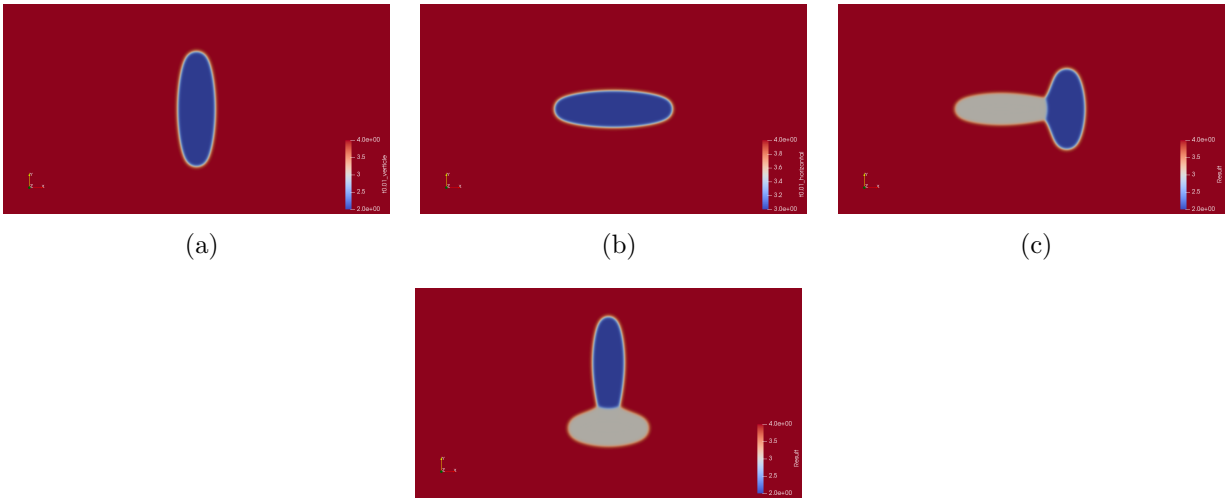

(a) (b) (c)

(d)

Figure 4.8: Equilibrium configurations of variants at $A_z = 3.0, t = 0.5, \mu = 1400$, (a) vertical and (b) horizontal variants of the precipitate, (c) and (d) are the two-variant configurations with different arrangement of the precipitates.

$\mu = 1400$ with no inhomogeneity in the phases i.e. $\delta = 1.0$, we can therefore derive two possible equilibrium variant structures. Accordingly, the first rotational variant enslaved to $\epsilon_{ij}^{*\alpha}$ acquires a vertically elongated shape, which is shown in the Fig. 4.8(a), while the other variant with a misfit-strain matrix $\epsilon_{ij}^{*\beta}$ has a horizontally elongated equilibrium structure as shown in Fig. 4.8(b).

Initiating with a configuration where both variants of the precipitates are disjoint, we obtain an equilibrium configuration of the precipitates as depicted in Fig. 4.8(c) and Fig. 4.8(d), where the horizontal variant of the precipitate aligns at right angles to the vertical precipitate. Conversely, by changing the initial configuration where the precipitates are separated vertically, an equilibrium configuration is achieved, which is also the same as a 90^0 rotation of the previous simulation. We have energetically evaluated the total elastic and interfacial energies of the configurations and compared it with respect to that of a single variant possessing the same equivalent volume. We plot the difference in the elastic energies between a single precipitate and the equilibrium configuration of the precipitates (1 precipitate - 2 precipitates) at a given volume as a function of precipitate size, in Fig.4.9. Similarly, the difference between the interfacial energies of the equilibrium configuration and the single precipitate (2 precipitate-1 precipitate) is also shown in the same plot. There exists a cross over point beyond which the difference in the elastic energies between the single precipitate and the two-precipitate configuration is larger in magnitude than the difference between the interfacial energies of the two precipitate configuration and the single precipitate. This has important implications, wherein, one of them is the possibility of co-nucleation, instead of separate nucleation of the individual variants. This is because for cluster volumes beyond the cross-over point, the cost of nucleation which is the sum of the interfacial energy and the elastic energy, will be lower for co-nucleation in configurations as depicted in Figs. 4.8(c) and 4.8(d), in comparison to the nucleation of a single precipitate of the same volume, as here the increase in the interfacial energy involved in the formation of co-nuclei will be well compensated by the reduction in elastic energy. Therefore, given this reduction in energy of formation(sum of the elastic energy and interfacial energy), the nucleation rate of such configurations should be higher. One should however bear in mind the stochastic nature of the nucleation events and that the nucleation rate varies inversely with the size of the nucleating volume. This implies that for volumes where it becomes feasible to co-nucleate, the corresponding nucleation rates for such volumes might not be significantly high as the corresponding probability for such large fluctuations in composition would be lower. For the critical characteristic length(around 9) in our simulations(see Fig.4.9), the radius of a single precipitate is 38nm. This is however with a interfacial energy of 150mJ/m^2. Solid-solid interfacial energies, depending on different alloy systems could exhibit a whole range of interfacial energies and if a value closer to the lower end of the spectrum is utilized for eg. 5 mJ/m^2, the radius for the critical characteristic length would reduce to 1nm. Therefore, the feasibility of co-nucleation will be possibly favorable for the latter case than in the former as there, the co-nucleation event would possibly be preceded by nucleation of smaller single precipitates with much larger nucleation rates. A second implication is the possibility of finding the configura-

tions Figs. 4.8(c) and 4.8(d) during growth, as with increasing size the elastic interactions between the unlike variants leads to an overall reduction in the elastic energy when compared to a single variant of the same volume. The mechanistic pathway for such agglomeration exists as there is an attractive interaction between the unlike variants. A corollary to the previous two possibilities is that of cooperative nucleation of the precipitates, where the precipitation of a particular variant creates a favorable stress environment in the neighborhood leading to the nucleation of the second variant and then possible agglomeration during growth. We also

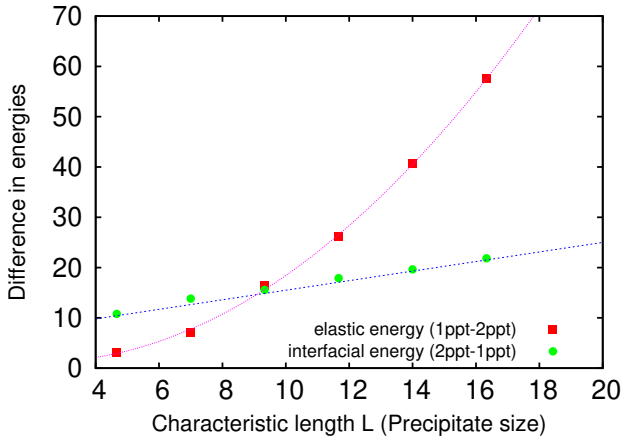

Figure 4.9: The plot showing energies of the equilibrium configurations as a function of increasing precipitate size (R) i.e. the characteristic length (L) of the precipitate which is essentially a ratio of the characteristic elastic energy to the parameter controlling the interfacial energy of the precipitate-matrix interface ($L = R\mu_{mat}\epsilon^{*2}_{xx}/\gamma_\alpha$), at $A_z = 3.0$, $t = 0.5$, $\mu = 1400$ for the case of cubic to tetragonal transition.

determine the equilibrium configuration of the precipitates by varying the anisotropy in the misfit-strain matrix, i.e. by changing the magnitude of the t. We choose five different cases where $t = +1.0, +0.5, -0.5, -1.0, 0$, where this change in strength of anisotropy of the misfit-strain gives rise to different equilibrium structures that are shown in Fig. 4.10. In the preceding simulations, we see that there is always an attractive interaction between the variants. For initial configurations starting with more number of precipitates, we find that either of the preceding structures could arise as the equilibrium configurations. In the context of investigating possibilities for the formation of compact microstructures, we have investigated an interesting three-precipitate condition wherein one of the precipitates in the configuration possesses a dilatational misfit-strain whereas the remaining are the tetragonal variants. This allows mediation of the interaction between the variants due to the presence of the third precipitate. For an attractive interaction between the precipitate with a dilatational misfit and the tetragonal variant, we have a test case wherein, we have chosen a cubic precipitate with only dilatational

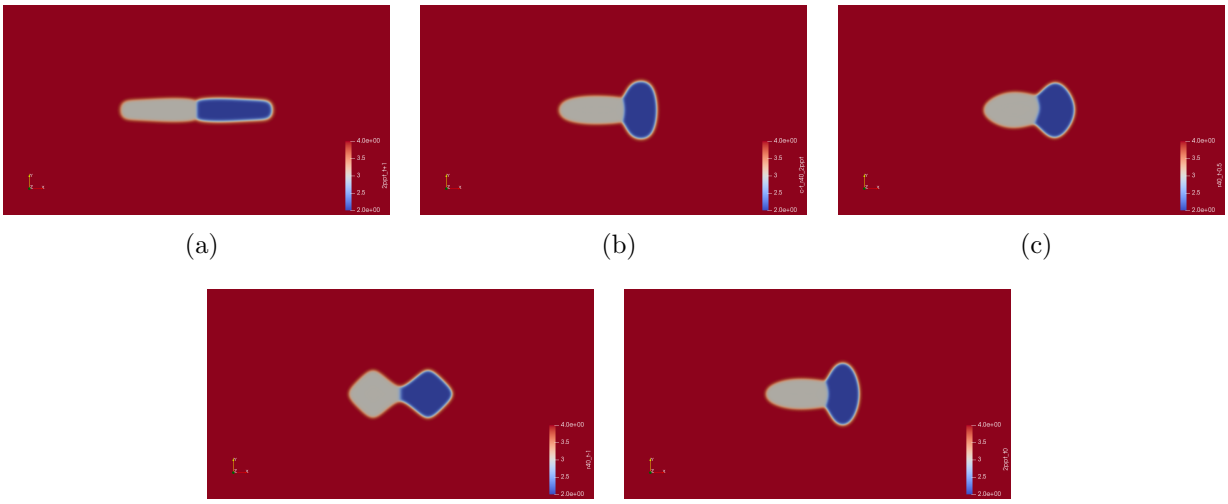

(a) (b) (c)

(d) (e)

Figure 4.10: Equilibrium configurations of precipitates with two variants for $A_z = 3.0, \mu = 1400$ with different strength of anisotropy in the misfit-strain (a) $t = +1.0$, (b) $t = +0.5$, (c) $t = -0.5$, (d) $t = -1.0$ and (e) $t = 0$.

component with a misfit-strain of 0.005, while the tetragonal variants correspond to a value of $t = -0.2$ and the value of $\epsilon^*_{xx} = -0.01$. We increase the magnitude of the misfit for the tetragonal variants in order to amplify the influence of the elasticity or in other words we have increased the characteristic length of the tetragonal precipitates, for the same precipitate sizes. Here, we start with two initial configurations as shown in the Fig. 4.11(a) and Fig.4.11(c), where the tetragonal precipitates are disjoint, surrounding the cubic dilatational precipitate at the center of the configuration. In the final equilibrium structures, we find unique configurations where the precipitates touch the central precipitate, giving rise to a sandwich-type structure as shown in Fig. 4.11(b) and a compact microstructure in Fig. 4.11(d). These kind of configurations are observed in Al-alloys [5], where the central precipitate with Al_3Zr(L12 type structure) is surrounded by θ''(tetragonal) plate-like precipitates. Further, in Ni-base superalloys such as IN718 and its modifications, structures such as Fig. 4.11(b) and Fig. 4.11(d) are observed where tetragonal variants are corresponding to γ'', while the cubic precipitate is γ' [67, 68, 69, 70, 71]. Such compact structures are often associated with increased thermal stability due to resistance to coarsening. The formation of such structures is typically observed during slow cooling rates and energetic calculations as performed by Phillips et al. [70] confirm that the co-precipitation of the γ'' on the γ' is due to the negative elastic/attractive interaction between the precipitates. This observation of the authors is similar to the conditions where such equilibrium structures arise in our simulations. Such compact structures arise for situations only when the tetragonal-

ity and the dilatational misfit strains are of opposite sign, that gives rise to an overall attractive interaction between all precipitates. On the other hand, if the tetragonality and the dilatational misfit strains possess the same sign, i.e. for the case where both the tetragonal precipitates have positive misfit strains corresponding to a value of $t = 0.2$ and $\epsilon^*_{xx} = 0.01$, the precipitates drive away from each other giving rise to the configurations shown in Fig. 4.12. The starting configuration is same as that of Fig. 4.11(c), except the characteristic length of the precipitate having dilatational misfit is different i.e. 9.33 (R=40) and 11.66 (R=50) in Fig. 4.12(e) and Fig. 4.12(f) respectively. In contrast to the results in Fig.4.11(d), the parallel components of the tetragonal variants disappear, which is evident from the time evolution of the configuration with characteristic length of 9.33 as shown in Fig. 4.12(a)-4.12(e). As the size of the precipitate with dilatational misfit increases, the contribution to the repulsive force between the tetragonal precipitate and the dilatational precipitate also increases. Thus, the variants of the tetragonal precipitates remain disjoint from each other, as shown in Fig. 4.12(f).

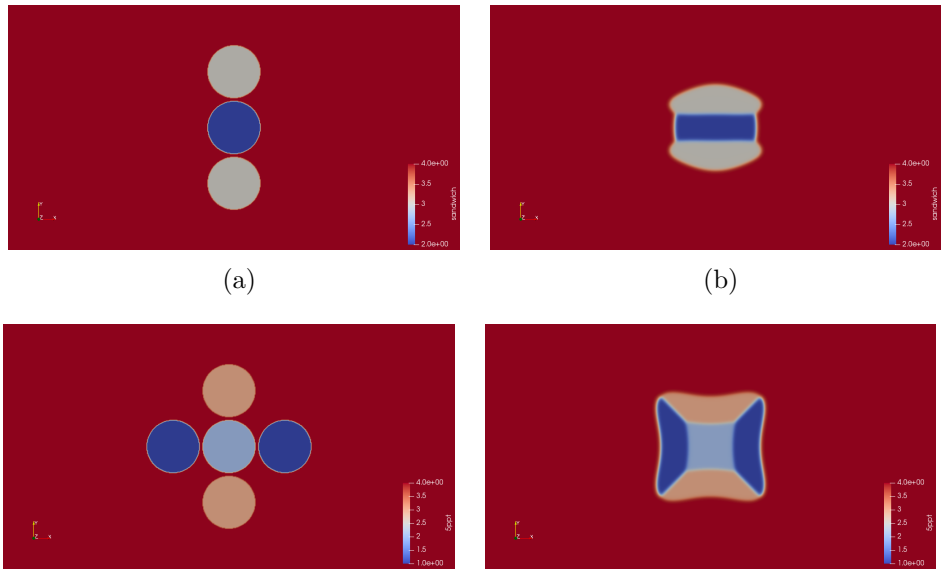

(a) (b)

(c) (d)

Figure 4.11: Equilibrium configurations of precipitates with multiple variants at $A_z = 3.0, \mu = 1400$ where central precipitate is with 0.005 of dilatational misfit-strain and other precipitates are the variants of tetragonal misfit with $t = -0.2$, $\epsilon^*_{xx} = -0.01$, (a) and (c) are initial configurations, whereas (b) and (d) are final equilibrium configuration of the variants of the precipitates.

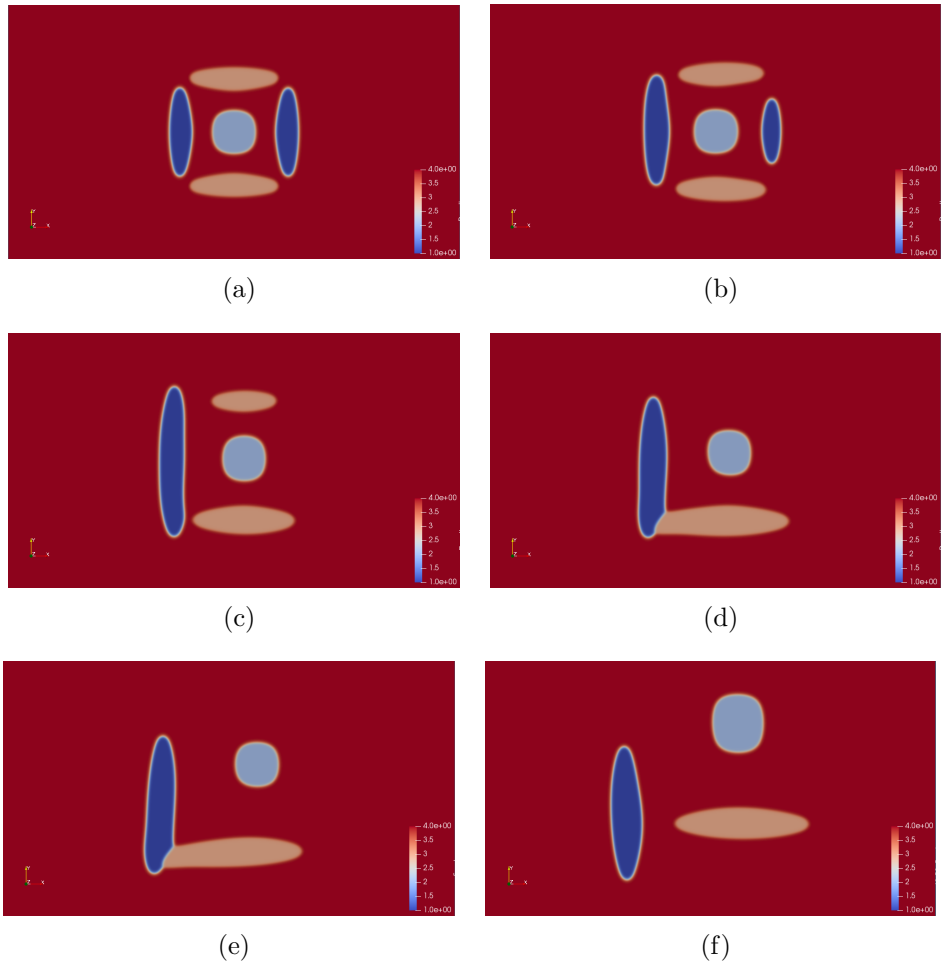

Figure 4.12: Evolution of the configurations of the precipitates with $L = 9.33$ ($R = 40$) at time (a) 120, (b) 280, (c) 475, (d) 600 and (e) 1650, where (e) 1650 is an equilibrium configuration of precipitates with multiple variants. Also, (f) is an equilibrium configuration of the precipitates, where the characteristic length of the precipitate with dilatational misfit is 11.66 ($R = 50$). $A_z = 3.0, \mu = 1400$, here the precipitates with light blue color possess dilatational misfit equals to 0.005 and other precipitates are the variants of tetragonal misfit with $t = 0.2$, $\epsilon^*_{xx} = 0.01$.

4.2.2 Hexagonal–orthorhombic transformation

As a second example of a symmetry-breaking phase transition, we study the structure of equilibrium configurations for a hexagonal (isotropic in 2D) to orthorhombic transformation. Here, our stiffness matrix is isotropic while there exist three possibilities for the variants that are rotationally related given the hexagonal base symmetry of the matrix. In order to describe this system, we incorporate anisotropy in the misfit-strain matrices, where the degree of anisotropy is characterized by t. Thus, we have three possible misfit-strain matrices for the three variants that read,

$$\begin{aligned}
\epsilon_{ij}^{*\alpha} &= \epsilon_{xx}^{*} \begin{bmatrix} 1 & 0 \\ 0 & t \end{bmatrix}, \\
\epsilon_{ij}^{*\beta} &= \epsilon_{xx}^{*} \begin{bmatrix} \dfrac{1+3t}{4} & \dfrac{\sqrt{3}(1-t)}{4} \\ \dfrac{\sqrt{3}(1-t)}{4} & \dfrac{3+t}{4} \end{bmatrix}, \\
\epsilon_{ij}^{*\gamma} &= \epsilon_{xx}^{*} \begin{bmatrix} \dfrac{1+3t}{4} & -\dfrac{\sqrt{3}(1-t)}{4} \\ -\dfrac{\sqrt{3}(1-t)}{4} & \dfrac{3+t}{4} \end{bmatrix},
\end{aligned} \tag{4.2}$$

where $\epsilon_{ij}^{*\alpha}$ corresponds to the misfit-strain matrix of the principal variant. We obtain $\epsilon_{ij}^{*\beta}$ and $\epsilon_{ij}^{*\gamma}$ by transforming $\epsilon_{ij}^{*\alpha}$ through a counter-clockwise rotation of 120^0 and 240^0 respectively. For the simulations in this section we will assume $\delta = 1.0$, and all the precipitate variants have the same stiffness matrix. The initial configuration of the precipitates are depicted in Fig. 4.13, where the precipitates are initially disjoint. With this initial setting, we perform different simulations

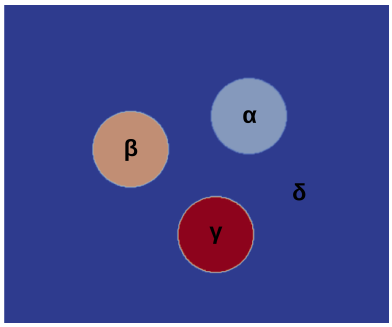

Figure 4.13: Schematic representation of different variants (α, β and γ) of the precipitate embedded in the matrix phase (δ).

by varying the anisotropy in the misfit strain (t), magnitude of shear moduli (μ) and precipitate size (L). The very first situation which we have studied is with anisotropy in the misfit strain $t = -1.0$ for two different magnitudes of the shear moduli, i.e. $\mu = 700$ and $\mu = 1400$. Since, the principal misfit strain matrix has only the shear component, the principal components of the misfit strain matrix are equal in magnitude and opposite in sign. Because of the anisotropy in the misfit strain and the rotational variants assigned to different precipitates, the precipitates acquire an equilibrium configuration with elongated structures aligned with respect to each other with a rotational angle of 120^0. Fig. 4.14 shows the evolution of the variants of the precipitates from its initial configuration to the final equilibrium configuration. An interesting observation here is that, at $\mu = 700$, the variants of the precipitates form an equilibrium configuration where the precipitates are not touching each other as depicted in Fig. 4.15(a). However, for $\mu = 1400$, we derive the equilibrium configuration as shown in Fig. 4.15(b), where all the precipitates are in contact. This is because of an increased elastic interaction between the precipitates for the simulation with the higher shear moduli, coupled with a change in the shape of the precipitates on account of an increase in the characteristic length. Similar to the cubic-tetragonal transformation, we will energetically evaluate the possibility of co-nucleation of these multi-precipitate configurations in contrast to a single precipitate nucleation for the same given volume. In order to verify this, we have computed the elastic energy as well as the interfacial energy of such an equilibrium configuration of the precipitates and a single precipitate of equivalent volume. We have also evaluated the difference between the elastic energies of a single precipitate and a three-precipitate configuration (1 precipitate - 3 precipitates) for a given precipitate volume and plotted it against the precipitate size. Similarly, we have computed the difference in interfacial energies between the three-precipitate configuration and a single precipitate (3 precipitates - 1 precipitate) for a given volume and plotted in Fig. 4.16. It is observed that after a certain critical precipitate size the energetic penalty due to the formation of additional interfaces in a three-precipitate configuration is well compensated by the reduction in the elastic energy of the three-precipitate configuration in comparison to the single precipitate. Thus, beyond a critical precipitate size, the formation of a equilibrium cluster or configuration of the precipitates is more favorable to a single precipitate nucleation of the same volume. Additionally, with an increase in the magnitude of the shear modulus ($\mu = 1400$), this critical precipitate size becomes smaller as shown in Fig. 4.16. We have repeated the calculations starting with different number of variants in the configuration and assess the energetic favorability for co-nucleation. These calculations are performed for $\mu = 1400$, where we have simulated configurations with two, three and six precipitates for different sizes and compared them energetically against the corresponding single precipitate of equivalent volume. The re-

spective equilibrium configurations are depicted in Fig. 4.17(a). As shown in Fig. 4.17(b), it is observed that the gain in the elastic energy difference is larger as compared to the penalty due to the formation of a multi-variant configuration of the precipitates. Moreover, this gain in the elastic energy (1 precipitate - multi-precipitate) increases with the number of variants in the configuration for a given volume. Additionally, the critical size beyond which a multi-variant configuration has lower energy becomes lower with an increasing number of precipitates. Given, the lower formation energy(elastic+interfacial) of the compact multi-variant structures it is reasonable to expect their occurrence in experiments on account of a larger nucleation rate. We note that, as in the case of cubic-tetragonal transformation the possibility of co-nucleation must be assessed based on the actual size of the cluster corresponding to the critical characteristic length where the cross-over occurs as in Fig.4.16. The size depends on the values of the interfacial energies and shear modulus. It is expected that with increase in the interfacial energies the possibility of co-nucleation decreases on account of increase in the value of the critical cluster size beyond which the elastic effects dominate. Conversely, an increase in the shear moduli or decrease in the interfacial energy will lead to increased favorability of co-nucleation events. Additionally, the other implications that we discussed for the case of cubic-to-tetragonal transformations which are the formation of such configurations by agglomeration during growth and cooperative nucleation of the variants are also possible here on the basis of the preceding energetic arguments.

We have also obtained the equilibrium configurations of the multi-variant precipitates by varying the anisotropy in the misfit-strain i.e. t-ratio, where we considered four possibilities i.e. $t = 0, +0.5, +1.0, -0.5$ (see Fig. 4.18). When $t = 0$, the base variant from this configuration elongates along the vertical axis whereas the other two variants are rotated 120^0 and 240^0 with respect to the base variant, forming plate-like structures. For $t = 0.5$, equilibrium configurations again give rise to the same configuration of the variants except the aspect ratios of the individual precipitates are larger. When $t = +1.0$, the variants of the precipitates remain circular, given that the elastic energy is isotropic, in which case there are no elastic interactions between the variants. At last, when, $t = -0.5$, the diagonal components of the principal misfit-strain matrix have opposite signs with unequal magnitudes. In this case, the variants elongate along their direction of lower absolute misfit giving rise to three-sided star-shaped equilibrium configuration. Bhattacharya et al. [83] have also investigated the dynamic evolution of such kind of microstructures.

Lastly, while we discuss configurations as equilibrium structures, we would like to state that such structures should be understood only as possible configurations that could arise during nucleation and growth. Strictly speaking, the cases we investigate arise out of a minimization

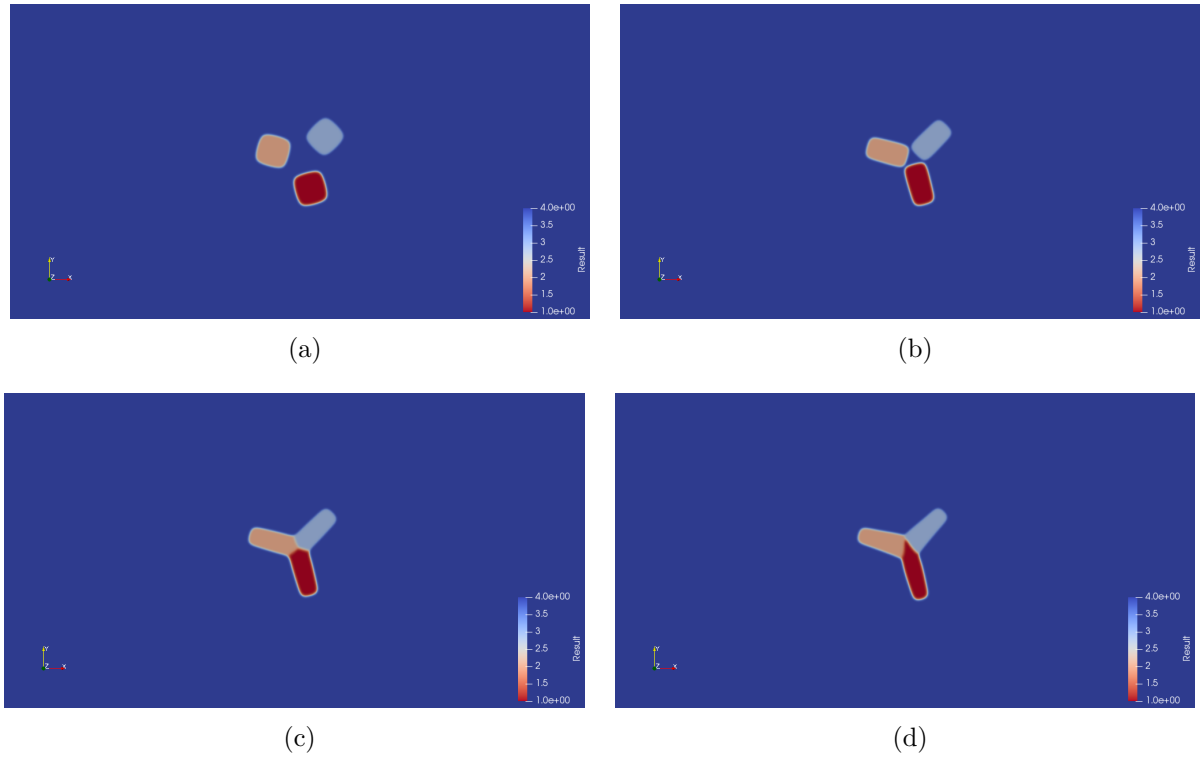

(a) (b)

(c) (d)

Figure 4.14: Evolution of three-variant precipitate structure to the equilibrium configuration at time (a)10, (b) 90, (c) 150 and (d) 300, for $A_z = 1.0$, $t = -1$, $\mu = 1400$.

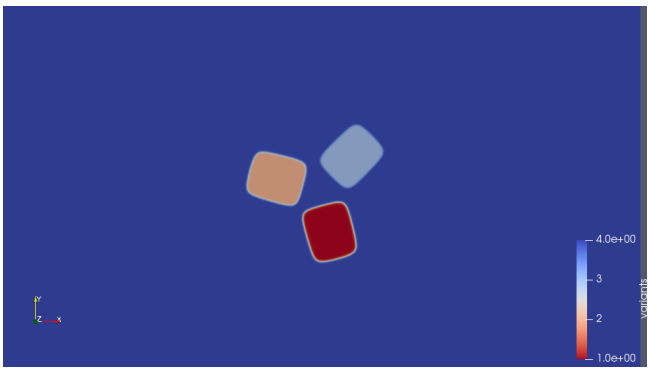

(a)

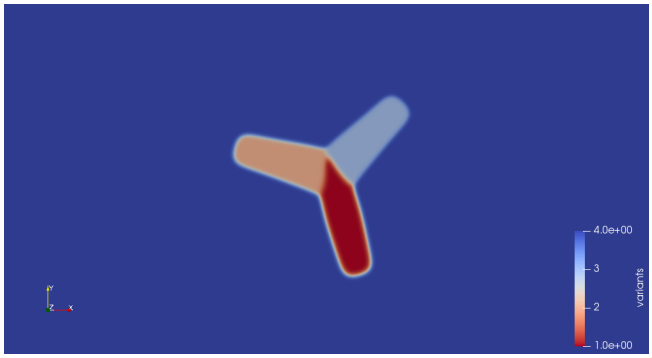

(b)

Figure 4.15: The equilibrium configurations of variants at $A_z = 1.0$, $t = -1$ with (a) $\mu = 700$ and (b) $\mu = 1400$.

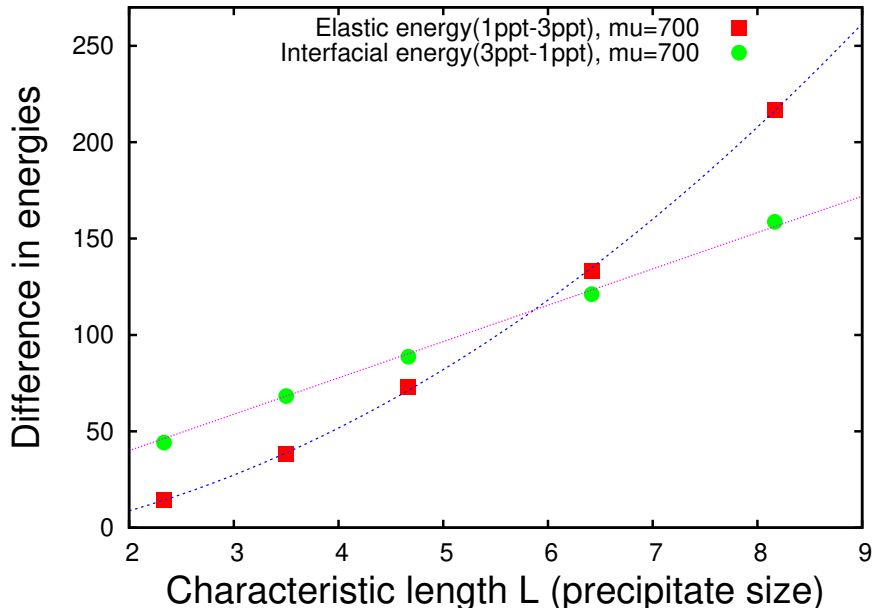

(a)

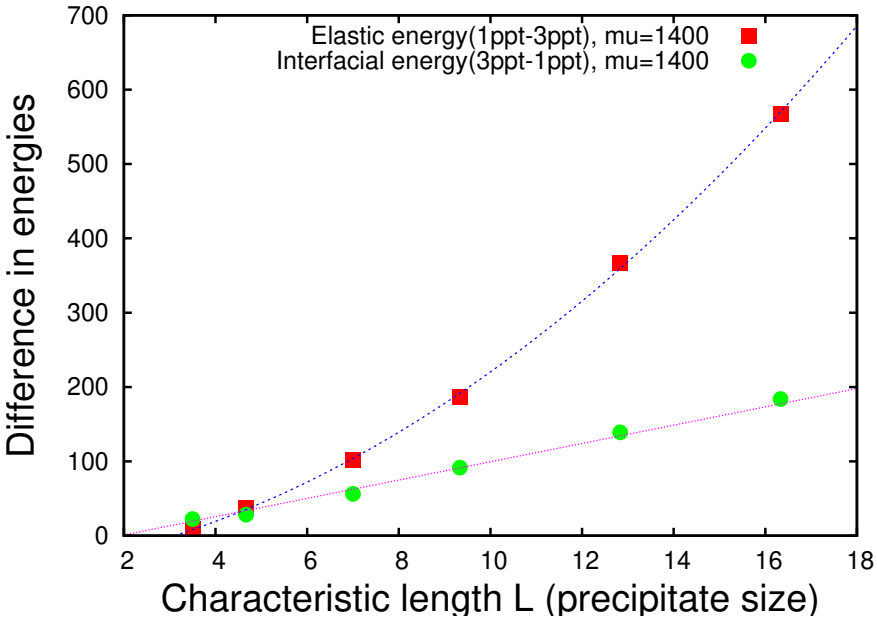

(b)

Figure 4.16: The plot showing the energies of the equilibrium configurations as a function of increasing characteristic length of the precipitate L (see Fig. 4.9 for the definition of L), at $A_z = 1.0$, $t = -1$ with (a) $\mu = 700$ and (b) $\mu = 1400$.

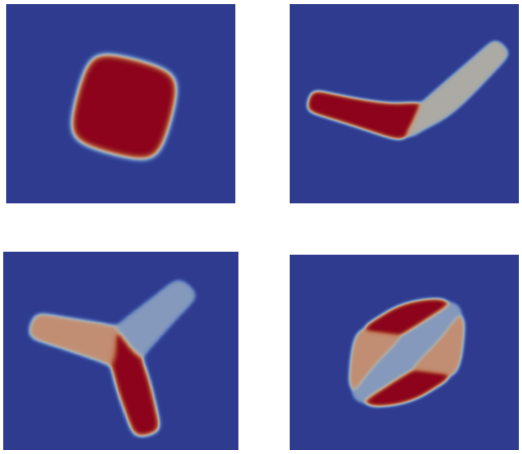

(a)

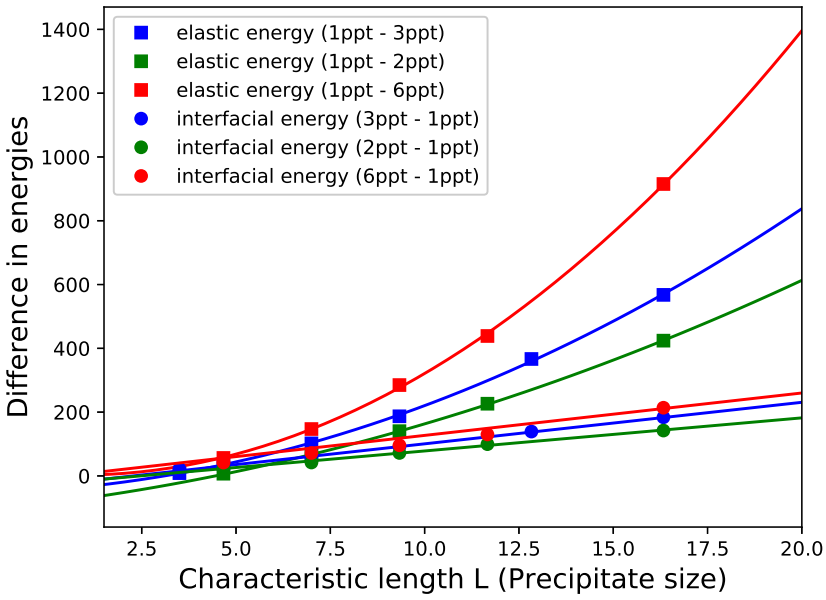

(b)

Figure 4.17: (a) Equilibrium configurations of the precipitates with increasing number of variants at a given volume and (b) the plot showing the difference in the energies of equilibrium configurations as a function of increasing characteristic length of the precipitate L (see Fig. 4.9 for the definition of L), at $A_z = 1.0, t = -1$ with $\mu = 1400$.

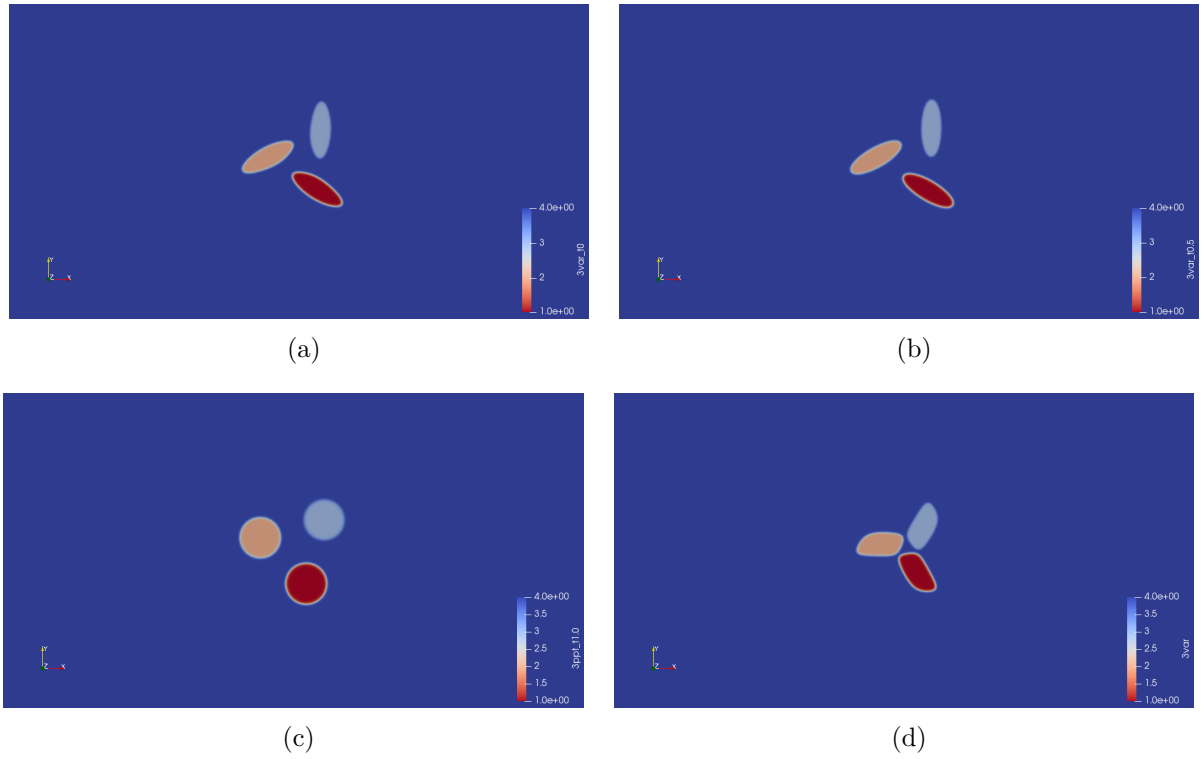

(a) (b)

(c) (d)

Figure 4.18: Equilibrium configurations of the precipitates with three variants at $A_z = 1.0, \mu = 1400$ at (a) $t = 0$, (b) $t = +0.5$, (c) $t = +1.0$ and (d) $t = -0.5$.

of elastic and interfacial energies for a constrained volume which is attained through the use of Lagrange parameters λ_α^v(see Eqn.2.37). Let us understand this firstly, for the case of a single precipitate configuration which involves a single Lagrange parameter. The Lagrange parameter changes with the constrained volume and hence may be seen as the uniform driving force of phase transformation, for which the particular configuration is critical. In other words, we solve for the critical shapes of the nucleus for a given size where we dynamically solve for the Lagrange parameter(read driving force) that leads to a stationary solution and thereby a equilibrium shape. Since we do not solve for diffusion, the implicit assumption is that the diffusion potential is uniform everywhere as in the case of classical nucleation, and therefore the Lagrange parameter that is utilized for the conservation of volume may thereby be related to the departure of the uniform diffusion potential from its equilibrium value for a planar interface and thus the required driving force for the nucleation of a given precipitate volume. Consequently, the method described is an elegant solution to the Euler-Lagrange problem of nucleation in the presence of coherency stresses. While, this is therefore a well defined methodology for single precipitate nucleation, as soon as multi-precipitate configurations are addressed the Lagrange parameters corresponding to each of the precipitates are going to depend on the elastic and interfacial properties of the respective precipitates. The values of the Lagrange parameters could therefore be unequal which would then be a picture different from the case of single precipitate nucleation, where for such a system to be existing in a real dynamical simulation would necessitate the presence of a non-uniform distribution of the diffusion potential. For the case of symmetric variants like in the cubic–tetragonal and hexagonal–orthorhombic transformations where the volumes corresponding to each of the variants is the same, it is expected that the Lagrange parameters for each of the phases are equal and hence they may be considered as true equilibrium shapes/configurations. However, this is not true for the case where different phases are involved like in the sandwich or the compact structures or in general when the variant volumes are unequal. Therefore, in this context, for such simulations of configurations with different variants/precipitates, the word "equilibrium" is utilized only in the context of stationary configurations in the present method. These configurations could therefore evolve further in a real dynamical simulation where diffusion is considered.

4.3 Summary

In this chapter, we have presented a multiphase-field model where we calculate the equilibrium structures or the configurations of the precipitates embedded in the matrix phase having a coherent interface, which is essentially an extension of Chapter 3. In this model (see Chapter 2.2),

we solve multiple Allen-Cahn equations coupled with the constraints of constant volume and mechanical equilibrium. Using this model, we have computed the equilibrium configurations of the precipitates at a given volume by varying the anisotropy in the elastic energy, the magnitude of the shear moduli and the interfacial energies, sign and the magnitude of the misfit-strain and the anisotropy in the misfit-strain. As a first study, we have determined the necessary and sufficient conditions for the formation of the core-shell microstructures for a two-precipitation reaction. We have observed that the core-shell structure forms if and only if the criteria of solid-state wetting is satisfied i.e. the magnitude of the interfacial energy of one of the interfaces has to be larger than the sum of the magnitudes of the interfacial energies of the remaining interfaces. However, elasticity influences the formation of such clusters by influencing the inter-precipitate interaction. Here we note that the precipitates with opposite sign and softer than the matrix phase ($\delta < 1.0$), have the most attractive interaction, whereas harder precipitates (i.e. for $\delta > 1.0$), repel. Thus, we postulate that, in the former situation where an attractive interaction exists, one would expect to find a statistically larger set of core-shell formation of the precipitate phases in the experiments than the latter, given that the solid-state wetting condition is satisfied. Secondly, we have determined the equilibrium configurations of the variants of the precipitates that form during two symmetry-breaking transitions namely, cubic to tetragonal and hexagonal to orthorhombic transitions. Here, in the cubic to the tetragonal transformation we have obtained the equilibrium configurations of the precipitates as a function of the precipitate size and the strength of anisotropy in the misfit-strain. Using energetic calculations, we have additionally determined that, beyond a critical precipitate size, it is energetically favorable to co-nucleate two variants in comparison to the nucleation of the single precipitate, as the increase in the interfacial energy due to formation of the cluster is well compensated by the reduction in the elastic energy. The possibility of such co-nucleation events however depends on the critical size where the elastic effects start to dominate, in terms of achieving an appreciable nucleation rate. We have also observed some interesting configurations that form out of the combination of tetragonal variants and a third precipitate with dilatational misfit-strain, that are observed in the experiments [5]. Here, when the sign of the tetragonal misfit strains are opposite to the dilatational misfit of the third precipitate, there exists a force of attraction between the precipitates giving rise to sandwich-type structures. In contrast to this, if both the misfit-strains i.e. tetragonal as well as the dilatational have the same signs there exists a repulsive interaction between the precipitates without the formation of compact structures. Lastly, for the case of hexagonal to orthorhombic transformation giving rise to three-variants, the co-nucleation of the multi-variant configuration of the precipitates is energetically favored to the nucleation of a single precipitate beyond a certain precipitate

size. We have also shown that, by varying the strength of anisotropy in the misfit-strain t, we can obtain a range of interesting equilibrium configurations of the variants of the precipitates. In summary, using this novel multiphase-field model, formation of a range of fascinating equilibrium configurations can be investigated providing useful insights about the possibilities in experiments.

Chapter 5

Precipitate growth under the influence of coherency stresses

In this chapter, we will systematically discuss the influence of strength of anisotropies in the elastic energy and the interfacial energy, magnitude of misfit strain and the supersaturation on the evolution of instabilities giving rise to dendrite-like structures.

5.1 Parameter initialization

In this section, we list out the material parameters that will be used in the subsequent sections. We use a non-dimensionalization scheme where the energy density scale is derived from the magnitude of the shear modulus $1 \times 10^9 J/m^3$, while the interfacial energy scale is given by $1 J/m^2$. Dividing the interfacial energy length scale with the scale for the energy density sets the length scale in the problem which is $l^* = 1\text{nm}$. In the chapter, hence all the parameters will be reported in terms of non-dimensional units. The anisotropy in the elastic energy is introduced through the Zener anisotropy parameter i.e. A_z which in turns modifies the magnitudes of the elastic constants, that are $C_{11} = C_{1111}$, $C_{12} = C_{1122}$ and $C_{44} = C_{1212}$. These elastic constants can further be elaborated in terms of the shear modulus (μ), Poisson's ratio (ν) and Zener anisotropy parameter (A_z) which controls the evolution and orientation of the instability.

$$C_{44} = \mu, \quad C_{12} = 2\nu \left(\frac{\mu}{1 - 2\nu} \right), \quad C_{11} = C_{12} + \frac{2C_{44}}{A_z}. \tag{5.1}$$

For all the cases, the precipitate and the matrix have the same magnitude of A_z. Unless otherwise specified, all results are produced with $\mu_{mat} = \mu_{ppt} = 100$, $\nu_{ppt} = \nu_{mat} = 0.3$ and

A_z varies from 2.0 to 3.0, which is typically observed in Ni-based superalloys. Here, the misfit strain or eigenstrain (ϵ^*) is dilatational. The magnitude of misfit strain is varied in the range from 0.5 to 1%. The simulation is initialized with a precipitate of initial radius, $R_0 = 40$, that is placed at the center of the domain. The simulation domain obeys periodic boundary conditions. The size of the domain is chosen such that the diffusion fields of the neighboring precipitates do not interact with each other. Equilibrium compositions in the bulk precipitate (c^{α}_{eq}) and the matrix (c^{β}_{eq}) are chosen to be 0.78125 and 0.5 respectively.

5.2 Evolution of the precipitate into a dendrite-like shape

We begin by describing the shape evolution of the precipitate giving rise to dendrite-like shapes. Fig. 5.1, shows such an exemplary simulation, in which the matrix is supersaturated at 53%, the misfit at the interface is $\epsilon^* = 1\%$, $A_z = 3.0$, while the interfacial energy is isotropic. We note that typical values of supersaturations where dendrites are observed experimentally are typically much lower because this leads to larger inter-precipitate distances allowing for free development of the instabilities without overlap of the composition and the elastic fields. In the simulations however, we are constrained by having to resolve the large elastic and composition boundary layers. Therefore, in order to derive results in reasonable time, we have performed simulations for higher supersaturations in comparison to experimentally observed situations. However, this should not alter the results that we derive from the simulations and should be generically applicable for interpreting experimentally observed microstructures and observed trends in the change of the morphologies upon alteration of the processing conditions or the material properties.

The precipitate with an initial circular shape grows into a square-like shape with rounded corners, where its faces are normal to $< 10 >$ directions. In the absence of interfacial energy anisotropy, precipitate shape and the eventual instabilities of the interface are determined by the elastic energy anisotropy. Further, with an increase in the size, the precipitate corners become sharper. Eventually, due to point effect of diffusion, the corners of the precipitate grow faster (along the $< 11 >$ directions) compared to its faces, which further gives rise to concavities on the precipitate faces, as shown in Fig. 5.1(c)-5.1(d). We note that this shape evolution is indeed due to a diffusive instability similar to the Mullins-Sekerka instability leading to the formation of dendrites during solidification for anisotropic interfacial energies, where the perturbations of the composition boundary layer ahead of the interface provide an amplifying feedback to the interface velocity leading to the development of the instability. Among the different possible perturbation modes, the elastic energy anisotropy determines the eventual

shape of the precipitate during growth giving rise to dendrite-like shapes. Fig.5.1(e) shows the contour plot of phase-field profiles at $\phi = 0.5$, i.e. the precipitate-matrix interface, which are plotted as a function of increasing time. The composition field around the precipitate also evolves as a function of time which is captured in Fig. 5.2. With an increase in the amount of the supersaturation, the precipitate grows faster into a dendritic shape. This can be seen in Fig. 5.3, where the precipitate with supersaturation $\omega = 53\%$, grows its arms faster along the $< 11 >$ directions giving rise to a dendrite-like morphology as compared to the one with supersaturation $\omega = 40\%$. Typical solidification dendrites are characterized by a unique tip radius and velocity and a dendritic shape that is a function of the strength of the anisotropy. In the following, we perform a similar characterization of our morphologies. A usual characteristic of dendrites during solidification is that apart from the the selection of a Peclet number, the product of the square of the dendrite tip radius with the velocity is also a constant. This constant is typically known as the microsolvability constant $\sigma^* = 2d_0D/R_{tip}^2V_{tip}$, where d_0 is the capillary length, D is the diffusivity, while R_{tip} and V_{tip} are the radius and the velocities respectively of the dendritic tip, that is either estimated using the linearized microsolvability theory as presented in [102] or using dynamical phase-field simulations [104]. We follow the route as the latter, where we derive the value of the selection constant σ^* as a function of the material parameters and supersaturation, from the measured values of the dendrite-tip radius and velocity from our phase-field simulations.

Fig.5.4(a) shows the variation of the selection constant σ^* as a function of time, scaled with the characteristic diffusion time. We find that the value of the selection constant has a transient where there is both an increase and decrease in the magnitude before settling into a regime where the values continue to change approximately linearly with simulation time. This linear regime initiates approximately when the primary arms have emerged as a result of the instability. This is quite different to dendrites in the presence of just interfacial energy anisotropy, where the value of σ^* becomes relatively constant (see Fig.5.6) quite early in the simulation (just as the primary arms appear), even though the R_{tip}(Fig.5.5(a)) and V_{tip}(Fig.5.5(b)) themselves have not yet attained their steady state values. A similar variation is also seen in the Peclet number $\frac{R_{tip}V_{tip}}{2D}$, where it continues to decrease approximately linearly with time as depicted in Fig.5.4(b) in the presence of elasticity, while a nearly constant value is attained for the dendrite with just interfacial energy anisotropy (see Fig.5.7). Therefore, we also do not derive any steady-state with respect to the shape of the tip as well as the velocity as highlighted in Figs.5.4(c) and 5.4(d) respectively in the presence of elasticity.

The reason for the non-attainment of a steady state is possibly linked to the variation of the jump in the value of the elastic energy at the interface. We have extracted the elastic

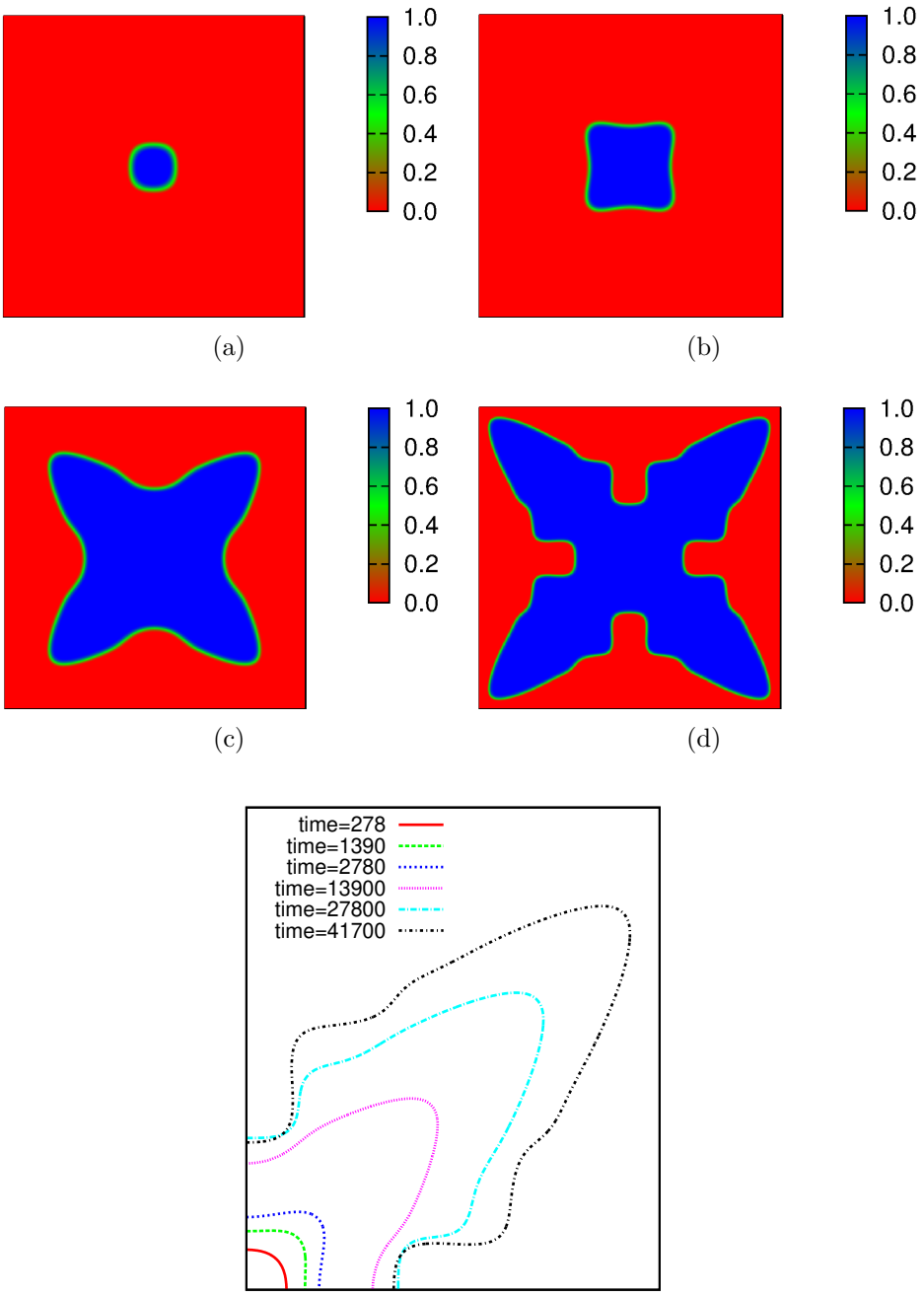

Figure 5.1: Evolution of the precipitate into dendritic structure for $A_z = 3.0$, $\epsilon^* = 1\%$ at normalized time: (a)278, (b)2780, (c)13900, (d)41700 and (e)contour plot of section at different times

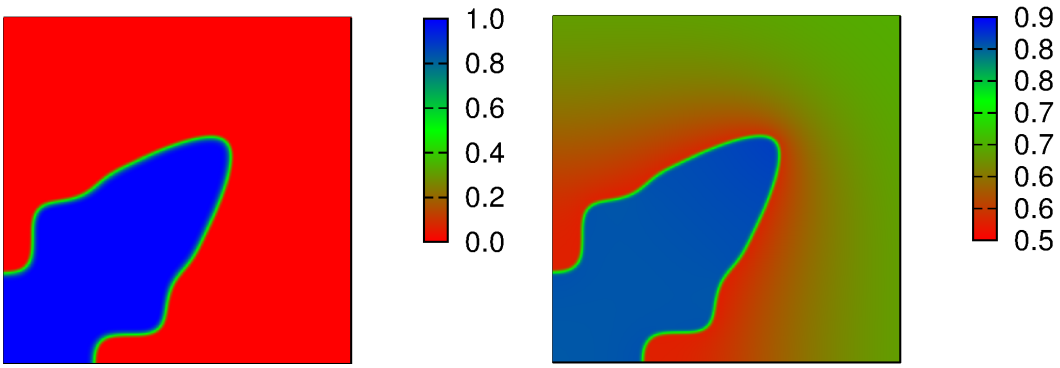

(a) (b)

Figure 5.2: (a) Phase field and (b) composition field of 1/4th section of the precipitate growing into dendritic structure

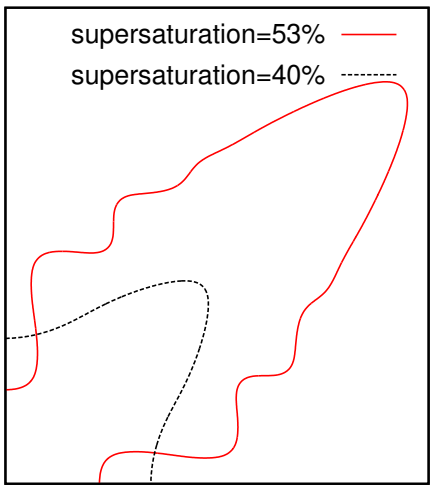

Figure 5.3: Evolution of precipitate into dendritic structure for different magnitudes of the supersaturation in the matrix phase captured for the same time.

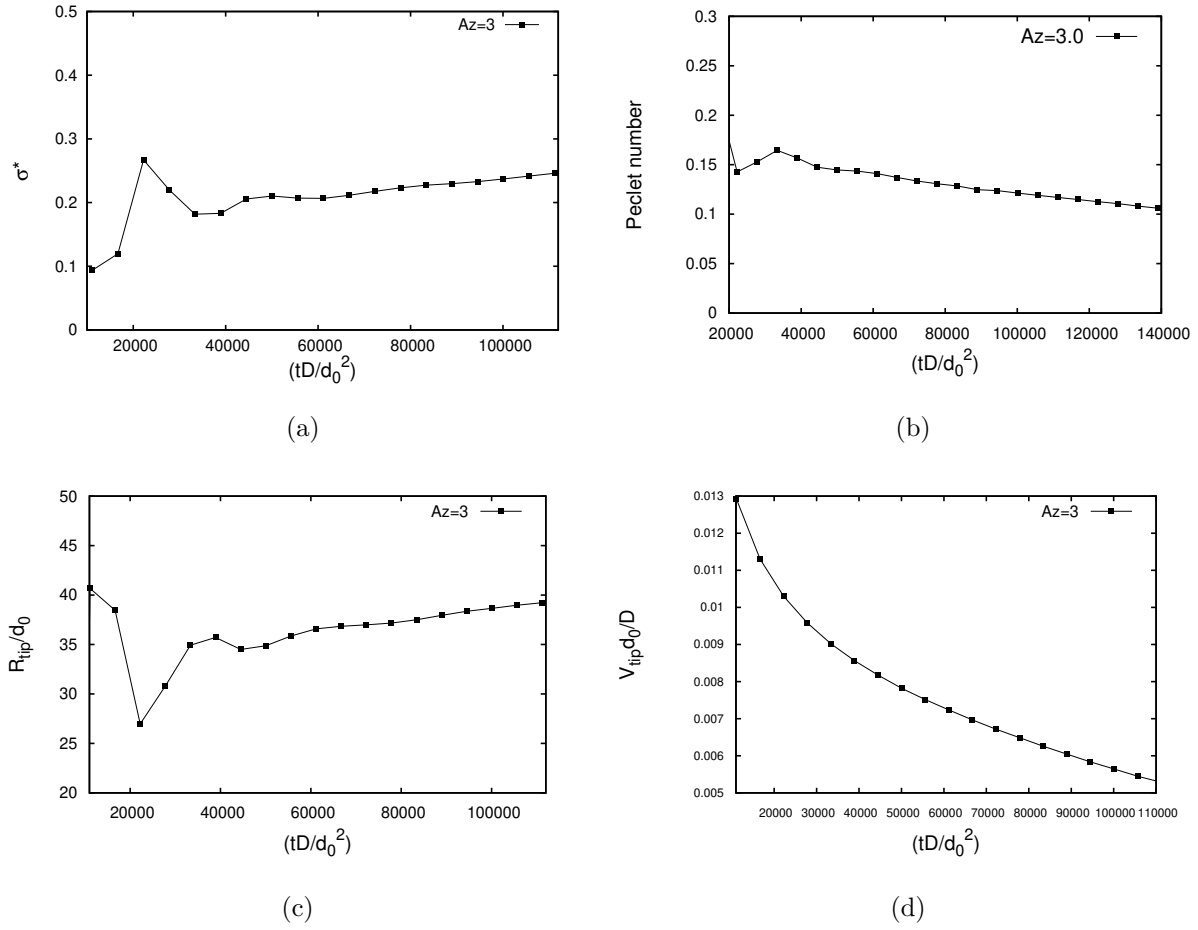

Figure 5.4: (a) Plot of the variation of σ^* as a function of time in the simulations (b)Variation of the Peclet number as a function of scaled time (c) and (d) show the variation of the dendrite tip radius and velocity as a function of time.

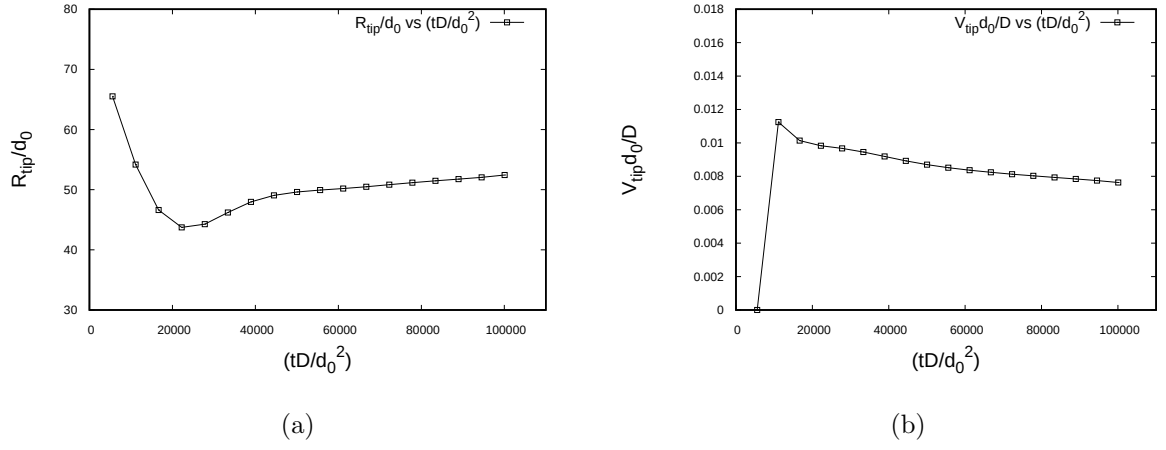

Figure 5.5: Variation of (a) R_{tip} and (b) V_{tip} as a function of normalized time without elasticity.

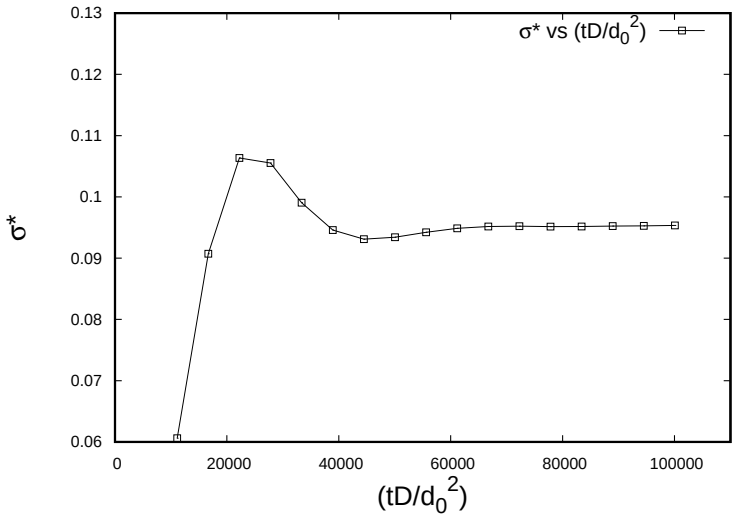

Figure 5.6: Variation of σ^* as a function of normalized time without elasticity.

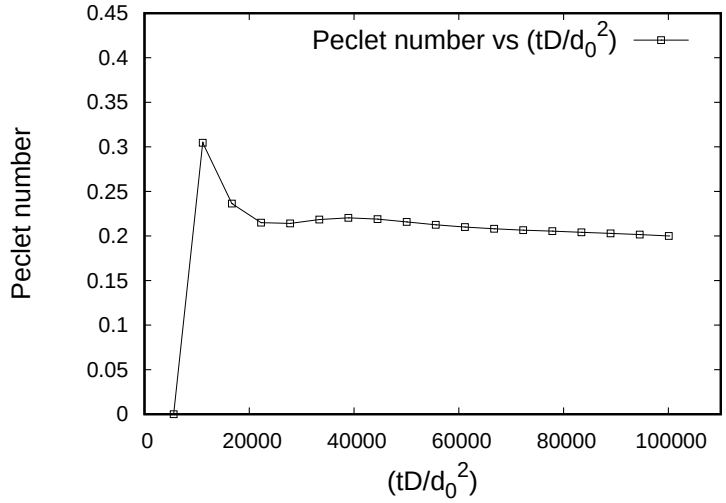

Figure 5.7: Variation of Peclet number $\frac{R_{tip}V_{tip}}{2D}$ as a function of normalized time without elasticity.

energy along the direction normal to the dendrite-tip for different simulation times. From this we compute the jump in the elastic energy(ΔF_{el}) by computing the difference in the values of the elastic energy on the precipitate side with the matrix side. Fig. 5.8 highlights the variation of the elastic energy density as a function of time, while the jump of the elastic energy at the interface is depicted in Fig. 5.9 that clearly shows an increase with simulation time. We note that although the variation is small, this will inturn lead to the change in the interfacial compositions as a function of time and thereby the Peclet number as well as the selection constant σ^* do not attain saturated values. This also means that the dendrite tip radius as well as the tip velocities never reach a steady state in contrast to the situation of dendritic growth in the presence of just interfacial energy anisotropy. Therefore, in relation to the classical dendritic structures observed during solidification, the simulated structures may only be referred to as dendrite-like. We note that although the variation of the ΔF_{el} at the dendrite tip will lead

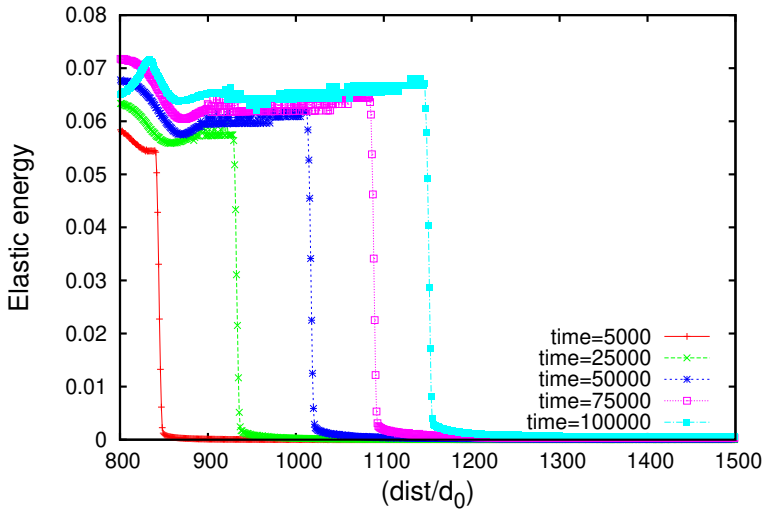

Figure 5.8: Variation of bulk elastic energy along $< 11 >$ direction i.e. along the tip of the precipitate at $A_z = 3.0$.

to the change in the interfacial compositions and therefore the Peclet number at the interface, the overall volume(area for 2D) as depicted in Fig. 5.10, still varies linearly with time which is the growth law one would expect for the growth of a precipitate in the parabolic growth regime and is also observed in the classical dendritic growth during solidification.

Further, we determine the effect of elastic anisotropy on the behavior of precipitate morphologies. Fig. 5.11 shows the difference in the tip shapes as a function of A_z at a normalized time=41700, where we plot only one of the symmetric quadrants for simplicity. Fig. 5.11 shows that with increase in the strength of anisotropy in the elastic energy ($A_z > 1.0$), the radius

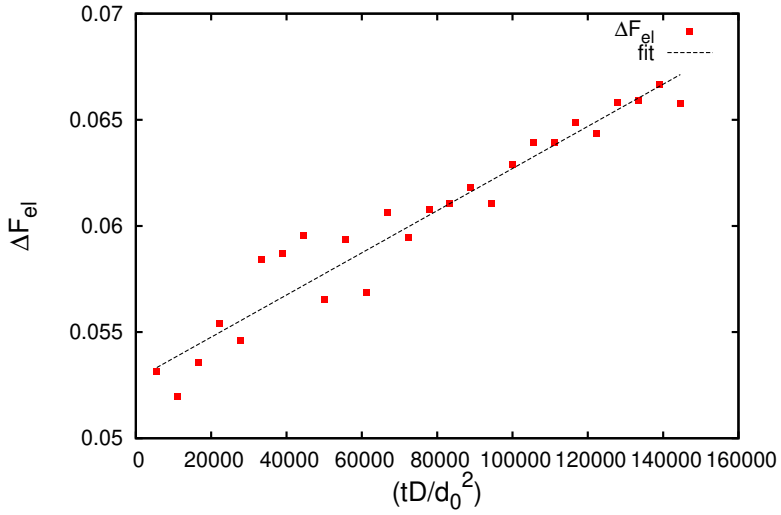

Figure 5.9: Variation of jump in the elastic energy across the precipitate-matrix interface,ΔF_{el}, calculated along the [11] direction i.e. along the vector joining the centre to the tip of the precipitate at $A_z = 3.0$.

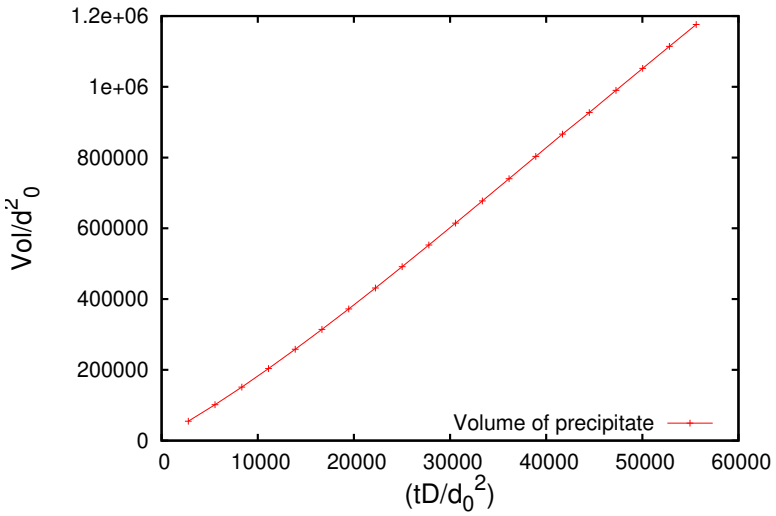

Figure 5.10: Variation of precipitate volume as a function of time at $A_z = 3.0$.

of the tip of the precipitate reduces i.e. the tip morphologies become sharper and elongated along $< 11 >$ directions that is also revealed in the plots showing the dendrite tip radius in Fig.5.12(a). Correspondingly, the velocities at the tip are also higher for larger values of A_z as highlighted in Fig. 5.12(b).

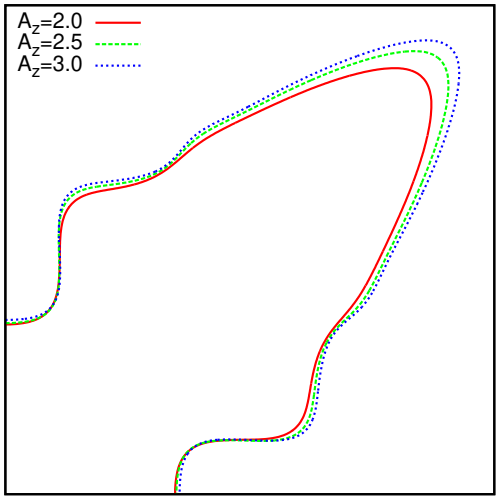

Figure 5.11: Solid state dendritic structure of precipitate with varying anisotropy in elastic energy (A_z) at a given time (t=41700).

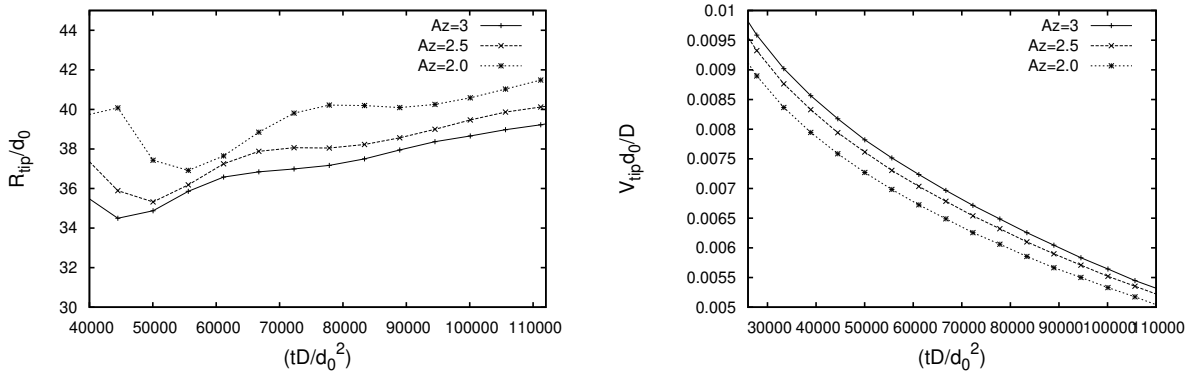

(a) (b)

Figure 5.12: Variation of R_{tip} and V_{tip} as function of time with varying the magnitude of A_z.

The plot in Fig. 5.13 shows that the magnitude of σ^* consistently increases with normalized time (tD/d_0^2) after the initial transient, whereas the magnitude of σ^* increases with the strength of anisotropy in the elastic energy i.e. A_z for a given time. Similarly, Fig. 5.15 shows that the

magnitude of σ^* increases with time for a given misfit strain. The plot also shows that, as the magnitude of the misfit strain increases, the value of the selection constant also becomes larger. There is no clear trend observable with the change in the velocities as seen in Fig.5.14(b), while the tip radius reduces with increase in the value of the misfit strain as depicted in Fig.5.14(a). Thus, there is no unique value of the selection constant (σ^*) at a given anisotropy strength of elastic energy and the magnitude of the misfit strain. While the variation of σ^* in the linear regime at a given time, is approximately linear with the variation of A_z, it changes approximately as $\epsilon^{*1.5}$ with the misfit strain (comparing values for a given time).

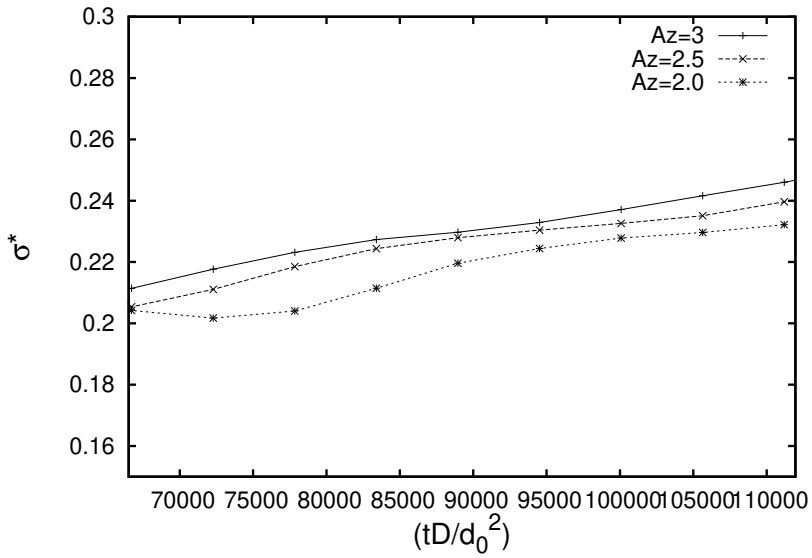

Figure 5.13: Variation of σ^* as a function of time (tD/d_0^2) for different strengths of anisotropies in elastic energies.

Fig. 5.16 depicts the effect of change in the magnitude of the supersaturation in the matrix, while the anisotropy in the elastic energy as well as the magnitude of the misfit strain are kept constant i.e. $A_z = 3.0$ and $\epsilon^* = 0.01$. The plots show that the radius of the dendritic tip become sharper (see Fig.5.16(a)) with increase in the magnitude of supersaturation whereas the velocity increases (see Fig.5.16(b)), but does not saturate. Similarly, the magnitude of the selection constant increases with time as shown in Fig. 5.17.

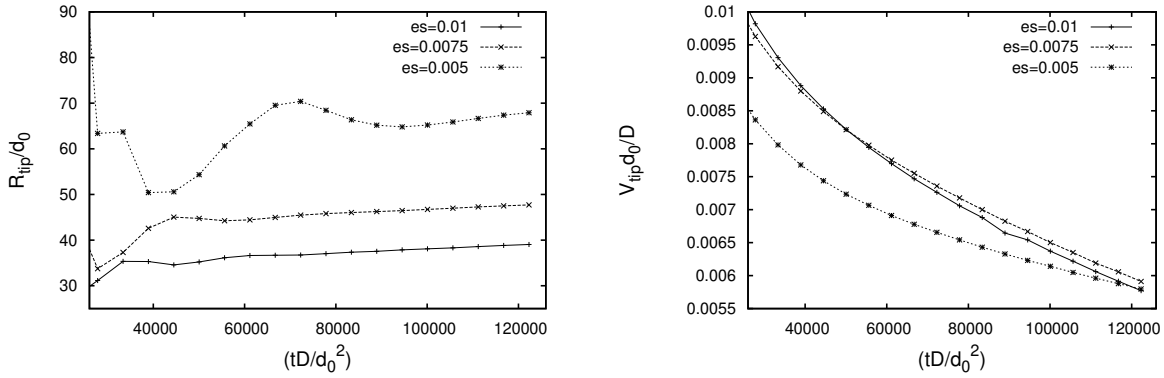

(a) (b)

Figure 5.14: Variation of R_{tip} and V_{tip} as a function of time for different magnitudes of misfit strain at $A_z = 3.0$.

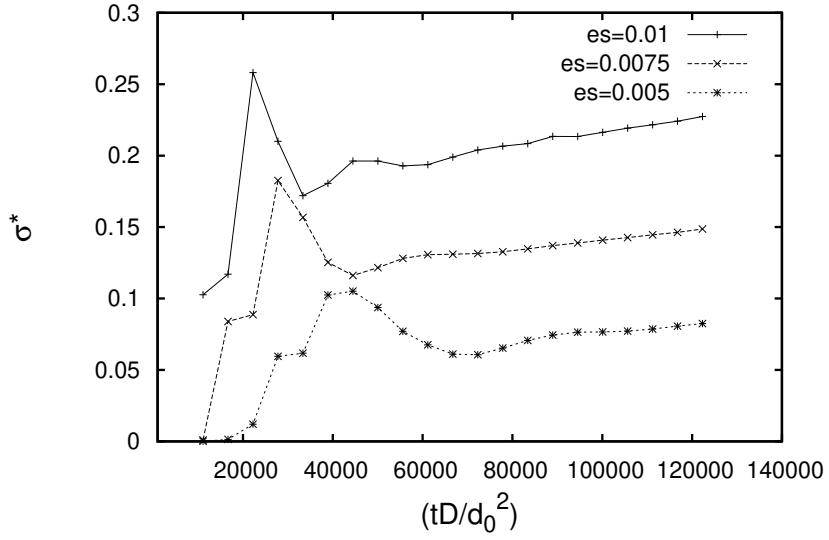

Figure 5.15: Variation of σ^* as a function of time (tD/d_0^2) for different misfit strains at $A_z = 3.0$.

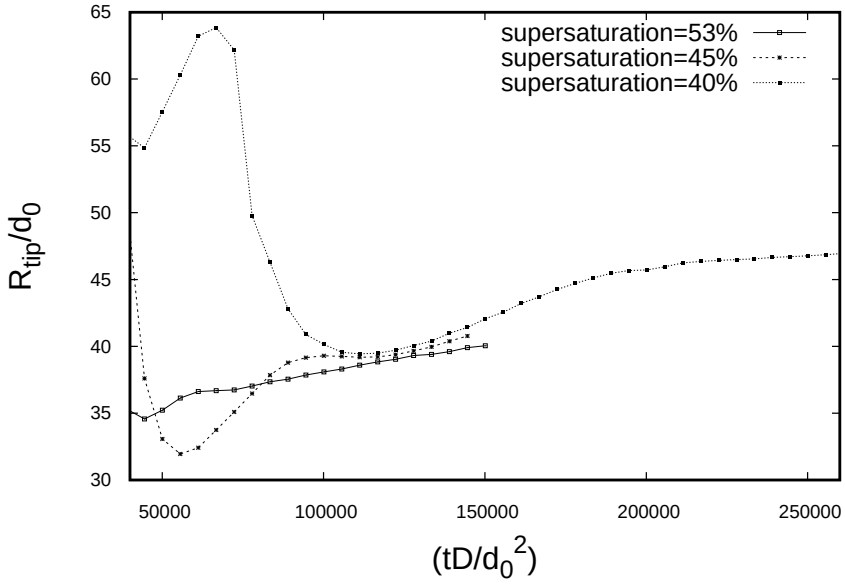

(a)

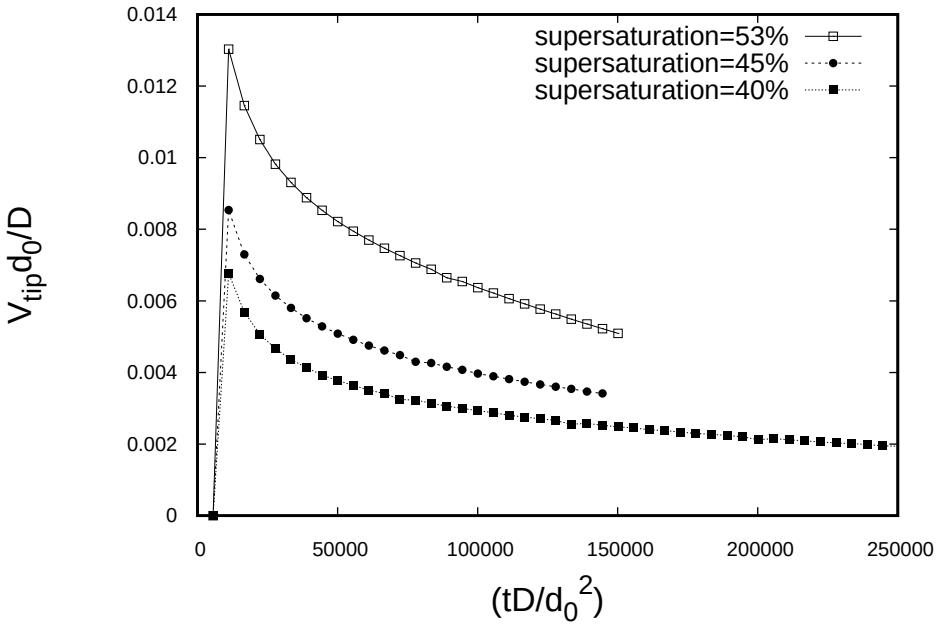

(b)

Figure 5.16: Variation of R_{tip} and V_{tip} as a function of time with different magnitudes of supersaturation in the matrix at $A_z = 3.0$.

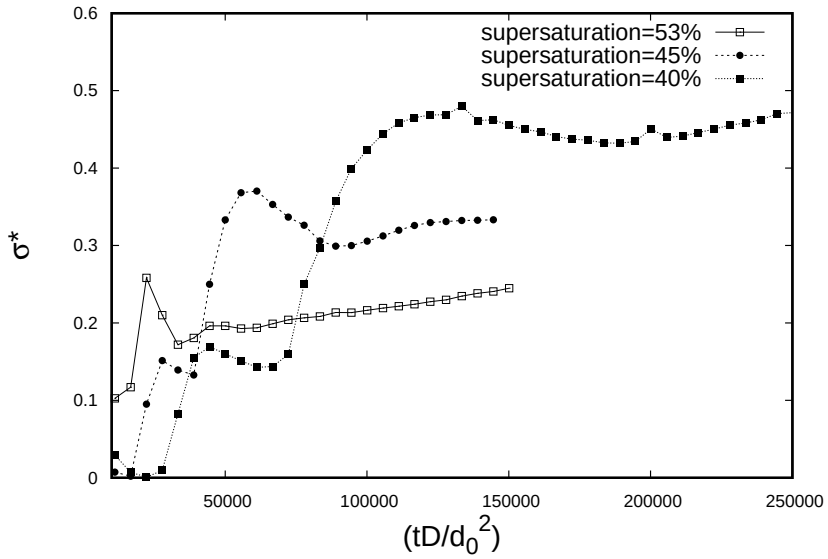

Figure 5.17: Variation of σ^* as a function of time (tD/d_0^2) for different magnitudes of supersaturation in the matrix strains at $A_z = 3.0$, $\epsilon^* = 0.01$.

5.3 Competition between anisotropies in the interfacial energy and elastic energy

In the previous section, we have seen the effect of different variables such as supersaturation, misfit strain and the anisotropy in elastic energy on the evolution of the dendrite-like morphologies. In this section we investigate the competition between the influence of anisotropies in the elastic energies and the interfacial energies. The anisotropy in the interfacial energy is modeled using the function [109] (see Chapter 2.3 Eqn. 2.48) which leads to the formation of dendrites aligned along the $< 10 >$ directions. Here, we keep the anisotropy in elastic energy (A_z) constant and allow the strength in anisotropy in interfacial energy to vary in the range 0.0 to 0.03. Also, here we have considered two broad categories with different magnitudes of elastic anisotropies i.e. $A_z = 3.0$ and $A_z = 0.5$. In the first case, as the magnitude of A_z is above one (similar to the case studied before), where the interfacial energy and the elastic energy anisotropies lead to the formation dendrites in $< 11 >$ and $< 10 >$ directions respectively, whereas in the second case for values of A_z less than unity, the anisotropies in the elastic energy and the interfacial energy superimpose.

5.3.1 Case A: Strength of elastic anisotropy $(A_z) > 1.0$

For this case where the anisotropies in the interfacial energy and elasticity lead to dendrite-like structures in different directions, the combined influence of anisotropies in both the energies gives rise to a precipitate shape which is nearly circular in the the early stage of growth as shown in Fig. 5.18, at $A_z = 3.0$ and $\varepsilon = 0.03$. But, with decrease in the strength of anisotropy

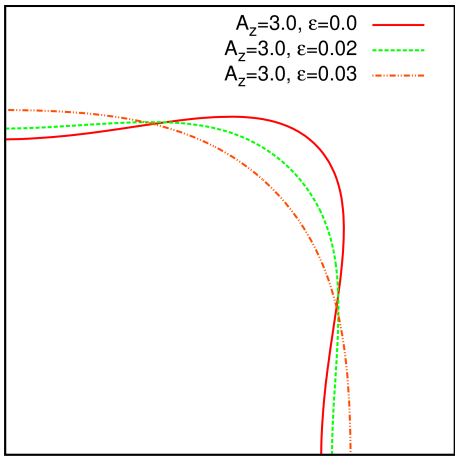

Figure 5.18: Early stage precipitate growth under influence of combined effect of anisotropies in the elastic energy and the interfacial energy: normalized time=2780 $A_z = 3.0, \varepsilon = 0.0$ to 0.03.

in the interfacial energy from 0.03 to 0.0, the precipitate not only develops sharp corners but also shows strong alignment along $< 11 >$ directions, that is the elastically preferred direction. Fig. 5.19, compares the morphologies for different strengths of anisotropies in interfacial energy ($\varepsilon = 0.0 - 0.03$) for a given value of $A_z = 3.0$ at the normalized simulation time of $t = 55600$. Fig. 5.20(a) depicts that as the interfacial energy anisotropy increases, the dendrite tip radius becomes larger while the velocity of the dendrite tip reduces as highlighted in Fig. 5.20(b).

Similarly, while the magnitude of σ^* again has a linearly increasing trend with simulation time(after the initial transient), the competition between the elastic energy anisotropy and the interfacial energy anisotropy leads to a decrease in the magnitude of σ^* at a given time of the evolution of the precipitate, which is expected as this is similar to the effective reduction of the anisotropy in the system (see Fig. 5.21).

5.3.2 Case B: Strength of elastic anisotropy $(A_z) < 1.0$

In the previous section the effect of varying the anisotropy in interfacial energy at constant elastic anisotropy i.e. $A_z = 3.0$ is elaborated. Here, we explore the results upon varying the

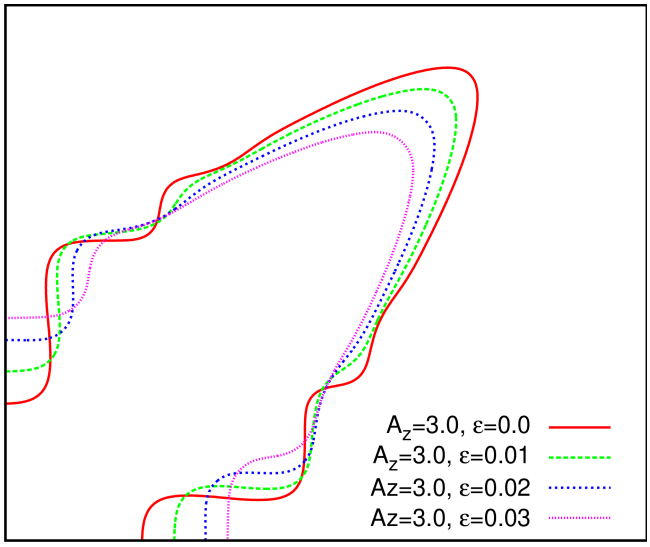

Figure 5.19: Precipitate grown into dendritic shapes under influence of combined effect of anisotropies in the elastic energy and the interfacial energy: time=55600 $A_z = 3.0, \varepsilon = 0.0 - 0.03$.

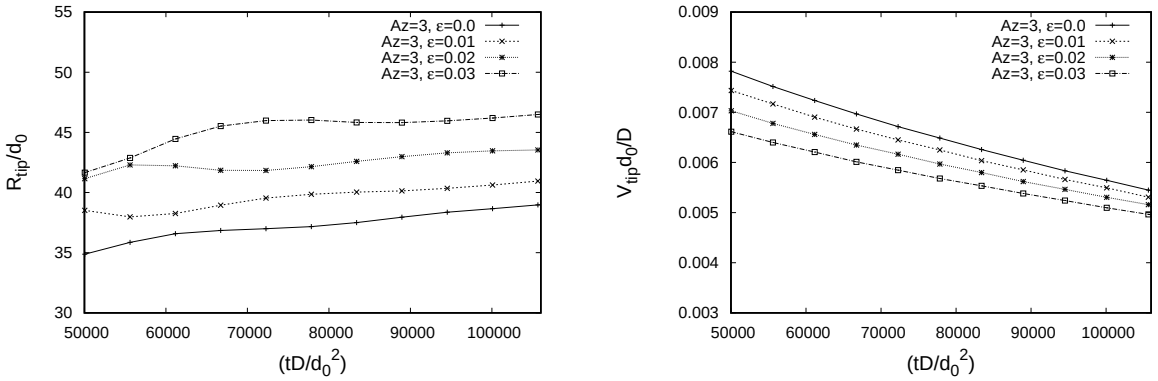

(a) (b)

Figure 5.20: Variation of R_{tip} and V_{tip} as a function of time with varying the magnitude interfacial anisotropy at $A_z = 3.0$.

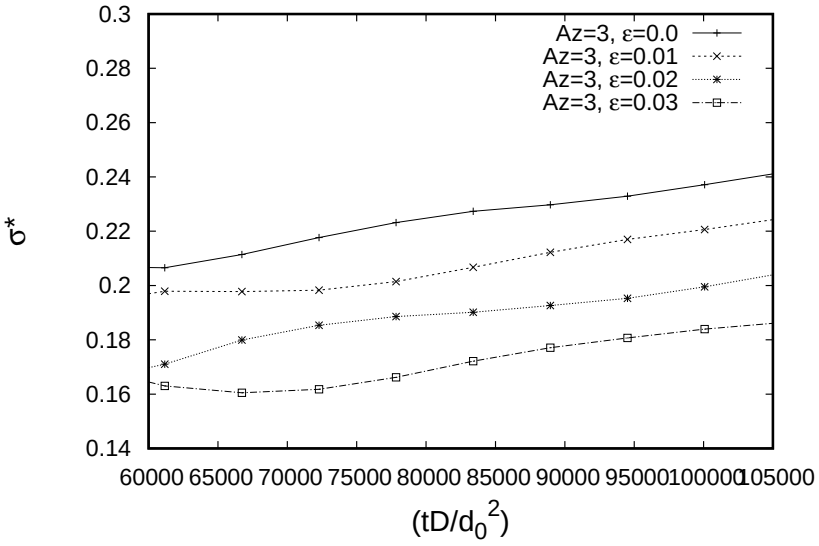

Figure 5.21: Variation of σ^* as a function of time (tD/d_0^2) for different strengths of anisotropies in interfacial energy at constant elastic anisotropy strength i.e. $A_z = 3.0$.

interfacial energy anisotropy while keeping the elastic energy anisotropy having the magnitude below one i.e. $A_z = 0.5$. An exemplary simulation with the combination of both anisotropies is depicted in Fig. 5.22, where the arms of the dendrite are oriented along $< 10 >$ directions. The

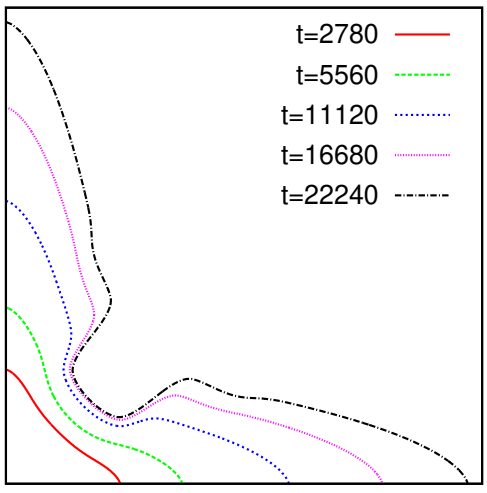

Figure 5.22: Evolution of the precipitate as a function of simulation normalized time at $A_z = 0.5, \varepsilon = 0.03$.

change in the dendrite shapes upon variation in the strength of anisotropy in the interfacial

energy is highlighted in Fig. 5.23. As the two anisotropies superimpose it leads to an effective increase in the anisotropy in the system. Thus, with increase in the magnitude of interfacial

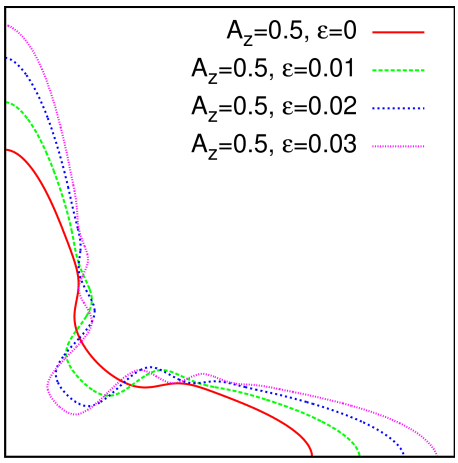

Figure 5.23: Comparison of dendrites at different strength of anisotropies in interfacial energy at $A_z = 0.5$.

energy anisotropy, the precipitate tip becomes more sharper and elongated along $< 10 >$ directions as highlighted in Fig. 5.24(a) while the dendrite tip velocity increases as the strength in anisotropy in the interfacial energy becomes larger, (see Fig. 5.24(b)). The variation of σ^*

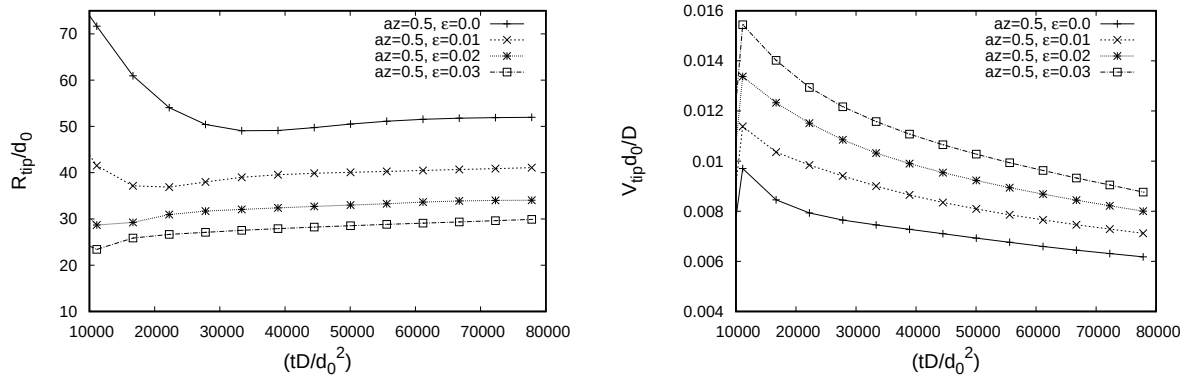

(a) (b)

Figure 5.24: Variation of R_{tip} and V_{tip} as a function of time with varying the magnitude interfacial anisotropy at $A_z = 0.5$.

with a combination of different anisotropies is portrayed in Fig. 5.25, where for a given time of evolution, with increase in the strength of anisotropy in the interfacial energy the magnitude of σ^* increases.

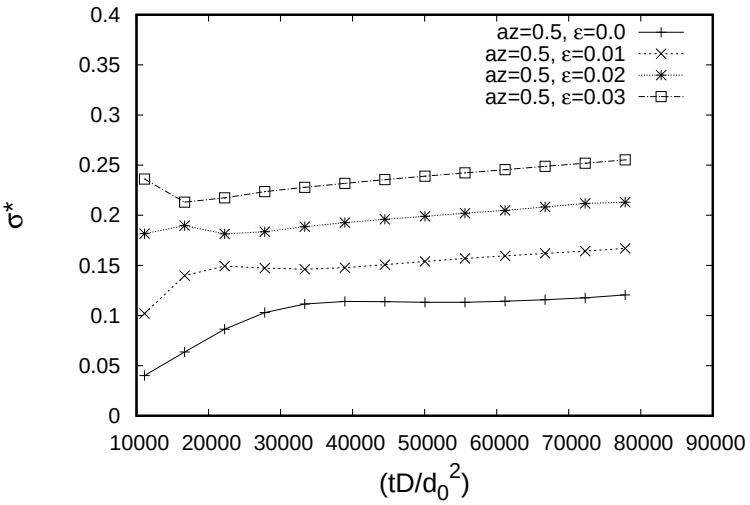

Figure 5.25: Variation of σ^* as a function time with different strengths of anisotropies in the interfacial energy at $A_z = 0.5$.

Finally, in order to show that anisotropy in either the interfacial energy or the elastic energy is required for the formation of dendrite-like structures, we consider the case of isotropic elastic and interfacial energies with the supersaturation at $\omega = 53\%$. As the precipitate grows in size, the instabilities at the interface trigger to give rise to a seaweed type structure (see Fig. 5.26), without the selection of a unique tip direction or shape. This situation can also occur for cases where the influence of the elastic energy anisotopy and the interfacial energy anisotropy cancel each other for certain combination of their respective strengths.

5.4 Summary

In this chapter, we have characterized the evolution of dendrite-like shapes as a function of elastic parameters such as the misfit-strains, Zener anisotropy strength A_z and supersaturation. We notice that while the simulated shapes resemble dendrites typically occurring during solidification, for solid-state structures in the presence of coherency stresses, the shapes of the tip as well as the velocity of the tip do not achieve a steady state. Moreover, the selection constant $\sigma^* = 2d_0D/R^2V$ increases linearly with simulation time once the primary arms appear, for all the simulation conditions, which is in contrast to dendrites derived just in the presence of interfacial energy anisotropy. This lack of steady state is due to a continuous change in the value of the jump in the elastic energy, between the precipitate and the matrix at the tip of the dendrite-like morphology, that increases as the shape of the tip evolves with time. Con-

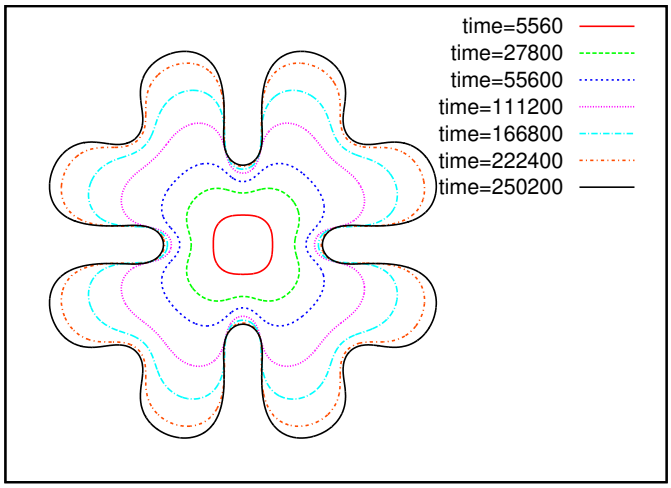

Figure 5.26: Precipitate growth without anisotropy in the elastic as well as the interfacial energy at $A_z = 1.0$ and $\epsilon^* = 0.01$.

sequently, the interfacial compositions as well as the Peclet number do not saturate. Thus, in the presence of coherency stresses, while the presence of anisotropy leads to the propagation of instabilities in well defined directions, there is no selection of a unique tip shape as in the case of solidification. Therefore, structures derived in solid-state in the presence of elastic anisotropy may only be referred to as dendrite-like. Finally, while in this study we have limited ourselves to homogenous elastic media, studies on the influence of inhomogeneity as well as combination of anisotropies in misfit strain on dendrite-tip selection remain as interesting perspectives for future work.

Chapter 6

Conclusions & Outlook

In this thesis, we have described calculations of equilibrium shapes of a precipitate and configurations of multivariant precipitates corresponding to different elastic and interfacial properties of the phases. This can provide valuable insights for the microstructures that are observed in precipitation-hardened alloys. Along with this, we have studied the growth instabilities that occur during the evolution of coherent precipitates in a supersaturated matrix in the presence of elastic anisotropy and additionally investigated the combined influence of anisotropy in the interfacial and the elastic energy.

In the following we point to the extent by which the study goes beyond the state-of-the art with respect to the phase-field studies of precipitation. Firstly, we note that ours is the first study which utilizes a phase-field model for the computation of equilibrium shapes in a setting that is similar to the sharp-interface problem of nucleation, i.e one searches for the shape of the precipitate that minimizes the sum of the elastic and the interfacial energies for a given volume or size of the precipitate. Phase-field studies exist which try to address this problem by solving the diffusional growth problem of precipitation in a closed box and the shape of the precipitate when the supersaturation goes to zero determines the equilibrium shape. Different sizes are simulated by starting with different alloy compositions. However, there is no previous phase-field study which constrains the precipitate volume while minimizing the elastic and interfacial free energies. Here, we have adapted a previously available volume-preserved Allen-Cahn approach by incorporating coherency stresses.

Secondly, we have utilized the phase-field model to present the first quantitative comparison against the bifurcation diagram derived from the theoretical approach of Johnson and Cahn. To our knowledge previous comparisons even with the sharp-interface approaches did not go beyond the comparison of the critical size for bifurcation, whereas we have have compared the entire shape of the bifurcation diagram between theory and phase-field simulations. In addition, we

have also compared the phase-field results against previous sharp-interface methods. Here, we have in addition compared the available interpolation approaches in literature for describing the variation of the elastic properties across the interfaces, which results in a remarkable finding that there is no advantage gained by adopting the complex tensorial approach against the simpler Khachaturiyan formulation. This is a non-trivial result that has not been reported before. The benchmarking of the phase-field method against known literature sets the stage for more complicated calculations involving combination of complex symmetries of the elastic misfit and stiffness matrices. Along with this, given the flexibility of the phase-field model, shapes arsing out of an interplay of the interfacial and elastic anisotropy can be readily simulated. Examples of these calculations have been presented in the thesis. In addition, a first attempt for deriving bifurcation diagrams for three-dimensional shapes using a phase-field method has been presented.

Thirdly, the extension of the model for predicting equilibrium configurations is again a new development that has been utilized to probe the existence of possible energy minimizing configurations during precipitation reactions involving multiple variants. While previous phase-field studies have been performed with multiple variants, where different configurations arising during growth are simulated, yet there has been no previous systematic study to probe the reason behind the formation of such configurations. Our study is a first attempt to address this question where the extension of the volume-preserved Allen-Cahn based approach for incorporating multiple phases allows one to investigate the probable minimizing configurations and additionally hierarchically characterize their feasibility based on their total energies. This feature of the model has the possibility to provide wide ranging insights in a large class of solid-state precipitations.

Finally, we have presented an extension of the grand-potential approach for the simulation of dendrite-like structures. This is the first reported attempt to do so. Additionally, to our knowledge there is only one paper in literature[46] that deals with the numerical simulation of such structures using a different phase-field model. In this regard the study presented in this thesis, reports results over and above that is already presented before.

Further, we review the key results from the respective chapters in the thesis.

6.1 Phase-field modeling of equilibrium shapes of the precipitate under the influence of coherency stresses

In Chapter 3, we present a vast range of equilibrium shapes of the precipitate that obtained in two dimensions as well as in three dimensions using a novel phase-field model. We observe and study a symmetry-breaking transition as the precipitate size is increased, which is seen in the classical theory proposed by Johnson and Cahn [3]. The shape bifurcation diagram calculated from our phase-field results corroborates with the analytical solution given in [3]. Also, there is an excellent agreement between the results obtained from our phase-field model and from a sharp-interface numerical technique [21]. In this analysis, in two dimensions, we have calculated the equilibrium shapes of the precipitate in the presence of anisotropies in both the energies i.e. the elastic energy as well as the interfacial energy. The corresponding analysis investigating the use of larger anisotropy strengths in the interfacial energy which could lead to formation of facets in the equilibrium shapes is yet to be performed. This will require regularization of the interfacial energy forms. Also, it remains a scope for future work to investigate the equilibrium shape of the precipitate in three dimensions in the presence of anisotropies in both the energies. Similarly, the influence of compositions on the misfit-strains can become critical in multi-component alloys where the compositions of the phases that arise are a function of the diffusivities of the relevant species. This might require an extension of the model for the computation of equilibrium shapes, where the chemical as well as the mechanical problem need to be solved in a coupled manner.

6.2 Equilibrium multi-precipitate configurations

In chapter 4, we present the results on equilibrium configurations of the precipitate that are calculated using the multiphase-field model elaborated in chapter 2.2. We first determine the necessary and sufficient conditions that give rise to the formation of the core-shell microstructures observed in certain precipitation-hardened alloys. We have observed that the core-shell structure forms if and only if the criteria of solid-state wetting is satisfied i.e. the magnitude of the interfacial energy of one of the interfaces has to be larger than the sum of the magnitudes of the interfacial energies of the remaining interfaces. The presence of elastic fields due to misfit at the interface, also plays a role, by influencing the interaction between the precipitates. We find that the softer precipitates ($\delta < 1.0$) with opposite sign, have the most attractive interaction, whereas harder precipitates (i.e. for $\delta > 1.0$), repel each other. Thus, we postulate that, in the

earlier situation where an attractive interaction exists, one would expect to find a statistically larger ensemble of core-shell formation of the precipitate phases in the experiments than the latter, provided the solid-state wetting condition is satisfied.

Another aspect that we have investigated, is the symmetry-breaking transitions that lead to the formation of multi-variant clusters where we study the organization of the precipitates as a function of the elastic properties of the precipitate and the matrix. In both the transformations, on the basis of the energetic calculations, we show that the co-nucleation of the multi-variant configuration of the precipitates is energetically favored to the nucleation of a single precipitate beyond a certain precipitate size, as the increase in the interfacial energy due to formation of the cluster is well compensated by the reduction in the elastic energy. Interesting directions for future work follow ideas similar to those described for single precipitate equilibrium, wherein, multi-component alloys with the additional complexity of the variation of misfit strains with equilibrium compositions might require the solution to the complete chemo-mechanical equilibrium solution. This will open new possibilities wherein apart from the different elastic properties, the alloy composition would possibly become an important parameter influencing both the shapes as well the self-organization of the configurations.

6.3 Precipitate growth under the influence of coherency stresses

In this chapter 5, unlike previous chapters, we allow the precipitate to evolve in size provided the matrix is supersaturated. Here, we study the precipitate shape evolution into a dendrite-like structure as a function of different parameters such as the misfit-strains, Zener anisotropy strength A_z, supersaturation and the competition between the strength of anisotropies in the elastic as well as the interfacial energies. We notice that although the precipitate grows into a dendrite-like structure with imposed anisotropy in the elastic energy, the shapes of the tip as well as the velocity of the tip do not achieve a steady state. Also, the selection constant $\sigma^* = 2d_0D/R_{tip}^2V_{tip}$ increases linearly along with the simulation time, once the primary arms appear for all the simulation conditions. Thus, the presence of elastic energy anisotropy gives rise to the propagation of instabilities in well-defined directions. However, there is no selection of a unique tip shape which is observed in classical solidification. Future directions of study involve understanding the influence of inhomogeneity in elastic moduli, combination of anisotropies in both the elastic-misfit and the elastic energy on the tip dynamics and shape. Additionally, in multi-component alloys, the relative diffusivities of the different elements can lead to widely

different dendritic shapes as the effective capillary length may change appreciably. Therefore, the relative ratio of the diffusivities becomes an important parameter whose influence on the instability needs to be established in alloys with three or more components. Finally, while we have discussed only precipitate growth, the model is generic and may be utilized for studies of late-stage coarsening, where extension to multi-component alloys will again bring in exciting new possibilities.

Appendices

.A Appendix

.A.1 Elastic free energy density

Eqn. 2.8 gives the elastic free energy density, which includes several prefactors i.e. Z_3, Z_2, Z_1, Z_0. These prefactors are dependent on particular values of elastic constant in respective phases i.e. the precipitate and matrix. Their expressions are as follows: Here $C_{11}^{\alpha,\beta} = C_{1111}^{\alpha,\beta}, C_{22}^{\alpha,\beta} = C_{2222}^{\alpha,\beta}, C_{44}^{\alpha,\beta} = C_{1212}^{\alpha,\beta}, C_{12}^{\alpha,\beta} = C_{1122}^{\alpha,\beta}$.

$$
\begin{aligned}
Z_3 &= \left(C_{11}^{\alpha} - C_{11}^{\beta} + C_{12}^{\alpha} - C_{12}^{\beta}\right)\epsilon^{*2}, \\
Z_2 &= (C_{11}^{\beta} - C_{11}^{\alpha})(\epsilon_{xx} + \epsilon_{yy})\epsilon^{*} + (C_{12}^{\beta} - C_{12}^{\alpha})(\epsilon_{xx} + \epsilon_{yy})\epsilon^{*} \\
&\quad + (C_{11}^{\beta} + C_{12}^{\beta})\epsilon^{*2}, \\
Z_1 &= \frac{1}{2}(C_{11}^{\alpha} - C_{11}^{\beta})(\epsilon_{xx} + \epsilon_{yy})\epsilon^{*} - C_{11}^{\beta}(\epsilon_{xx} + \epsilon_{yy})\epsilon^{*} \\
&\quad + (C_{12}^{\alpha} - C_{12}^{\beta})\epsilon_{xx}\epsilon_{yy} - \frac{1}{2}C_{12}^{\beta}(\epsilon_{xx} + \epsilon_{yy})\epsilon_{yy} \\
&\quad + 2(C_{44}^{\alpha} - C_{44}^{\beta})\epsilon_{xy}^{2}, \\
Z_0 &= \frac{1}{2}(C_{11}^{\beta}(\epsilon_{xx}^{2} + \epsilon_{yy}^{2}) + C_{44}^{\beta}\epsilon_{xy} + C_{12}^{\beta}\epsilon_{xx}\epsilon_{yy}).
\end{aligned}
$$

.A.2 Stress-strain profiles

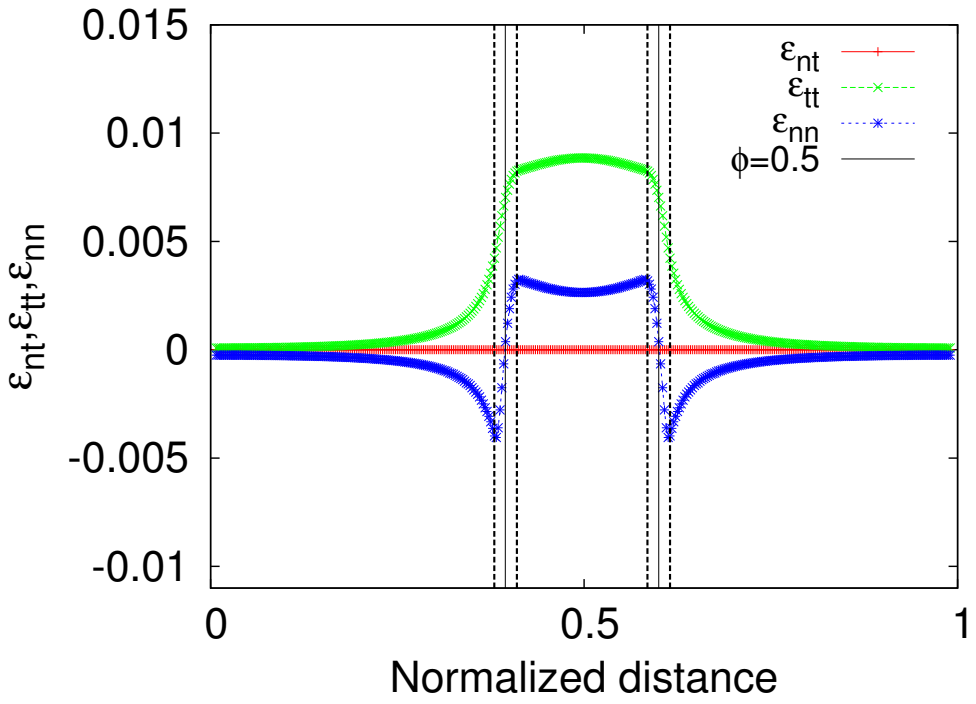

Figure 1: 1D section of strain profile obtained from 2D domain across the center of precipitate where the region occupied between the dotted lines represents the diffuse interface, at $\delta = 0.5$, $\mu_{mat} = 125$.

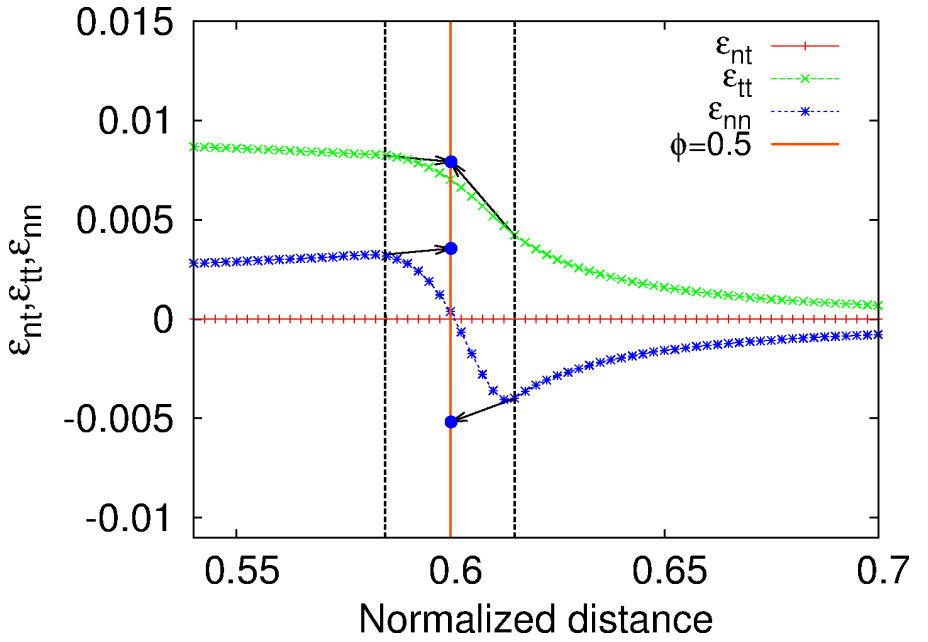

Figure 2: The zoomed section of the interface showing strain profile across the center of precipitate, thick orange line passes through the interface at $\phi = 0.5$.

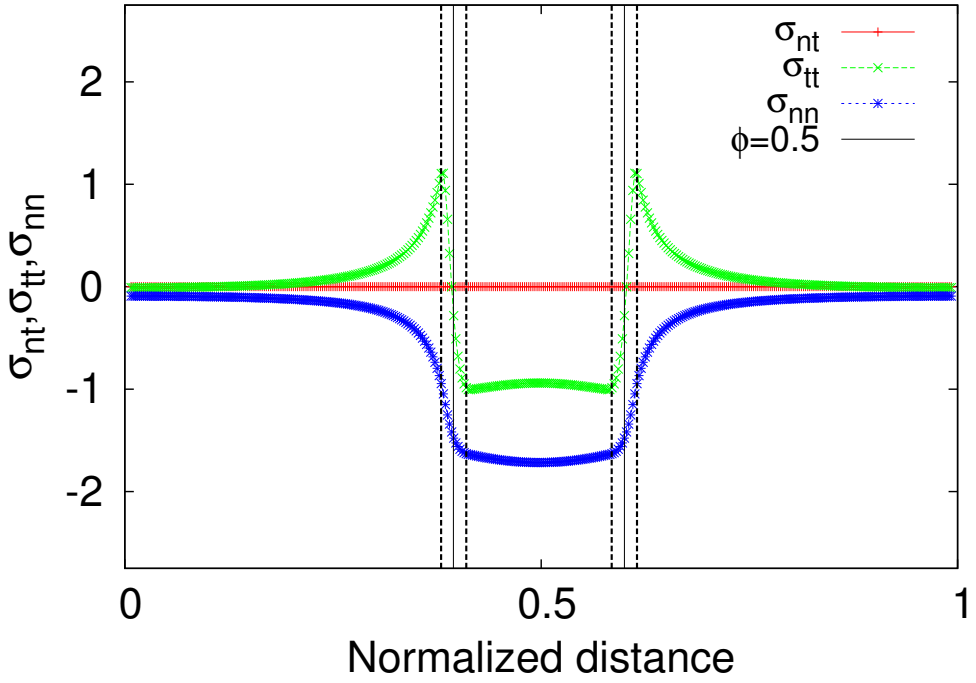

Figure 3: 1D section of stress profile obtained from 2D domain across the center of precipitate where the region occupied between the dotted lines represents the diffuse interface, at $\delta = 0.5$, $\mu_{matrix} = 125$.

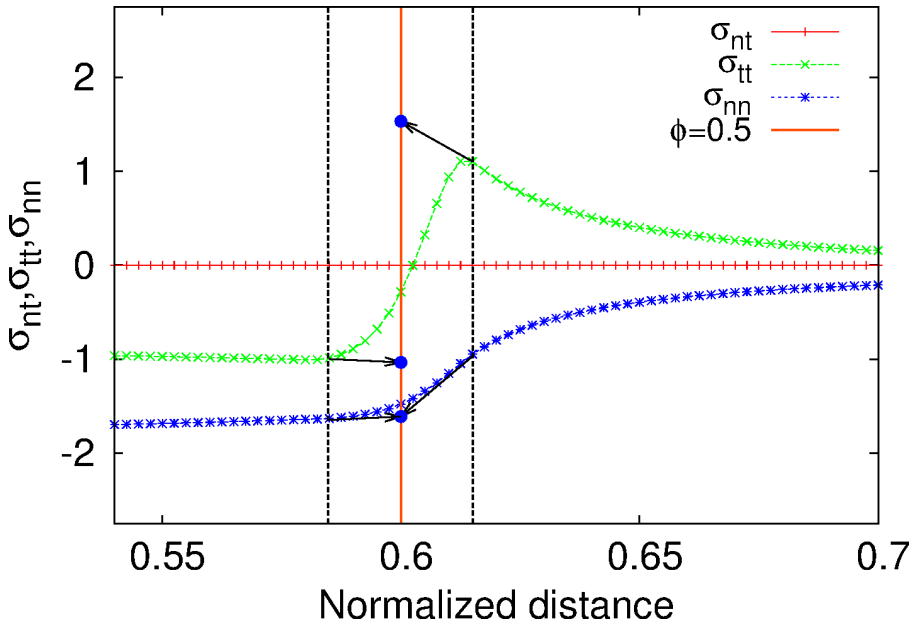

Figure 4: The zoomed section of the interface showing 1D stress profile across the center of precipitate, thick orange line passes through the interface at $\phi = 0.5$.

.A.3 Implementation in OpenFoam

Here, We elaborate how the different equations from the formulations of multi-precipitate equilibrium configurations are implemented in OpenFoam. The Allen Cahn dynamics for the evolution of phase-field variables (ϕ_α) is given by following equations,

$$\tau W \frac{\partial \phi_\alpha}{\partial t} = -\frac{\delta \mathcal{F}}{\delta \phi_\alpha}, \tag{1}$$

$$\tau W \frac{\partial \phi_\alpha}{\partial t} = -\frac{\delta \mathcal{F}}{\delta \phi_\alpha} - \lambda_p - \lambda_\alpha^v h'\left(\phi_\alpha\right), \tag{2}$$

for the precipitate phases $\alpha = 1, 2, 3, ..N-1$, while for the matrix phase the evolution equation reads,

$$\tau W \frac{\partial \phi_\alpha}{\partial t} = -\frac{\delta \mathcal{F}}{\delta \phi_\alpha} - \lambda_p. \tag{3}$$

Further, this can be implemented in OpenFoam as follows:

```
strain=((gradD-((T0*T0*(3-2*T0)*cEigenStrain0)
        +(T1*T1*(3-2*T1)*cEigenStrain1)+(T2*T2*(3-2*T2)*cEigenStrain2)))
         &&symmTensor(1,0,0,0,0,0))*symmTensor(1,0,0,0,0,0)
         +((gradD-((T0*T0*(3-2*T0)*cEigenStrain0)
         +(T1*T1*(3-2*T1)*cEigenStrain1)
         +(T2*T2*(3-2*T2)*cEigenStrain2)))
         &&symmTensor(0,0,0,1,0,0))*symmTensor(0,0,0,1,0,0)
         +((gradD-((T0*T0*(3-2*T0)*cEigenStrain0)
         +(T1*T1*(3-2*T1)*cEigenStrain1)
         +(T2*T2*(3-2*T2)*cEigenStrain2)))
         &&symmTensor(0,0,0,0,0,1))*symmTensor(0,0,0,0,0,1);


Sigma = (2*(mu0*T0*T0*(3-2*T0) + mu1*T1*T1*(3-2*T1)
         +mu2*T2*T2*(3-2*T2) +mu3*T3*T3*(3-2*T3))*(symm(fvc::grad(D))
         -(T0*T0*(3-2*T0)*cEigenStrain0 + T1*T1*(3-2*T1)*cEigenStrain1
```

```
        +T2*T2*(3-2*T2)*cEigenStrain2))
        +(lambda0*T0*T0*(3-2*T0) + lambda1*T1*T1*(3-2*T1)
        + lambda2*T2*T2*(3-2*T2)
        +lambda3*T3*T3*(3-2*T3))*(I*tr(fvc::grad(D)
        -(T0*T0*(3-2*T0)*cEigenStrain0 + T1*T1*(3-2*T1)*cEigenStrain1
        +T2*T2*(3-2*T2)*cEigenStrain2))))
        +(mu0_*T0*T0*(3-2*T0) + mu1_*T1*T1*(3-2*T1)
        +mu2_*T2*T2*(3-2*T2) +mu3_*T3*T3*(3-2*T3))*strain;

deltaSigmaD = ((mu0)*twoSymm(fvc::grad(D))
              +(lambda0)*(I*tr(fvc::grad(D)))
              -2*(mu0)*(T0*T0*(3-2*T0)*cEigenStrain0
              +T1*T1*(3-2*T1)*cEigenStrain1
              +T2*T2*(3-2*T2)*cEigenStrain2)
              -(lambda0)*(I*tr((T0*T0*(3-2*T0)*cEigenStrain0
              +T1*T1*(3-2*T1)*cEigenStrain1
              +T2*T2*(3-2*T2)*cEigenStrain2))))
              +(mu0_)*strain;


fvScalarMatrix T0Eqn
(
        sigt*Tau*Epsilon*fvm::ddt(T0)
        -2.0*gamma_0*Epsilon*sig1*fvm::laplacian(DTs, T0)
        ==
        -(18.0*gamma_0*T0*(1.0 -T0)*(1.0 -2.0*T0))/(Epsilon)
        -(6.0*T0*(1-T0)*(0.5*(deltaSigmaD && (symm(fvc::grad(D))
        -T0*T0*(3-2*T0)*cEigenStrain0 - T1*T1*(3-2*T1)*cEigenStrain1
        -T2*T2*(3-2*T2)*cEigenStrain2))-(Sigma && cEigenStrain0)))
);
    deltaSigmaD = ((mu1)*twoSymm(fvc::grad(D))
                +(lambda1)*(I*tr(fvc::grad(D)))
                -2*(mu1)*(T0*T0*(3-2*T0)*cEigenStrain0
                +T1*T1*(3-2*T1)*cEigenStrain1
                +T2*T2*(3-2*T2)*cEigenStrain2)
```

```
                -(lambda1)*(I*tr((T0*T0*(3-2*T0)*cEigenStrain0
                +T1*T1*(3-2*T1)*cEigenStrain1
                +T2*T2*(3-2*T2)*cEigenStrain2))))
                +(mu1_)*strain;

fvScalarMatrix T1Eqn
(
        sigt*Tau*Epsilon*fvm::ddt(T1)
        -2.0*gamma_1*Epsilon*sig1*fvm::laplacian(DTs, T1)
        ==
        -(18.0*gamma_1*T1*(1.0 -T1)*(1.0 -2.0*T1))/(Epsilon)
        -(6.0*T1*(1-T1)*(0.5*(deltaSigmaD && (symm(fvc::grad(D))
        -T0*T0*(3-2*T0)*cEigenStrain0 - T1*T1*(3-2*T1)*cEigenStrain1
        -T2*T2*(3-2*T2)*cEigenStrain2))-(Sigma && cEigenStrain1)))
);
    deltaSigmaD = ((mu2)*twoSymm(fvc::grad(D))
                +(lambda2)*(I*tr(fvc::grad(D)))
                -2*(mu2)*(T0*T0*(3-2*T0)*cEigenStrain0
                +T1*T1*(3-2*T1)*cEigenStrain1
                +T2*T2*(3-2*T2)*cEigenStrain2)
                -(lambda2)*(I*tr((T0*T0*(3-2*T0)*cEigenStrain0
                +T1*T1*(3-2*T1)*cEigenStrain1
                +T2*T2*(3-2*T2)*cEigenStrain2))))
                +(mu2_)*strain;

fvScalarMatrix T2Eqn
(
        sigt*Tau*Epsilon*fvm::ddt(T2)
        -2.0*gamma_2*Epsilon*sig1*fvm::laplacian(DTs, T2)
        ==
        -(18.0*gamma_2*T2*(1.0 -T2)*(1.0 -2.0*T2))/(Epsilon)
        -(6.0*T2*(1-T2)*(0.5*(deltaSigmaD && (symm(fvc::grad(D))
        -T0*T0*(3-2*T0)*cEigenStrain0 - T1*T1*(3-2*T1)*cEigenStrain1
        - T2*T2*(3-2*T2)*cEigenStrain2))-(Sigma && cEigenStrain2)))
);
```

```
    deltaSigmaD = ((mu3)*twoSymm(fvc::grad(D))
                +(lambda3)*(I*tr(fvc::grad(D)))
                -2*(mu3)*(T0*T0*(3-2*T0)*cEigenStrain0
                +T1*T1*(3-2*T1)*cEigenStrain1
                +T2*T2*(3-2*T2)*cEigenStrain2)
                -(lambda3)*(I*tr((T0*T0*(3-2*T0)*cEigenStrain0
                +T1*T1*(3-2*T1)*cEigenStrain1
                +T2*T2*(3-2*T2)*cEigenStrain2))))
                +(mu3_)*strain;

fvScalarMatrix T3Eqn
(
        sigt*Tau*Epsilon*fvm::ddt(T3)
        -2.0*gamma_3*Epsilon*sig1*fvm::laplacian(DTs, T3)
        ==
        -(18.0*gamma_3*T3*(1.0 -T3)*(1.0 -2.0*T3))/(Epsilon)
        -6.0*T3*(1-T3)*(0.5*(deltaSigmaD && (symm(fvc::grad(D))
        -T0*T0*(3-2*T0)*cEigenStrain0 - T1*T1*(3-2*T1)*cEigenStrain1
        -T2*T2*(3-2*T2)*cEigenStrain2)))
);

T0Eqn.solve();
T1Eqn.solve();
T2Eqn.solve();
T3Eqn.solve();

scalar numphases = 4.0;

lambda_phase = sigt*((fvc::ddt(T0) + fvc::ddt(T1) + fvc::ddt(T2)
             + fvc::ddt(T3))/numphases);
Info<< "Min/max␣lambda_phase:" << min(lambda_phase()).value()
<< '\t'<< max(lambda_phase()).value() << endl;

deltaT0 = sigt*fvc::ddt(T0) - lambda_phase;
deltaT1 = sigt*fvc::ddt(T1) - lambda_phase;
```

```
deltaT2 = sigt*fvc::ddt(T2) - lambda_phase;
deltaT3 = sigt*fvc::ddt(T3) - lambda_phase;

T0 -=  lambda_phase*runTime.deltaTValue();
T1 -=  lambda_phase*runTime.deltaTValue();
T2 -=  lambda_phase*runTime.deltaTValue();
T3 -=  lambda_phase*runTime.deltaTValue();

scalar lambdaVol_0 = 0.0;
scalar lambdaVol_1 = 0.0;
scalar lambdaVol_2 = 0.0;

scalar sumHprime_0 = 0.0;
scalar sumHprime_1 = 0.0;
scalar sumHprime_2 = 0.0;

scalar sumRHS0 = 0.0;
scalar sumRHS1 = 0.0;
scalar sumRHS2 = 0.0;

sumRHS0 = gSum(deltaT0());
sumRHS1 = gSum(deltaT1());
sumRHS2 = gSum(deltaT2());


volScalarField Hphi_0 =  6.0*T0*(1-T0);
volScalarField Hphi_1 =  6.0*T1*(1-T1);
volScalarField Hphi_2 =  6.0*T2*(1-T2);

sumHprime_0 = gSum(Hphi_0());
sumHprime_1 = gSum(Hphi_1());
sumHprime_2 = gSum(Hphi_2());

lambdaVol_0  = (2.0*sumRHS0 + sumRHS1 + sumRHS2)/sumHprime_0;
lambdaVol_1  = (sumRHS0 + 2.0*sumRHS1 + sumRHS2)/sumHprime_1;
```

```
lambdaVol_2  = (sumRHS0 + sumRHS1 + 2.0*sumRHS2)/sumHprime_2;
volScalarField lambdaVol_3
= ((6.0*T0*(1-T0)*lambdaVol_0 + 6.0*T1*(1-T1)*lambdaVol_1
+ 6.0*T2*(1-T2)*lambdaVol_2)/numphases);

Info<< "Min/max␣sum_lambda:" << min((6.0*T0*(1-T0)*lambdaVol_0
+ 6.0*T1*(1-T1)*lambdaVol_1 + 6.0*T2*(1-T2)*lambdaVol_2)
-numphases*lambdaVol_3).value() << '\t'<<
max((6.0*T0*(1-T0)*lambdaVol_0 + 6.0*T1*(1-T1)*lambdaVol_1
+ 6.0*T2*(1-T2)*lambdaVol_2)-numphases*lambdaVol_3).value()
<< endl;

deltaT0 = -(6.0*T0*(1-T0)*lambdaVol_0 -lambdaVol_3);
deltaT1 = -(6.0*T1*(1-T1)*lambdaVol_1 -lambdaVol_3);
deltaT2 = -(6.0*T2*(1-T2)*lambdaVol_2 -lambdaVol_3);
deltaT3 = lambdaVol_3;

scalar gsum_lambdaVol_0 = 0.0;
scalar gsum_lambdaVol_1 = 0.0;
scalar gsum_lambdaVol_2 = 0.0;

gsum_lambdaVol_0 = gSum(deltaT0());
gsum_lambdaVol_1 = gSum(deltaT1());
gsum_lambdaVol_2 = gSum(deltaT2());

Info<< "gsum_lambdaVol_0:␣" << (gsum_lambdaVol_0) << endl;
Info<< "gsum_lambdaVol_1:␣" << (gsum_lambdaVol_1) << endl;
Info<< "gsum_lambdaVol_2:␣" << (gsum_lambdaVol_2) << endl;

T0 +=  deltaT0*runTime.deltaTValue();
T1 +=  deltaT1*runTime.deltaTValue();
T2 +=  deltaT2*runTime.deltaTValue();
T3 +=  deltaT3*runTime.deltaTValue();
```

Similarly, for the calculation of displacement fields $(\boldsymbol{u_x}, \boldsymbol{u_y})$ which is given by momentum

conservation of solid body which includes the stress developed due to phase transformation.

$$\rho\frac{d^2\boldsymbol{u}}{dt^2} + b\frac{d\boldsymbol{u}}{dt} = \nabla\cdot\boldsymbol{\sigma}, \tag{4}$$

which is implemented in OpenFoam as:

```
#include "fvCFD.H"
#include "fvOptions.H"
#include "simpleControl.H"
#include "Switch.H"

// * * * * * * * * * * * * * * * * * * * * * * * * *//

int main(int argc, char *argv[])
{
    #include "postProcess.H"

    #include "setRootCase.H"
    #include "createTime.H"
    #include "createMesh.H"
    #include "createControls.H"
    #include "createFields.H"

    // * * * * * * * * * * * * * * * * * * * * * * * //

 Info<< "Calculating␣displacement␣field" << endl;
 while (runTime.loop())
 {
    Info<< "Iteration:␣" << runTime.value() << nl << endl;
    #include "readSolidDisplacementFoamControls.H"
    int iCorr = 0;
    scalar initialResidual = 0;
    D.correctBoundaryConditions();
    gradD = fvc::grad(D);
    #include "TEqnVarElast.H"
do
```

```
{
 {
   fvVectorMatrix DEqn
   (
     fvm::d2dt2(D)
      ==
      sig3*fvm::laplacian(2*(mu0*T0*T0*(3-2*T0)
      +mu1*T1*T1*(3-2*T1) +mu2*T2*T2*(3-2*T2)
      +mu3*T3*T3*(3-2*T3)) +(lambda0*T0*T0*(3-2*T0)
      +lambda1*T1*T1*(3-2*T1) +lambda2*T2*T2*(3-2*T2)
      +lambda3*T3*T3*(3-2*T3)),D,"laplacian(DD,D)")
      +(sig3/sig2)*divSigmaExp
      -(sig3)*fvc::div(2*(mu0*T0*T0*(3-2*T0)
      +mu1*T1*T1*(3-2*T1) +mu2*T2*T2*(3-2*T2)
      +mu3*T3*T3*(3-2*T3))*(T0*T0*(3-2*T0)*cEigenStrain0
      +T1*T1*(3-2*T1)*cEigenStrain1 +T2*T2*(3-2*T2)*cEigenStrain2)
      +(lambda0*T0*T0*(3-2*T0) +lambda1*T1*T1*(3-2*T1)
      +lambda2*T2*T2*(3-2*T2) +lambda3*T3*T3*(3-2*T3))
      *I*tr(T0*T0*(3-2*T0)*cEigenStrain0
      +T1*T1*(3-2*T1)*cEigenStrain1 +T2*T2*(3-2*T2)*cEigenStrain2))
    );


 initialResidual = DEqn.solve().max().initialResidual();

 if (!compactNormalStress)
  {
   divSigmaExp = fvc::div(DEqn.flux());
  }
 }

{
  gradD = fvc::grad(D);

   strain=((gradD-((T0*T0*(3-2*T0)*cEigenStrain0)
```

```
      +(T1*T1*(3-2*T1)*cEigenStrain1)
      +(T2*T2*(3-2*T2)*cEigenStrain2)))
      &&symmTensor(1,0,0,0,0,0))*symmTensor(1,0,0,0,0,0)
      +((gradD-((T0*T0*(3-2*T0)*cEigenStrain0)
      +(T1*T1*(3-2*T1)*cEigenStrain1)
      +(T2*T2*(3-2*T2)*cEigenStrain2)))
      &&symmTensor(0,0,0,1,0,0))*symmTensor(0,0,0,1,0,0)
      +((gradD-((T0*T0*(3-2*T0)*cEigenStrain0)
      +(T1*T1*(3-2*T1)*cEigenStrain1)
      +(T2*T2*(3-2*T2)*cEigenStrain2)))
      &&symmTensor(0,0,0,0,0,1))*symmTensor(0,0,0,0,0,1);


 sigmaD =(mu0*T0*T0*(3-2*T0) +mu1*T1*T1*(3-2*T1)
        +mu2*T2*T2*(3-2*T2)
        +mu3*T3*T3*(3-2*T3))*twoSymm(gradD)
        +(lambda0*T0*T0*(3-2*T0)
        +lambda1*T1*T1*(3-2*T1) +lambda2*T2*T2*(3-2*T2)
        +lambda3*T3*T3*(3-2*T3))*(I*tr(gradD))
        +(mu0_*T0*T0*(3-2*T0) +mu1_*T1*T1*(3-2*T1)
        +mu2_*T2*T2*(3-2*T2)
        +mu3_*T3*T3*(3-2*T3))*strain;


if (compactNormalStress)
{
 divSigmaExp = sig2*fvc::div
 (
    sigmaD -(2*(mu0*T0*T0*(3-2*T0) + mu1*T1*T1*(3-2*T1)
    +mu2*T2*T2*(3-2*T2) + mu3*T3*T3*(3-2*T3))
    +(lambda0*T0*T0*(3-2*T0) + lambda1*T1*T1*(3-2*T1)
    +lambda2*T2*T2*(3-2*T2) + lambda3*T3*T3*(3-2*T3)))*gradD,
     "div(sigmaD)"
   );
 }
```

```
    else
    {
     divSigmaExp += sig2*fvc::div(sigmaD);
     }
 }

 }while(initialResidual>convergenceTolerance && ++iCorr<nCorr);

#include "calculateStress.H"

Info<< "ExecutionTime=" << runTime.elapsedCpuTime() << "s"
        << "ClockTime=" << runTime.elapsedClockTime() << "s"
        << nl << endl;

    volScalarField consta(0.5*(Sigma && (symm(gradD)
    -T0*T0*(3-2*T0)*cEigenStrain0
    -T1*T1*(3-2*T1)*cEigenStrain1
    -T2*T2*(3-2*T2)*cEigenStrain2)));

    volScalarField constc((1-T3)*(0.5*(Sigma && (symm(gradD)
    -T0*T0*(3-2*T0)*cEigenStrain0
    -T1*T1*(3-2*T1)*cEigenStrain1
    -T2*T2*(3-2*T2)*cEigenStrain2))));

  volVectorField gradT0(fvc::grad(T0));
  volVectorField gradT1(fvc::grad(T1));
  volVectorField gradT2(fvc::grad(T2));
  volVectorField gradT3(fvc::grad(T3));

  volScalarField constb(2.0*gamma_0*Epsilon*(magSqr(gradT0))
  +2.0*gamma_1*Epsilon*(magSqr(gradT1))
  +2.0*gamma_2*Epsilon*(magSqr(gradT2))
  +2.0*gamma_3*Epsilon*(magSqr(gradT3)));

  dimensionedScalar elasticEnergyGsum = gSum(consta());
```

```
  dimensionedScalar surfaceEnergyGsum = gSum(constb());
  dimensionedScalar totalEnergyGsum   = elasticEnergyGsum
                                      + surfaceEnergyGsum;
  dimensionedScalar elasticEnergyPrecipitateGum
        = gSum(constc());

  Info<< "elasticEnergyGsum: " << (elasticEnergyGsum) << endl;
  Info<< "surfaceEnergyGsum: " << (surfaceEnergyGsum) << endl;
  Info<< "totalEnergyGsum: " << (totalEnergyGsum) << endl;
  Info<< "elasticEnergyPrecipitateGum:
  " << (elasticEnergyPrecipitateGum) << endl;

    }
 Info<< "End\n" << endl;
 return 0;
}
```

Bibliography

[1] Bhalchandra Bhadak, R Sankarasubramanian, and Abhik Choudhury. Phase-field modeling of equilibrium precipitate shapes under the influence of coherency stresses. *Metallurgical and Materials Transactions A*, 49(11):5705–5726, 2018. iii, 27

[2] Harald Garcke, Britta Nestler, Bjorn Stinner, and Frank Wendler. Allen–cahn systems with volume constraints. *Mathematical Models and Methods in Applied Sciences*, 18(08):1347–1381, 2008. iii, 4, 10, 14, 27

[3] WC Johnson and JW Cahn. Elastically induced shape bifurcations of inclusions. *Acta metallurgica*, 32(11):1925–1933, 1984. iv, 2, 37, 41, 75, 88, 128

[4] CS Jog, R Sankarasubramanian, and TA Abinandanan. Symmetry-breaking transitions in equilibrium shapes of coherent precipitates. *Journal of the Mechanics and Physics of Solids*, 48(11):2363–2389, 2000. iv, xvi, xvii, 3, 4, 5, 39, 40, 42, 44, 45, 49, 50, 75

[5] Surendra Kumar Makineni, Sandeep Sugathan, Subhashish Meher, Rajarshi Banerjee, Saswata Bhattacharya, Subodh Kumar, and Kamanio Chattopadhyay. Enhancing elevated temperature strength of copper containing aluminium alloys by forming l1 2 al 3 zr precipitates and nucleating theta prime precipitates on them. *Scientific reports*, 7(1):1–9, 2017. viii, 5, 7, 92, 104

[6] JG Conley, ME Fine, and JR Weertman. Effect of lattice disregistry variation on the late stage phase transformation behavior of precipitates in ni al mo alloys. *Acta Metallurgica*, 37(4):1251–1263, 1989. 1

[7] Abhay Maheshwari and Alan J Ardell. Elastic interactions and their effect on gamma prime precipitate shapes in aged dilute ni-al alloys. *Scripta Metallurgica et Materialia;(United States)*, 26, 1992. 1, 5

[8] AJ Ardell. The growth of gamma prime precipitates in aged ni- ti alloys. *Metallurgical and Materials Transactions B*, 1(2):525–534, 1970. 1, 5

[9] PK Rastogi and A Jo Ardell. The coarsening behavior of the precipitate in nickel-silicon alloys. *Acta Metallurgica*, 19(4):321–330, 1971. 1, 5

[10] DJ Chellman and AJ Ardell. The coarsening of precipitates at large volume fractions. *Acta Metallurgica*, 22(5):577–588, 1974. 1

[11] AJ Ardell. Precipitation hardening. *Metallurgical Transactions A*, 16(12):2131–2165, 1985. 1

[12] David N Seidman, Emmanuelle A Marquis, and David C Dunand. Precipitation strengthening at ambient and elevated temperatures of heat-treatable al (sc) alloys. *Acta Materialia*, 50(16):4021–4035, 2002. 1

[13] Tresa M Pollock and Sammy Tin. Nickel-based superalloys for advanced turbine engines: chemistry, microstructure and properties. *Journal of propulsion and power*, 22(2):361–374, 2006. 1, 5

[14] PETER W Voorhees, GB McFadden, and WC Johnson. On the morphological development of second-phase particles in elastically-stressed solids. *Acta Metallurgica et Materialia*, 40(11):2979–2992, 1992. 2, 4, 5, 74, 75

[15] ME Thompson, CS Su, and PW Voorhees. The equilibrium shape of a misfitting precipitate. *Acta metallurgica et materialia*, 42(6):2107–2122, 1994. 2, 11, 71

[16] ME Thompson and PW Voorhees. Equilibrium particle morphologies in elastically stressed coherent solids. *Acta materialia*, 47(3):983–996, 1999. 2

[17] XIAOFAN Li, KATSUYO Thornton, Q Nie, PW Voorhees, and JOHN S Lowengrub. Two-and three-dimensional equilibrium morphology of a misfitting particle and the gibbs-thomson effect. *Acta materialia*, 52(20):5829–5843, 2004. 2

[18] I Schmidt and D Gross. The equilibrium shape of an elastically inhomogeneous inclusion. *Journal of the Mechanics and Physics of Solids*, 45(9):1521–1549, 1997. 2, 4, 5, 74, 75

[19] I Schmidt, R Mueller, and D Gross. The effect of elastic inhomogeneity on equilibrium and stability of a two particle morphology. *Mechanics of Materials*, 30(3):181–196, 1998. 3

[20] R Mueller and D Gross. 3d simulation of equilibrium morphologies of precipitates. *Computational materials science*, 11(1):35–44, 1998. 3

[21] R Sankarasubramanian, CS Jog, and TA Abinandanan. Symmetry-breaking transitions in equilibrium shapes of coherent precipitates: Effect of elastic anisotropy and inhomogeneity. *Metallurgical and Materials Transactions A*, 33(4):1083–1090, 2002. 3, 128

[22] H-J Jou, Perry H Leo, and John S Lowengrub. Microstructural evolution in inhomogeneous elastic media. *Journal of Computational Physics*, 131(1):109–148, 1997. 3, 4

[23] S Kolling, R Mueller, and D Gross. The influence of elastic constants on the shape of an inclusion. *International journal of solids and structures*, 40(17):4399–4416, 2003. 3

[24] Norio Akaiwa, K Thornton, and Peter W Voorhees. Large-scale simulations of microstructural evolution in elastically stressed solids. *Journal of computational physics*, 173(1):61–86, 2001. 3

[25] Ravindra Duddu, David L Chopp, Peter Voorhees, and Brian Moran. Diffusional evolution of precipitates in elastic media using the extended finite element and the level set methods. *Journal of Computational Physics*, 230(4):1249–1264, 2011. 3, 4

[26] Xujun Zhao, Ravindra Duddu, Stephane PA Bordas, and Jianmin Qu. Effects of elastic strain energy and interfacial stress on the equilibrium morphology of misfit particles in heterogeneous solids. *Journal of the Mechanics and Physics of Solids*, 61(6):1433–1445, 2013. 3, 4, 74, 75

[27] Xujun Zhao, Stéphane PA Bordas, and Jianmin Qu. Equilibrium morphology of misfit particles in elastically stressed solids under chemo-mechanical equilibrium conditions. *Journal of the Mechanics and Physics of Solids*, 81:1–21, 2015. 3, 4, 74, 76

[28] Yunzhi Wang, Long-Qing Chen, and AG Khachaturyan. Shape evolution of a precipitate during strain-induced coarsening: a computer simulation. *Scripta metallurgica et materialia*, 25(6):1387–1392, 1991. 3

[29] John W Cahn and John E Hilliard. Free energy of a nonuniform system. i. interfacial free energy. *The Journal of chemical physics*, 28(2):258–267, 1958. 3

[30] PH Leo, JS Lowengrub, and Herng-Jeng Jou. A diffuse interface model for microstructural evolution in elastically stressed solids. *Acta materialia*, 46(6):2113–2130, 1998. 4, 75, 76

[31] Andrea M Jokisaari, Shahab S Naghavi, Chris Wolverton, Peter W Voorhees, and Olle G Heinonen. Predicting the morphologies of gamma prime precipitates in cobalt-based superalloys. *Acta Materialia*, 141:273–284, 2017. 4, 75

[32] JZ Zhu, T Wang, AJ Ardell, SH Zhou, ZK Liu, and LQ Chen. Three-dimensional phase-field simulations of coarsening kinetics of gamma prime particles in binary ni-al alloys. *Acta materialia*, 52(9):2837–2845, 2004. 4

[33] Tao Wang, Guang Sheng, Zi-Kui Liu, and Long-Qing Chen. Coarsening kinetics of gamma prime precipitates in the ni–al–mo system. *Acta Materialia*, 56(19):5544–5551, 2008. 4

[34] Yuhki Tsukada, Yoshinori Murata, Toshiyuki Koyama, and Masahiko Morinaga. Phase-field simulation of the effect of elastic inhomogeneity on microstructure evolution in ni-based superalloys. *Materials transactions*, 50(4):744–748, 2009. 4

[35] J Kundin, L Mushongera, T Goehler, and H Emmerich. Phase-field modeling of the gamma prime-coarsening behavior in ni-based superalloys. *Acta Materialia*, 60(9):3758–3772, 2012. 4

[36] LT Mushongera, M Fleck, J Kundin, Y Wang, and H Emmerich. Effect of re on directional gamma prime-coarsening in commercial single crystal ni-base superalloys: a phase field study. *Acta Materialia*, 93:60–72, 2015. 4

[37] M Cottura, Y Le Bouar, B Appolaire, and A Finel. Role of elastic inhomogeneity in the development of cuboidal microstructures in ni-based superalloys. *Acta Materialia*, 94:15–25, 2015. 4

[38] Y Wang and AG Khachaturyan. Shape instability during precipitate growth in coherent solids. *Acta metallurgica et materialia*, 43(5):1837–1857, 1995. 4, 75

[39] MP Gururajan and TA Abinandanan. Phase field study of precipitate rafting under a uniaxial stress. *Acta Materialia*, 55(15):5015–5026, 2007. 4

[40] Yuhki Tsukada, Yoshinori Murata, Toshiyuki Koyama, and Masahiko Morinaga. Phase-field simulation on the formation and collapse processes of the rafted structure in ni-based superalloys. *Materials transactions*, 49(3):484–488, 2008. 4

[41] A Gaubert, Yann Le Bouar, and Alphonse Finel. Coupling phase field and viscoplasticity to study rafting in ni-based superalloys. *Philosophical Magazine*, 90(1-4):375–404, 2010. 4

[42] Guillaume Boussinot, Yann Le Bouar, and Alphonse Finel. Phase-field simulations with inhomogeneous elasticity: Comparison with an atomic-scale method and application to superalloys. *Acta Materialia*, 58(12):4170–4181, 2010. 4

[43] Ning Zhou, Chen Shen, Michael Mills, and Yunzhi Wang. Large-scale three-dimensional phase field simulation of gamma prime-rafting and creep deformation. *Philosophical Magazine*, 90(1-4):405–436, 2010. 4

[44] Yuhki Tsukada, Yoshinori Murata, Toshiyuki Koyama, Nobuhiro Miura, and Yoshihiro Kondo. Creep deformation and rafting in nickel-based superalloys simulated by the phase-field method using classical flow and creep theories. *Acta Materialia*, 59(16):6378–6386, 2011. 4

[45] Perry H Leo, John S Lowengrub, and Qing Nie. Microstructural evolution in orthotropic elastic media. *Journal of Computational Physics*, 157(1):44–88, 2000. 4

[46] Michael Greenwood, Jeffrey J Hoyt, and Nikolas Provatas. Competition between surface energy and elastic anisotropies in the growth of coherent solid-state dendrites. *Acta Materialia*, 57(9):2613–2623, 2009. 4, 9, 127

[47] Zhen Zhang, Ming Li, Dejiang Pan, Hailin Su, Xiaodong Du, Ping Li, Yucheng Wu, et al. Effect of sc on microstructure and mechanical properties of as-cast al–mg alloys. *Materials and Design*, 90:1077–1084, 2016. 5

[48] EA Marquis and David N Seidman. Nanoscale structural evolution of al3sc precipitates in al (sc) alloys. *Acta materialia*, 49(11):1909–1919, 2001. 5

[49] A Tolley, V Radmilovic, and U Dahmen. Segregation in al3 (sc, zr) precipitates in al–sc–zr alloys. *Scripta materialia*, 52(7):621–625, 2005. 5, 6

[50] Richard A Karnesky, David C Dunand, and David N Seidman. Evolution of nanoscale precipitates in al microalloyed with sc and er. *Acta Materialia*, 57(14):4022–4031, 2009. 5, 6

[51] Christian Monachon, Matthew E Krug, David N Seidman, and David C Dunand. Chemistry and structure of core-double-shell nanoscale precipitates in al–6.5 li–0.07 sc–0.02 yb. *Acta Materialia*, 59(9):3398–3409, 2011. 5, 6

[52] V Radmilovic, A Tolley, EA Marquis, MD Rossell, Zonghoon Lee, and U Dahmen. Monodisperse al3 (lisczr) core shell precipitates in al alloys. *Scripta Materialia*, 58(7):529–532, 2008. 5, 6

[53] V Radmilovic, Colin Ophus, Emmanuele A Marquis, Marta D Rossell, Alfredo Tolley, Abbey Gautam, Mark Asta, and Ulrich Dahmen. Highly monodisperse core shell particles created by solid-state reactions. *Nature materials*, 10(9):710–715, 2011. 5, 6

[54] BA Chen, L Pan, RH Wang, G Liu, PM Cheng, L Xiao, and J Sun. Effect of solution treatment on precipitation behaviors and age hardening response of al–cu alloys with sc addition. *Materials Science and Engineering: A*, 530:607–617, 2011. 5

[55] ME Krug, David C Dunand, and David N Seidman. Effects of li additions on precipitation-strengthened al–sc and al–sc–yb alloys. *Acta Materialia*, 59(4):1700–1715, 2011. 5

[56] Dinc Erdeniz, Wahaz Nasim, Jahanzaib Malik, Aaron R Yost, Sally Park, Anthony De Luca, Nhon Q Vo, Ibrahim Karaman, Bilal Mansoor, David N Seidman, et al. Effect of vanadium micro-alloying on the microstructural evolution and creep behavior of al-er-sc-zr-si alloys. *Acta Materialia*, 124:501–512, 2017. 5

[57] Bo Jiang, Danqing Yi, Xiaoou Yi, Feng Zheng, Haisheng Wang, Bin Wang, Huiqun Liu, and Zhan Hu. Effect of trace amounts of added sc on microstructure and mechanical properties of 2055 aluminum alloy. *Materials Characterization*, 141:248–259, 2018. 5, 6

[58] Marsha E Van Dalen, Thomas Gyger, David C Dunand, and David N Seidman. Effects of yb and zr microalloying additions on the microstructure and mechanical properties of dilute al–sc alloys. *Acta Materialia*, 59(20):7615–7626, 2011. 5, 6

[59] Z Mao, Wei Chen, David N Seidman, and C Wolverton. First-principles study of the nucleation and stability of ordered precipitates in ternary al–sc–li alloys. *Acta Materialia*, 59(8):3012–3023, 2011. 6

[60] JW Cahn. Critical point wetting. *The Journal of Chemical physics*, 66(8):3667–3672, 1977. 6

[61] Jong K Lee. Morphology of coherent precipitates via a discrete atom method. *Materials Science and Engineering A*, 238(1):1–12, 1997. 6, 85, 87, 88

[62] Jong K Lee. Overview. *Journal of Materials*, pages 37–40, 1997. 6, 85, 88

[63] Alexandre Devaux, Loic Naze, Regine Molins, Andre Pineau, A Organista, JY Guedou, JF Uginet, and P Heritier. Gamma double prime precipitation kinetic in alloy 718. *Materials Science and Engineering: A*, 486(1-2):117–122, 2008. 6

[64] Aliou Niang, Bernard Viguier, and Jacques Lacaze. Some features of anisothermal solid-state transformations in alloy 718. *Materials characterization*, 61(5):525–534, 2010. 6

[65] Cheng Zhang, Liming Yu, and Hui Wang. Kinetic analysis for high-temperature coarsening of gamma double prime phase in ni-based superalloy gh4169. *Materials*, 12(13):2096, 2019. 6

[66] R Sundararaman, P Mukhopadhyay, and S Banerjee. *Metallurgical and Materials Transactions A*, 23(7):2015–2028, 1992. 6

[67] J He, H Han, S Fukuyama, and K Yokogawa. Interface in a modified inconel 718 with compact precipitates. *Acta Materialia*, 46(1):215–223, 1998. 6, 92

[68] R Cozar and A Pineau. Morphology of gamma prime and gamma double prime precipitates and thermal stability of inconel 718 type alloys. *Metallurgical Transactions*, 4(1):47–59, 1973. 6, 92

[69] AJ Detor, R DiDomizio, N Zhou, R Shi, Y Wang, D Mcallister, and M Mills. Enabling large superalloy parts using compact coprecipitation of gamma prime and gamma double prime. *Metallurgical and Materials Transactions A*, 49(3):708–717, 2018. 6, 92

[70] PJ Phillips, D Mcallister, Y Gao, D Lv, REA Williams, B Peterson, Y Wang, and MJ Mills. Nano gamma prime gamma double prime composite precipitate in alloy 718. *Applied Physics Letters*, 100(21):211913, 2012. 6, 92

[71] Rongpei Shi, Donald P McAllister, Ning Zhou, Andrew J Detor, Richard DiDomizio, Micheal J Mills, and Yunzhi Wang. Growth behavior of gamma prime gamma double prime coprecipitates in ni-based superalloy. *Acta Materialia*, 164:220–236, 2019. 6, 92

[72] Ch Leroux, A Loiseau, D Broddin, and G Vantendeloo. Electron microscopy study of the coherent two-phase mixtures l10 l12, in co–pt alloys. *Philosophical Magazine B*, 64(1):57–82, 1991. 6

[73] D Schryvers, G Van Tendeloo, J Van Landuyt, and S Amelinckx. Some examples of electron microscopy studies of microstructures and phase transitions in solids. *Meccanica*, 30(5):433–438, 1995. 6

[74] Arthur H Heuer. Transformation toughening in zro2-containing ceramics. *Journal of the American Ceramic Society*, 70(10):689–698, 1987. 6

[75] Yunzhi Wang, Hong-Ying Wang, Long-Qing Chen, and Armen G Khachaturyan. Microstructural development of coherent tetragonal precipitates in magnesium-partially-stabilized zirconia: A computer simulation. *Journal of the American Ceramic Society*, 78(3):657–661, 1995. 6

[76] K Muraleedharan, D Banerjee, S Banerjee, and S Lele. The alpha2-to-o transformation in ti-al-nb alloys. *Philosophical magazine A*, 71(5):1011–1036, 1995. 7

[77] Soumya Nag, Y Zheng, Richard EA Williams, Arun Devaraj, Andrew Boyne, Yunzhi Wang, Peter C Collins, Gopal Babu Viswanathan, JS Tiley, Barrington Charles Muddle, et al. Non-classical homogeneous precipitation mediated by compositional fluctuations in titanium alloys. *Acta Materialia*, 60(18):6247–6256, 2012. 7

[78] Naoki Miyano, Takahiro Norimura, Teruhiko Inaba, and Kei Ameyama. Reasons for formation of triangular alpha precipitates in ti–15v–3cr–3sn–3al beta titanium alloy. *Materials transactions*, 47(2):341–347, 2006. 7

[79] Shanoob Balachandran, Ankush Kashiwar, Abhik Choudhury, Dipankar Banerjee, Rongpei Shi, and Yunzhi Wang. On variant distribution and coarsening behavior of the alpha phase in a metastable beta titanium alloy. *Acta Materialia*, 106:374–387, 2016. 7

[80] YH Wen, Y Wang, and Long-Qing Chen. Effect of elastic interaction on the formation of a complex multi-domain microstructural pattern during a coherent hexagonal to orthorhombic transformation. *Acta materialia*, 47(17):4375–4386, 1999. 7

[81] YH Wen, Y Wang, LA Bendersky, and Long-Qing Chen. Microstructural evolution during the alpha2 to alpha and o transformation in ti–al–nb alloys: phase-field simulation and experimental validation. *Acta materialia*, 48(16):4125–4135, 2000. 7

[82] YH Wen, Y Wang, and Long-Qing Chen. Influence of an applied strain field on microstructural evolution during the alpha2 to o-phase transformation in ti–al–nb system. *Acta materialia*, 49(1):13–20, 2001. 7

[83] Saswata Bhattacharyya and TA Abinandanan. Evolution of multivariant microstructures with anisotropic misfit: A phase field study. *Acta Materialia*, 57(3):646–656, 2009. 7, 97

[84] W Kurz and DJ Fisher. Fundamentals of solidification, trans. tech. publ. 1984. 8

[85] James S Langer. Instabilities and pattern formation in crystal growth. *Reviews of modern physics*, 52(1):1, 1980. 8

[86] JS Langer. Lectures in the theory of pattern formation. *Chance and matter*, pages 629–711, 1987. 8

[87] David A Kessler, Joel Koplik, and Herbert Levine. Pattern selection in fingered growth phenomena. *Advances in physics*, 37(3):255–339, 1988. 8

[88] Pierre Pelce and A Libchaber. Dynamics of curved fronts. 2012. 8

[89] W Kurz and R Trivedi. Overview no 87 solidification microstructures: Recent developments and future directions. *Acta Metallurgica et Materialia*, 38(1):1–17, 1990. 8

[90] R Trivedi and W Kurz. Dendritic growth. *International Materials Reviews*, 39(2):49–74, 1994. 8

[91] R Trivedi and W Kurz. Solidification microstructures: A conceptual approach. *Acta metallurgica et materialia*, 42(1):15–23, 1994. 8

[92] YS Yoo, DY Yoon, Henry, and MF. The effect of elastic misfit strain on the morphological evolution of gamma prime-precipitates in a model ni-base superalloy. *Metals and materials*, 1(1):47–61, 1995. 8

[93] R Doherty. Physical metallurgy. pages 933–1030, 1983. 8

[94] S Wilayat Husain, M Saeed Ahmed, and Ihtzaz Qamar. Dendritic morphology observed in the solid-state precipitation in binary alloys. *Metallurgical and Materials Transactions A*, 30(6):1529–1534, 1999. 8

[95] YS Yoo. Morphological instability of spherical gamma prime precipitates in a nickel base superalloy. *Scripta materialia*, 53(1):81–85, 2005. 8

[96] A Nusair Khan, I Salam, and A Tauqir. Formation of solid-state dendrites in an alloy steel. *Surface and Coatings Technology*, 179(1):33–38, 2004. 8

[97] Perry Howard Leo and RF Sekerka. The effect of elastic fields on the morphological stability of a precipitate grown from solid solution. *Acta metallurgica*, 37(12):3139–3149, 1989. 9

[98] William W Mullins and Robert F Sekerka. Morphological stability of a particle growing by diffusion or heat flow. *Journal of applied physics*, 34(2):323–329, 1963. 9

[99] David A Kessler and Herbert Levine. Velocity selection in dendritic growth. *Physical Review B*, 33(11):7867, 1986. 9

[100] David A Kessler, Joel Koplik, and Herbert Levine. Steady-state dendritic crystal growth. *Physical Review A*, 33(5):3352, 1986. 9

[101] Angelo Barbieri, Daniel C Hong, and JS Langer. Velocity selection in the symmetric model of dendritic crystal growth. *Physical Review A*, 35(4):1802, 1987. 9

[102] A Barbieri and JS Langer. Predictions of dendritic growth rates in the linearized solvability theory. *Physical Review A*, 39(10):5314, 1989. 9, 108

[103] Samuel M Allen and John W Cahn. A microscopic theory for antiphase boundary motion and its application to antiphase domain coarsening. *Acta metallurgica*, 27(6):1085–1095, 1979. 10

[104] Alain Karma and Wouter-Jan Rappel. Phase-field method for computationally efficient modeling of solidification with arbitrary interface kinetics. *Physical review E*, 53(4):R3017, 1996. 12, 108

[105] AG Khachaturyan. Theory of structural transformations in solids wiley. *New York. transforms*, 1983. 16

[106] Daniel Schneider, Oleg Tschukin, Abhik Choudhury, Michael Selzer, Thomas Bohlke, and Britta Nestler. Phase-field elasticity model based on mechanical jump conditions. *Computational Mechanics*, 55(5):887–901, 2015. 16, 17, 41, 72, 76

[107] A Durga, Patrick Wollants, and Nele Moelans. Evaluation of interfacial excess contributions in different phase-field models for elastically inhomogeneous systems. *Modelling and simulation in materials science and engineering*, 21(5):055018, 2013. 17

[108] Miroslav Silhavy. *The mechanics and thermodynamics of continuous media*. Springer Science and Business Media, 2013. 18

[109] Alain Karma and Wouter-Jan Rappel. Quantitative phase-field modeling of dendritic growth in two and three dimensions. *Physical review E*, 57(4):4323, 1998. 31, 119

[110] M Fahrmann, P Fratzl, O Paris, E Fahrmann, and William C Johnson. Influence of coherency stress on microstructural evolution in model ni-al-mo alloys. *Acta metallurgica et materialia*, 43(3):1007–1022, 1995. 67

[111] CA Bateman and MR Notis. Coherency effects during precipitate coarsening in partially stabilized zirconias. *Acta metallurgica et materialia*, 40(9):2413–2421, 1992. 71

[112] Vincenzo Lanteri, TE Mitchell, and Arthur H Heuer. Morphology of tetragonal precipitates in partially stabilized zro2. *Journal of the American Ceramic Society*, 69(7):564–569, 1986. 71

[113] JD Eshelby. The elastic energy-momentum tensor. *Journal of Elasticity*, 5(3-4):321–335, 1975. 74

[114] Jl Cahn and Dl Hoffman. A vector thermodlnamics for anisotropic surfaces—ii. curved and faceted surfaces. *Acta Metallurgica*, 22(10):1205–1214, 1974. 75

[115] Y Wang, D Banerjee, CC Su, and AG Khachaturyan. Field kinetic model and computer simulation of precipitation of l12 ordered intermetallics from fcc solid solution. *Acta materialia*, 46(9):2983–3001, 1998. 75

[116] J Lee. *Scripta Metallurgica et Materialia*, 32(4):559–564, 1995. 85, 88